University of Bath

UNIVERSITY OF
BATH

PHD

Phase Preserving 3D Micro-Navigation for Interferometric Synthetic Aperture Sonar

Thomas, Benjamin

Award date:
2020

Awarding institution:
University of Bath

Link to publication

Alternative formats

If you require this document in an alternative format, please contact:
openaccess@bath.ac.uk

Download date: 11. May. 2021

Phase Preserving 3D Micro-Navigation for Interferometric Synthetic Aperture Sonar

submitted by

Benjamin Thomas, MEng

for the degree of PhD

of the

University of Bath

Mechanical Engineering

January 2020

COPYRIGHT

Signature of Author . . . .

Benjamin Thomas, MEng

Summary

High-precision navigation is vital to the production of all Synthetic Aperture Sonar (SAS) data products. The required sub-wavelength precision is typically achieved using the Redundant Phase Centre (RPC) micro-navigation algorithm, which exploits time delays measured between redundant signals from adjacent pings to estimate the motion of the vehicle. Today's SAS-equipped Autonomous Underwater Vehicles (AUVs) typically feature two arrays on one or both sides of the vehicle. These interferometric SAS systems are able to make high-resolution estimates of sea-floor bathymetry in addition to the standard SAS imagery. The addition of interferometric arrays also dramatically increases the number of redundant signal pairs between pings that contain useful information.

This thesis describes novel techniques which enable this information to be exploited in order to simultaneously make high-precision navigation and coarse sea-floor bathymetry estimates. Central to the new method is the concept of the *triad of confounding factors*; that is, time delays measured between redundant signals are affected by three quantities: 1) the motion of the vehicle, 2) the sea-floor bathymetry, and 3) the speed of sound. Consequently, inversion of a model of sufficient accuracy allows high-precision estimation of these three quantities.

Results from a novel algorithm that simultaneously estimates the vehicle path to sub-wavelength precision and makes a coarse bathymetry estimate are presented, using both simulated and experimental SAS data. The method yields improved SAS image quality when compared to conventional slant-plane RPC micro-navigation, which is demonstrated using experimental data collected by the $270\text{-}330\,\text{kHz}$ SAS of the CMRE MUSCLE AUV. Since ground-truth is not available using experimental data, the precision of the navigation and coarse bathymetry estimates is demonstrated using simulated data.

The new algorithm has the potential to improve the navigation precision of SAS-equipped AUVs, improving SAS image geo-referencing precision and allowing AUVs to perform longer duration surveys without surfacing. The method is designed to be easily generalisable to repeat-pass SAS, and as such it has the potential to provide the sub-wavelength track co-registration that is required for repeat-pass interferometric bathymetry estimation.

Acknowledgements

Preface

This work initially aimed to develop algorithms for high resolution bathymetry estimation using repeat-pass interferometric synthetic aperture sonar (SAS). The intention was to build upon the repeat pass generalisation of redundant phase centre (RPC) micro-navigation developed by Hunter et al. [1]. However, it became clear that it was not possible to use the resulting estimates of the repeat pass interferometric phase for bathymetry estimation. This limitation is primarily caused by the slant-plane assumption, while the simplifying assumption of a constant and known sound speed is a secondary limitation. These assumptions result in RPC time delays being interpreted only as navigation errors in the slant-plane. For this reason the focus of the project changed to the generalisation of RPC micro-navigation for simultaneous estimation of the vehicle path and the sea-floor bathymetry in three-dimensional space. This development removes the slant-plane assumption, allowing RPC time delays to be attributed to both navigation and bathymetry. The algorithm has been developed and demonstrated for single pass SAS, and has been designed to be simple to generalise to repeat pass collection geometries. This is intended to allow co-registered images to be formed, where the interferometric phase may be used for high resolution bathymetry estimation.

The central theme in this thesis is the idea that time delays measured between redundant signals for the purpose of micro-navigation and/or interferometry are dependent on three observable properties. These relate to the geometry of the observation and the speed of acoustic propagation in the medium. The observation geometry can be considered to be comprised of the sensor geometry and motion, and also the shape of the sea-floor or *bathymetry*. We have termed these three phase influencing properties the '*triad of confounding factors*':

1. The sensor geometry and motion (navigation)

2. The shape of the sea-floor (bathymetry)

3. The acoustic propagation speed (medium)

The triad is 'confounding' due to the link between the three properties, which each contribute to RPC time delays and interferometric phase. Inaccurate knowledge of one member of the triad results in errors in the estimation of the other two. For example, bathymetry estimates derived from the interferogram presented by Hunter et al. [1] would be inaccurate, because navigation errors introduced by the slant-plane assumption cause errors in the repeat-pass interferometric phase and hence bathymetry estimate.

This thesis asserts that accurate estimation of any member of the triad is conditional on having accurate knowledge of the other two members. This is almost never the case; the lack of radio-navigation underwater precludes accurate positioning, the sea-floor is mostly uncharted to the resolution required, and the ocean medium is constantly fluctuating. It is therefore necessary to make *in situ* measurements of each member of the triad. The simultaneous micro-navigation and bathymetry estimation algorithm described in this thesis represents a significant step forward towards this goal, estimating vehicle motion and sea-floor bathymetry using the sound speed measured by the vehicle.

Publications

A number of local and international conferences were attended during the preparation of this thesis. The following authored and co-authored journal publications, conference articles, and conference poster presentations were prepared.

Journal Articles

- B. Thomas, A. Hunter, and S. Dugelay, "Phase Wrap Error Correction by Random Sample Consensus With Application to Synthetic Aperture Sonar Micronavigation," *IEEE Journal of Oceanic Engineering*, pp. 1–15, 2020. [Online]. Available: https://ieeexplore.ieee.org/document/9001250/

Conference articles

- B. W. Thomas, A. J. Hunter, and S. Dugelay, "Model-based 3D micro-navigation and bathymetry estimation for interferometric synthetic aperture sonar," in *Proceedings of the Underwater Acoustics Conference and Exhibition (UACE)*, 2019.

- B. W. Thomas, A. J. Hunter, and S. Dugelay, "Repeat-pass micro-navigation and bathymetry estimation using interferometric synthetic aperture sonar," in *Proceedings of the Institute of Acoustics*, vol. 40, no. 2, Lerici, Italy, 2018.

- B. W. Metcalfe, B. W. Thomas, A. A. Treloar, Z. Rymansaib, A. J. Hunter, and P. R. Wilson, "A compact, low-cost unmanned surface vehicle for shallow inshore applications," in *Intelligent Systems Conference, IntelliSys*, 2017, pp. 961–968. [Online]. Available: https://ieeexplore.ieee.org/document/8324246

- B. W. Thomas and A. J. Hunter, "An investigation into optimal acquisition geometries for repeat-pass synthetic aperture sonar bathymetric mapping," in *Proceedings of the Intitute of Acoustics*, vol. 38, no. 3, 2016.

Conference posters and presentations

- B. W. Thomas, A. J. Hunter, and S. Dugelay, "Time delay estimation for repeat-pass synthetic aperture sonar micro-navigation," in *UKAN UK/US Underwater Acoustics Conference*, 2018.

- B. W. Thomas and A. J. Hunter, "Synthetic Aperture Sonar Simulation using MATLAB with GPU Acceleration," in *Univeristy of Bath HPC Symposium*, Bath, UK, 2017.

- B. W. Metcalfe, B. W. Thomas, A. J. Hunter, and P. R. Wilson, "Rapid-prototyping and field deployment of a USV for the Metropolitan Police," in *IEEE International Conference on Robotics and Automation*, 2016.

Contents

List of Acronyms

ACR area coverage rate

ATR automated target recognition

AUV autonomous underwater vehicle

CCD coherent change detection

CCD coherent change detection

CMRE Centre for Maritime Research and Experimentation

COTS commercial off-the-shelf

CRLB Cramer-Rao lower bound

CSAS circular SAS

CVL correlation velocity log

DEM digital elevation model

DOA direction of arrival

DPCA displaced phase centre antenna

DPIA displaced ping imaging autofocus

DRDC Defence Research and Development Canada

DVL Doppler velocity log

FM frequency modulated

GPGPU general purpose graphics processing unit

HPC high performance computing

IID independent and identically distributed

INS inertial navigation system

InSAR interferometric synthetic aperture radar

InSAS interferometric synthetic aperture sonar

LFM linear frequency modulated

MANEX Multinational AutoNomous EXperiment

MUD Mine Underwater Detection

MUSCLE Minehunting Unmanned underwater vehicle for
Shallow water Covert Littoral Expeditions

NATO North Atlantic Treaty Organisation

NRV NATO research vessel

NUWC Naval Undersea Warfare Centre

PCDL phase centre double localisation

PD propagation delay

PDD propagation delay difference

PRF ping repetition frequency

RANSAC random sample and consensus

ROV remotely operated vehicle

RPC redundant phase centre

RRA redundant receiver array

SAR synthetic aperture radar

SAS synthetic aperture sonar

SIFT scale-invariant feature transform

SLL side lobe level

SNR signal to noise ratio

SPRPC slant-plane redundant phase centre

SRTM shuttle radar tomography mission

SURF speeded up robust features

TDOA time difference of arrival

TOA time of arrival

TOF time of flight

TOFD time of flight difference

UXO unexploded ordinance

1 Introduction

1.1 Synthetic aperture sonar

Synthetic aperture sonar (SAS) is a coherent acoustic imaging technology capable of generating sea-floor imagery with centimetre-scale resolution, which is theoretically independent of range and frequency [2]. This is a distinct advantage over more conventional sidescan sonar, which creates images with resolution that deteriorates with range. This makes SAS systems highly desirable in survey applications where both high resolution and high area coverage rate are required. In recent years, commercially available SAS hardware [3, 4, 5] has been used to perform high resolution sea-bed mapping for numerous applications, such as the detection of naval mines [6] or unexploded ordinance (UXO) [7], sub-sea archaeology [8, 9], monitoring of World War II munitions dumps [10], and surveying underwater assets, such as oil and gas pipelines [11]. SAS was used during the search for the missing airliner MH370 [12], due to its favourable combination of high resolution and large area coverage rate. In addition, SAS has been demonstrated in underwater geological surveying, for example in mapping hydrothermal systems [13] and detecting sea-floor gas seepage [14].

Figure 1.1 contains a selection of SAS images that showcase the impressive capabilities of modern SAS systems. Figure 1.1a is a reproduction of the lower panel of [9, Fig. 6], which is a false-colour image of one of the many shipwrecks in the Skagerrak WWII munitions dump site[1], where colour encodes depth. This image was captured using a HiSAS 1030 manufactured by Kongsberg Maritime, mounted on a HUGIN autonomous underwater vehicle (AUV) during surveys of the site in 2015 and 2016. Figure 1.1b is a reproduction of [6, Fig. 1], which shows two distinct types of sea-floor and seven mine-like targets. The upper left region of the image contains sand ripples, while the remainder shows a flat sandy seabed. This image was generated by the Minehunting Unmanned underwater vehicle for

Shallow water Covert Littoral Expeditions (MUSCLE) AUV, which is a Bluefin 21 AUV equipped with an interferometric synthetic aperture sonar (InSAS) manufactured by Thales Underwater Systems. The MUSCLE system is operated by the NATO Centre for Maritime Research and Experimentation (CMRE). Figure 1.1c is a reproduction of [15, Fig. 3], which clearly shows artificial objects on the sea-floor. This image was captured using an AquaPix® InSAS manufactured by Kraken Robotics mounted on the Arctic Explorer AUV from Defence Research and Development Canada (DRDC). Figure 1.1d is a further HiSAS 1030 image reproduced from [7, Fig. 2], which shows the extent to which UXOs have migrated around the Skagerrak dump site.

1.2 Interferometric synthetic aperture sonar

Depth estimates, encoded by colour in Figures 1.1a and 1.1d, are made by the process of interferometry. This involves capturing multiple (typically two) images of the same scene with

---

[1]After World War II, the Skagerrak strait, an area of deep water between Norway and Denmark, was used as a chemical munitions dump site. Cargo ships were loaded with munitions, positioned in the strait, and sunk. At least 170,000 tons of chemical munitions were dumped there by British and American authorities.

(a)

(b)

(c)

(d)
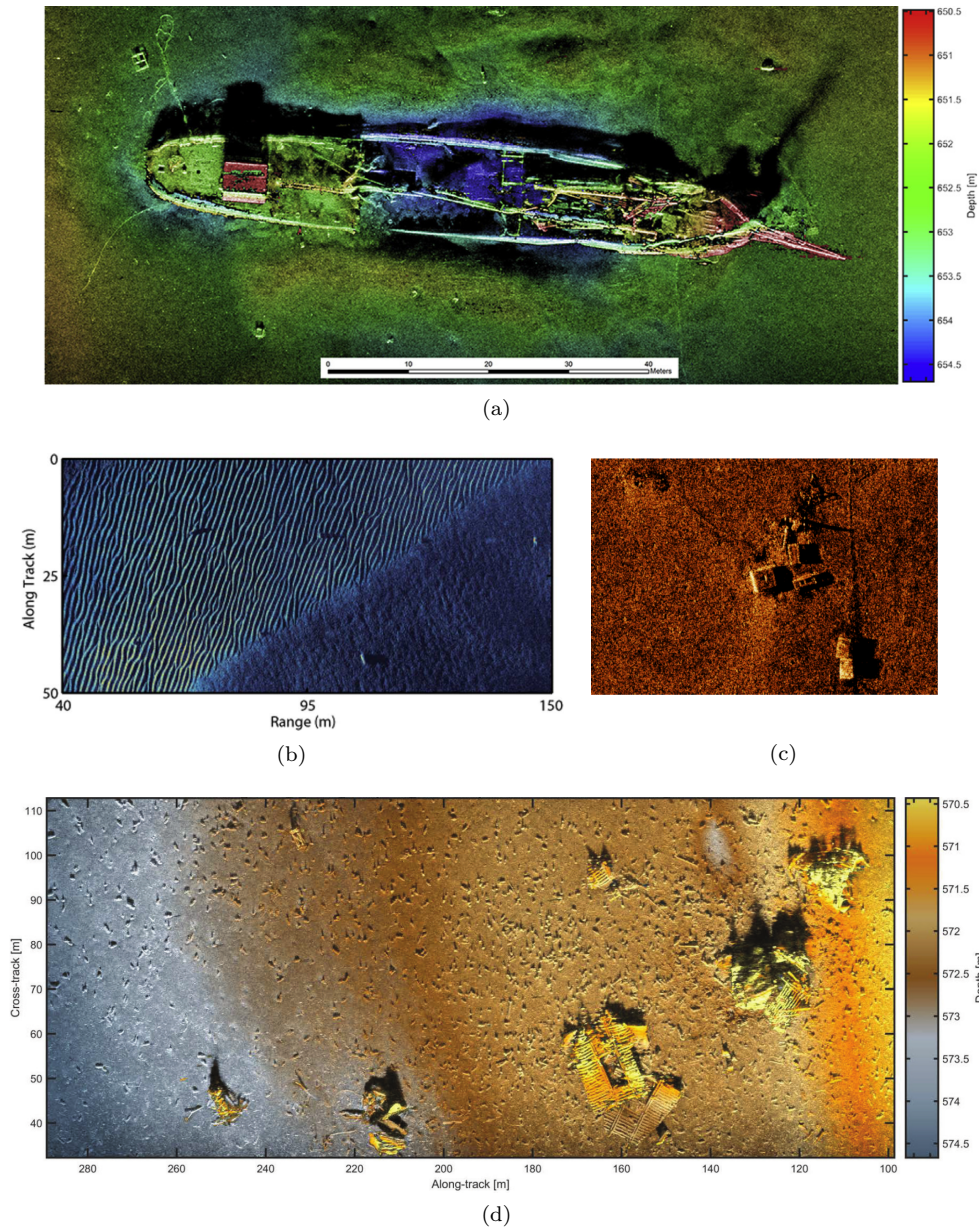
Figure 1.1: Example imagery from various SAS systems. (a) A false-colour HiSAS 1030 image of a shipwreck in the Skagerrak WWII dump site where colour encodes depth[3][9]. (b) A MUSCLE SAS image containing two distinct sea-floor morphologies and seven mine-like objects. Reproduced with permission from [6], © 2015 IEEE. (c) An AquaPix® SAS image showing man-made objects on the sea-floor. Reproduced with permission from [15]. (d) A further HiSAS 1030 image of debris in the Skagerrak site [7]. Image courtesy of and used with permission of the Norwegian Defence Research Establishment (FFI) and the Norwegian Coastal Administration.

---

[3]Reprinted from Journal of Archaeological Science, Volume 89, Ødegård, Øyvind et.al., Archaeological use of Synthetic Aperture Sonar on deepwater wreck sites in Skagerrak, Page 7, Copyright 2019, with permission from Elsevier.
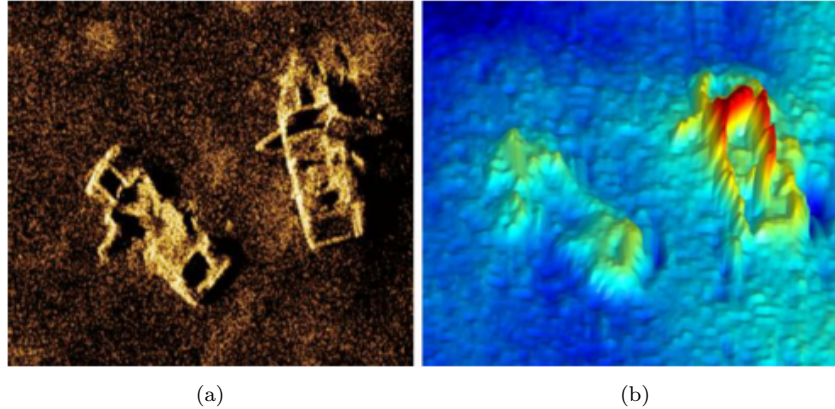
Figure 1.2: SAS data products captured by the Kraken AquaPix® InSAS of two objects resembling cars on the sea-floor, reproduced with permission from [4]. (a) Intensity image, with theoretical resolution of 3×3 cm (b) The corresponding bathymetry estimate, with theoretical resolution of 12.5×12.5 cm.

slightly differing acquisition geometries, where the difference in acquisition geometry is well known. Small differences between sub-windows of the images are used to infer sea-floor depth. This is typically achieved in a single pass of a vehicle equipped with multiple receiving arrays with known separation, as described in Section 2.

This technique has some limitations, which are well illustrated by Figure 1.2. It shows the intensity image and corresponding bathymetry estimate of two objects that resemble cars on the sea-floor, captured by a Kraken Aquapix® InSAS system. The intensity image in Figure 1.2a has a theoretical resolution of 3×3 cm, while the bathymetry estimates in Figure 1.2b have a spatial resolution of 12.5×12.5 cm. This disparity between image and bathymetry resolution is typically around an order of magnitude, and is caused by the size of the sub-windows inherent to interferometric processing (see Section 2.4.2). Improved bathymetry resolution can be obtained by reducing the sub-window size at the expense of vertical precision [16, Ch. 8.1]. Improved vertical precision can be achieved by increasing the separation between the receiver arrays [16, Ch. 3.3], and the number of separated receiver arrays [17].

1.3 Repeat-pass interferometric synthetic aperture sonar

Since the number of receiver arrays and their separation cannot be increased without limit due to the size constraints imposed by underwater vehicles, there is considerable interest in repeat-pass interferometric depth estimation. This allows multiple images to be acquired with arrays separated by an arbitrary distance. However, repeat-pass interferometry introduces a challenge; the repeat-pass acquisition geometry must be estimated to sub-wavelength precision to support the coherent, phase reliant processing [18, 19, 20, 21].

Another common application of repeat-pass interferometric processing is coherent change detection (CCD). This allows detection of sub-wavelength scale changes in the scene by analysis

of the magnitude of the complex coherence function between co-registered images [22, 23, 24]. However, the co-registration accuracy requirements are relaxed when compared to repeat-pass depth estimation (needing only sub-pixel accuracy), which is achievable with conventional sparse feature-based [25] and dense [22] image registration approaches.

1.4 Synthetic aperture sonar systems

A typical SAS system consists of a transmitter that regularly projects acoustic pulses or *pings* into the medium, and at least one vernier array of receiving transducers which sense the echoes reflected by the environment. These reflections originate from the sea-floor, objects on the sea-floor, and objects in the water column. The assembly of transducers is moved along a path, which is typically nominally rectilinear (strip-map SAS) or circular (CSAS), forming a densely sampled *synthetic aperture*. The geometry for strip-map SAS is pictured in Figure 2.10. If the path traversed by the sonar is known to sufficient precision, the reflected echoes collected along this synthetic array can be coherently combined to form a focused SAS image, where the along-track synthetic array footprint size is independent of range.

Due to the side-looking geometry used by SAS systems, the platform carrying the SAS hardware is required to travel relatively close to the sea-floor, at an altitude of approximately 1/10 of the maximum range. For shallow-water environments, the SAS can be mounted on a surface vessel, such as the TNO Mine Underwater Detection (MUD) system [26] or smaller systems such as remotely operated vehicles (ROVs) [27]. In deeper water, underwater vehicles are required, which fall into two groups, tow-fish and AUVs. Tow-fish are pulled behind a surface ship, approximately following the path taken by the ship (many with the help of actuated control surfaces), while AUVs are not tethered to a surface ship. Being tethered to a supporting vessel has both advantages and disadvantages. The tether can contain a high-bandwidth communication link, allowing data to be processed and analysed in near real time on-board the surface ship. However, they are not suitable when a surface ship cannot be used, for example in covert operations, under ice, or in high seas. A further advantage of AUVs is the ability for a single surface ship to operate multiple assets simultaneously, reducing the total survey cost and increasing the overall area coverage rate (ACR).

Photographs of the three AUVs already mentioned are shown in Figure 1.3. These vehicles are all equipped with interferometric SAS systems, where the vertically separated receiver arrays are clearly visible on the HUGIN and REMUS vehicles in Figures 1.3b and 1.3c respectively. AUVs are required to carry out pre-planned or adaptive missions with minimal human intervention, due to the high latency and low data bandwidth inherent to acoustic communications [28]. However, underwater navigation is challenging, due to the lack of radio-navigation services underwater. Therefore these AUVs are equipped with sophisticated navigation systems, typically comprising a high-grade inertial navigation system (INS) and an aiding sensor such as a Doppler velocity log (DVL) or correlation velocity log (CVL). Measurements of linear accelerations and angular rates are available from an INS, while a DVL or CVL measures linear velocities. Measurements from these systems are typically combined using a state-estimation

13

algorithm such as a Kalman filter [29]. However, integrating velocity measurements in this manner suffers from drift caused by accumulated errors, which are typically larger than the precision requirement for generating focused SAS images.

The experimental SAS data used in this thesis were collected by the MUSCLE AUV provided by CMRE, during the Multinational AutoNomous EXperiment (MANEX) sea trial in 2014. Therefore, MUSCLE system parameters are used throughout this thesis when hardware-specific parameters are required. However, the concepts presented in this thesis are intended to be applicable to a wide range of SAS systems.

1.5 Synthetic aperture sonar motion estimation challenge

The maximum tolerable accumulated position error for generating focused SAS images is commonly quoted as $\lambda_0/16$ along the length of the synthetic aperture [2] where λ_0 denotes wavelength. For example, for the MUSCLE system with $\lambda_0 \approx 5\,\mathrm{mm}$, this equates to approximately $0.3\,\mathrm{mm}$ over a maximum synthetic array length of approximately $15\,\mathrm{m}$ at maximum range. This precision is unachievable with typical on-board navigation hardware, which has been a significant challenge for the development of SAS technology.

A common method for achieving the required navigation precision is the slant-plane redundant phase centre (RPC) micro-navigation algorithm [30, 31]. These algorithms exploit the time delays that can be measured between signals received by overlapping (redundant) portions of the array between pings. In these micro-navigation implementations, it is assumed that the vehicle and sea-floor exist in a two-dimensional *slant-plane*, and to attribute time delays solely to the motion of the sonar in this plane. However, inevitable deviations from the ideal linear trajectory break the assumption of rotational symmetry about the track upon which the slant-plane assumption is based, which causes image defocusing [16, 32].

In general, the time delays between RPC arrays are a function of the motion of the sonar, the sea-floor bathymetry, and the speed of acoustic propagation in the medium. Therefore, the slant-plane assumption has been abandoned in most developments of through-the-sensor navigation estimation algorithms. Instead, estimates of the bathymetry are included in the micro-navigation algorithms, either by assuming a flat sea-floor at a given depth [33], or by estimating the bathymetry using the interferometric arrays as a sidescan interferometer [16, 32].

Synthetic aperture sonar micro-navigation has been the subject of much research in recent years, with many different algorithms having been developed. However, there is scope for improvement for four main reasons:

1. The majority of research effort has been towards making a navigation estimate that results in focused images. However, this is not necessarily the same as the path of the vehicle, due to certain model simplifications or errors in the bathymetry or speed of acoustic propagation. Attempts to integrate micro-navigation estimates into the vehicle navigation solution have therefore seen limited success [34].

2. Interferometric SAS systems create multiple RPC array pairs between pings. For example,
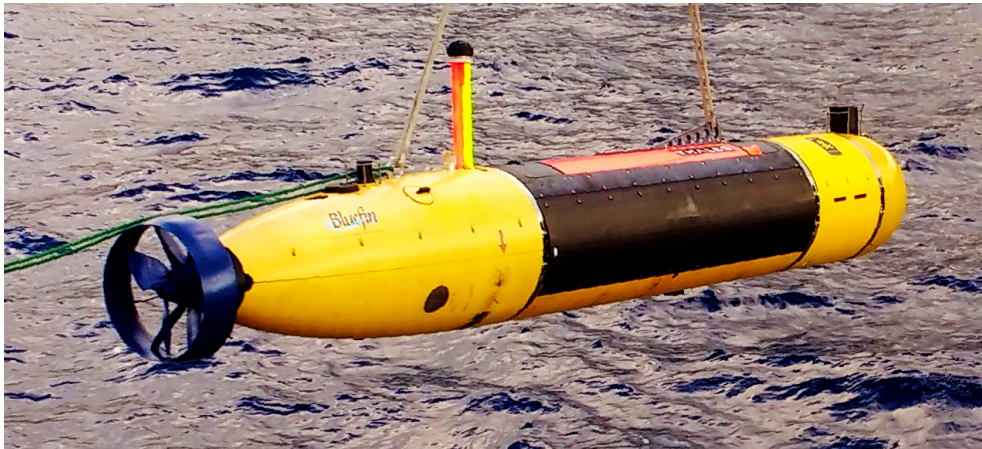
(a)

(b)

(c)

Figure 1.3: Examples of AUV equipped with SAS (a) The MUSCLE AUV. The black section is an acoustically transparent window, behind which the transducers are positioned. Produced with permission from CMRE. (b) The HUGIN AUV equipped with a HiSAS 1030. The two receiver arrays that allow interferometry are clearly visible, with the transmitter between them. Image courtesy of Kongsberg Maritime AS. (c) A REMUS 600 AUV equipped with a Kraken AquaPix® InSAS2 system. The black rectangles are the transducers; the smallest (fore-most) is the transmitter and the remainder are modular receiving arrays. Reproduced with permission from [4].

a conventional dual-sided InSAS creates 8 RPC array pairs between adjacent pings[4]. A maximum of 4 of these pairs have been exploited for the purpose of micro-navigation in the published literature [35].

3. It is common to use a piece-wise process to estimate bathymetry using sidescan interferometry, and then make a micro-navigation estimate using this bathymetry estimate. This has the potential to introduce errors, because different data are used for each step. However, if the mutual information contained in the multiple RPC pairs is used judiciously, a coarse bathymetry estimate and a navigation estimate can be made simultaneously using the same data.

4. Repeat-pass interferometric bathymetry estimation is yet to be demonstrated for strip-map SAS.

1.6 Research question

Given the existing scope for improvement in synthetic aperture sonar micro-navigation performance, the question this thesis aims to answer is:

How can redundant data collected by interferometric synthetic aperture sonar be best exploited for accurate and precise navigation of autonomous underwater vehicles?

To answer this question, we first introduce the idea of the *triad of confounding factors*.

1.6.1 The 'triad of confounding factors'

It is well known that the time delays measured between RPC array pairs are a function of the motion of the sonar (in all 6 degrees of freedom), the sea-floor bathymetry, and the speed of acoustic propagation in the medium [33]. We refer to these quantities as the '*triad of confounding factors*' [21]; navigation, bathymetry, and medium.

With this in mind, one of the main novel contributions of this thesis is the generalisation of the RPC micro-navigation algorithm for interferometric synthetic aperture sonar (InSAS). Under the assumption of a known acoustic propagation speed, the new algorithm is capable of simultaneously making both a three-dimensional vehicle navigation estimate and a coarse bathymetry estimate using the redundant data collected by overlapping portions of the phase centre arrays of adjacent pings. The new algorithm addresses points 1-3 above, by using the redundant data collected between adjacent pings for mutual estimation of bathymetry and navigation. The method

1. avoids model simplifications that have the potential to cause navigation or bathymetry errors,

2. utilises more of the redundant data collected by RPC arrays between adjacent pings, and

---

[4]This number is increased to 12 if the interferometric RPC array pairs (i.e. within the same ping) are included.

3. simultaneously estimates navigation and bathymetry using the same data.

While point 4 above has not been completely addressed, preliminary work towards extending the algorithm to repeated passes has shown significant promise [21]. However, generalisation of the algorithm to repeat pass acquisitions is considered to be outside of the scope of this thesis and is suggested as further work.

1.7   Thesis outline

The structure of this thesis is as follows. Chapter 2 gives an introduction to interferometric synthetic aperture sonar (InSAS). The chapter begins with the concept of echo sounding and its development into sidescan sonar. The achievable resolution of such a real-aperture system is presented, and its inherent limitations are identified. The concept of synthetic aperture imaging is then introduced, and an analysis of the errors introduced by the phase centre and stop-and-hop approximations is given. Finally, a summary of depth estimation using interferometry is given.

Chapter 3 presents a thorough decomposition of the literature relevant to synthetic aperture sonar micro-navigation. We identify the limitations of existing micro-navigation approaches and motivate the development of the new algorithm developed in Chapter 6.

In Chapter 4 we describe methods ubiquitous to the field of micro-navigation; range windowing, surge estimation and time delay estimation. These methods are used in the method developed in Chapter 6.

Chapter 5 describes and evaluates a novel method for identifying and correcting phase wrap errors in time delay estimates used in micro-navigation. The method is a local phase unwrapping method which utilises a robust regression to fit a model to the error-free samples. Samples that do not fit the model are corrected by unwrapping them around the fitted model. We demonstrate superior performance to the branch-cuts method, which has also been used to solve this problem.

Chapter 6 describes a novel algorithm for interferometric SAS systems that simultaneously estimates a high-precision 3D path of the vehicle and makes a coarse bathymetry estimate. The method is verified and assessed using both experimental and simulated data, and superior SAS imagery is demonstrated when compared to the conventional slant-plane RPC micro-navigation algorithm.

Chapter 7 summarises the thesis and makes suggestions for future work.

2 Interferometric Synthetic Aperture Sonar

The principle of all active sonar systems is to transmit acoustic energy into a propagation medium, and to receive echoes of the signal reflected off a target or the environment after a measured delay. This propagation time can be converted into a distance, using an assumed speed of sound and the collection geometry.

2.1 Echo sounding

The simplest sonar for depth or range measurement is the *echo sounder*, shown in Figure 2.1. A pulse of acoustic energy or *ping* is transmitted downwards into the water column. The acoustic waves travel until they are reflected off the sea-floor. These reflected waves propagate and spread, and a replica of the transmitted waveform is received by the receiver after a propagation delay τ_{p}. The distance to the sea-floor is given by

$$r = \frac{\tau_{\mathrm{p}} c}{2},\tag{2.1}$$

where c is the average speed of sound along the path, under the assumption that the transmitter and receiver are co-located and stationary.
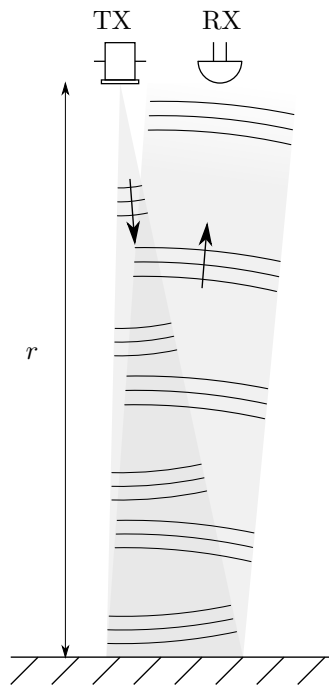
Figure 2.1: Geometry of an echo sounder. An acoustic signal is transmitted by the transmitter (TX) downwards towards the sea-floor. A reflection is received by the receiver (RX) after some delay. The range to the sea-floor can be estimated using (2.1).

2.1.1   The sonar equation

The monostatic sonar equation [36] below describes the sound intensity in decibels at the receiver

$$RL = SL - 2TL + TS \tag{2.2}$$

where SL, TL and TS are the source level, transmission loss, and target strength respectively in decibels. The source level (SL) is defined as the intensity in decibels of the transmitted signal measured at a distance of $1\,\mathrm{m}$ from the transmitter. The target strength (TS) describes the acoustic reflectivity of a scatterer. It is defined as the intensity of the reflected signal at a distance of $1\,\mathrm{m}$ from the scatterer relative to the intensity of the transmitted signal at the scatterer. The transmission loss (TL) describes the amount of energy lost between the transducer and the scatterer in each direction and is given by

$$TL = -20 \log\left(\frac{|\psi|}{|\psi_0|}\right) \tag{2.3}$$

for a plane wave, where ψ is the field intensity and ψ_0 is the field intensity at a distance of $1\,\mathrm{m}$ from the source.

The losses that the acoustic signal experiences as it propagates are due to the signal spreading and absorption processes. Acoustic absorption converts acoustic energy to heat through internal friction, thermal conduction, and via chemical relaxation processes in aqueous solutions e.g. sea-water [36].

The spreading loss for a spherically spreading wave is given by

$$TL_{\mathrm{spreading}} = 10 \log(r^2) = 20 \log(r) \tag{2.4}$$

where r is the distance from the source. Spreading losses motivate the use of high power transmitted signals and narrow acoustic beams in order to achieve favourable signal to noise ratio (SNR) at the receiver. Since beam-width is inversely proportional to frequency and proportional to transducer size, lower frequency systems suffer from higher spreading losses unless the size of the transducer is increased to compensate.

Absorption losses are typically described using empirical formulae. In sea-water, the loss in decibels due to absorption over a propagation distance r meters is approximated by

$$TL_{\mathrm{absorption}} = r \left(\frac{A_{\mathrm{abs}}}{f_1^2 + f^2} + \frac{B_{\mathrm{abs}}}{f_2^2 + f^2} + C_{\mathrm{abs}} \right) f^2 \times 10^{-3} \tag{2.5}$$

19
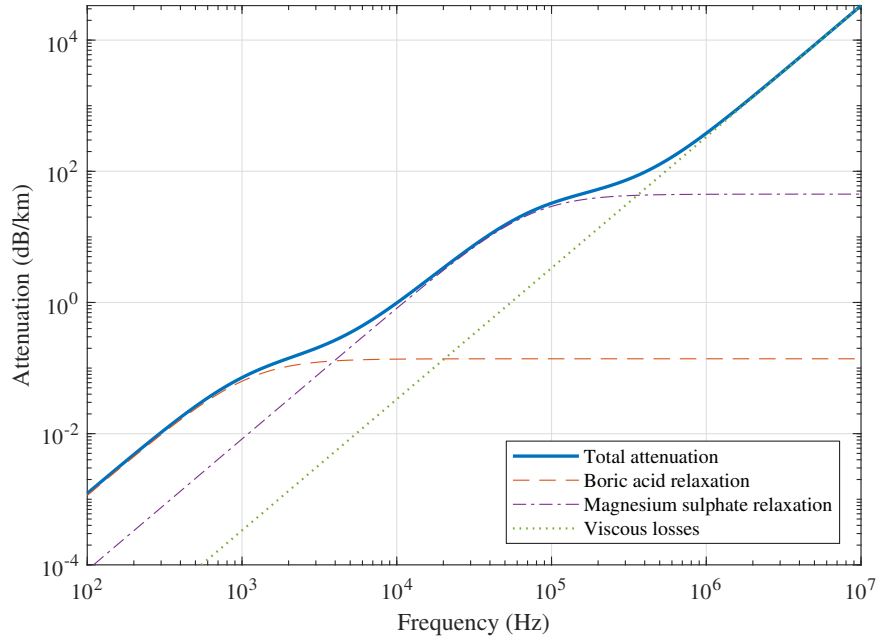
Figure 2.2: Frequency dependent absorption losses are caused by chemical relaxation processes of boric acid and magnesium sulphate, in addition to viscous friction. The absorption loss is shown for a temperature of $10\,^{\circ}\mathrm{C}$, a salinity of $35\,\mathrm{ppt}$, a depth of $0\,\mathrm{m}$ and a pH of 8.1.

where f denotes frequency, with

$$A_{\mathrm{abs}} = 0.0024 S \exp(0.032T - 0.011z + 1.8(\mathrm{pH} - 8)) \tag{2.6}$$

$$B_{\mathrm{abs}} = 0.63 S \exp(0.071T - 0.17z) \tag{2.7}$$

$$C_{\mathrm{abs}} = 4.9 \times 10^{-10} \exp(-0.038T - 0.040z) \tag{2.8}$$

$$f_1 = 780 \exp(0.034T) \tag{2.9}$$

$$f_2 = 42000 \exp(0.056T), \tag{2.10}$$

where T is the temperature in degrees Celsius, S is the salinity in parts per thousand (ppt), z is the depth in meters and

$$\mathrm{pH} = \log_{10}\left(\frac{1}{a_{H^+}}\right) \tag{2.11}$$

describes the acidity of the solution where a_{H^+} is the hydrogen ion activity [37].

The first term describes the chemical relaxation of the boric acid ⇔ borate systems as discovered by Yeager [38]. The second term describes the effect of relaxation of magnesium sulphate [39]. The mechanism and kinetics of this relaxation are complex, and the interested reader is referred to [40] for further detail. The third term is due to shear and bulk viscosity of pure water, which does not exhibit a relaxation frequency. Losses due to thermal conduction are negligible [41]. Figure 2.2 shows the absorption loss as a function of frequency for a temperature of $10\,^{\circ}\mathrm{C}$, a salinity of $35\,\mathrm{ppt}$, a depth of $0\,\mathrm{m}$ and a pH of 8.1.
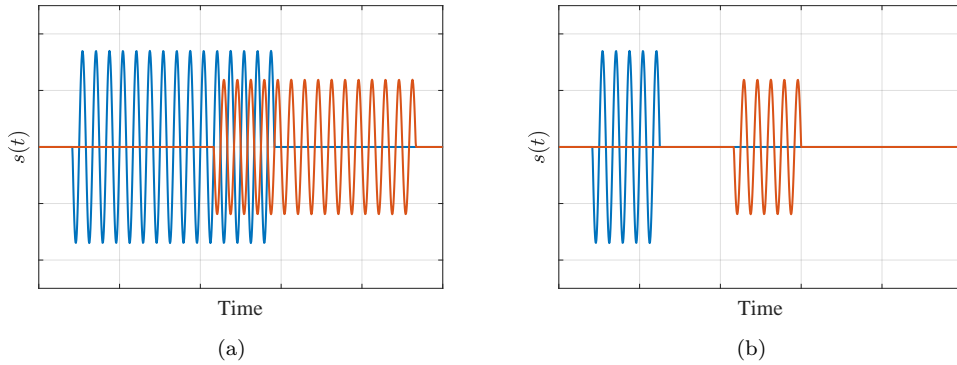
Figure 2.3: The range resolution of a pulsed echo ranging system is dependent on the length of the pulse. (a) Simulated response from two separated targets insonified by a tone burst. The length of the tone burst is such that the two targets cannot be resolved. (b) Simulated response using a shorter tone burst, with the same separation between the targets. The two targets can be resolved, but the total signal energy is reduced.

2.1.2   Range resolution

The range resolution of a pulsed echo ranging system is proportional to the duration of the pulse, with short pulses giving high range resolution. However, the use of short impulse-like pulses limits the total transmitted energy, since water has an upper acoustic amplitude limit due to cavitation [36]. Consider the simulated echoes received from two separated targets insonified by a tone burst shown in Figure 2.3. The target responses cannot be resolved if the responses are not separated by longer than the duration of the signal. That is, the resolution of a pulsed echo ranging system is

$$\Delta r = \frac{cT}{2} \tag{2.12}$$

were T is the pulse duration, so shorter pulses give better range resolution at the expense of total signal energy and hence SNR.

If both high range resolution and high SNR are desired, a combination of longer duration pulses and pulse compression is required. This improves the range resolution to

$$\Delta r = \frac{c}{2B} \tag{2.13}$$

where B is the band-width of the pulse. This removes the resolution dependence on signal duration, allowing the use of longer signals and hence improved SNR.

2.1.2.1   Pulse compression / matched filtering

Pulse compression allows high range resolution to be obtained from wide bandwidth, long duration pulses. Any signal with a narrow auto-correlation function is suitable, however the linear frequency modulated (LFM) chirp is commonly used either with increasing (up chirp) or decreasing (down chirp) frequency. It is desirable for the pulse length to be shorter than the

propagation delay at minimum range to avoid cross-talk [42].

A complex LFM chirp is defined by

$$s(t) = A \operatorname{rect}\left(\frac{t}{T}\right) \exp\left(j2\pi f_c t + j\pi \frac{B}{T} t^2\right), \tag{2.14}$$

where t is the time axis, A is the peak amplitude, T is the chirp length, and f_c and B are the centre frequency and bandwidth of the chirp respectively.

Figure 2.4 shows an example LFM up chirp. Figure 2.4a shows the chirp amplitude as a function of time. The pulse has duration T and peak-to-peak amplitude $2A$. Figure 2.4b shows the Fourier transform of the same up chirp, which is approximately rectangular. Windowing this frequency domain signal allows adjustment of the ratio of side lobe level (SLL) to range resolution [43]. Figure 2.4c is a time-frequency representation of the up chirp, showing that the instantaneous frequency is linearly swept over the bandwidth B, from $f_c - \frac{B}{2}$ to $f_c + \frac{B}{2}$ over the time duration of the pulse T. The auto-correlation of the chirp is shown in Figure 2.4d.

The matched filter is the pulse compression method which maximises SNR in the presence of white, Gaussian noise [16]. The matched filter is a cross-correlation with a replica of the transmitted signal, giving the match filtered signal as

$$e(t) = \int_{-\infty}^{\infty} e'(\tau) s(\tau + t) d\tau \tag{2.15}$$

$$= e'(t) \star s(t), \tag{2.16}$$

where $e'(t)$ is the received echo data and $s(t)$ is the transmitted signal, and $\star$ denotes convolution. The pulse compression operation is commonly performed as a multiplication in the frequency domain using the convolution theorem [44],

$$e(t) = \mathcal{F}^{-1}\left\{E(\omega)\right\} \tag{2.17}$$

$$= \mathcal{F}^{-1}\left\{E'(\omega) \cdot S(\omega)\right\}, \tag{2.18}$$

where $E'(\omega)$, $S(\omega)$ and $E(\omega)$ are the Fourier transforms of the echo data, transmitted signal, and pulse-compressed echo data respectively.

The Fourier transform of a time domain signal $x(t)$ is given by

$$X(\omega) = \mathcal{F}\left(x(t)\right) \tag{2.19}$$

$$= \int_{-\infty}^{\infty} x(t) e^{-j\omega t} dt \tag{2.20}$$

where $\omega = 2\pi f$ is the angular frequency.

The $-3\,\mathrm{dB}$ width of the resulting auto-correlation function is often quoted as the ideal range resolution of the match-filtered pulse, given by

$$\delta_r = \varpi_r \frac{c}{2B} \tag{2.21}$$

22
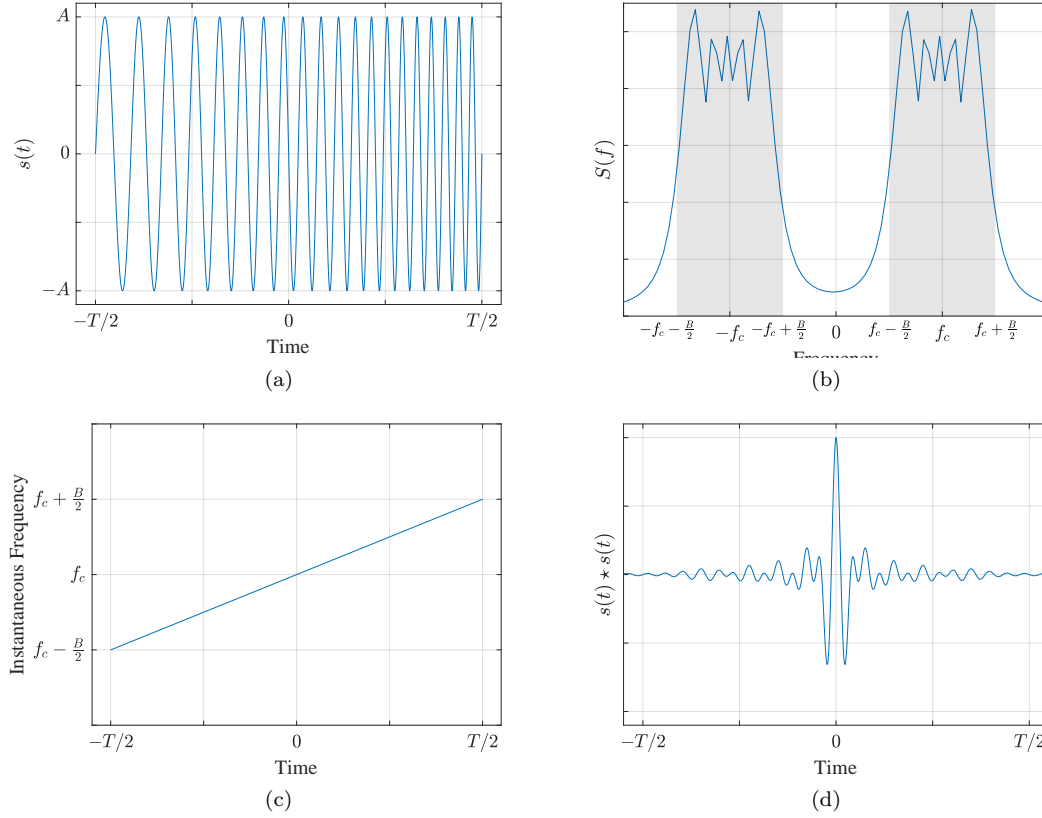
Figure 2.4: A linear frequency modulated (LFM) up chirp (a) in the time domain (b) frequency domain (c) time frequency domain (d) autocorrelation function.

[45] where c is the speed of sound and B is the band-width of the chirp. The constant ϖ_r reflects the effect of any windowing of the signal to adjust the level of range side-lobes.

2.1.3 Ping repetition frequency

Unambiguous range measurements are only obtainable if a maximum of one ping is in flight at a time, unless multiple orthogonal pulses are used. This means the maximum ping repetition frequency is range-dependent, and is given by

$$\text{PRF}_{\max} = \frac{c}{2R_{\max}} \tag{2.22}$$

where $R_{\max}$ is the maximum range between the sonar and the sea-floor.

2.2 Real-aperture imaging

A common real-aperture sea-floor imaging system is sidescan sonar. Acoustic pings are regularly transmitted as the sonar travels along a straight track. Each ping is transmitted normal to the direction of travel, at an angle slightly below horizontal, as depicted in Figure 2.5. The echo
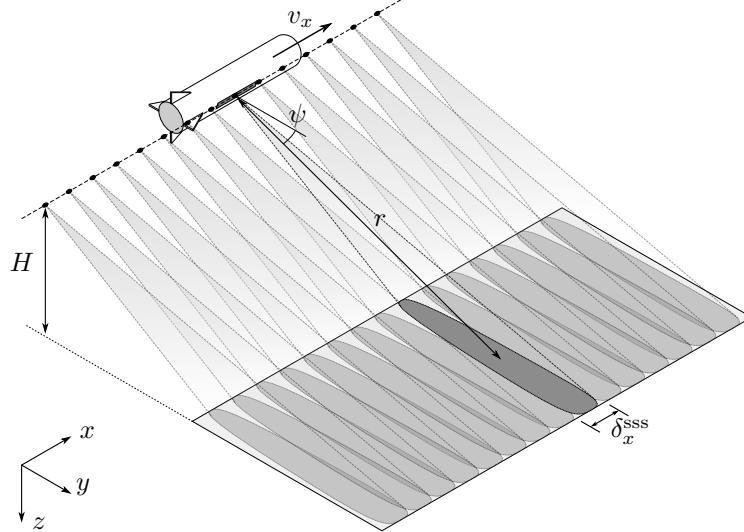
Figure 2.5: Sidescan sonar imaging geometry. The platform travels at an along-track velocity of v_x at an altitude of H above the sea-floor. The along-track -3 dB width of the real aperture footprint is δ_x^{sss} and the across-track -3 dB resolution is δ_y^{sss} at a range of r from the sonar. The range-dependent grazing angle is denoted ψ.

amplitude from each ping is recorded as a function of time, and an image can be formed by stacking these echo recordings. An example sidescan sonar image using the 270-330 kHz SAS[5] of the MUSCLE AUV is shown in Figure 2.9a.

2.2.1 Across-track resolution

The across-track resolution of a sidescan sonar is a function of the range-dependent depression angle. It is given by

$$\delta_y^{\text{sss}} = \frac{\delta_r}{\cos(\psi)} \tag{2.23}$$

where $\psi = \sin^{-1}(H/r)$ is the range-dependent grazing angle, and H is the vertical distance between the sonar and sea-floor at range r.

Sidescan sonar systems typically operate with small grazing angles with $H \ll r$, such that $\cos(\psi) \approx 1$. Making this approximation and substituting (2.21) gives

$$\delta_y^{\text{sss}} = \delta_r \tag{2.24}$$

$$= \varpi_r \frac{c}{2B}, \tag{2.25}$$

that is, for small grazing angles the across-track resolution is equal to the range resolution.

---

[5]A SAS can operate as a sidescan sonar by summing the echoes received by all of the receivers. This is equivalent to beam-forming the real array in the broad-side direction.
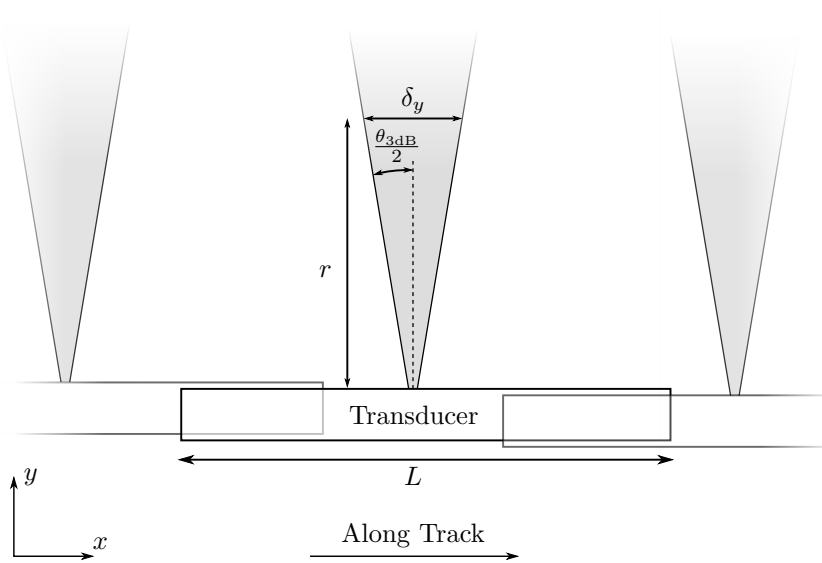
Figure 2.6: The along-track -3 dB resolution of a sidescan sonar is proportional to range, and depends on the aperture length and the operating frequency.

2.2.2 Along-track resolution

Consider the sidescan sonar depicted in Figure 2.6, which consists of a mono-static aperture of length L in the along-track direction. The Fraunhoffer approximation to the Fresnel-Kirchoff diffraction formula is used to describe the effect of the aperture on the radiation pattern in the *far field* or *Fraunhoffer region*. The Fraunhoffer approximation is valid at ranges larger than the Rayleigh distance, defined by [46]

$$R_{\text{Rayleigh}} = \frac{2L^2}{\lambda} \tag{2.26}$$

where L is the largest aperture dimension and λ is the wavelength.

The Fraunhoffer approximation to the field radiated from an aperture is given by

$$\psi(\boldsymbol{x}) = S(f)B(\theta, \phi)\frac{\exp(-jkr_0)}{4\pi r_0} \tag{2.27}$$

where $S(f)$ is the signal spectrum, $B(\theta, \phi)$ is known as the *beam-pattern*, and the last term is the expression for the free-space Green's function, where $k = 2\pi f/c$ is the wave-number [41].

The expression for the aperture beam-pattern is given by

$$B(\theta, \phi) = jk(1 + \cos\phi)A\left(\frac{f}{c}\cos\theta\sin\phi, \frac{f}{c}\sin\theta\sin\phi\right) \tag{2.28}$$

where $(1 + \cos\phi)$ is the obliquity factor and A is the Fourier transform of the aperture function, where ϕ is the angle from the aperture normal (the polar angle) and θ is the azimuthal angle,

25
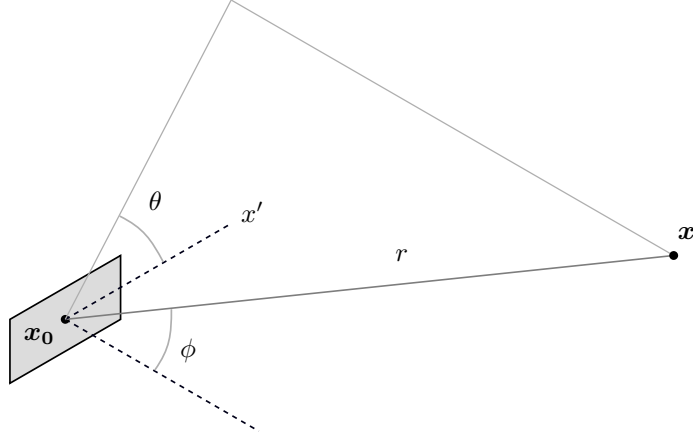
Figure 2.7: The aperture beam-pattern is a function of the angles θ and ϕ from the centre of the aperture at $\boldsymbol{x_0}$ to the point $\boldsymbol{x}$.

as shown in Figure 2.7 [41].

A common aperture shape is the rectangular aperture, with one dimensional aperture function

$$a(x') = \text{rect}\left(\frac{x'}{L}\right), \tag{2.29}$$

where x' is an axis along the transducer length, which has Fourier transform

$$A(u') = L\,\text{sinc}(Lu') \tag{2.30}$$

where L is the aperture length and u' is the spatial frequency [41].

A weighting can be applied to the aperture such that

$$a(x') = \text{win}(x')\text{rect}(x') \tag{2.31}$$

where $\text{win}(x')$ defines the window function. The weighting can be caused by the physical construction of the transducer or due to weighting of individual array elements. The window function can be used to alter the side-lobe ratio and beam-width, where an increase of the sidelobe ratio increases the beam-width. For example, Figure 2.8 shows the beam-pattern of a $5\,\text{cm}$ plate being excited at a frequency of $300\,\text{kHz}$, with and without a Hann window. The side-lobe ratio of the rectangular aperture is $13\,\text{dB}$, and a Hann window improves this to above $30\,\text{dB}$ at the expense of an increase in main-lobe width. Often a large side-lobe ratio is desired and a compromise between side-lobe ratio and main-lobe width is made.

The $-3\,\text{dB}$ width of the main-lobe from a rectangular aperture is

$$\theta_{3\,\text{dB}} \approx \varpi\frac{\lambda}{L} \tag{2.32}$$

where L is the along-track aperture length, $\lambda = c/f$ is the wavelength with f denoting frequency,

26
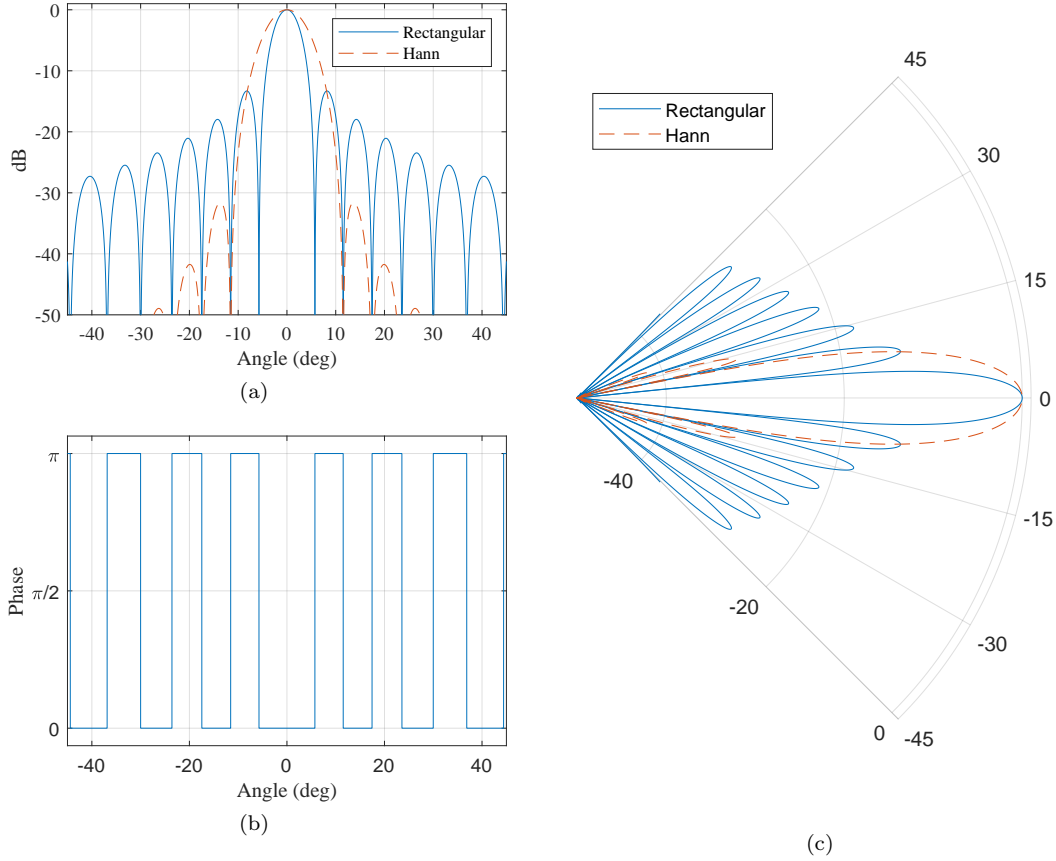
Figure 2.8: Example beam-patterns for a 5 cm aperture with rectangular and Hann weighting, excited at a frequency of 300 kHz. (a) The magnitude of the amplitude function in decibels. (b) The beam-pattern phase for the un-weighted aperture. (c) A polar representation of the beam-pattern magnitude in decibels. While the side-lobe ratio of the rectangular aperture is 13 dB, the Hann weighting improves this to above 30 dB, at the expense of increased main-lobe width.

and ϖ is a constant defined by the window function [41]. A rectangular window has $\varpi = 0.891$, corresponding to no weighting[6].

This results in an along-track resolution given by

$$\delta_x^{\text{sss}} = 2r \sin\left(\frac{\theta_{3\,\text{dB}}}{2}\right) \tag{2.33}$$

$$\approx \varpi_x r \frac{\lambda}{L} \tag{2.34}$$

where ϖ_x is a constant determined by the aperture window function and where the approximation is reached by substitution of (2.32) and using the small angle approximation $\sin(\theta) \approx \theta$.

Inspection of (2.34) shows that the along-track image resolution can be improved by in-

---

[6]This value for a rectangular window is often approximated as $\varpi \approx 1$, which results in the 3.9 dB beam-width for a rectangular aperture. This value is extensively used in derivations of the along-track resolution of SAS images, and results in a slightly poorer theoretical resolution than that reached using $\varpi \approx 0.891$.

creasing the frequency or the array length. However, the array length cannot be increased arbitrarily due to size constraints of the vehicle. There are a large number of commercially available sidescan sonar systems operating between 100 kHz and 1.6 MHz [47, 48, 49]. High frequency systems have very short maximum ranges (around 35 m at 1.6 MHz) due to high absorption losses, but have extremely narrow beams for high resolution imagery. Low frequency systems have comparatively long maximum ranges (hundreds of meters), but have wider beams resulting in lower resolution images. The choice of operating frequency is therefore application dependent, which has led to the development of multi-frequency systems [47], which allows a single system to be used for a range of applications.

The spatial sampling period of a sidescan sonar is determined by the platform velocity and the ping repetition frequency. For a system with maximum ping rate defined by (2.22), the distance travelled between pings is given by

$$\Delta_x = \frac{v_x}{\text{PRF}_{\text{max}}} \tag{2.35}$$

$$= \frac{2v_x R_{\text{max}}}{c}, \tag{2.36}$$

where v_x is the velocity in the along-track direction, and the maximum ping repetition frequency (PRF) is given by (2.22).

2.2.3 Limitations

Sidescan sonar is a highly effective, low-cost tool for a wide variety of sea-floor mapping applications. However, the following limitations exist which can constrain its applicability.

2.2.3.1 Range dependent along-track resolution

The images generated by sidescan sonar systems have along-track resolution that deteriorates with range. Figure 2.9a shows a sidescan sonar image of a sandy sea-floor with some artificial objects, captured by the MUSCLE AUV. The along-track resolution is visibly much poorer than the across-track resolution, which makes interpretation of the image challenging. The along-track resolution may be improved by using a higher frequency, but this limits the maximum survey range due to high absorption losses. This compromise between maximum range and along-track resolution limits the attainable area coverage rate at a given resolution.

Additionally, the range-dependence of along-track resolution means that the optimal choice of operating frequency is highly application dependent. A low frequency system is suitable for high area coverage rate at low resolution, whereas a high frequency system achieves high resolution at the expense of poor area coverage rate. This means multiple assets are often required for different phases of a survey, increasing both cost and complexity, unless multiple frequency systems are used.

2.2.3.2   Narrow beams and path deviations

Underwater platforms such as tow-fish and AUVs inevitably exhibit deviations from the ideal linear trajectory. Small heading differences between pings can result in gaps in the survey area, particularly for narrow beam systems. These systems are therefore unsuitable for applications which require full coverage of the survey area, for example in military mine-hunting operations or when searching for unexploded ordinance.

A related limitation is that sidescan sonar systems have a reduced capacity for through-the-sensor navigation estimation. This is because they typically provide intensity-only data, and do not have an array of receivers that allow for the collection of redundant data between adjacent pings. This means that they must rely on other sensors for navigation.

2.3   Synthetic aperture imaging

Synthetic aperture sonar addresses the limitations of real aperture sonar, theoretically giving range- and frequency-independent image resolution, while using a wide beam. The use of wide beams enables lower frequencies to be used, which allows SAS systems to generate very high resolution images at long range. This is a key advantage over conventional sidescan sonar.

Figure 2.9b shows a slant-plane SAS image of the same scene as the sidescan sonar image in Figure 2.9a. The difference in resolution between these images is striking; it is clear to the experienced observer that the bright regions are caused by a pipe and concrete block shown in the SAS image. There are some replicas of the bright targets, particularly visible around the concrete block in the top-centre of the image. This indicates that there may be errors in the navigation, bathymetry, or sound speed used to focus the image.

The acquisition geometry of rectilinear or strip-map SAS is shown in Figure 2.10. The vehicle travels along its path, repeatedly projecting pings with a wide beam sidewards and toward the sea-floor, in the same manner as sidescan sonar. Each location on the sea-floor is insonified by multiple pings, meaning it contributes to the received echo data for each of those pings. Synthetic aperture processing coherently combines these echo data in order to create a virtual array with a length much larger than that of the physical array.

2.3.1   The phase centre approximation

The typical configuration of a SAS is depicted in Figure 2.11a. The length of the receiver array is given by

$$L_{\mathrm{ss}} = L_{\mathrm{im}} + L_{\mathrm{rpc}}, \tag{2.37}$$

as shown in Figure 2.11a where the length of the array used for imaging is

$$L_{\mathrm{im}} = N_{\mathrm{im}} d_{\mathrm{rx}} \tag{2.38}$$

and the length of the array that collects redundant data used for micro-navigation is

$$L_{\mathrm{rpc}} = N_{\mathrm{rpc}} d_{\mathrm{rx}}, \tag{2.39}$$

29
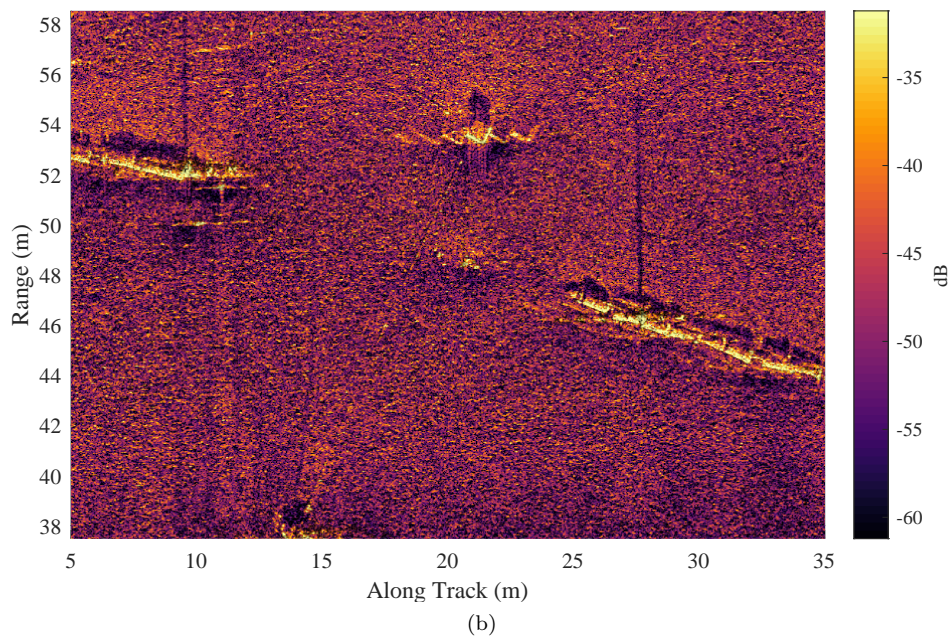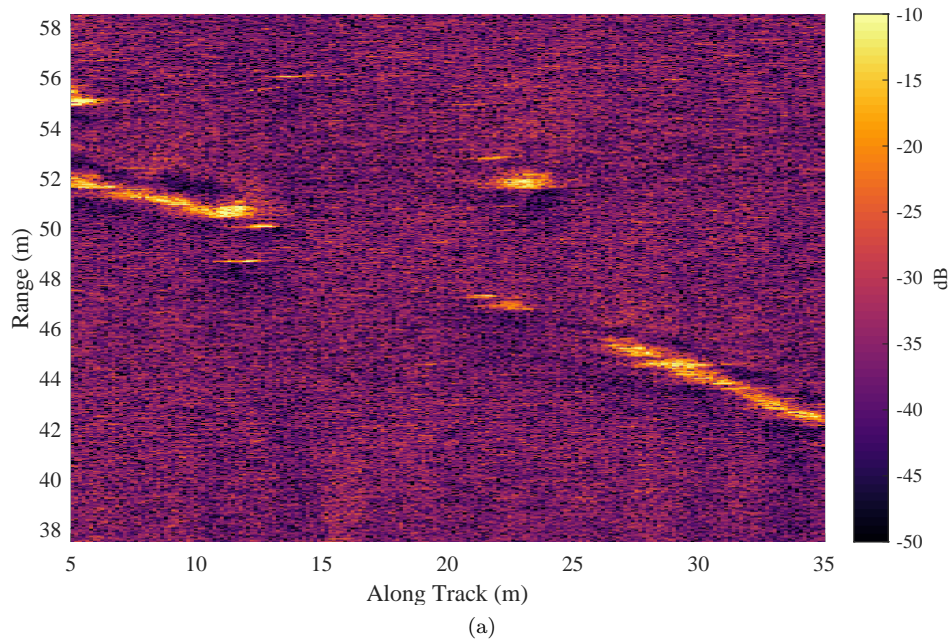
Figure 2.9: Example images of artificial objects on a sandy sea-floor captured by the MUSCLE AUV during the 2014 MANEX sea trial. (a) Sidescan sonar image. The along-track resolution worsens with range, and is much poorer than the across-track resolution. Bright objects indicate the presence of objects, but it is challenging to identify them. (b) Slant-plane synthetic aperture sonar image of the same scene, focused using navigation estimates from the slant-plane RPC micro-navigation algorithm. A disused pipe and a concrete block are visible. There are some replicas around bright targets, which suggest errors exist in the navigation, bathymetry, or sound speed used to focus the image.
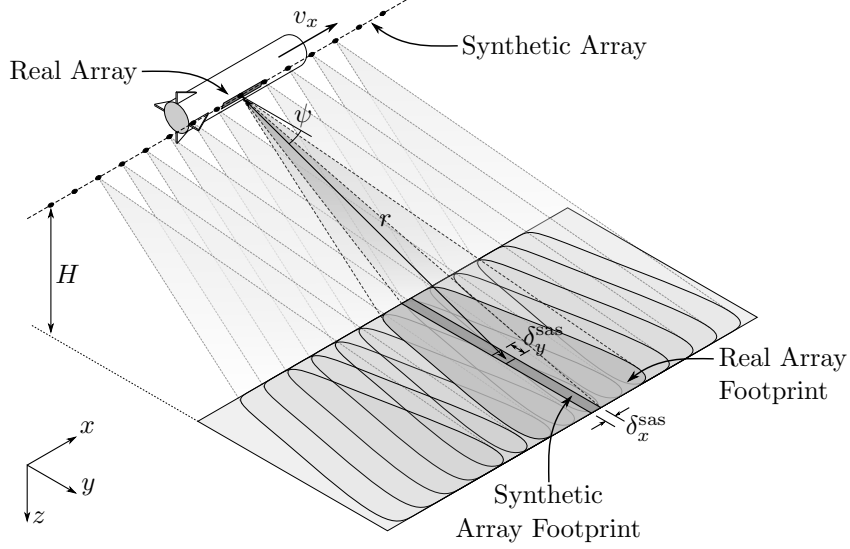
Figure 2.10: Strip-map synthetic aperture sonar imaging geometry. The sonar regularly transmits acoustic pings using a wide beam. This ensures that all locations in the imaged swath are insonified by multiple pings. Coherent processing of the echoes received allows formation of an image with range-independent resolution.

with N_{im} and N_{rpc} denoting the number of phase centres used for imaging and motion estimation respectively, and d_{rx} denoting the along-track distance between receivers. The total number of receivers is given by $N = N_{\text{im}} + N_{\text{rpc}}$.

Figure 2.11a shows the weakly bi-static geometry formed by the transmitting element and the array of receiving elements. The 'phase centre' approximation replaces this geometry with an array of virtual monostatic phase centres, each located at the mid-point of its corresponding transmitter-receiver pair, as shown in Figure 2.11b.

2.3.1.1   Phase centre approximation error for a stationary system

The error introduced by the phase centre assumption can be calculated with the aid of the diagram in Figure 2.12. It depicts a transmitter, located at the origin, a point, located at $\boldsymbol{x}_p$, and a receiver located at $\boldsymbol{x}_{\text{rx}}(0)$. This bi-static geometry is approximated by a phase centre located at $\boldsymbol{x}_{\text{pc}} = \boldsymbol{x}_{\text{rx}}(0)/2$. The range error introduced by the phase centre assumption is

$$\epsilon_{\text{pc}} = r_{\text{tx}} + r_{\text{rx}}(0) - 2r_{\text{pc}} \tag{2.40}$$

where

$$r_{\text{tx}} = \|\boldsymbol{x}_p\| \tag{2.41}$$

$$= \sqrt{\left(\frac{\Delta}{2}\right)^2 + r_{\text{pc}}^2 + \Delta r_{\text{pc}} \sin(\theta)} \tag{2.42}$$
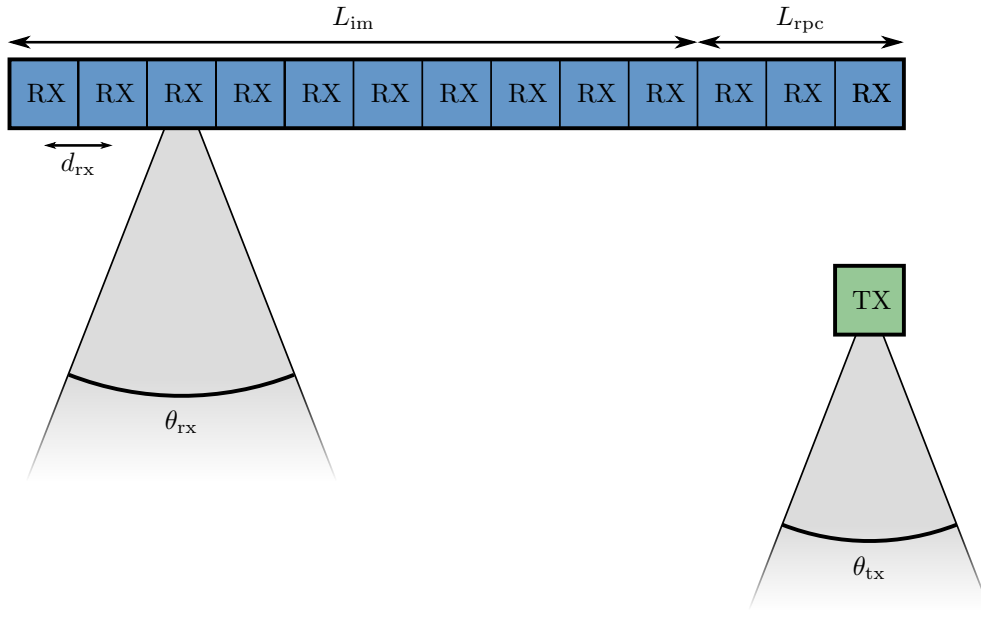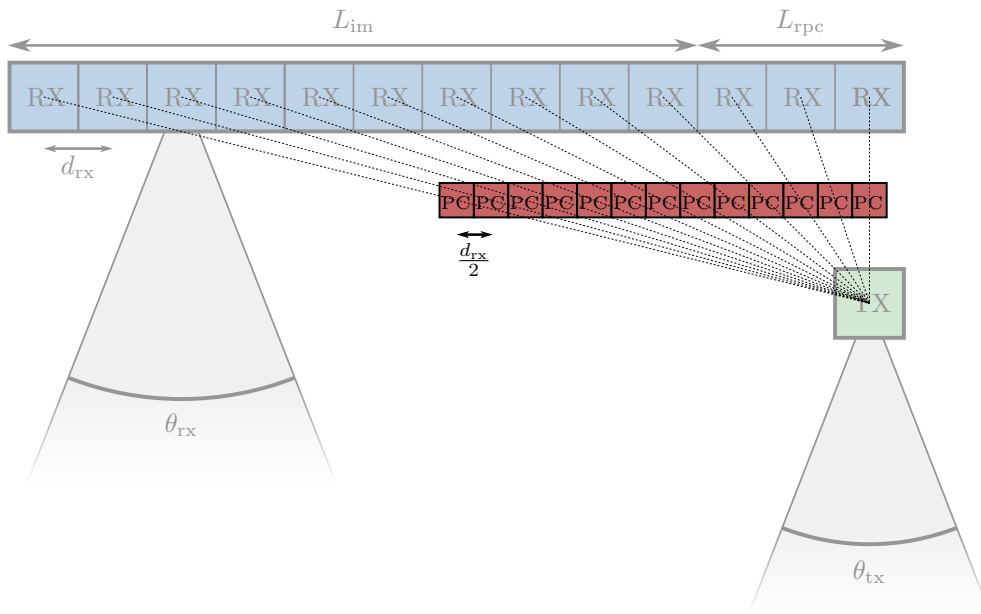
Figure 2.11: The typical construction of a synthetic aperture sonar system. The length of the receiving array is comprised of a length used for imaging L_{im}, and a length used for micro-navigation L_{rpc}. (a) The transmitter (TX) and array of receiving elements (RX) forms a weakly bi-static geometry. (b) This geometry is often simplified by the phase centre approximation, which replaces each transmitter-receiver pair with a virtual monostatic 'phase centre'. Each phase centre (PC) is located at the mid-point between each transmitter-receiver pair.
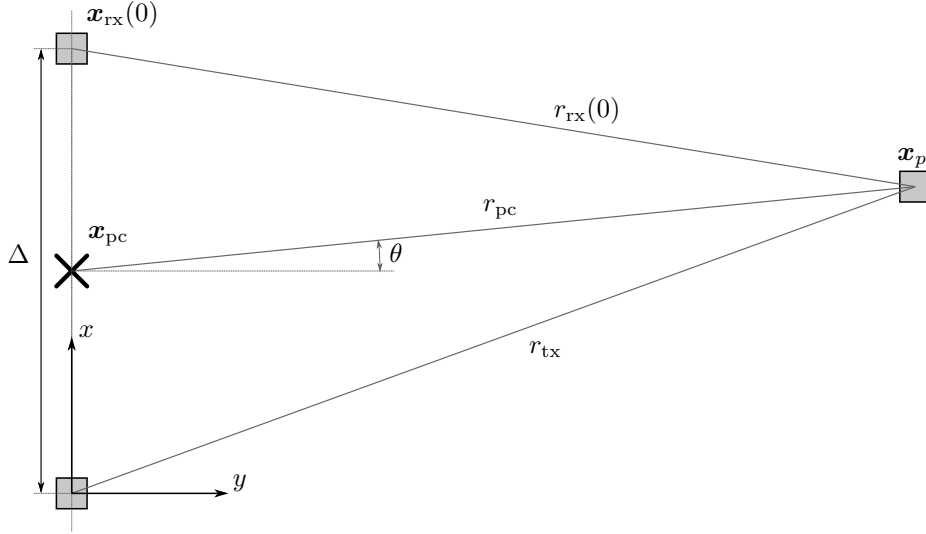
Figure 2.12: The geometry of the phase centre approximation. The phase centre at $\boldsymbol{x}_{\mathrm{pc}}$ is located at the mid-point between the transmitter and receiver elements, where the transmitter is located at the origin and the receiver is located at $\boldsymbol{x}_{\mathrm{rx}}(0)$. A point is located at $\boldsymbol{x}_p$, at a range of r_{pc} from the phase centre, a range of r_{tx} from the transmitter and $r_{\mathrm{rx}}(0)$ from the receiver. The true two-way range is given by $r_{\mathrm{tx}} + r_{\mathrm{rx}}(0)$ and using the phase centre approximation by $2r_{\mathrm{pc}}$.

is the range from the transmitter to the point with θ being the angle to the point as shown in Figure 2.12,

$$r_{\mathrm{rx}}(0) = \|\boldsymbol{x}_p - \boldsymbol{x}_{\mathrm{rx}}(0)\| \tag{2.43}$$

$$= \sqrt{\left(\frac{\Delta}{2}\right)^2 + r_{\mathrm{pc}}^2 - \Delta r_{\mathrm{pc}}\sin(\theta)} \tag{2.44}$$

is the range from the receiver to the point, and

$$r_{\mathrm{pc}} = \|\boldsymbol{x}_p - \boldsymbol{x}_{\mathrm{pc}}\| \tag{2.45}$$

is the range from the phase centre to the point.

The phase centre approximation error can be written as

$$\epsilon_{\mathrm{pc}} = r_{\mathrm{tx}} + r_{\mathrm{rx}}(0) - 2r_{\mathrm{pc}} \tag{2.46}$$

$$= r_{\mathrm{pc}}\left(\sqrt{1 + \frac{1}{4}\left(\frac{\Delta}{r_{\mathrm{pc}}}\right)^2 + \frac{\Delta}{r_{\mathrm{pc}}}\sin\theta} + \sqrt{1 + \frac{1}{4}\left(\frac{\Delta}{r_{\mathrm{pc}}}\right)^2 - \frac{\Delta}{r_{\mathrm{pc}}}\sin\theta} - 2\right), \tag{2.47}$$

33

which can be approximated as [31]

$$\epsilon_{\mathrm{pc}} \approx \frac{\Delta^2}{4r_{\mathrm{pc}}} \cos^2\theta + \frac{\Delta^4}{64r_{\mathrm{pc}}^3} \cos^2\theta(4 - 5\cos^2\theta) + \ldots \tag{2.48}$$

by linearisation around $\Delta/r_{\mathrm{pc}} = 0$ using a Taylor series expansion. This expression is plotted for a number of ranges in Figure 2.13a, using $\Delta = 1\,\mathrm{m}$. Examination of this expression shows that the phase centre approximation holds when $\Delta^2/4r_{\mathrm{pc}} \ll \lambda$ where lambda is the wave-length at the centre frequency. This can be rearranged to $r_{\mathrm{pc}} \gg \Delta^2/4\lambda$, which has been interpreted as a far-field condition. However, a modern multi-channel SAS may have a transmitter-receiver separation in excess of $1\,\mathrm{m}$. For example, for a system with $\Delta = 1\,\mathrm{m}$ and $\lambda = 5\,\mathrm{mm}$, the condition which must be satisfied for the phase centre assumption to hold becomes

$$r_{\mathrm{pc}} \gg \frac{\Delta^2}{4\lambda} \tag{2.49}$$

$$\gg \frac{1}{4 \times 5 \times 10^{-3}} \tag{2.50}$$

$$\gg 50\,\mathrm{m}, \tag{2.51}$$

which is not the case for most modern SAS systems. For example, the MUSCLE system has a theoretical maximum range of $187.5\,\mathrm{m}$ when pinging at $4\,\mathrm{Hz}$.

This error can be partly compensated for by advancing the received signals by a time of $\Delta^2/4cr_{\mathrm{pc}}$ where c is the speed of acoustic propagation [31]. For a stationary system where Δ is well known, the compensation results in a reduction of the phase centre approximation error to

$$\epsilon'_{\mathrm{pc}} \approx \frac{\Delta^2}{4r_{\mathrm{pc}}}(\cos^2\theta - 1) + \frac{\Delta^4}{64r_{\mathrm{pc}}^3} \cos^2\theta(4 - 5\cos^2\theta) + \ldots \tag{2.52}$$

which is plotted in Figure 2.13b using $\Delta = 1\,\mathrm{m}$. The compensation is shown to remove the phase centre approximation error almost completely in the broad-side direction at all ranges. However, there is residual error at off-broad-side angles, which is most severe at short ranges.

2.3.1.2 Phase centre approximation error for a moving system

For a moving system with along-track velocity v_x and no across-track velocity, an improved compensation can be applied by advancing the signal by $(\Delta')^2/4cr_{\mathrm{pc}}$, where

$$\Delta' = \Delta_0 + v_x\frac{2r_{\mathrm{pc}}}{c} \tag{2.53}$$

is the distance between the transmitter at the time of transmission and the receiver at the time of reception.

Figure 2.14 compares possible phase centre assumption error compensations. Figure 2.14a (copy of Figure 2.13a) shows the uncompensated phase centre approximation error for a stationary system with $\Delta = 1\,\mathrm{m}$. Figure 2.14b shows the uncompensated phase centre assumption error for the same system with along-track velocity $v_x = 1\,\mathrm{m\,s^{-1}}$. Figures 2.14c and 2.14d

34
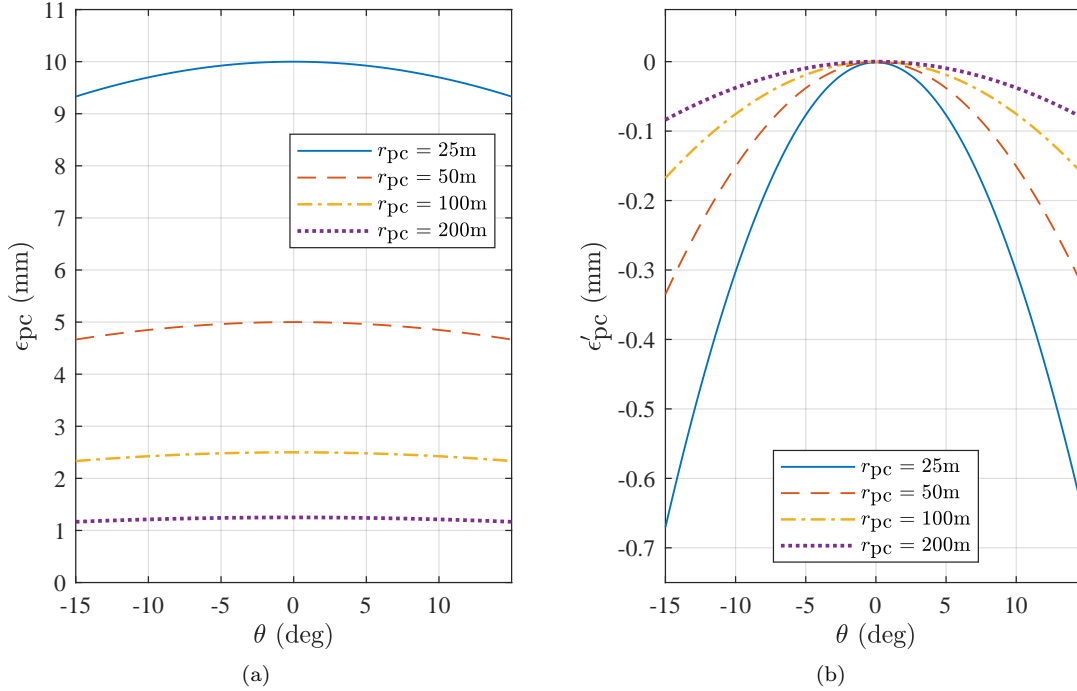
Figure 2.13: Use of the phase centre approximation introduces range errors when compared to the true bi-static geometry. (a) The two-way range error introduced by the phase centre approximation for a transmitter-receiver separation of $1\,\mathrm{m}$. (b) The two-way range error introduced by the phase centre assumption after the received signal is advanced by $\Delta^2/4cr_\mathrm{pc}$. The error is almost entirely eliminated in the broad-side direction at all ranges, however the residual error may be significant for some systems, particularly those that operate at short range with wide beams.

show the result of compensating for the phase centre assumption by advancing the signals by $\Delta^2/4cr_\mathrm{pc}$ and $(\Delta')^2/4cr_\mathrm{pc}$ respectively.

These show that the two-way range error introduced by the phase centre assumption can be removed in the broadside direction using a simple delay function. However, a more complex angle-dependent correction is likely to be required for short-range, wide beam systems [50].

2.3.1.3 The phase centre approximation and RPC micro-navigation

The un-compensated phase centre assumption introduces errors in RPC micro-navigation algorithms because the value of Δ for the overlapping portions of the phase centre arrays of adjacent pings is different. This has the effect of introducing a bias error on the RPC time delay measurements. A simple method has been described for removing this bias error for a moving system, which is typically applied by advancing short-time windowed signals in time by a value calculated at the centre of the window. This method has several limitations: it requires prior knowledge of the along-track velocity of the platform, assumes no across-track platform velocity, and is only correct at the centre of the short-time windowed signals and in the broadside direction.
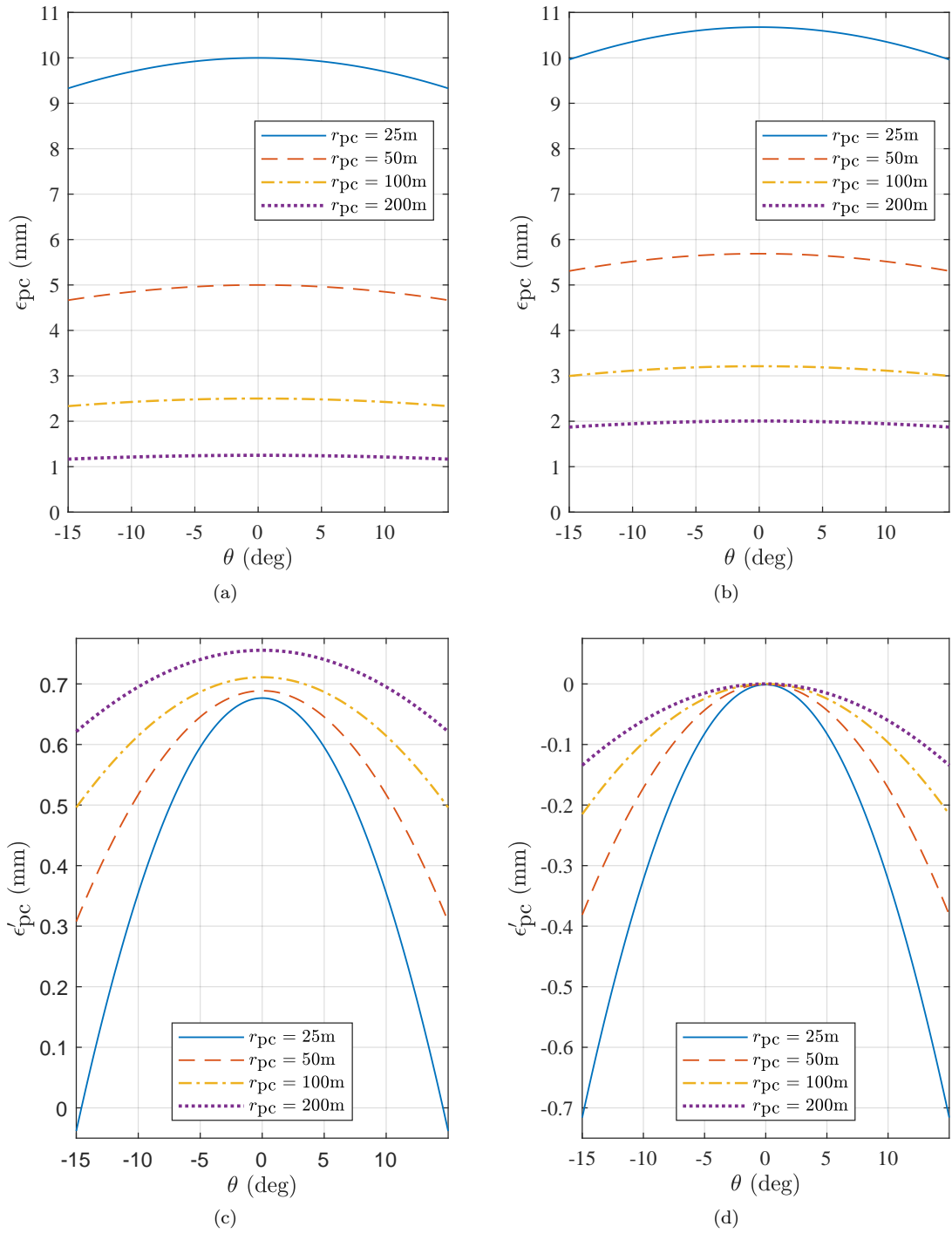
Figure 2.14: (a) Phase centre assumption error for a stationary system (copy of Figure 2.13a). (b) Phase centre assumption error for a system with along-track velocity $v_x = 1\,\mathrm{m\,s^{-1}}$. (c) The residual error when the stationary system compensation is applied. (d) The residual error when the moving system compensation is applied.

The methods developed in this thesis do not employ the phase centre assumption in order to avoid these limitations when accurate estimation of time delays between redundant signals is required. Instead, the bi-static acoustic propagation is modelled explicitly.

2.3.2   The stop-and-hop assumption

The continuous motion of the sonar results in a loose coupling of *fast time* and *slow time*, the time vectors associated with the delay between transmitting a ping and receiving its echoes, and with the motion of the vehicle along its path, respectively. The stop-and-hop assumption removes this coupling, making the assumption that the sonar is stationary while the sonar transmits, and waits for the last echo signal to be received before instantaneously moving to the next ping position. The assumption introduces errors via two processes, temporal Doppler and geometrical two-way range error.

2.3.2.1   Temporal Doppler

Both the transmitted and received signals are affected by temporal Doppler due to the along-track motion of the sonar. Targets ahead of the sonar experience a slight compression of the signal while those aft of the sonar experience a slight expansion of the signal. The single-frequency Doppler shift for the echo received by a phase centre moving with constant velocity is given by

$$f_0' = f_0 \left(\frac{1 - \frac{\dot{r}}{c}}{1 + \frac{\dot{r}}{c}} \right) \tag{2.54}$$

$$\approx f_0 \left(1 - \frac{2\dot{r}}{c} \right) \tag{2.55}$$

where $\dot{r}$ is the rate of change of range to a point and f_0 is the frequency of the transmitted signal [50], and where the approximation is valid for $\dot{r} \ll c$.

Temporal Doppler has been shown to induce a minor image quality degradation for a typical modern, multi-receiver SAS system operating in strip-map mode [51]. It is suggested that Temporal Doppler compensation is applied by a minor modification to the time domain back-projection imaging algorithm [51]. Systems operating in a circular geometry i.e. circular SAS (CSAS) do experience significant image degradation due to temporal Doppler, and should be compensated accordingly [52].

It has been stated that temporal Doppler has no effect on data-driven navigation estimation, since it induces a negligible RPC time delay error [51]. Therefore it is unnecessary to apply a temporal Doppler compensation method when estimating time delays between redundant signals.

2.3.2.2   Geometrical error

The stop-and-hop assumption causes two-way range errors due to the geometrical difference between the stop-and-hop propagation model and the true geometry. These errors cause a

37
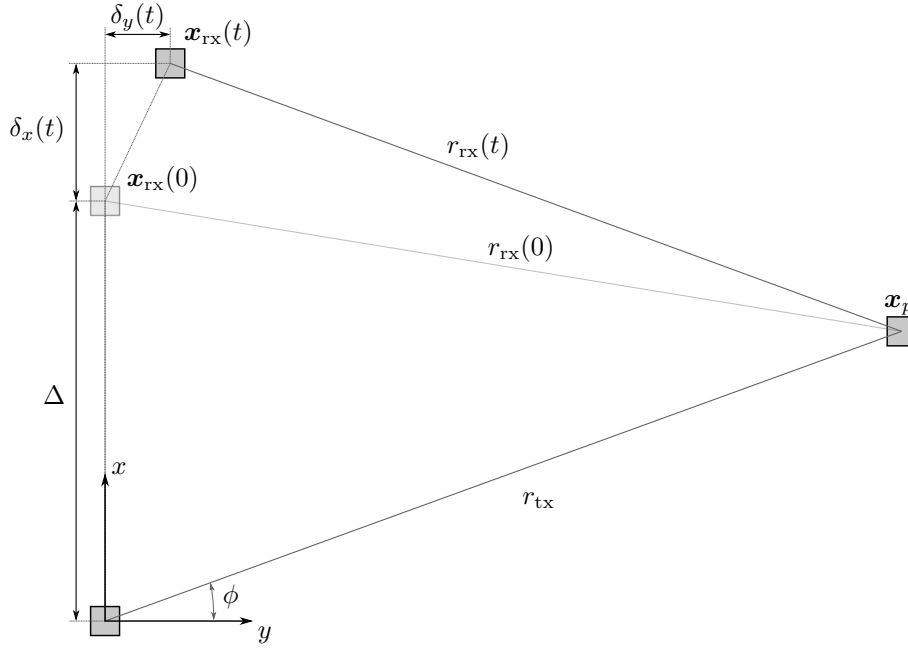
Figure 2.15: The geometry of the stop-and-hop assumption. The transmitter is located at the origin, with the receiver located at $\boldsymbol{x}_{\mathrm{rx}}(0)$ with a separation of Δ at the time of transmission. In the time between transmission and reception, the receiver moves to $r_{\mathrm{rx}}(t)$, a distance of $\delta_x(t)$ in the along-track direction and $\delta_y(t)$ in the across-track direction. A point is located at $\boldsymbol{x}_p$, at a range of r_{tx} from the transmitter, a range of $r_{\mathrm{rx}}(0)$ from the receiver at the time of transmission and at $r_{\mathrm{rx}}(t)$ from the receiver at the time of reception. The true two-way range is given by $r_{\mathrm{tx}} + r_{\mathrm{rx}}(t)$ and using the stop-and-hop assumption by $r_{\mathrm{tx}} + r_{\mathrm{rx}}(0)$.

skewing and slight defocusing of the image [53].

Consider the diagram in Figure 2.15. The transmitting transducer is located at the origin, and the receiving transducer is located at $\boldsymbol{x}_{\mathrm{rx}}(0)$ at the time of transmission, moving to $\boldsymbol{x}_{\mathrm{rx}}(t)$ at the time of reception.

The range between the receiver at the time of transmission and the point at $\boldsymbol{x}_p$ is given by

$$r_{\mathrm{rx}}(0) = \sqrt{r_{\mathrm{tx}}^2 + \Delta^2 - 2\Delta r_{\mathrm{tx}} \sin(\phi)} \tag{2.56}$$

where Δ is the known distance between the transmitter and receiver at the time of transmission and ϕ is the angle to the point from the transmitter. The range between the receiver and the point at $\boldsymbol{x}_p$ at the time of reception is given by

$$r_{\mathrm{rx}}(t) = \sqrt{(\Delta + \delta_y(t) - r_{\mathrm{tx}} \sin \phi)^2 + (r_{\mathrm{tx}} \cos \phi - \delta_x(t))^2} \tag{2.57}$$

where the along- and across-track distances travelled by the sonar while the ping is in flight are given by

$$\delta_x(t) \approx v_x \frac{2r_{\mathrm{tx}}}{c} \tag{2.58}$$

38

and

$$\delta_y(t) \approx v_y \frac{2r_{\mathrm{tx}}}{c} \tag{2.59}$$

respectively, where v_x is the along-track velocity, v_y is the across-track velocity, r_{tx} is the range from the transmitter to the point at $\boldsymbol{x}_p$ and $r_{\mathrm{rx}}(t)$ is the range from the receiver to the point at $\boldsymbol{x}_p$. The approximation is valid for $v_x \ll c$ and $v_y \ll c$.

The range error introduced by the stop-and-hop assumption is given by

$$\epsilon_{\mathrm{sh}} = r_{\mathrm{tx}} + r_{\mathrm{rx}}(t) - (r_{\mathrm{tx}} + r_{\mathrm{rx}}(0)) \tag{2.60}$$

which is plotted with $\Delta = 1\,\mathrm{m}$, for $v_x = 0\,\mathrm{m\,s^{-1}}, v_y = 1\,\mathrm{m\,s^{-1}}$ and for $v_x = 0.01\,\mathrm{m\,s^{-1}}, v_y = 1\,\mathrm{m\,s^{-1}}$ in Figures 2.16a and 2.16b respectively, zooms of which are shown in Figures 2.16c and 2.16d. The range error introduced by the stop-and-hop assumption for pure along-track motion is range-variant as shown in Figure 2.16a, with largest error at long ranges, and is approximately linear with angle. These range errors cause a geometrical skewing of SAS images focused using the stop-and-hop assumption. Figure 2.16a shows that across-track motion alters the two-way range error introduced by the stop-and-hop assumption. This modulation of the stop-and-hop error is not compensated by the scheme suggested in [51], and may therefore lead to defocusing of the image. The algorithms developed in this thesis thus avoid the geometrical error introduced by the stop-and-hop assumption by explicitly modelling the time-varying, bi-static, two-way propagation geometry.

2.3.3 Across-track resolution

The across-track resolution of a synthetic aperture sonar system is the same as that of sidescan sonar stated in Section 2.2.1,

$$\delta_y^{\mathrm{sas}} = \delta_y^{\mathrm{sss}}. \tag{2.61}$$

2.3.4 Along-track resolution

The along track resolution of a synthetic aperture sonar is given by [45]

$$\delta_x^{\mathrm{sas}} = \varpi_x \frac{\lambda}{2L_{\mathrm{sa}}} r, \tag{2.62}$$

where L_{sa} is the length of the synthetic aperture and ϖ_x is determined by a window function which is chosen to compromise between resolution and side-lobe ratio. Comparison with (2.34) shows that the along track resolution of a synthetic aperture system is a factor of 2 better than a real aperture system with an aperture of equal length, that is, $L_{\mathrm{ss}} = L_{\mathrm{sa}}$. This factor of two resolution improvement can be explained by applying the phase centre approximation (Section 2.3.1) to the real aperture. The length of the array of phase centres, where each phase centre is located at the mid-point between the transducer centre (from which the signal is assumed to be transmitted) and each location on the transducer (from which the signal is received), is half as long as the physical transducer. However, because both the transmitter and receivers move

39
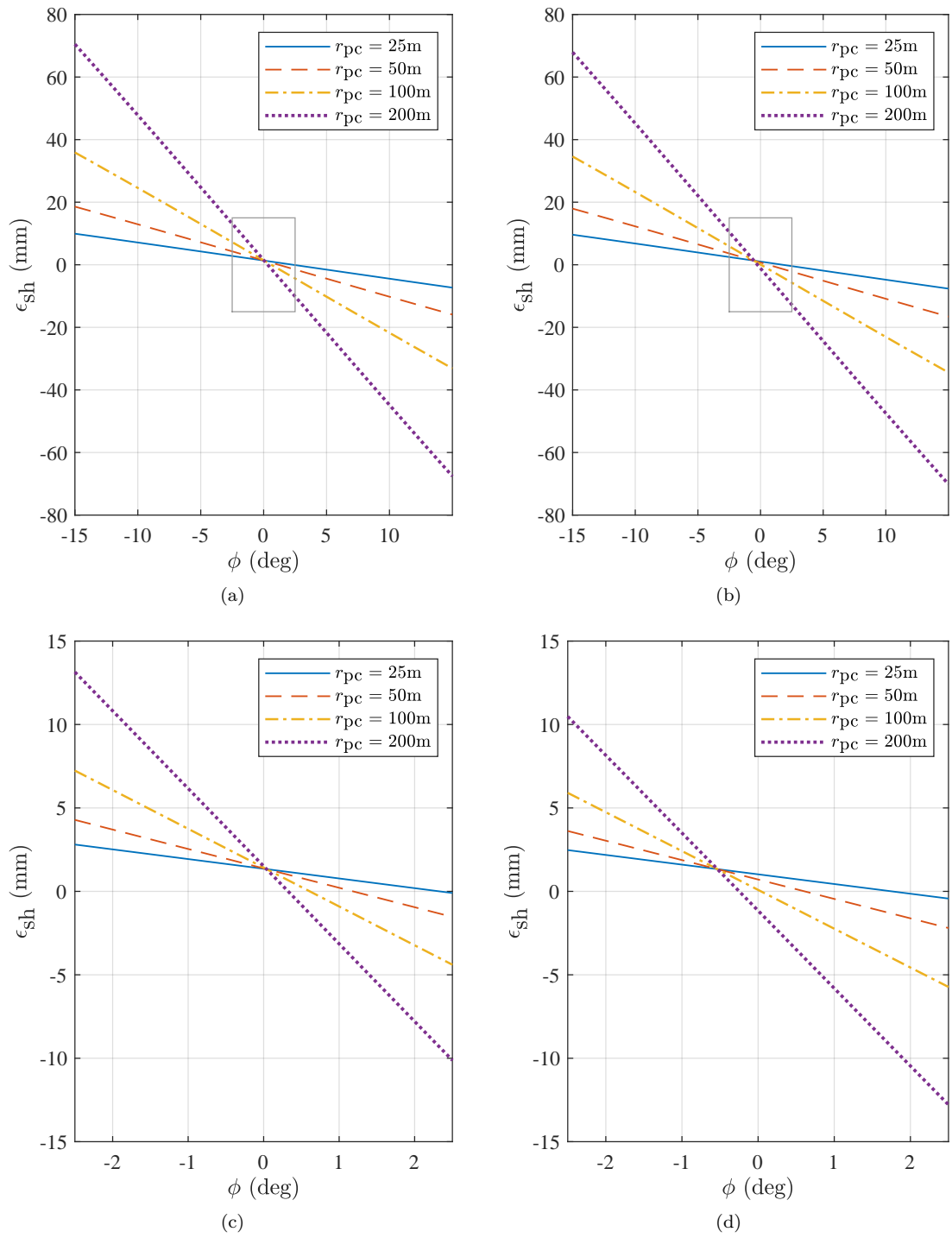
Figure 2.16: The error in two-way range caused by the stop-and-hop assumption for (a) pure along-track motion at $v_y = 1\,\mathrm{m\,s^{-1}}$ (b) with additional across track motion at $v_x = 0.01\,\mathrm{m\,s^{-1}}$. (c) Zoom of (a). (d) Zoom of (b).

along the synthetic aperture, the array of phase centres is the same length as the synthetic aperture.

The length of the synthetic aperture is governed by the beam-width of either the transmitter or receiver elements, whichever is narrower (i.e. the widest element). The synthetic aperture length is given by

$$L_{\mathrm{sa}} \leq \frac{\lambda}{D} r, \tag{2.63}$$

where D is the transmitter or receiver element with the largest along-track size[7]. Combining (2.62) and (2.63) gives the along track resolution of synthetic aperture sonar [2] as

$$\delta_x^{\mathrm{sas}} \approx \frac{D}{2}. \tag{2.64}$$

The same expression can be reached via consideration of the bandwidth of the spatial doppler spectrum [45]. Crucially, this result shows that the resolution of a SAS image is range independent, and that the along-track resolution can be improved by reducing the along-track size of the largest element (increasing the beam-width). This is the opposite of a real aperture sonar, which has improved along-track resolution with increased transducer length. The diffraction limit is $\lambda/4$, so no improvement is gained by reducing the transducer dimensions below $\lambda/2$ [16].

Wider beam systems will suffer from greater spreading losses, and reducing the transducer size limits the total energy that can be transmitted into the medium. A longer synthetic aperture created by a wider beam requires the challenging navigation requirements to be met over a larger number of pings. Also, wide beams cause a reduction in shadow contrast due to the change in look angle along the synthetic aperture [54]. For these reasons, many demonstrated SAS systems operate with relatively small along-track beam-widths. For example, the SAS of the MUSCLE AUV has an along-track beam-width of around 5 degrees.

Nevertheless, there has been considerable recent interest in low frequency SAS systems, with multiple designs in development having been tested on rail-based systems [55, 56, 57]. This interest is because low frequencies penetrate a greater distance into the sea-floor and into objects than high frequencies, potentially enabling the detection of buried targets [58] and imaging inside targets [59]. Low frequencies excite resonances in certain targets, which can make the resulting SAS images challenging to interpret. However, data representations like acoustic colour plots have been used to depict aspect dependent scattering strength, which have the potential to be used for target classification [60, 61].

2.3.5   Area coverage rate

The area coverage rate of SAS is limited by the fact that the vehicle may not advance by more than $L_{\mathrm{im}}/2$ per ping, in order to allow redundant signals to be received for the purpose

---

[7]This is likely to be the transmitter, because a larger transducer area allows more energy to be transmitted into the water, and produces a narrower beam. It is common to choose the receiver element size to be slightly smaller, so that the first null in the receiver beam-pattern occurs at the same angle as the first side-lobe of the transmitter beam-pattern.

of motion estimation. The factor of 2 is caused by the bi-static geometry of a multi-receiver SAS, with phase centre array length half that of the real aperture. Using the maximum ping repetition frequency in (2.22), the maximum along-track platform velocity is given by

$$v_{x\max} = \frac{L_{im}}{2}\text{PRF}_{\max} \tag{2.65}$$

$$= \frac{cL_{im}}{4R_{\max}} \tag{2.66}$$

$$= \frac{c(N - N_{rpc})d_{rx}}{4R_{\max}} \tag{2.67}$$

where $R_{\max}$ is the largest imaged range. The maximum area coverage rate (ACR) is given by the product of the along-track velocity and the image swath width, given by

$$\text{ACR} = \frac{cL_{im}}{4R_{\max}}(R_{\max} - R_{\min}) \tag{2.68}$$

$$= \frac{c(N - N_{rpc})d_{rx}}{4R_{\max}}(R_{\max} - R_{\min}) \tag{2.69}$$

where $R_{\min}$ is the minimum imaged range. Area coverage rate of a dual-sided SAS is complicated by the gap that exists at the nadir (below the vehicle). Unless a gap-filling sensor is used, such as a forward-looking sonar or multi-beam echo-sounder, paired tracks must be used to fill the nadir gap. A good overview of the area coverage rate for a dual-sided SAS, with and without gap-filling is given in [62].

2.3.6 Imaging algorithms

A thorough review of the multiplicity of imaging algorithms that have been used by the SAS community is given in [63, Section IV]. The most flexible imaging algorithm is delay-and-sum beam-forming, also known as back-projection [64](Ch 4.1) [65](Ch 4.7). This flexibility allows images to be formed from any arbitrary platform motion onto an arbitrary surface, including for wide-beam systems. Conventional back-projection neglects the frequency dependence of the ideal imaging algorithms, but methods such as sub-band processing or Fourier windowing of an up-sampled image can resolve this limitation [66]. Unfortunately, the flexibility of time-domain back-projection comes at a significantly higher computational cost [67] when compared to Fourier-domain methods such as the range-Doppler [68, 69], wave-number [70], chirp-scaling [71, 72], fast factorised back-projection [73] and fast polar back-projection [74] algorithms. However, recent hardware developments in multi-core processors and particularly in general purpose graphics processing unit (GPGPU) computing have enabled time-domain back-projection algorithms to produce SAS images in reasonable time-scales [75].

2.3.6.1 Time domain delay-and-sum back-projection

Throughout this thesis, a custom delay-and-sum back-projection implementation has been used to generate the SAS images, since the images can be formed directly from an estimated vehicle path onto an estimated bathymetry with few approximations.

The time-domain back-projection algorithm operates by performing a weighted summation of the echoes received by each receiver on every contributing ping, delayed by the appropriate two-way travel time defined by the relative positions of the sensor and image pixel. For each point $\boldsymbol{x}(x, y, z)$, the estimated scene reflectivity $I(x, y, z)$ is given by

$$I(x, y, z) = \sum_{p} \sum_{n=1}^{N} W(x, y, z) e'_{p,n}(\tau_{p,n}(x, y, z)) \qquad (2.70)$$

where p is the subset of the pings which contribute to the point $\boldsymbol{x}(x, y, z)$, n indexes over the receiver elements, and $e'_{p,n}$ is the match-filtered echo data received by receiver n and ping p delayed by the two-way travel time given by

$$\tau_{p,n}(x, y, z) = \frac{2r_{\mathrm{pc},p,n}(x, y, z)}{c} \qquad (2.71)$$

under the phase centre assumption where $r_{\mathrm{pc},p,n}(x, y, z)$ is the range from the nth phase centre of ping p, or

$$\tau_{p,n}(x, y, z) = \frac{r_{\mathrm{tx},p,n}(x, y, z) + r_{\mathrm{rx},p,n}(x, y, z)}{c} \qquad (2.72)$$

respecting the true bi-static geometry, where $r_{\mathrm{tx},p,n}(x, y, z)$ and $r_{\mathrm{rx},p,n}(x, y, z)$ are the ranges from the transmitter to the point and from the receiver to the point. The range from the receiver to the point is calculated using the receiver position at the time of ping transmission under the stop-and-hop assumption, or at the time of reception respecting the true time-dependent geometry. However, the exact time of reception is challenging to compute, and is approximated by $2 * r_{\mathrm{tx},p,n}(x, y, z)/c$. The weighting function $W(x, y, z)$ is a function of the angle from broadside to account for the beam-pattern of the transmitter-receiver pair. The weighting function can be chosen to trade-off between along-track resolution and side lobe level (SLL).

This algorithm has been implemented in MATLAB® using the built-in support for GPU computing, enabling image formation. The algorithm as implemented does not employ the phase centre assumption and assumes constant translational and angular velocities between pings, avoiding the stop-and-hop assumption.

2.4   SAS Interferometry

Interferometry in general aims to measure small shifts between signals, by means of their mutual interference. In the context of array processing, these shifts can be used to estimate the angle of arrival of the signals. This is the case with interferometric SAS, the geometry of which is shown in Figure 2.17. The interference between images formed with slightly differing acquisition geometries is used to estimate the spatially-varying angle of arrival, which combined with the known range allows estimation of sea-floor depth, or bathymetry. [16] is an excellent reference for bathymetry estimation using InSAS.

The simple representation of the geometry of InSAS in Figure 2.17 shows a vehicle with a transmitter and two receiver arrays separated by a baseline of D_{in}. The difference between
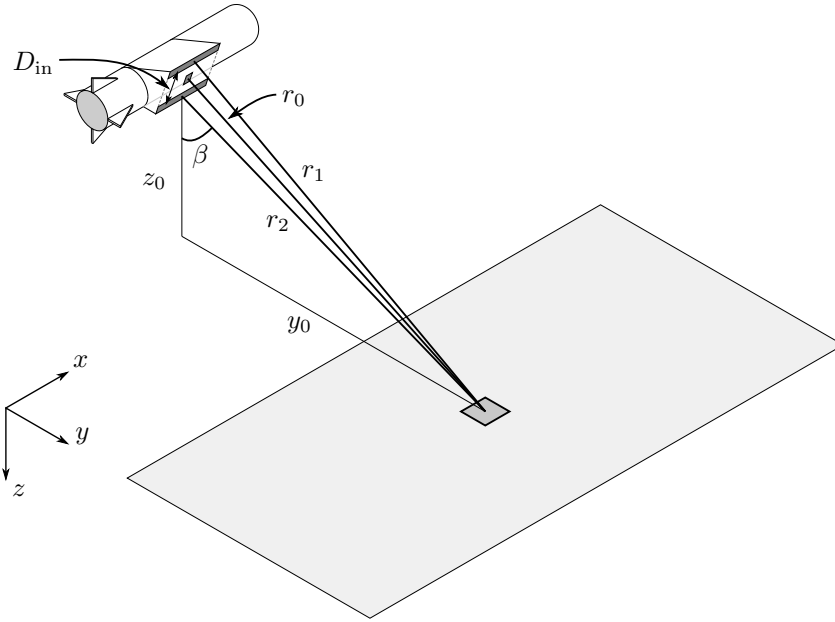
Figure 2.17: Geometry of an interferometric SAS. Two receiving arrays are separated by a baseline of D_{in}, and the ranges from the upper and lower arrays to a point on the sea-floor are r_1 and r_2 respectively. The difference between these ranges allows calculation of the interferometric angle β, from which the sea-floor depth z_0 can be calculated.

the ranges from the upper and lower receiver arrays to a point, r_1 and r_2 respectively, allows calculation of the angle of arrival β and hence the depth of the sea-floor z_0. An expression for z_0 is derived in Section 2.4.1.

A typical interferometric SAS consists of a single transmitter and two receiving arrays, separated by a *baseline* approximately normal to the array line of sight. Most modern SAS equipped platforms include an InSAS on both sides of the platform; we refer to these systems as dual-sided InSAS.

Three dimensional scene estimation using interferometry was simultaneously developed underwater as bathymetric sidescan sonar and in the radar domain as interferometric synthetic aperture radar (InSAR) [76]. However, the use of interferometric processing in SAS was first proposed in 1997 [77], and was considered to be a 'natural extension' of the analogous InSAR, first described as early as 1974 [78]. However, there are significant differences between the collection geometries. Typically, SAS systems operate close to the sea-floor with a small depression angle, allowing operation in shallow water. Owing to size constraints on the platform, the interferometric baseline is often small. In contrast, most synthetic aperture radar (SAR) systems operate at a much larger depression angle and with larger interferometric baselines [16].
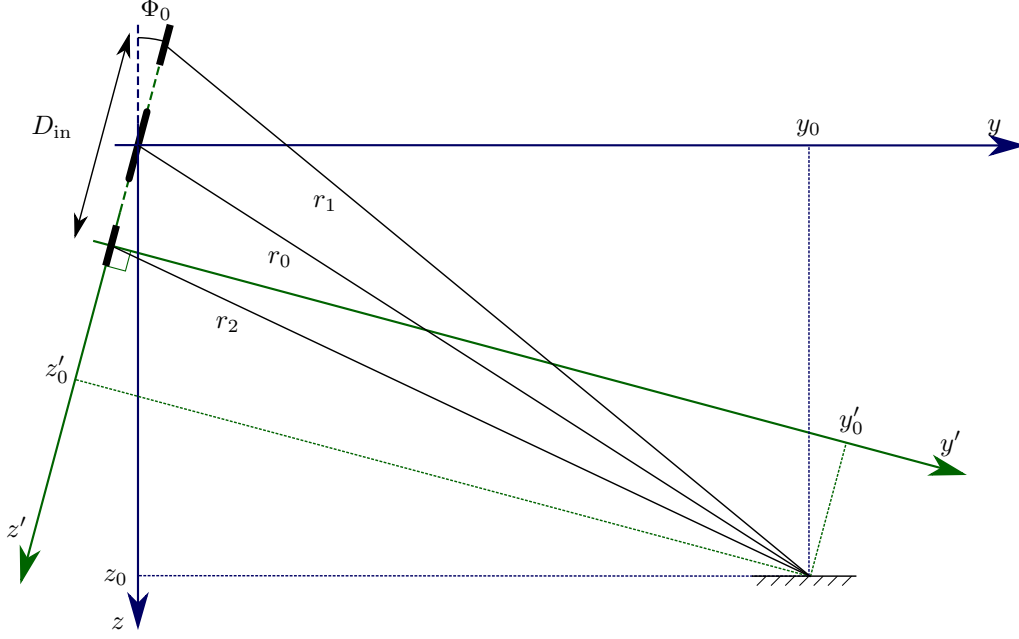
Figure 2.18: Geometry of an interferometric SAS in the vertical y-z plane. A rotated coordinate frame y'-z' is also shown, which is rotated by the tilt angle of the interferometer.

2.4.1 Acquisition geometry

The time for a signal to propagate through the medium, reflect off the sea-floor, and be received is variously known as the time of flight (TOF), the time of arrival (TOA) and the propagation time. The difference between pairs of these two-way times is known as the time of flight difference (TOFD) and the time difference of arrival (TDOA), or simply the time delay. We use the terms propagation time and time delay to denote the two-way travel time and differences between two-way travel times respectively. SAS interferometry relies on measurements of both propagation time and time delay to make bathymetry estimates.

Consider the diagram in Figure 2.18, which depicts an interferometric SAS in two co-ordinate frames. The transmitter is located at the origin of the $[y, z]$ co-ordinate frame, with the receivers above and below and inclined at a tilt angle of Φ_0 separated by baseline D_{in}. The time delay between the signals reflected by a scatterer with location $[y, z]$ is given by

$$\tau(y, z) = t_1(y, z) - t_2(y, z) \tag{2.73}$$

$$= \frac{1}{c} \left((r_0(y, z) + r_1(y, z)) - (r_0(y, z) + r_2(y, z)) \right) \tag{2.74}$$

$$= \frac{1}{c} \left(r_1(y, z) - r_2(y, z) \right) \tag{2.75}$$

where c is the speed of sound and $t_1(y, z)$ and $t_2(y, z)$ are the times of arrival of the signal at the upper and lower receivers respectively. It is helpful to introduce a new co-ordinate frame $[y', z']$, centred on the lower receiver and with z' inclined at the tilt angle Φ_0 [16]. The scatterer

location is given by

$$y' = y \cos \Phi_0 + z \sin \Phi_0 \tag{2.76}$$

$$z' = z \cos \Phi_0 - y \sin \Phi_0 - \frac{D_{\text{in}}}{2} \tag{2.77}$$

in the new co-ordinate frame, assuming that the transmitter lies at the mid-point between the receivers. The ranges from the receivers to the scatterer are given by

$$r_1(y', z') = \sqrt{(y')^2 + (z' + D_{\text{in}})^2} \tag{2.78}$$

$$r_2(y', z') = \sqrt{(y')^2 + (z')^2}, \tag{2.79}$$

and expanding and squaring (2.78) allows $r_1(y', z')$ to be written in terms of $r_2(y', z')$,

$$r_1(y', z')^2 = (y')^2 + (z')^2 + 2z' D_{\text{in}} + D_{\text{in}}^2 \tag{2.80}$$

$$= r_2(y', z')^2 + D_{\text{in}}(2z' + D_{\text{in}}) \tag{2.81}$$

and the time delay can be written as

$$\tau(y', z') = \frac{1}{c} \left(r_1(y', z') - r_2(y', z') \right) \tag{2.82}$$

$$= \frac{1}{c} \left((r_2(y', z') + D_{\text{in}}(2z' + D_{\text{in}}))^{1/2} - r_2(y', z') \right) \tag{2.83}$$

$$= \frac{r_2}{c} \left(\left(1 + \frac{D_{\text{in}}(2z' + D_{\text{in}})}{r_2^2} \right)^{1/2} - 1 \right) \tag{2.84}$$

as shown in (3.5) of [16].

Since $r_2 = ct_2/2$ is derived from the propagation time, and $\tau(y', z')$ is the measured time delay, inverting for z' gives the sea-floor depth in the rotated co-ordinate frame

$$z' = r_2 \frac{c\tau}{D_{\text{in}}} \left(\frac{c\tau}{2r_2} + 1 \right) - \frac{D_{\text{in}}}{2} \tag{2.85}$$

$$\approx r_2 \frac{c\tau}{D_{\text{in}}} - \frac{D_{\text{in}}}{2} \tag{2.86}$$

where the approximation $c\tau/2r_2 \approx 0$ assumes a flat incoming wavefront. Analysis of the modest error introduced by this approximation for a typical geometry is shown in Figure 3.3 of [16]. Returning to the original co-ordinate frame, the depth of the sea-floor relative to the transmitter is given by ([16] Eq. 3.8)

$$z = \sqrt{r_2^2 - (z')^2} \sin \Phi_0 + \left(z' + \frac{D_{\text{in}}}{2} \right) \cos \Phi_0 \tag{2.87}$$

in terms of only measured or known quantities.

The standard deviation of the depth estimate σ_z can be found as a function of σ_t, the

46

standard deviation on the time delay estimate, by taking the partial derivative of (2.87) with respect to τ given by

$$\frac{\partial z}{\partial \tau} = \frac{\partial z'}{\partial \tau} \left(\frac{\partial a}{\partial z'} \sin \Phi_0 + \cos \Phi_0 \right) \tag{2.88}$$

where $a = \sqrt{r_2^2 - (z')^2}$ such that

$$\frac{\partial a}{\partial z'} = \frac{-z'}{\sqrt{r_2^2 - (z')^2}} \tag{2.89}$$

and where

$$\frac{\partial z'}{\partial \tau} = \frac{c}{D_{\text{in}}} \left(r_2 + c\tau \right) \tag{2.90}$$

using (2.85) or

$$\frac{\partial z'}{\partial \tau} = \frac{c}{D_{\text{in}}} r_2 \tag{2.91}$$

using the planar wave-front approximation in (2.86). This gives

$$\sigma_z = \frac{c \left(r_2 + c\tau \right)}{D_{\text{in}}} \left(\frac{-z'}{\sqrt{r_2^2 - (z')^2}} \sin \Phi_0 + \cos \Phi_0 \right) \sigma_t \tag{2.92}$$

without the flat wave-front approximation or

$$\sigma_z = \frac{c r_2}{D_{\text{in}}} \left(\frac{-z'}{\sqrt{r_2^2 - (z')^2}} \sin \Phi_0 + \cos \Phi_0 \right) \sigma_t \tag{2.93}$$

assuming a flat wave-front. The implication of these expressions is that a larger interferometric baseline D_{in} results in a more precise bathymetry estimate, with performance that degrades with range.

The achievable interferometric baseline D_{in} for SAS systems is constrained by the size of the vehicle on which they are carried. For example, the receiver arrays on the MUSCLE system are separated by a distance of 9.5 cm (19 wavelengths) [54]. This is in contrast to the interferometric baseline used, for example, on the shuttle radar tomography mission (SRTM)[8] of 60 m, or ≈ 2000 wave-lengths of 3.1 cm [79]. This limitation has motivated the use of repeated passes in both sonar and radar, as it allows the receivers to be separated by an arbitrary distance. Additionally, performing multiple repeated passes allows the formation of a two-dimensional synthetic array, allowing high resolution three-dimensional imaging [19, 80].

The limitations of this model are twofold, however both can be compensated if extra information is included. The first limitation is that the ray paths are assumed straight, which is derived from the assumption of a constant speed of sound. This is known to cause range-dependent bathymetry estimation errors in environments with a non-constant sound speed profile, however these errors can be compensated for [16] by dividing the sound speed profile into a number of segments with a linear sound speed gradient. The rays in these segments

---

[8]The SRTM was the first space-borne single-pass interferometric SAR, and created a near-global digital elevation model (DEM) from 54˚S to 60˚N at a horizontal resolution of ≈ 30 m with absolute height error under 16 m.

propagate along an arc, and the compensated depth estimate is obtained once the ray path has travelled a distance of r_2. The second limitation is that the sonar is assumed to be motionless between ping transmission and reception. The most problematic motion for interferometry is roll, since it causes opposing path length changes to r_1 and r_2. This can be compensated by making the tilt angle $\Phi_0(t)$ a function of time, and using $\Phi_0(t_1)$ in (2.87).

2.4.2 Phase differencing

It is common to measure the time delay between narrow-band interferometric SAS images via phase differencing. The maximum-likelihood phase difference estimator is a 2D zero-lag cross-correlation [16] over a local window. This estimate is the angle of the complex coherence between two images $I_1(x, y)$ and $I_2(x, y)$, which is given by

$$\gamma(x, y) = \frac{\mathbb{E}\left\{I_1(x, y)I_2^*(x, y)\right\}}{\sqrt{\mathbb{E}\left\{|I_1(x, y)|^2\right\}\mathbb{E}\left\{|I_2(x, y)|^2\right\}}} \tag{2.94}$$

where $\mathbb{E}$ is the expectation operator. However, it is not possible to compute the ensemble averages in (2.94) and they must be approximated instead by a spatial average over a local neighbourhood, for example over a patch of $L_{\text{in}} \times L_{\text{in}}$ pixels, by

$$\gamma_{\text{in}}(x, y) \approx \frac{\sum_i I_1[i]I_2^*[i]}{\sqrt{\sum_i |I_1[i]|^2 \sum_i |I_2[i]|^2}} \tag{2.95}$$

where i indexes over the two-dimensional neighbourhood. The magnitude of the complex coherence function $\Gamma_{\text{in}}(x, y) = |\gamma_{\text{in}}(x, y)|$, referred to as the coherence, gives a measure of the similarity between the two images, ranging from 1 for identical patches to $1/L_{\text{in}}$ for uncorrelated noise [81].

The phase of the complex coherence function $\theta'_{\text{in}}(x, y) = \angle\gamma_{\text{in}}(x, y)$ is referred to as the interferogram or interferometric phase, and can be related to a time delay by

$$\tau(x, y) = \frac{\theta_{\text{in}}(x, y)}{2\pi f_0} \tag{2.96}$$

where $\theta_{\text{in}}(x, y) = \mathcal{U}\left\{\theta'_{\text{in}}(x, y)\right\}$ and $\mathcal{U}\{\cdot\}$ is the unwrap operator. That is, the phase measured by the phase differencing operator $\theta'_{\text{in}}(x, y)$ is wrapped modulo 2π, and must be correctly unwrapped before it is converted to a time delay.

Of notable importance is that if the interferometric SAS images are focussed onto the correct bathymetry, the interferometric phase is zero. The interferogram is thus a metric for bathymetry error, under the assumption of accurate navigation parameters and sound speed during SAS image formation.

An interferogram of the scene depicted in Figure 2.9 is shown in Figure 2.19. Slant-plane SAS images I_1 and I_2 were formed from each of the interferometric arrays on the MUSCLE AUV using the same navigation and sound speed parameters. No attempt has been made to co-register the images to improve coherence. An interferogram was taken according to (2.95) with
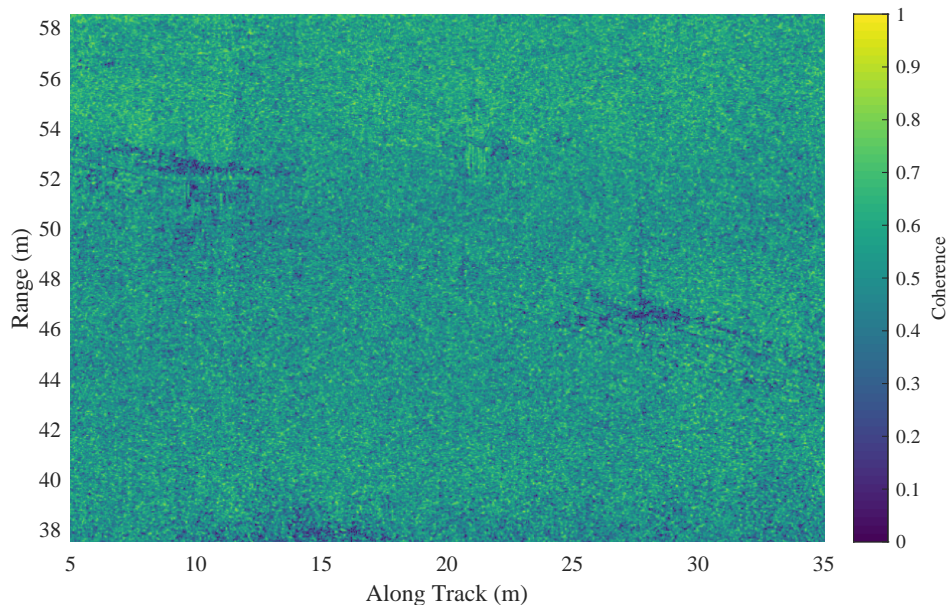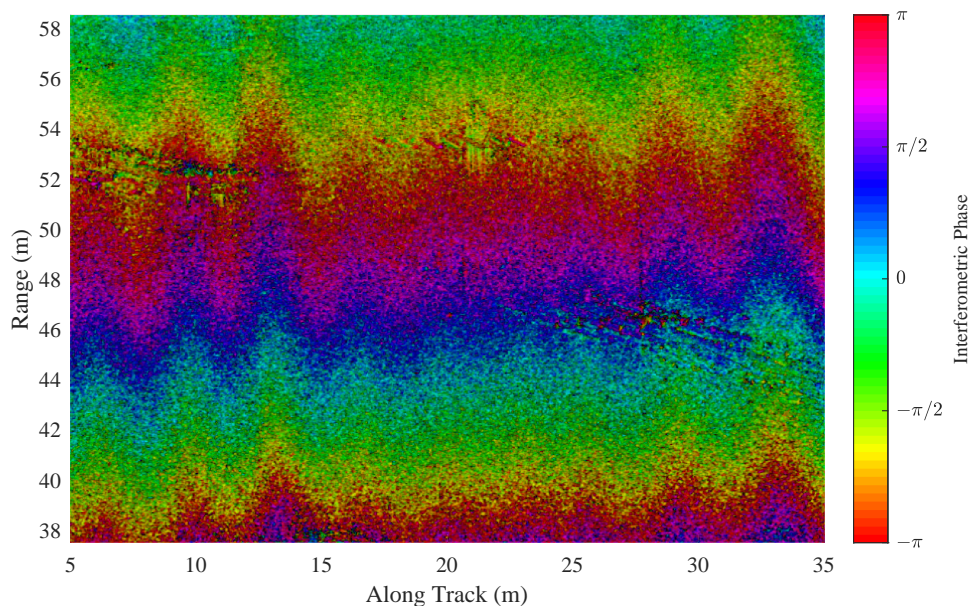
Figure 2.19: An example interferogram of the same scene as Figure 2.9b. (a) The magnitude of the complex interferogram is known as the coherence. (b) The phase of the complex interferogram can be used to estimate the sea-floor bathymetry. The rapidly varying phase in the range direction is caused by the slant-plane assumption. The oscillating variations in the along-track direction are caused by vehicle roll.

$L_{in} = 9$, and the magnitude and phase are plotted in Figures 2.19a and 2.19b respectively. The across-track phase gradient is typical of slant-plane interferograms, and must be unwrapped correctly before the phase can be interpreted into a bathymetry estimate. The along-track phase oscillations are caused by vehicle roll.

2.4.3 Phase unwrapping

Phase unwrapping is a broad and well researched topic. Techniques developed for interferometric SAR have been successfully adopted by the interferometric SAS community, such as the popular and widely used Goldstein's branch cuts algorithm [82, 83]. A recent review of phase unwrapping methods developed by the SAR community [84] is recommended to the interested reader, which reviews techniques for single baseline, multi-baseline and large scale phase unwrapping applications.

2.4.4 Discussion

Synthetic aperture sonar interferometry enables high resolution 3D mapping with high area coverage rate. However, the spatial resolution of the bathymetry estimates is typically an order of magnitude poorer than the image resolution, due to the size of the window used in the interferometric processing for spatial averaging in place of ensemble averaging. The choice of window size is a trade-off between spatial resolution and vertical accuracy; small windows provide high spatial resolution at the expense of vertical precision, while larger windows result in poorer spatial resolution but high precision bathymetry estimates. The comparatively low resolution of bathymetry estimates is likely to reduce the effectiveness of classification features derived from 3-D shape information.

The vertical precision of the bathymetry estimates can be improved by increasing the interferometric baseline. However, the receiver arrays cannot be separated without bound due to size constraints imposed by the vehicle. This limitation may be overcome by repeat-pass interferometric bathymetry estimation, which allows the receiver arrays to be separated by an arbitrary distance within the limits imposed by baseline decorrelation. However, this has yet to be successfully demonstrated for strip-map geometries. This is because achieving the required navigation precision between multiple passes is extremely challenging, and new data-driven micro-navigation algorithms are required to realise the exciting potential of repeat-pass interferometric SAS.

3 Synthetic Aperture Sonar Micro-Navigation

The principle of SAS is to form an image by coherent integration of the echo data collected along the track traversed by the vehicle, as described in Section 2. Doing so may be thought of as forming a *synthetic array* that is many times longer than the physical array length, where the location of each element of this virtual array is derived from the path of the sensor. It is intuitive then to consider that in order to beam-form using this virtual array its shape must be known precisely.

The maximum allowable phase error along the synthetic aperture length can be as small as $\lambda/8$, where λ is the wave-length at the centre frequency [2]. This leads to a maximum allowable position error in the line-of-sight direction of $\lambda/16$ accounting for two-way travel [16, 23]. It has been noted that this condition is more challenging to meet for SAS systems than SAR systems, due to the slower speed of propagation and instability of the acquisition platforms [30]. This leads to the paths traversed by underwater vehicles being further from the ideal rectilinear geometry. However, so long as the traversed path can be accurately estimated, non-ideal paths do not cause significant reduction in image resolution unless either

1. the surface onto which the image is formed is not close to the true bathymetry [85, 86], or

2. significant yaw reduces the synthetic aperture length or introduces coverage gaps along the aperture.

It is therefore desirable to have *a priori* knowledge of bathymetry prior to the image formation process [16, 32].

There are two families of techniques that are used to generate focused imagery from a non-linear collection geometry; *micro-navigation* and *autofocus*. Micro-navigation approaches exploit redundancy in either the collected echo data or the scene to estimate the ping-to-ping motion of the sonar. Autofocus refers to methods that perform a parameter optimisation to improve a chosen image metric using the image itself. A review of micro-navigation methods is the subject of Section 3.1, while the interested reader is directed to [53, Chapter 7] for a review of autofocus methods. A typical approach to generating focused images is to perform micro-navigation, followed by an autofocus method.

It is important to distinguish between motion estimation and motion compensation. Motion estimation can be split into two groups of methods; those that aim to estimate an equivalent sonar path which achieves well focused images, or those that seek to estimate the true path of the vehicle. Simply put, the aim of motion estimation methods is either focused imagery or accurate navigation estimation. Historically, the focus of through-the-sensor navigation estimation has been on generating well focussed imagery, with long-term navigation performed using other sensors on the vehicle such as an INS combined with a DVL or CVL. However, there has been recent interest in using through-the-sensor navigation estimates to supplement these sensors [34, 87].

The distinction between different groups of motion estimation methods is typically based on the data product and assumptions used to estimate navigation parameters. For example, the true three-dimensional geometry is simplified to the two-dimensional slant-plane geometry in the slant-plane RPC micro-navigation method [33], and the phase centre and stop-and-hop assumptions are used. The slant-plane simplification makes the assumption that the sonar and the sea-floor exist on a plane, with the sonar path being estimated in that plane. Imaging onto this plane using the estimated navigation solution often results in well-focused imagery, but including the through-the-sensor navigation estimates in the vehicle navigation solution requires knowledge of the bathymetry. In contrast, the aim of the new simultaneous micro-navigation and bathymetry estimation algorithm [21] described in Section 6 avoids these assumptions in order to make a three-dimensional navigation estimate. While accurate estimation of the bathymetry, navigation and medium speed allows the formation of well focused imagery [85], we consider the main benefit of the simultaneous micro-navigation and bathymetry estimation algorithm to be accurate three-dimensional navigation estimates and a coarse bathymetry estimate. This allows interferometric images to be focused directly onto the coarse bathymetry without requiring co-registration.

Motion compensation is the term used for the adjustment of raw, multiple-receiver bi-static sonar echo data collected from a multi-receiver system along a non-linear geometry into equivalent mono-static data collected along a straight path. This is an important pre-processing step required for the computationally efficient Fourier-domain imaging methods briefly discussed in Section 2.3.6. However, this falls out of the scope of this thesis due to our use of a time domain back-projection method for image formation, which allows image formation from an arbitrary acquisition geometry onto an arbitrary surface. The reader is directed to [33, Chapter 6] for a review of motion compensation methods.

3.1 Existing micro-navigation methods

It was recognised as early as 2003 by Gough and Miller in [88] that

> ...we could consider the multiple hydrophone receiver SAS as no more than a very sophisticated multibeam, Doppler velocity profiler. Thus it could be possible that sometime in the future, all AUVs will be deployed with an array SAS on board not for imaging, but for navigation.

While this assertion is not strictly true since no SAS micro-navigation method in the literature exploits temporal Doppler, it can certainly be considered to be a very high precision *correlation* velocity log. Neglecting this distinction, the point still stands; multi-array, dual-sided interferometric SAS can be considered a high precision navigation instrument in addition to its impressive sea-floor imaging capabilities. Indeed, it has been found that navigation estimates derived from a SAS have measurement noise roughly two orders of magnitude lower than those estimated by a DVL using a similar frequency [34, 87].

A multitude of micro-navigation methods have been documented in the literature. As previously mentioned, they can be divided into those that exploit either redundancy in echo

data or scene redundancy. The methods in the first group require the SAS to travel slower than the maximum allowable speed for a fully sampled synthetic array, $cL/4R_{\max}$, resulting in overlap between the phase centre arrays between adjacent pings. Signals received by these overlapping elements receive highly correlated signals, from which navigation estimates can be made. However, this carries a cost due to the associated reduction in ACR, which motivates the use of methods that exploit scene redundancy and thus do not require ping-to-ping overlap.

Table 1 groups micro-navigation methods into those that operate in single- and repeat-pass, those that operate using individual multiple arrays, and those that utilise echo-data redundancy, coherence of complex imagery, similarity of intensity images and similarity of bathymetry estimates. We review each group in the following sections.

Table 1: Families of micro-navigation methods used in SAS

Exploiting:	Single pass		Repeat pass	
	Single array	Multiple arrays	Single array	Multiple arrays
Echo data redundancy	[30, 31, 33]	[33, 16, 89, 32, 90]	[91, 1, 92, 87]	[21]
Complex images	[93, 94, 95]		[96]	[19, 80]
Intensity images	[88, 97, 94, 98]		[20, 24]	
Bathymetry estimates	-	[94]	-	[99]

3.2 Micro-navigation methods exploiting echo data redundancy

Navigation estimation exploiting echo data redundancy is the most common and well-generalised family of methods, having been demonstrated in all columns of Table 1. This family of methods is popular for multiple reasons. They require few assumptions to be made about the scene, apart from the requirement for ping-to-ping coherence obtained for fully-developed speckle [100]. They normally operate on a ping-by-ping basis and are typically computationally inexpensive, allowing them to be used in real-time applications.

3.2.1 Single-pass methods

3.2.1.1 Single array methods

The slant-plane redundant phase centre (RPC) algorithm has been described as the 'quintessential' SAS motion estimation algorithm [33], from which most data domain micro-navigation methods are derived. The basis of the RPC technique is found in the radar literature [101], which describes motion compensation of a multi-element antenna termed a displaced phase centre antenna (DPCA). The motion estimates are derived from phase differences recorded by overlapping (redundant) phase centres at a number of sliding range windows, first demonstrated in the SAS domain in [30]. The lower bound on the variance of an unbiased estimator is given by its Cramer-Rao lower bound (CRLB). The CRLB for through-the-sensor slant-range

sway and yaw estimation was reported by Bellettini and Pinto [31] and the CRLB for surge has since been reported by Brown [102, Appendix B]. A thorough description of the slant-plane redundant phase centre (SPRPC) method is given in [33, Chapter 5.4].

While this micro-navigation method allows the formation of focused imagery in benign situations e.g. straight tracks [85], it has a number of limitations. The independent measurement of inter-ping slant-plane sway and yaw results in different navigation estimates at each range window. This is clearly non-physical; the SAS cannot be in multiple places at the same time. This is a result of the assumption that all RPC time delays are caused by ping-to-ping motion in the slant-plane. This assumption has the effect of partially compensating for the portion of RPC time delays caused by bathymetry and medium fluctuations, leading to its ability to focus images even in challenging environments and conditions. However, slant-plane images are less suitable for use in interferometry [103, 32] than images formed onto an *a priori* bathymetry estimate. In addition, it is challenging to incorporate the 2D range-dependent slant-plane navigation estimates into the 3D vehicle navigation estimate.

It has been shown that the range-dependent slant-plane ping-to-ping navigation estimates can be converted into a three-dimensional estimate in full three-dimensional Cartesian space if an estimate or assumption of the bathymetry exists [33, Ch. 5.5],[33, Ch. 5.6]. These methods involve simultaneous use of the slant-plane time differences of arrival at multiple range windows. The method described in [33, Ch. 5.5] assumes that the vehicle attitude and angular velocities are measured by an on-board sensor such as an INS. The method involves performing a non-linear least-squares optimisation using Newton's method to find the across-track and vertical velocities for each ping pair. Parametrising the solution using velocities allows the stop-and-hop assumption to be avoided, and instead an assumption of zero accelerations during the ping pair is made.

The method described in [33, Ch. 5.6] uses a simplified model employing the stop-and-hop assumption to find the inter-ping sway and heave displacements between each pair of redundant phase centres. A linear regression is then used to estimate the sway, heave, pitch and yaw between arrays. However, the accuracy of the yaw and pitch estimates is dependent on the number of RPC pairs formed between pings, and the method was demonstrated with ten RPC pairs. This large inter-ping overlap would likely reduce the area coverage rate below practical limits apart from for certain short-range systems [27]. Both of these approaches allow formation of ground-plane images onto an *a priori* depth estimate from a single array SAS. However any errors in the assumed bathymetry corrupt the navigation estimate and lead to a reduction in image quality.

3.2.1.2 Multiple array methods

These single-pass methods can be split into methods that utilise a single array on both sides of the vehicle, those that use the two arrays of a single-sided interferometric system, and those that make use of the four arrays of a dual-sided interferometric system for navigation estimation. There are strong motivations for using data from multiple sensors for micro-navigation; increased robustness and accuracy [104, 89], and to allow SAS image formation onto an *a priori*

bathymetry estimate [103, 32].

Dual-sided methods The method described in [33, Ch. 5.7] utilises RPC time delay measurements to estimate ping-to-ping sway and heave. Using the stop-and-hop assumption, the phase centre assumption, a flat-sea-floor assumption, uniform and known sound speed, and an assumption of perfect along-track RPC alignment, a closed-form solution exists for inter-ping sway and heave. This is achieved by mapping the dual-sided data onto a virtual array at the centre of the vehicle by addition of a time delay. This closed form method is fast, but relies on having high-quality data on both sides of the vehicle and relies on a large number of simplifying assumptions.

Another method has been demonstrated that fuses micro-navigation estimates from both the port and starboard sides using a Kalman filter [89]. This reduces the requirement for having good data on both sides of the platform, but does make a flat-sea-floor assumption and the details of the micro-navigation implementation are not disclosed. The authors note that the flat-sea-floor assumption can be removed if bathymetry estimates derived from an interferometric SAS are available. It was noted that for the MUSCLE AUV, adjustments to the calibration of the sonar were required to remove the effect of array misalignment.

Interferometer methods The approach taken in [33, Ch. 5.6] has been developed to make use of bathymetry estimates that can be made using an interferometric SAS in [32, Chapter 4.2.6]. This sequential estimation of bathymetry and navigation goes some way to removing the navigation corruption caused by errors in the assumed bathymetry. However, any errors in the bathymetry estimate will be carried forward into the navigation solution.

The approach taken in [16, Ch. 5.2] involves a similar, sequential estimation of bathymetry using the real aperture interferometer before estimating ping-to-ping navigation parameters. However, the method used to integrate the slant-range navigation estimates using the bathymetry is not described.

The sequential nature of these methods has the potential to cause errors for two reasons. Any errors in the bathymetry estimate will be carried forward to corrupt the navigation estimate. More significantly, the bathymetry and navigation estimates are made using different data; the initial bathymetry estimate is typically derived from the full real aperture interferometer, but the navigation estimate is derived from only the RPC arrays. An attempt is made to counter this effect by weighting the bathymetry estimates in each range window by the image intensity in [103]. However, the method is found to be computationally expensive. A possible solution to this problem is to use the redundant portion of the array to derive both the bathymetry and navigation estimates.

Dual-sided interferometer methods The dual-sided micro-navigation fusion method in [89] was built upon in [35], which introduces the fusion of micro-navigation measurements made between all 4 arrays of a dual-sided interferometric SAS, again using a Kalman filter. This resulted in an improvement to image quality, which was concluded to be due to improved

navigation estimation.

The novel approach taken in Section 6 operates on either one-sided or dual-sided interferometric systems. The crucial difference between this approach and other methods is that it simultaneously estimates navigation and a coarse bathymetry using the same redundant data. Time delay measurements made between signals received by all redundant arrays formed between pings are utilised in making the navigation and bathymetry estimates. The method is built upon the minimisation of the difference between modelled and measured RPC time delays and surges using iterative inversion of a linearised model. This approach allows the model to be tuned to the desired accuracy; the method as presented uses a model that does not employ the phase centre assumption and assumes constant inter-ping velocities and angular velocities, replacing the stop-and-hop assumption with a constant-velocity assumption. The method could be improved further by fusing the resulting navigation estimates with those derived from the navigation hardware using a Kalman filter.

3.2.2 Repeat-pass methods

3.2.2.1 Single array methods

Repeat-pass coherence of echo data was demonstrated in [91], and cross-correlation of the redundant signals allowed estimation of the relative slant-plane displacement between repeat-passes. In addition, the effect of across-track separation and element size on the correlation coefficient was investigated. This work was extended in [1], where the relative slant-plane tracks of repeated passes were estimated and demonstrated to be sufficiently accurate to achieve good coherence between repeat-pass SAS images. However, the interferogram formed between these images did not appear to contain useful phase for high resolution bathymetry estimation. This is a consequence of the assumption that all RPC time delays are caused by navigation differences in the slant-plane, that the sea-floor exists in the slant-plane, and the sound speed is accurately known. It has been proposed that the algorithm could be used to reduce the navigation drift of a sonar survey by modifying the paired track pattern such that small regions of overlap exist [92].

3.2.2.2 Multiple array methods

Systems with interferometric arrays have been used to obtain repeat-pass navigation estimates in three dimensions. Preliminary results from a repeat-pass development of the method in Section 6 were presented in [21]. The method estimates inter-pass across-track and vertical displacements using repeat-pass time delay measurements from the raw echo data on a ping-by-ping basis. The repeat-pass navigation estimates are estimated simultaneously with bathymetry by iterative inversion of a linearised model parametrising sea-floor bathymetry and displacements in the across-track and vertical directions.

3.3 Complex image methods

3.3.1 Single-pass methods

The method in [94, 3.1] involves forming an interferogram between images generated from only the RPC arrays formed between adjacent pings. An iterative search is performed which minimizes the difference between measured and modelled interferograms, resulting in a navigation update.

Bonifant [105] makes reference to Tonard's 'beam to beam correlation' algorithm [106], which forms a number of beams from the RPC arrays formed between adjacent pings. This is analogous to the formation of polar images from the RPC arrays. All pairs of beams are cross-correlated between pings, and analysis of the locations of the cross-correlation maxima allows estimation of the relative yaw and across-track array motion. Bonifant suggested that the method would also be successful with no inter-ping overlap, as long as a strong scatterer is present in both images of each ping pair.

The approach taken in [95] for focusing single pass images appears to operate on images formed from array elements with ping-to-ping redundancy. However, the implementation is unclear and the measured shifts are used to motion compensate the data rather than improve the navigation estimate.

There are also methods derived from the cascade algorithm in SAR [93] which exploit the same assumptions used in autofocus algorithms, which operate on scene redundancy rather than redundancy in echo data from overlapping elements. However, it is suggested that in some common scenarios the technique is likely to fail, and suggests instead encoding the magnitude information into a phase term, effectively performing amplitude-only correlation.

3.3.2 Repeat-pass methods

There are numerous implementations of sub-pixel precision image co-registration methods developed for coherent change detection (CCD) applications [107, 108, 99, 22], which typically compute relative image shifts using 2D complex cross-correlations. These shifts are then used to warp images until they are co-registered. This method is typically sufficiently accurate for CCD, but often does not preserve the image phase, making the repeat-pass interferogram difficult to interpret. It is uncommon to convert these relative shifts to an updated navigation solution.

The method in [109] does attempt to extract navigation corrections using repeat-pass image shifts, but identifies a number of challenges which cause the repeat-pass interferograms to be difficult to interpret. The most significant misregistration error found in the results was identified to be in the along-track direction, caused by vehicle speed errors. It is claimed that a higher order warping function would improve the repeat-pass coherence.

A recent method uses complex cross-correlations to find misregistration in the along- and across-track directions by a local two-dimensional cross-correlation method [24]. Inversion of a model based on [20] is used to estimate corrections to the across-track position, altitude, heading and sound speed for the slave track. The track registration appears to be sufficiently

accurate to achieve high repeat-pass coherence, but repeat-pass phase is not presented. The authors suggest that along-track misregistration may be caused by uncompensated array pitch, leading to along-track position errors.

It was noted in the radar domain [96] that image shifts between sub-aperture images from different passes could be used to make both scene topography estimates and platform navigation estimates simultaneously, down to a co-ordinate system rotation. It is possible to remove this ambiguity using multiple-array systems with high-precision roll measurement systems, or alternatively single array systems with independent, high-precision depth measurement hardware. Typically the depth measurement hardware on AUVs is less precise than the INS angular positioning. The method was adopted for interferometric SAS for circular [19] and helical [80] collection geometries. This method included estimation of the sound speed error in the inversion.

3.4 Intensity image methods

3.4.1 Single pass methods

The displaced ping imaging autofocus (DPIA) algorithm [97] (based on the map-drift algorithm adapted from the SAR literature [88]) was developed with the aim of increasing the ACR by removing the necessity for overlapping phase centres. It operates by estimating shifts between magnitude images formed from the physical apertures of adjacent pings. While the original paper showed promising results on simulated data, a recent implementation [98] concluded that it was no more successful than conventional RPC micro-navigation for the subset of real data used. The authors propose that the low azimuthal resolution of, and low similarity between, single-ping images could be the cause of the poor results [98].

An approach that has been used in circular SAS is to form sub-aperture images from multiple pings in a technique known as map drift [53, 94], measuring shifts between sub-aperture images by incoherent cross-correlation. The use of images formed from multiple pings improves their azimuthal resolution and thus the precision of the shift estimated between images by cross-correlation. Also, the circular geometry results in greater overlap between sub-aperture images. This suggests that the technique may be more applicable to circular SAS acquisition geometries than linear ones.

3.4.2 Repeat-pass methods

A common and efficient method of computing shifts between images is to match corresponding image regions using feature descriptors such as scale-invariant feature transform (SIFT) [110] or speeded up robust features (SURF) [111]. For optical images taken with a camera, it is possible to use these correspondences to estimate the relative position and orientation of the cameras while simultaneously estimating the positions of the features in three-dimensional space [112].

Use of the SIFT descriptor has been demonstrated with SAS images for co-registration [25, 22], and an analysis of the performance of the SIFT and SURF descriptors on speckle

imagery has been performed [113]. Feature matching between SAS images has been performed for track registration of repeated passes on both simulated [25] and real data [20].

An alternative method to feature detection and matching is to cross-correlate intensity images to find the shift between them [92]. These incoherent, image domain methods have the advantage of simplicity and efficiency. However, they rely on consistent scene features and are therefore unsuitable for benign terrain. They are also orders of magnitude less precise than coherent methods [92], but are less sensitive to differences in the acquisition geometries between passes. It is suggested that a combination of incoherent and coherent approaches is pragmatic; an incoherent approach can be used to make a coarse estimate, which can be refined by a coherent approach [22].

3.5 Methods utilising bathymetry estimates

3.5.1 Single-pass methods

The micro-navigation and image registration methods described make use of cross-correlations of redundant echo data, complex images and magnitude images. An interferometric SAS is able to generate bathymetry estimates (from a single ping, a subset of pings, or over an entire image), which can also be cross-correlated to estimate a relative shift. Cross-correlation of bathymetry estimates requires no coherence in the raw data or beam-formed images. It is therefore robust to significantly different acquisition geometries and temporal decorrelation. However, the spatial resolution of InSAS bathymetry estimates is typically an order of magnitude poorer than the image quality. Therefore navigation estimates derived from cross-correlation of bathymetry estimates are expected to be poorer than those derived from image correlations [94].

3.5.2 Repeat-pass methods

An important parameter for repeat-pass interferometry is the *perpendicular baseline*, the distance between acquisitions in the direction normal to the line of sight. A simple method for perpendicular baseline estimation using InSAS bathymetry estimates has been proposed and demonstrated on real data [99]. The method is thought to be useful for vehicles without a high precision navigation system or where the raw data is unavailable. However, the poor spatial resolution of InSAS bathymetry estimates may limit the precision of the perpendicular baseline estimates.

3.6 Other relevant work

The micro-navigation methods described exploit through-the-sensor measurements to make navigation estimates, often discarding those made by the on-board navigation hardware. While the navigation hardware is insufficiently precise along the length of a synthetic aperture to produce focused imagery, the measurement error from one ping to the next is typically small. This has been exploited by Prater et. al. [114], where the separation between the RPC arrays

formed between adjacent pings has been estimated from the navigation hardware. Estimation of coarse bathymetry is demonstrated using this separation as an interferometric baseline.

This is an excellent demonstration of the 'triad of confounding factors' in action. In this example, the navigation and sound speed are assumed to be well known, allowing estimation of bathymetry. This is in contrast to many micro-navigation approaches, which assume the bathymetry and sound speed are well known in order to estimate navigation. The simultaneous micro-navigation and bathymetry estimation method developed in Section 6 can be considered to be a fusion of these approaches, assuming the sound speed is well known in order to make both bathymetry and navigation estimates.

3.7 Summary

There are numerous different implementations of through-the-sensor micro-navigation methods described in Sections 3.2-3.5. However, there are some clear trends in the published research.

The first is the novel idea that RPC time delays and inter-image shifts are affected by a 'triad of confounding factors' in navigation, bathymetry and sound speed. This has led to the development of methods that utilise sidescan bathymetry estimates derived from a single-ping of an interferometric SAS to improve the navigation estimate, techniques that simultaneously make bathymetry and navigation estimates, and methods that include through-the-sensor sound speed estimation [16, 32, 19].

The second trend is towards the development of high-precision repeat-pass micro-navigation methods that result in co-registered SAS images. Sufficient co-registration precision has been demonstrated for CCD applications, which typically require registration down to 1/10 of a pixel. However, the potential for high-precision bathymetry estimation from multiple passes in a strip-map geometry has yet to be realised, as it requires even higher co-registration precision.

The third trend is the reduction of the dependence on simplifying assumptions in models. For example, the phase centre assumption is known to bias RPC time delays estimates and must be compensated for [31, 115] or avoided entirely [116]. The effect of the stop-and-hop assumption on image quality has been investigated, [117, 51] and found that image quality is degraded with a high platform speed. The effect of the stop-and-hop assumption on micro-navigation performance does not seem to have been investigated in-depth. However, roll errors are known to be detrimental to interferometric SAS performance [105, Ch. IV.4.1.4]. The use of the stop-and-hop assumption in the presence of roll angular velocity causes a roll error, and therefore the stop-and-hop assumption should be avoided when interferometric arrays are used for micro-navigation or bathymetry estimation.

This thesis proposes that the best chance of achieving sub-wavelength navigation precision for repeat-pass interferometric phase exploitation is through simultaneous estimation of navigation, bathymetry and sound speed using as much redundant data collected between pings as possible. To this end a simultaneous navigation and bathymetry estimation algorithm has been developed and demonstrated in Section 6, which utilises time delay estimates between all RPC arrays. The method requires accurate time delay estimates free of phase cycle errors, which

has motivated the development of the novel phase cycle detection and correction algorithm described in Section 5. The simultaneous micro-navigation and bathymetry estimation algorithm is considered to be a significant step towards full inversion of the 'triad of confounding factors'. The advantages of the method are three-fold.

1. The coarse bathymetry estimate allows formation of co-registered images from interferometric arrays in near-ground range, for immediate application of interferometric methods without requiring image co-registration in regions of benign bathymetry.

2. The method operates on unfocused echo data, and does not require iterative SAS image formation, which is computationally expensive.

3. The same data are used for bathymetry and navigation estimation simultaneously, reducing the possibility of bathymetry errors corrupting the navigation solution.

4 Exploiting echo data redundancy

Through-the-sensor measurements derived from the redundant data collected by overlapping phase centres exploit the coherence of the acoustic field scattered from the sea-floor. The along-track motion of the array or *surge* is measured using the predictable decrease in coherence magnitude between redundant signals with spatial separation, that is, the shape of the scattered field coherence. The time delay between signals is derived from cross-correlation of the redundant data, utilising the complex coherence of the acoustic field itself.

4.1 Temporal windowing

The methods described in Section 3.1 that rely on exploiting echo data redundancy perform a short-time windowing of the echo data before a surge or time delay estimation method is used. The process of short-time windowing is depicted in Figure 4.1. Figure 4.1a shows an example signal $s(t)$, plotted as a function of time and equivalent range ($r = ct/2$, $c \approx 1500\,\mathrm{m\,s^{-1}}$). Figure 4.1b shows a number of windows $w_q(t)$ where $q \in [0, Q-1]$ indexes over the range windows and Q is the number of range windows. Each window function is given by

$$w_q(t) = \begin{cases} g\left(t - t_q\right) & t_q - \frac{T_\mathrm{w}}{2} \leq t \leq t_q + \frac{T_\mathrm{w}}{2} \\ 0 & \text{otherwise} \end{cases} \tag{4.1}$$

where

$$t_q = \frac{2R_q}{c} \tag{4.2}$$

defines the time of the centre of the qth range window at a range of R_q, and

$$T_\mathrm{w} = \frac{2L_\mathrm{w}}{c} \tag{4.3}$$

is the temporal length of the window [118] with spatial length L_w, and $g(t)$ defines the window function. The window function pictured in Figure 4.1c is a Tukey window with $L_\mathrm{w} = 7.5\,\mathrm{m}$ defined by

$$g(t) = \begin{cases} \frac{1}{2}\left[1 + \cos\left(\pi\left(1 + \frac{2t}{\alpha T_\mathrm{w}} + \frac{1}{\alpha}\right)\right)\right] & \frac{-T_\mathrm{w}}{2} \leq t < \frac{-\alpha T_\mathrm{w}}{2} \\ 1 & \frac{-\alpha T_\mathrm{w}}{2} \leq t \leq \frac{\alpha T_\mathrm{w}}{2} \\ \frac{1}{2}\left[1 + \cos\left(\pi\left(1 + \frac{2t}{\alpha T_\mathrm{w}} - \frac{1}{\alpha}\right)\right)\right] & \frac{\alpha T_\mathrm{w}}{2} \leq t < \frac{T_\mathrm{w}}{2} \end{cases} \tag{4.4}$$

where α controls the ratio of the unity region to the cosine-tapered region. Setting $\alpha = 0$ results in a rectangular window, $\alpha = 1$ results in a Hann window.

The windowed signal for the qth range window is given by

$$s_q(t) = s(t) \cdot w_q(t), \tag{4.5}$$

which is a point-wise multiplication of the signal $s(t)$ with the window function $w_q(t)$. An example of the resulting signals is plotted in Figure 4.1c, and Figure 4.1d plots these windowed
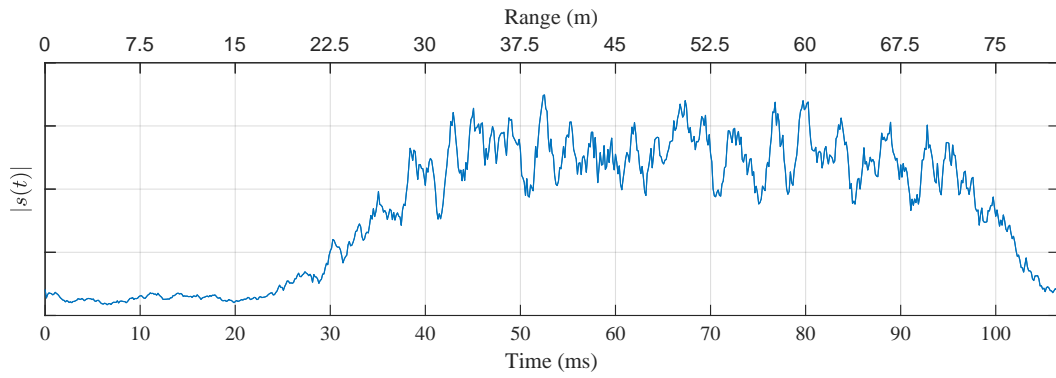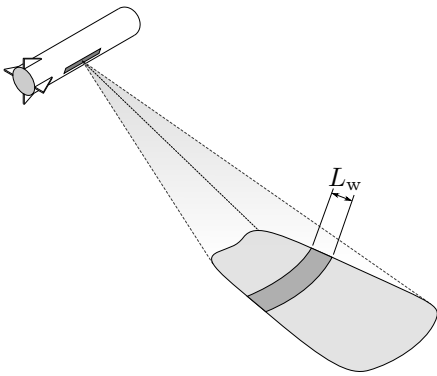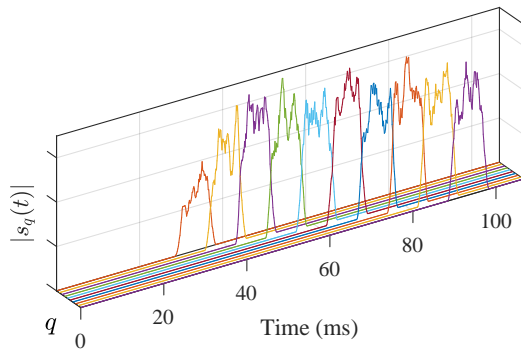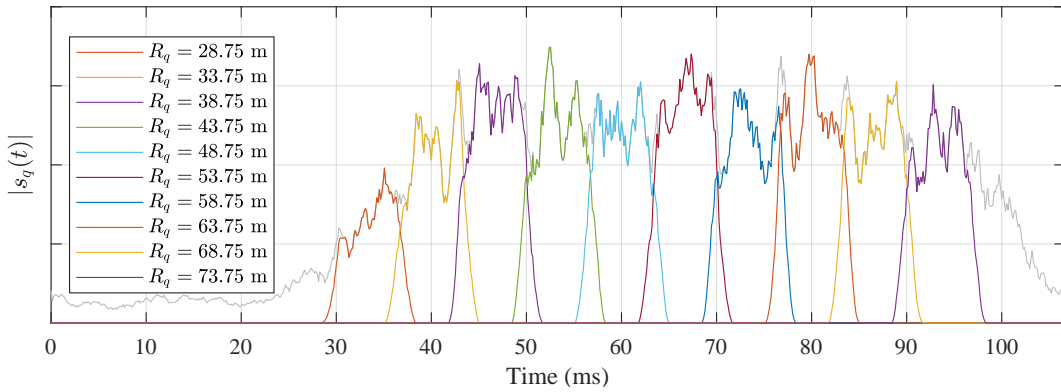
Figure 4.1: An example illustration of the process of range windowing. (a) A signal $s(t)$ is plotted against time and the equivalent range of $r = ct/2$ where $c = 1500\,\mathrm{m\,s^{-1}}$. (b) The temporal windowing limits the sonar footprint in range. (c) An array of window functions $w_q(t)$ are point-wise multiplied by $s(t)$, resulting in the range-windowed signals $s_q(t)$. (d) The coloured signals represent the signals windowed around each range, and are short-time windowed versions of the original signal shown in grey.

signals on top of the original signal shown in grey. The windowing process results in signals with many zero elements; it is common to truncate the signal by discarding the samples of $s_q(t)$ for which $w_q(t) = 0$.

4.1.1 Choice of window length

It is natural to seek the optimal window length for the time delay estimation application. However, it is generally acceptable to choose a window length according to some general observations. Long windows have more independent samples, which generally improves the performance of time delay estimators. The CRLB may be used to estimate the best performance of a time delay estimator as a function of the signal properties. For example, the CRLB for the high precision time delay estimates made using the cross-correlation function in the slant-plane RPC algorithm have been reported to be

$$\sigma_{\mathrm{CRLB}} \approx \frac{1}{2\pi f_0 \sqrt{BT_{\mathrm{w}}}} \sqrt{\frac{1}{\Omega} + \frac{1}{2\Omega^2}} \tag{4.6}$$

for band-width sampled signals by Bellettini and Pinto [31] where f_0 is the signal centre frequency, B is the signal bandwidth, and

$$\Omega = \frac{\rho}{1 - \rho} \tag{4.7}$$

is an estimate of the SNR as a function of ρ, the peak magnitude of the cross-correlation function.

This relationship can be derived by considering the signal s with two additive independent and identically distributed (IID) noise sources n_1 and n_2 not correlated with s, giving a pair of signals $s_1 = s + n_1$ and $s_2 = s + n_2$. The correlation between these signals is given by

$$\rho = \frac{\langle s_1 s_2^* \rangle}{\langle s_1 s_1^* \rangle \langle s_2 s_2^* \rangle} \tag{4.8}$$

where $\langle \cdot \rangle$ denotes ensemble averaging [119]. Exploiting the fact that the noise and signal are uncorrelated, this results in the expression

$$\rho = \frac{|s|^2}{|s|^2 + |n|^2} \tag{4.9}$$

which can be rearranged by noting that $\Omega = |s|^2/|n|^2$ is the SNR, to give

$$\Omega = \frac{1}{1 + \rho^{-1}} \tag{4.10}$$

which can be rearranged to give (4.7). The CRLB for the time delay estimation in the slant-plane RPC micro-navigation algorithm is plotted for a number of window lengths in Figure 4.2, for the specifications of the MUSCLE SAS ($f_0 = 300\,\mathrm{kHz}$, $B = 60\,\mathrm{kHz}$). These curves show that the accuracy of the time delay estimate can be expected to improve with a longer window
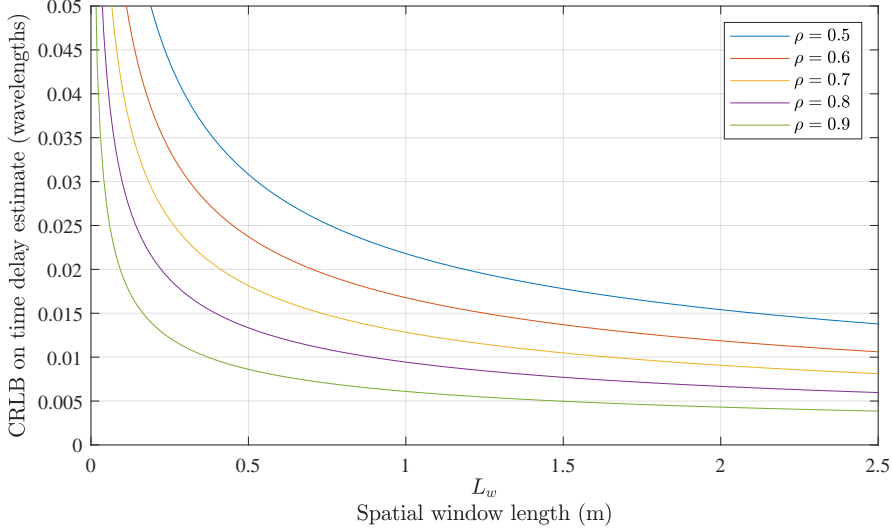
Figure 4.2: The CRLB for the time delay estimate in the SPRPC micro-navigation algorithm, plotted as a fraction of a wavelength for a number of signal coherences and a range of spatial window lengths. The values for the frequency and bandwidth match those of the MUSCLE SAS, with $f_0 = 300\,\mathrm{kHz}$ and $B = 60\,\mathrm{kHz}$.

length, although this is subject to diminishing returns.

The use of the cross-correlation operator in time delay estimation assumes the time delay does not vary along the length of the windowed signal. However, the signals received by RPC arrays are non-linear geometrical transformations of a single realisation of the underlying sea-floor reflectivity function [16, Ch. 4.1.3]. This non-linear geometrical transformation results in signals that are dilated with respect to one another. When the signals are short-time windowed, this dilation manifests as the combination of a delay and a relative dilation.

Using the rotated co-ordinate system introduced in Section 2.4, the relative dilation between signals received by interferometric arrays separated by a distance D is given by [16, Eq. 3.14]

$$\alpha(y') = \left(\frac{(y')^2 + (z')^2}{(y')^2 + (z' + D)^2} \right)^{1/2} \tag{4.11}$$

which is plotted in Figure 4.3a for typical operating parameters of the MUSCLE AUV for three values of interferometric baseline, $D = [1, 5, 10]D_{\mathrm{M}}$ where $D_{\mathrm{M}} = 19\lambda_0 = 95\,\mathrm{mm}$ at $\lambda_0 = 5\,\mathrm{mm}$. The platform altitude is $10\,\mathrm{m}$ and the inclination of the interferometer is $4\,°$. The dilation is seen to approach unity at long range, but at short range the dilation diverges from unity.

A brief numerical study has been performed to estimate the coherence loss due to this relative dilation. Figure 4.3b shows the coherence

$$\rho_{\mathrm{dilation}} = \max \left\{ \int_{-\frac{T_{\mathrm{w}}}{2}}^{\frac{T_{\mathrm{w}}}{2}} (w(t)\sin(2\pi f_0 t))^*(w(t - \tau)\sin(2\pi\alpha f_0(t - \tau)))d\tau \right\} \tag{4.12}$$

65
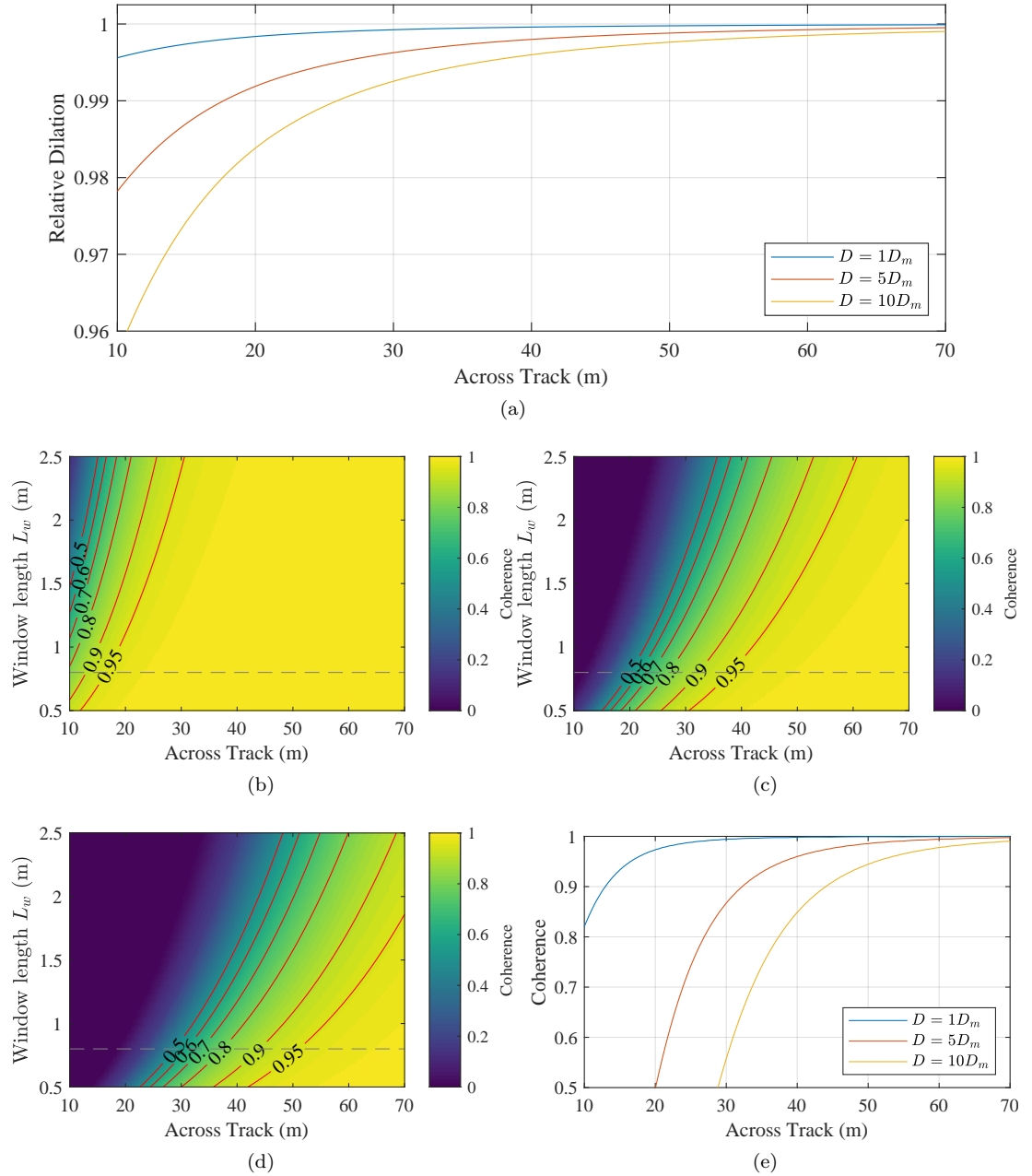
Figure 4.3: (a) The relative dilation between signals as a function of across track position, computed using typical survey parameters for the MUSCLE AUV. The three lines refer to baselines of 1, 5 and 10 times the interferometric baseline on the MUSCLE SAS, $D_M = 19\lambda_0 = 95\,\text{mm}$ at $\lambda_0 = 5\,\text{mm}$. These represent the baseline for a single-pass interferometer and two possible repeat-pass interferometric baselines. (b-d) The modelled coherence due to dilation computed for a range of patch lengths and across-track positions, for $D = D_M$, $D = 5D_M$ and $D = 10D_M$. (e) Sections through (b-d) at $L_w = 0.8\,\text{m}$, showing that the coherence loss due to dilation can be considered insignificant at the ranges of interest for the single-pass interferometric baseline, but may be significant for larger baselines achievable using repeat-pass interferometry.

which is the maximum value of the cross-correlation of a tone[9] of frequency f_0 with a dilated version of the same signal at a frequency of αf_0, where $w(t)$ is a windowing function, computed over the interval $-T_w/2 \leq \tau \leq T_w/2$. A Hann window has been used here.

Figures 4.3b-d show that relative signal dilation causes the greatest coherence loss at short range and large window sizes. Figure 4.3c shows sections through Figures 4.3b-d at $L_w = 0.8\,\mathrm{m}$, which is the window length used in Section 6. This shows that at the across-track positions of interest for the MUSCLE system ($y \geq 20\,\mathrm{m}$) the reduction in coherence due to dilation is minor for the physical interferometric baseline, but may be significant for larger baselines achievable with repeated passes.

In situations where the decorrelation due to relative signal dilation are significant, i.e. systems with large grazing angles or large baselines, the more computationally expensive cross-uncertainty function [16, Ch. 4.3-4.4] should be used in place of the cross-correlation function.

A further factor in the choice of window length is that short windows have the advantage of being robust to local reductions in coherence. Such coherence reductions may be caused by biological activity, such as moving fish and sea-grass, shadows behind proud objects, or rapidly varying bathymetry. Additionally, the use of short windows can allow a larger total number of range windows, increasing the number of independent time delay estimates. This may improve the performance of micro-navigation algorithms that simultaneously exploit multiple time delay estimates to reach a navigation estimates.

4.2 Surge estimation

Surge estimation for SAS systems can be achieved by analysis of the spatial coherence of sea-floor echo returns measured between pings [120]. This analysis relies on having a model of the spatial coherence of the scattered field [102, Ch. 2]. The method is analogous to the operation of correlation velocity logs, which were first developed for aircraft using radar [121] and extended to sonar in [122]. Correlation velocity logs have been used for velocity estimation of surface ships [123, 124, 125, 126] as well as underwater vehicles [127, 128, 129], and at least one commercial off-the-shelf (COTS) package is available [130]. Developments to CVL inversion methods incorporating multiple pings may allow the package footprint to be reduced, for use on small, low cost AUVs with small power budgets [131].

4.2.1 Correlation and Doppler velocity logs

The use of a CVL has multiple advantages over a DVL. DVLs use multiple, narrow beams inclined at an angle ($\approx 30°$) away from vertical, measuring the Doppler shift on each. Using the known geometry of the sensor and an estimate of the speed of sound, the velocity of the platform can be inferred. Narrow beams necessitate high frequencies for realistic transducer sizes. By comparison, the beam of a CVL is pointed directly downward, and can be significantly wider. The normal incidence of the acoustic pulse on the sea-floor produces a stronger echo,

---

[9]The choice of a tonal signal represents the upper limit of the decorrelation due to the relative dilation, because the signals employed in SAS systems are not tonal - they have some bandwidth. Similar analysis for a more representative signal is suggested for future work.

reducing the transmitted power requirement. In addition, the relaxed beam-width requirement means that lower frequencies can be used, significantly reducing attenuation. The result is a system with improved maximum range to input power ratio. Additionally, they are well suited to complex manoeuvres, with high accuracy at low speeds [132]. A crucial advantage is that the operation of a CVL does not require knowledge of the sound speed, whereas DVL accuracy is affected by refraction and sound speed errors.

4.2.2 Synthetic aperture sonar as a correlation velocity log

Single-array synthetic aperture sonar may be considered to be a one-dimensional CVL, mounted at a shallow grazing angle rather than directly towards the sea-floor. An interferometric SAS, with two arrays, can sample the spatial coherence in two dimensions. This leads to the possibility of estimating the ping-to-ping motion of the sensor in both the along-track and heave directions using the spatial coherence of the scattered field. However, this has not been demonstrated in the literature and could be investigated in the future.

Along-track motion estimation for SAS has been described in [133, 134, 33, 120, 135]. The methods involve range-windowing the data received by the phase centres of adjacent pings, and computing cross-correlations between all (or if an *a priori* surge estimate exists, a subset of) pairs of phase centres between adjacent pings.

Consider the signals received by the phase centres of consecutive pings $p - 1$ and p. Let $s_{m,p-1}(t)$ represent the signals received by the phase centres indexed by $m \in [1, N]$ on ping $p - 1$, where N is the total number of elements in the phase centre arrays. The sampled signals are indexed by $t \in [0, N_s]\Delta t$ where $\Delta t = 1/f_s$ is the sample period and f_s is the sampling frequency. Additionally let $s_{m,p-1}(t)$ represent the signals received by the phase centres indexed by $n \in [1, N]$ on ping p. The windowed signals are given by

$$s_{m,p-1,q}(t) = s_{m,p-1}(t) \cdot w_q(t) \tag{4.13}$$

$$s_{n,p,q}(t) = s_{n,p}(t) \cdot w_q(t) \tag{4.14}$$

where $w_q(t)$ is the window function corresponding to the qth range window. Performing a cross-correlation between all pairs of phase centres m and n, and suppressing subscripts $p - 1$, p and q for concise notation, gives

$$\gamma_{m,n}(l) = s_m(t) \star s_n(t), \tag{4.15}$$

where $\star$ denotes the normalised cross-correlation operator. An illustration of this three-dimensional grid of data is given in Figure 4.4a.

Taking the maximum magnitude of $\gamma_{m,n}(l)$ in the time delay dimension l for all m and n results in the matrix of cross-correlation maxima

$$\boldsymbol{C} = \begin{bmatrix} c_{1,1} & \cdots & c_{1,N} \\ \vdots & c_{m,n} & \vdots \\ c_{N,1} & \cdots & c_{N,N} \end{bmatrix} \tag{4.16}$$

68
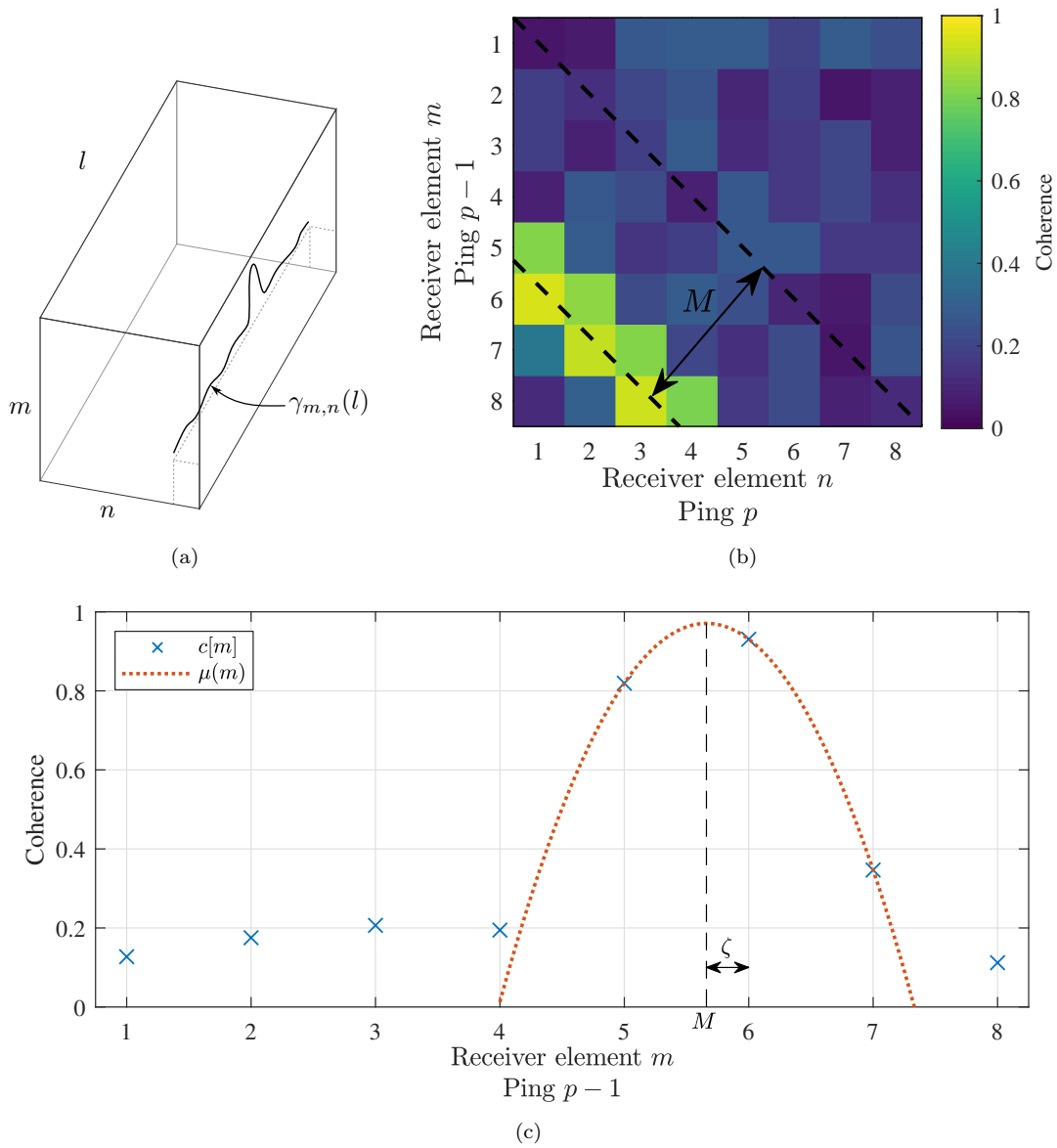
Figure 4.4: Illustration of the surge estimation process (a) Visualisation of the array of cross-correlations $\gamma_{m,n}(l)$ (b) An example of $\boldsymbol{C}$, the matrix of maximum coherence between all pairs of receive elements between adjacent pings, obtained from the maximum value of $\gamma_{m,n}(l)$ in the l direction. (c) The mean along each diagonal of the lower triangle of $\boldsymbol{C}$ is taken, giving $c[m]$. An interpolation kernel $\mu(m)$ is used to give an estimate of the sub-sample peak location M.

where each element is given by

$$c_{m,n} = \max\left\{|\gamma_{m,n}(l)|\right\}. \tag{4.17}$$

Assuming favourable SNR, $\mathbf{C}$ contains high coherence values on a diagonal, as illustrated for an 8-element array in Figure 4.4b.

The matrix $\mathbf{C}$ is reduced to the vector $c[m]$ by taking the mean value along each diagonal of its lower triangle, such that

$$c[m] = \sum_{i=0}^{N-m} \frac{c_{m+i,i+1}}{N-i-1}, \tag{4.18}$$

an example of which is shown as blue crosses in Figure 4.4c. Sub-sample precision can be achieved by interpolating around the largest value of $c[m]$. Cook [33] and Groen [133] do not recommend a specific interpolation kernel, but Oeschger [134] suggests the use of a quadratic, as is shown in Figure 4.4c. However, Brown [120] shows that a quadratic interpolation kernel introduces bias errors, which are significantly reduced with a triangular kernel and almost eliminated with a Gaussian kernel. A recent in-depth study comparing Gaussian and quadratic kernels has been performed by Brown [135], with qualitative and quantitative assessment of the difference in resulting image quality, showing that the best results are obtained when a Gaussian interpolation kernel is used. Therefore, the methods developed in this work use a Gaussian interpolation kernel for surge estimation.

A Gaussian interpolation kernel takes the form

$$\mu(m) = \mu_0 \exp\left\{-\frac{1}{2}\frac{(m-\zeta)^2}{\sigma^2}\right\} \tag{4.19}$$

where μ_0 is the peak correlation coefficient, σ defines the peak width, and ζ defines the offset of the peak. The offset of the peak is then given by

$$\zeta = \frac{1}{2}\frac{\ln(c[\hat{m}-1]) - \ln(c[\hat{m}+1])}{\ln(c[\hat{m}-1]) - 2\ln(c[\hat{m}]) + \ln(c[\hat{m}+1])}. \tag{4.20}$$

This takes the same form as the solution for a quadratic interpolation kernel, given by

$$\mu(m) = a_1 + a_2 m + a_3 m^2 \tag{4.21}$$

where a_k are constants. Using the Lagrange three-point interpolation formula [136] as proposed in [105, 135], the offset of the peak of $\mu(m)$ from the sample-precision maximum location is given by

$$\zeta = \frac{1}{2}\frac{c[\hat{m}-1] - c[\hat{m}-1]}{c[\hat{m}+1] - 2c[\hat{m}] + c[\hat{m}+1]}, \tag{4.22}$$

where

$$\hat{m} = \arg\max_{m}(c[m]) \tag{4.23}$$

is the estimate of the integer number of phase centres advanced.

70

The sub-sample number of phase centres advanced using either interpolation kernel is reached by

$$M = \hat{m} + \zeta. \tag{4.24}$$

Having estimated the sub-sample number of phase centres advanced M, the surge between phase centre arrays is given by

$$\nu = \frac{d_{\mathrm{rx}}}{2} M \tag{4.25}$$

where $d_{\mathrm{rx}}/2$ is the distance between phase centres.

Because of the side-looking geometry of a SAS, the process of surge estimation can be performed at multiple short-time windows corresponding to different ranges. This is in comparison to a CVL, which transmits vertically towards the sea-floor, allowing only one velocity measurement to be made per ping. Under the assumption that the measured surge is independent of range (and therefore fast time), the weighted mean of the surge estimates at all range windows may be used as the overall estimate of inter-array surge. The index $q \in [1, Q]$ is reintroduced to index over short-time windows, where Q is the number of short-time windows. The surge measured at each window is denoted ν_q, and the overall inter-array surge estimate is given by

$$\overline{\nu} = \frac{\sum_{q=0}^{Q-1} \nu_q \Omega_q}{\sum_{q=0}^{Q-1} \Omega_q}, \tag{4.26}$$

using the SNR estimate defined by (4.7) as the weighting.

4.3 Time delay estimation

As discussed in Section 4.1, the relative dilation of RPC signals manifests as a time delay and a local dilation when they are windowed in time. When the local dilation is not severe, i.e. when the separation between RPCs is small or the range is large, estimation of the time delay between the signals can be achieved by finding the sub-sample peak of their cross-correlation function [137, 138, 33, 16]. A two-step process is generally employed for complex signals, where a coarse estimate is made by finding the peak of the cross-correlation function magnitude and then refined using the phase at the location of the coarse estimate [33].

Recall the array of cross correlations calculated in (4.15), $\gamma_{m,n}(l)$. Having estimated the integer number of phase centres advanced $\hat{m}$, a matrix of cross-correlations of maximally redundant signals can be formed by a re-indexing as shown in Figure 4.5. This re-indexing results in an array of cross-correlations given by

$$\gamma'(l, m') = \gamma_{\hat{m}+m'-1, m'}(l) \tag{4.27}$$

where $m' \in [1, N_{\mathrm{rpc}}]$ indexes the redundant elements, where $N_{\mathrm{rpc}} = N - \hat{m} + 1$ where N is the number of elements in the phase centre array. This matrix of cross-correlations may then be
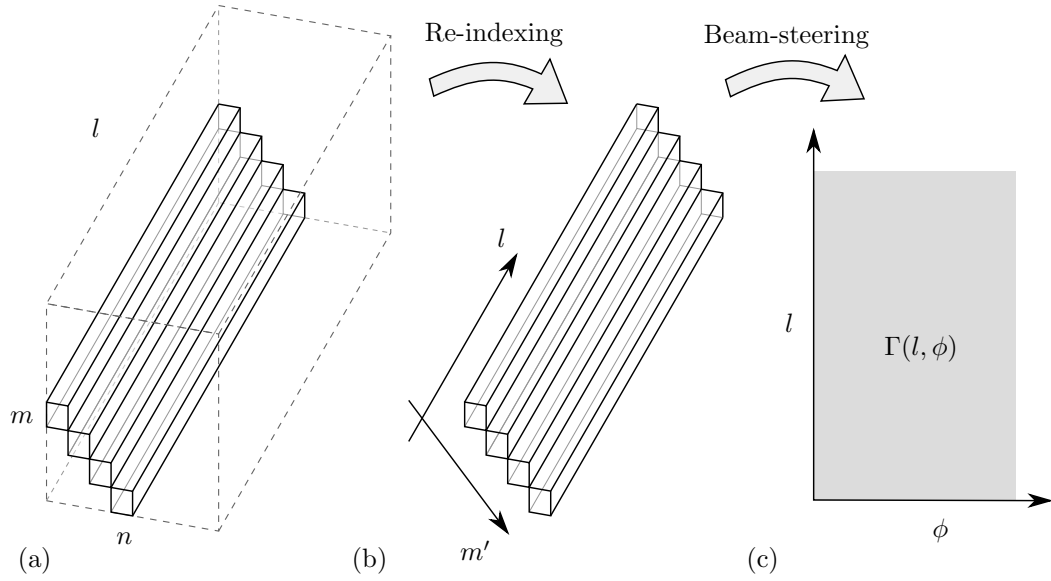
Figure 4.5: An illustration showing the formation of the beamformed cross-correlation matrix, from which the time delay is estimated. (a-b) The grid of cross-correlations between pairs of phase centres of adjacent pings $\gamma_{m,n}(l)$ is re-indexed, extracting the diagonal with highest coherence to give $\gamma'(l,m')$. (b-c) This data is beamformed to give the beam-formed cross-correlation matrix $\Gamma(l,\phi)$.

beam-steered over a range of angles ϕ, giving

$$\Gamma(l,\phi) = \sum_{m'=1}^{N_{\text{rpc}}} \gamma'(l,m') \exp\left(jk_c u \sin\left(\phi\right)\right) \tag{4.28}$$

where

$$u = \frac{d_{\text{rx}}}{2}\left(m' - \frac{N_{\text{rpc}}+1}{2}\right) \tag{4.29}$$

is the RPC array axis and $k_c = 2\pi f_c/c$ is the wave-number at the centre frequency f_c. The location of the maximum magnitude of the beam-steered cross-correlation function

$$(\tau'', \psi) = \arg\max_{l,\phi}\left\{|\Gamma(l,\phi)|\right\} \tag{4.30}$$

gives the 'very coarse' time delay estimate τ'' and an inter-array yaw estimate ψ in the slant-plane. If the time delay at a specific angle is desired, this can be achieved by setting ϕ to the desired value in (4.30).

The very coarse time delay estimate can be refined using a parabolic kernel. This gives the

'coarse' time delay

$$\tau' = \tau'' + \frac{1}{2} \frac{\left(|\Gamma(\tau'' - \Delta t, \psi)| - |\Gamma(\tau'' + \Delta t, \psi)|\right) \Delta t}{|\Gamma(\tau'' - \Delta t, \psi)| - 2|\Gamma(\tau'', \psi)| + |\Gamma(\tau'' + \Delta t, \psi)|} \tag{4.31}$$

The 'fine' time delay estimate is given by

$$\tau = \left(-\frac{\alpha}{2\pi} + M\right) \frac{1}{f_c} \tag{4.32}$$

where

$$\alpha = \angle\Gamma(\tau'), \tag{4.33}$$

is the phase of the complex cross-correlation function linearly interpolated at τ'', by interpolating the real and imaginary parts independently. $M \in \mathbb{Z}$ is the number of phase wraps, given by

$$M = \left\lfloor f_c \tau' + \frac{\alpha}{2\pi} \right\rceil, \tag{4.34}$$

where $\lfloor \ldots \rceil$ denotes rounding to the nearest integer and f_c is the centre frequency of the signals.

Figure 4.6 depicts the time delay estimation process. Figure 4.6a shows a typical cross-correlation function, where the location of the maximum cross-correlation magnitude gives the very coarse time delay estimate τ''. The peak and its adjacent values are plotted in Figure 4.6b, through which a parabola is fitted. The location of the peak of this parabola gives the coarse time delay estimate τ', at which the phase of the cross-correlation function is interpolated, to give α. The underlying phase of the modulated cross-correlation function,

$$\beta(t) = \angle\exp\left(j\left(2\pi f_c\left(t - \tau\right) + \alpha\right)\right) \tag{4.35}$$

is assumed to be linear, as shown in Figure 4.6c. The correlation function at the carrier frequency is known to have zero phase at the true peak [16], and therefore candidate fine time delay estimates occur when the modulated phase of the cross correlation function crosses zero, i.e. when $\beta = 0$. The grey region centred on τ' has a width equal to the period at the centre frequency, such that the only candidate in this region is the fine time delay estimate τ. However, noise can cause a shift in the location of the cross-correlation peak τ', especially when the frequency-to-bandwidth ratio is high. This can result in an incorrect candidate fine time delay being chosen and thus errors in the phase cycle number estimate M. These phase cycle errors result in time delay errors of an integer number of time periods at the centre frequency. These errors must be detected and corrected before the time delay measurements can be used for navigation estimation.

The time delay measurements are made at each range window and for every ping. This results in a two-dimensional array of time delay estimates, which can often be assumed to vary continuously and smoothly. This smoothness can be exploited to detect and correct phase cycle number errors. A novel method of doing so by fitting a model to subsets of the time delay estimates is presented in Section 5.
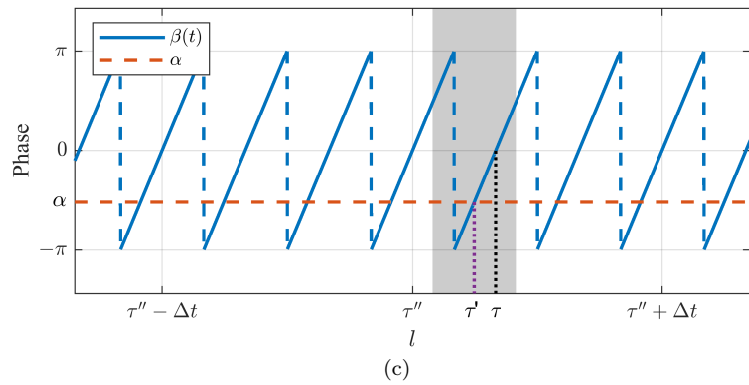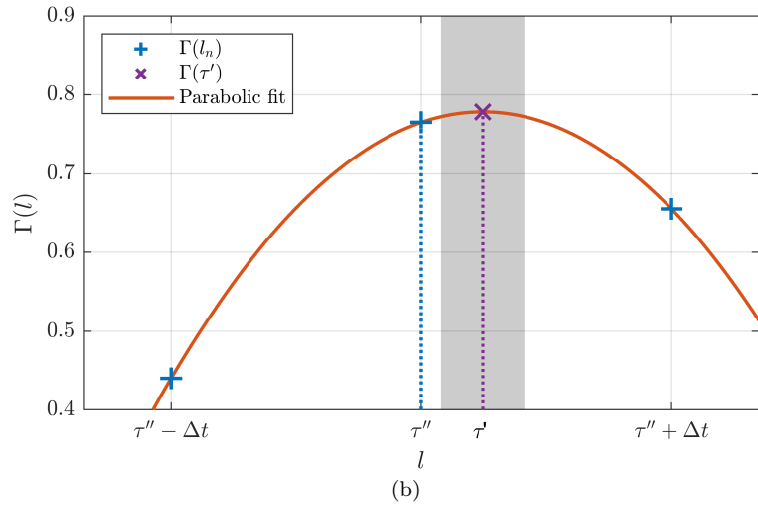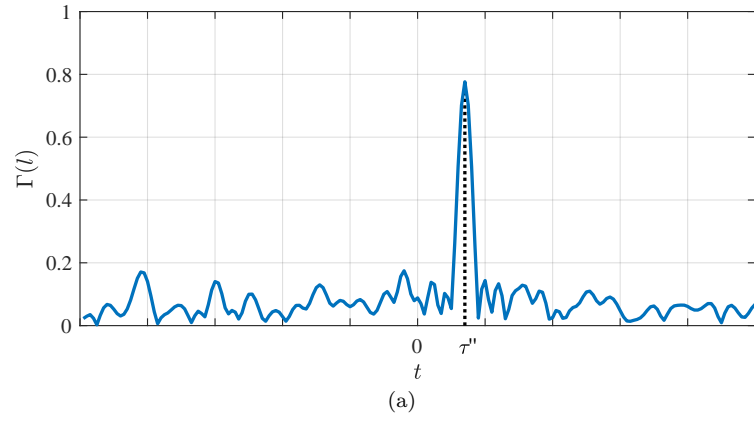
Figure 4.6: Multi-stage time delay estimation. (a) A typical cross-correlation function, whose maximum at τ'' gives the very coarse time delay. (b) A parabola is fitted to peak of $\Gamma(t_n)$ and its adjacent samples. The peak of the parabola is the coarse time delay estimate τ'. (c) Candidate fine time delay estimates are shown at intersections of the modulated phase β with the measured phase α. The candidate closest to the parabola peak is chosen as the fine time delay estimate τ. The grey region has a width of one period at the centre frequency and is centred on τ', so the location of the only zero-crossing of the modulated phase function within this region gives the fine time delay estimate.

74

4.3.1 A note on yaw estimation

A method for integration of slant-plane inter-ping sway and yaw into a slant-plane path is given in [31, Sec. V]. It is noted in this example that while slant-plane sway errors accumulate like a random walk, slant-plane yaw errors accumulate more severely, like an integrated random walk. Thus, SAS image quality is more significantly impacted by ping-to-ping slant-plane yaw errors than ping-to-ping slant-plane sway errors. Most platforms equipped with SAS are equipped with a high-precision navigation unit comprised of an INS and an aiding sensor such as a DVL or CVL. While the attitude measurements from the INS are inevitably corrupted by small amounts of measurement noise, the measurements are relative to a world co-ordinate frame and as such should not drift. It is therefore very common to use the INS heading estimates rather than those measured through-the-sensor, which has been termed 'gyro-stabilised DPCA' micro-navigation [54].

4.4 Summary

The methods described for estimating surge, time delay and slant-plane yaw using the redundant data collected between adjacent pings are standard in the SAS literature. The key to the success of these micro-navigation algorithms is the extraordinary precision with which the time delay estimates can be made, as evidenced by the CRLB [31]. It is how these surge, time delay and yaw values are exploited that differentiates most of the micro-navigation methods based on echo data redundancy.

The link between navigation and bathymetry is well-documented, with many micro-navigation implementations utilising a coarse bathymetry estimate from an interferometric SAS to allow estimation of both heave and surge using the time delay measurements at multiple ranges. However, this is often performed as a sequential process, where the bathymetry estimation is performed using the full length of the array (termed sidescan bathymetry [16, 32]), but the navigation estimation utilises only the redundant portion of the array.

Methods of fusing the navigation estimates from dual sided systems using a Kalman filter have been demonstrated for single array [89] and interferometric [35] systems. This has been shown to improve image quality, indicating an improvement in navigation accuracy.

There is also interest in integrating real-time SAS micro-navigation estimates into the vehicle navigation solution, as predicted by Gough and Miller [88] in order to improve long-term navigation accuracy. Preliminary work towards this goal has showed good potential, with SAS micro-navigation measurements exhibiting significantly lower measurement noise to a DVL of a similar frequency [34].

Two main areas for potential improvement over current micro-navigation methods have been identified:

1. The phase centre assumption and stop-and-hop assumption have both been shown to introduce two-way range errors in Sections 2.3.1 and 2.3.2 respectively. Removing these simplifying assumptions may improve the accuracy of micro-navigation algorithms.

2. There is an opportunity to exploit more of the redundant data collected by adjacent pings of multi-array SAS platforms. This is possible by realising that time delays measured between all pairs of inter-ping redundant arrays are affected by, and thus contain information about, the 'triad of confounding factors'; navigation, bathymetry, and sound speed.

The novel simultaneous navigation and bathymetry estimation algorithm described in Section 6 aims to address these areas for improvement. This is achieved though explicit modelling of the time-dependent bi-static geometry, and by implementation of a non-linear least squares minimisation of modelled and measured time delays between all pairs of redundant signals.

5 Detection and correction of phase wrap errors in time delay estimates

The time delay estimation method described in Section 4.3 showed that the high precision time delay estimate can be considered to be made up of a number of full phase wraps, plus a fraction of a phase wrap. In the presence of noise the estimate of the number of full phase wraps can be ambiguous [103, 32, 115], which is exacerbated for low fractional bandwidth signals. This ambiguity can corrupt the time delay estimate, reducing the accuracy of resulting data products such as through-the-sensor navigation [34, 87] or bathymetry estimates [16]. Therefore, detection and correction of phase wrap errors is desirable. This can be achieved by making an assumption of smoothness of an ensemble of time delay estimates.

There are existing methods of detecting phase wrap errors in RPC micro-navigation, which exploit the assumption of smoothly varying time delay estimates as a function of range and ping number. By extension, this assumes a smoothly varying sea-floor depth, and a smooth and continuous vehicle path. One method of removing outliers is to perform conventional phase unwrapping on the time delays from a single ping as a function of range only. This method achieves smoothly varying time delays, but is dependent on the seed used in the phase unwrapping and is not robust to the presence of gaps in the time delay estimate function [16, Ch. 5.1.3]. Two dimensional unwrapping methods such as the popular Goldstein's branch-cuts algorithm [82] have also been used [16]. Such phase unwrapping algorithms are only suitable if a correct unwrapping path exists where the maximum true change of phase per sample is less than π radians, which cannot be guaranteed for all applications. A further approach uses model fitting to the time delay estimates in order to detect outliers. The random sample and consensus (RANSAC) algorithm [139] has been proposed to achieve this [115], which is a popular method for model fitting in the presence of outliers. This method is more robust, but in this case only assumes smoothness of the time delay estimates in the range direction. A further method which exploits the smoothness of the time delay function in two dimensions has also been proposed [32]. The method relies on finding regions of constant phase wrap number, by detecting the location of phase wraps and discarding adjacent time delay estimates. The most commonly occurring phase wrap number estimate in each region is used to recalculate the time delays. This algorithm appears to give good performance. However it results in large amounts of data being discarded in applications where the phase gradient is large.

In this section a generalised model-based method is proposed that detects and corrects phase wrap errors in time delay estimation problems. A model of arbitrary dimension can be chosen and fitted to regions of the time delay estimates using the RANSAC algorithm, which finds model parameters by iteratively fitting the model based on a minimal data subset. The optimal model parameters result in the greatest number of samples within a chosen threshold. The outliers detected by this algorithm can be corrected, using the model to re-estimate the phase wrap number.

Field data collected by the CMRE MUSCLE AUV using its 270-330 kHz SAS during the MANEX14 sea trial are used to demonstrate the method. In order to compare the phase
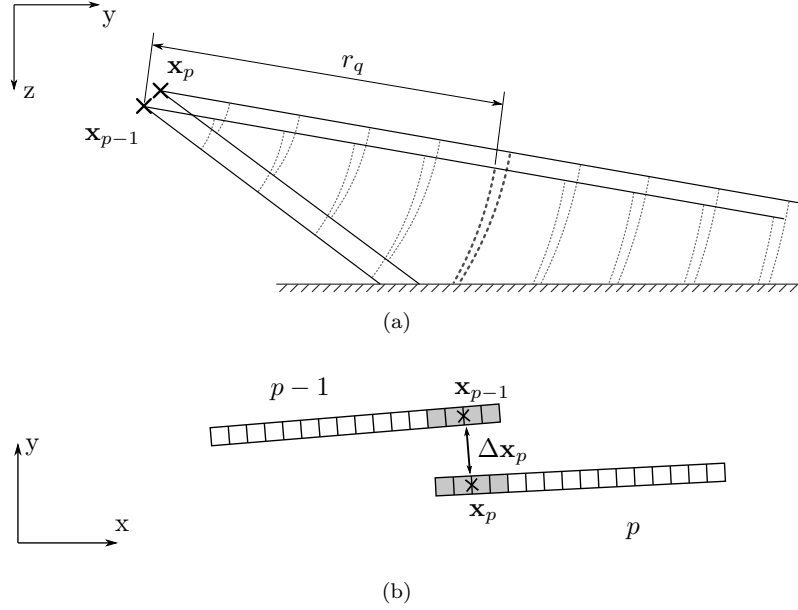
Figure 5.1: (a) The side-looking geometry of RPC micro-navigation. $\mathbf{x}_{p-1}$ and $\mathbf{x}_p$ represent the RPC array positions for pings $p-1$ and p respectively. The straight lines represent the edges of the sonar beam, while dotted arcs represent lines of constant range from the sonar. Inspection of the intersection of these arcs with the flat sea-floor reveals a range-dependent difference in two-way travel time difference due to inter-ping sway and heave (b) The side view of two arrays between pings, showing the overlapping phase centre array elements and the unknown displacement $\Delta\mathbf{x}_p$ to be measured by RPC micro-navigation.

wrap error detection and correction method using 1D and 2D models, systems with a higher frequency-to-bandwidth ratio are emulated by artificially reducing the bandwidth of the sonar data before time delay estimation. This reduction in fractional bandwidth causes an increased number of phase wrap errors. The performance of the RANSAC methods with 1D and 2D models is assessed by comparing the resulting time delay estimates to those obtained from the full bandwidth data. The Goldstein branch-cuts method has been applied with the same region size as the 2D RANSAC method for comparison.

5.1 Time delay model

Figure 5.1a is a side view of the imaging geometry, where the vehicle is shown to travel close to the sea-floor, with the sensor looking side-ward and toward the sea-floor. Arcs of constant range from the sensor are shown, and inspecting the intersection of these arcs with the flat sea-floor demonstrates a range-dependent difference in two-way range and hence travel time difference to a point on the sea-floor, caused by the sway and heave of the sensor. Figure 5.1b is a top view, showing the overlapping array elements between sonar pings. $\Delta\mathbf{x}_p$ represents the inter-ping displacement measured by RPC micro-navigation.

5.1.1 Exploitation of sea-floor continuity

It is often reasonable to assume the sea-floor is continuous and has a shape that changes smoothly. As a consequence, the time delays measured between signals received by overlapping array elements can be expected to change smoothly with range.

An example one-dimensional flat sea-floor model has been used to demonstrate this, as illustrated in Figure 5.2. Let $\mathbf{x}_{p-1} = (y_{p-1}, z_{p-1})^T$ and $\mathbf{x}_p = (y_p, z_p)^T$ denote the positions of the RPC arrays for pings $p-1$ and p in the plane defined by the across-track y and vertical z directions. A point on the sea-floor is denoted $\mathbf{x}_b = (y_b, z_b)^T$ and the inter-ping sway and heave are given by

$$\Delta y_p = y_p - y_{p-1} \tag{5.1}$$

and

$$\Delta z_p = z_p - z_{p-1} \tag{5.2}$$

respectively.

The one dimensional model for the time delay between the signals received by the overlapping arrays formed between ping $p-1$ and p is given by

$$\tau_{\text{flat}}(r) = \frac{2}{c}(r_p - r_{p-1}) \tag{5.3}$$

where c is the speed of sound in the medium,

$$r_{p-1} = \sqrt{(y_{\text{b},q} - y_{p-1})^2 + (z_{\text{b},q} - z_{p-1})^2} \tag{5.4}$$

is the distance between $\mathbf{x}_{p-1}$ and $\mathbf{x}_{\text{b},q}$ and

$$r_p = \sqrt{(y_{\text{b},q} - y_{p-1} - \Delta y_p)^2 + (z_{\text{b},q} - z_{p-1} + \Delta z_p)^2} \tag{5.5}$$

is the distance between $\mathbf{x}_p$ and $\mathbf{x}_{\text{b},q}$.

The resulting time delays as a function of range window for an example set of values for inter-ping sway and heave are shown in Figure 5.3, for a sensor altitude of $z_p = 12\,\text{m}$. The resulting time delays vary smoothly with range window. This model is representative of realistic time delay estimates between signals collected by the overlapping elements for a pair of pings during an experiment in the Ligurian sea, which are shown in Figure 5.4a. The majority of the experimental time delay estimates vary smoothly in the across-track direction, but there appear to be some outliers caused by phase wrap errors.

5.2 Phase wrap error correction algorithm

In this section the algorithms used to perform phase wrap number error detection and correction are described. Firstly, a brief overview of the RANSAC [139] algorithm is given in Section 5.2.1. In Section 5.2.2, an overview of the method proposed in [115] is presented, which uses the RANSAC algorithm to fit a one-dimensional model to the time delay estimates as a function
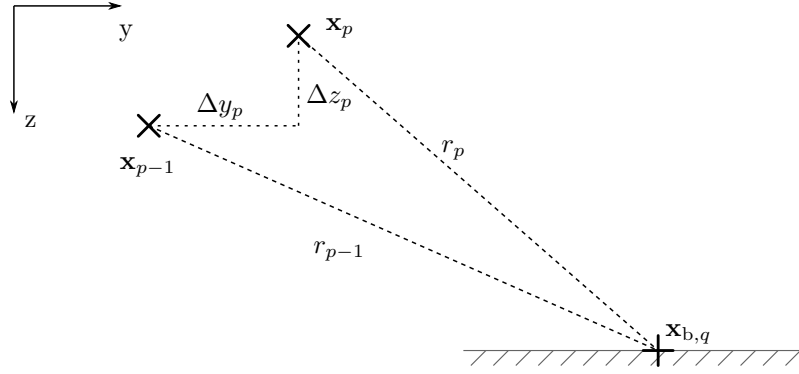
Figure 5.2: The geometry for time delay estimation between signals collected by overlapping array elements in RPC micro-navigation, for a flat sea-floor.

(a)

(b)
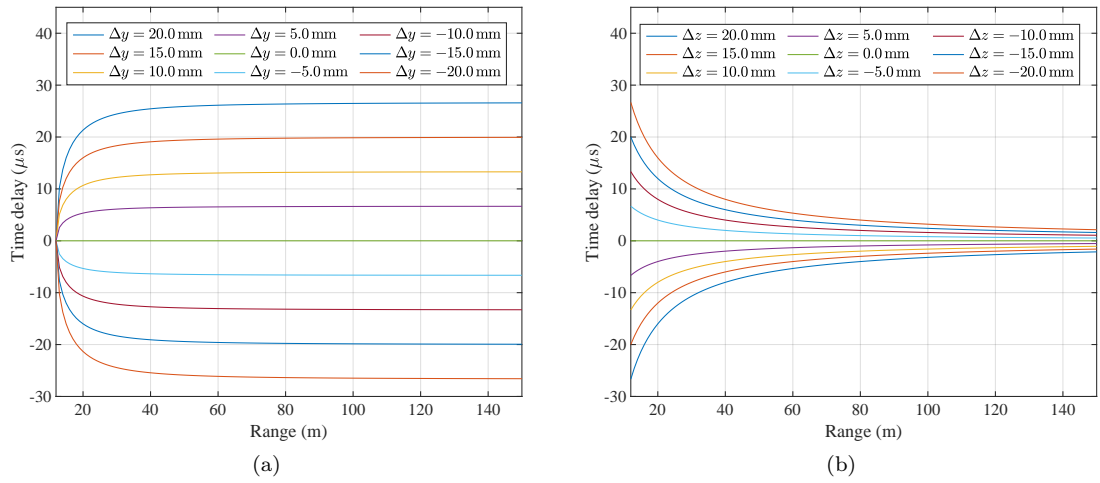
Figure 5.3: Time delays caused by inter-ping (a) sway only, (b) heave only, for a sensor altitude of $z_p = 12\,\text{m}$.

of range window. This model is used to detect and correct phase wrap errors.

The method is then developed and generalised in two salient ways described in Section 5.2.3. The first is the use of a two dimensional model in order to exploit the smoothness of the time delay estimates in a second dimension. Also, the size of the domain over which the model is fitted can be chosen in both dimensions. This allows the complexity of the model to be reduced while improving the resilience of the method to rapidly varying time delay estimates.

5.2.1 Random sample and consensus algorithm

The RANSAC algorithm is a popular and robust method for detecting outliers, which is capable of finding a consensus set even when the ratio of outliers to samples is significant [139]. The algorithm repeatedly computes a model using a minimal data subset (i.e. the minimum number

of samples required to fit the model), and finds the number of inliers for each candidate model. After a certain number of trials, the model with the largest number of inliers over all trials is deemed the optimal model.

The number of trials required to achieve a probability p_{suc} of randomly drawing an all-inlier minimal subset can be adaptively computed on each iteration. It is given by

$$K = \left\lceil \frac{\log_{10}(1 - p_{\text{suc}})}{\log_{10}(1 - \hat{w}^s)} \right\rceil, \tag{5.6}$$

where

$$\hat{w} = \frac{\hat{\eta}}{\Lambda} \tag{5.7}$$

is the largest estimate of the inlier ratio over all previous trials, where $\hat{\eta}$ is the largest number of inliers for all previous trials, Λ is the total number of data points and s is the number of samples in the minimal subset (i.e. the number of parameters in the model). The required number of trials K is impacted heavily by the number of parameters in the chosen model when the inlier ratio is not close to 1. This is because the denominator of (5.6) approaches zero as $\hat{w}^s$ approaches zero. This motivates the use of a model with as few parameters as possible.

5.2.2 Phase wrap error correction using a 1D model

The use of a 1D model in the RANSAC error detection procedure exploits the expected smoothness of the time delay estimates as a function of range. The expected smoothness of the time delay estimates in the range direction was shown in Section 5.1.1. In this work a quadratic model has been chosen to model the time delay estimates as a function of range. This choice is made without loss of generality due to the simplicity with which it can be computed and because it produces an acceptable fit to field data. An overview of the method applied to the time delays estimated between each pair of pings is given in Algorithm 1, and explained in more detail below with illustrations in Figure 5.4.

Consider fine time delay estimates $\tau_k[q]$, where $q \in [0, Q-1]$ is the range index and Q is the number of range windows. Additionally, let $k \in [0, K-1]$ denote the iteration number where K is the adaptively computed number of trials (5.6). Also let $\alpha_k[q]$ represent the phase measured at the cross-correlation function peaks.

On each iteration of the RANSAC algorithm a quadratic model is fitted to a minimal data subset (3 samples in this case). The general form of the quadratic model for iteration k is given by

$$\widetilde{\tau}_k(r) = a_k r^2 + b_k r + c_k \tag{5.8}$$

where the coefficients a_k, b_k and c_k of the model that passes through the minimal data subset are computed by

$$\boldsymbol{a}_k = \boldsymbol{R}_k^{-1} \boldsymbol{\tau}_k \tag{5.9}$$

81

Algorithm 1 1D RANSAC

// *Setup:*
$k \leftarrow 0$ // *Initialise trial number*

$K \leftarrow \infty$ // *Initialise max. number of trials*

$\hat{\eta} \leftarrow 0$ // *Initialise number of inliers*

// *Iterate:*

while $k < K$ **do**

    // *Draw minimal data subset:*

    $q_{1,k} \sim \{x \in \mathcal{U}(0, Q-1)\}$

    $q_{2,k} \sim \{x \in \mathcal{U}(0, Q-1) \,|\, x \notin q_{1,k}\}$

    $q_{3,k} \sim \{x \in \mathcal{U}(0, Q-1) \,|\, x \notin \{q_{1,k}, q_{2,k}\}\}$

    // *Calculate model coefficients:*

    $\boldsymbol{a}_k \leftarrow \boldsymbol{R}_k^{-1} \boldsymbol{\tau}_k$

    // *Calculate model time delays:*

    $\widetilde{\tau}_k(r) \leftarrow a_k r^2 + b_k r + c_k$

    // *Count number of inliers:*

    $\eta_k \leftarrow \sum_{q=0}^{Q-1} \left[|\tau[q] - \widetilde{\tau}_k(r[q])| < t_{\text{thresh}} \right]$

    // *Test if model is better than previous best:*

    if $\eta_k > \hat{\eta}$ **then**   // *Update*

        $\hat{\eta} \leftarrow \eta_k$

        $\hat{w} \leftarrow \eta_k / Q$

        $K \leftarrow \lceil \log_{10}(1 - p_{\text{suc}}) / \log_e(1 - \hat{w}^s) \rceil$

        $\kappa \leftarrow k$ // *Store trial number of best model*

    end if

    $k \leftarrow k + 1$ // *Increment trial number*

end while

// *Re-calculate phase wrap numbers using model:*

$\hat{M}[q] = \lfloor f_c \widetilde{\tau}_\kappa(r[q]) + \alpha[q]/2\pi \rceil$

// *Re-calculate fine time delay estimates:*

$\hat{\tau}[q] = \left(-\alpha[q]/2\pi + \hat{M}[q] \right) / f_c$

---

where

$$\boldsymbol{a}_k = \begin{pmatrix} a_k \\ b_k \\ c_k \end{pmatrix}, \tag{5.10}$$

is the vector containing the model coefficients,

$$\boldsymbol{R}_k = \begin{pmatrix} r^2[q_{1,k}] & r[q_{1,k}] & 1 \\ r^2[q_{2,k}] & r[q_{2,k}] & 1 \\ r^2[q_{3,k}] & r[q_{3,k}] & 1 \end{pmatrix} \tag{5.11}$$
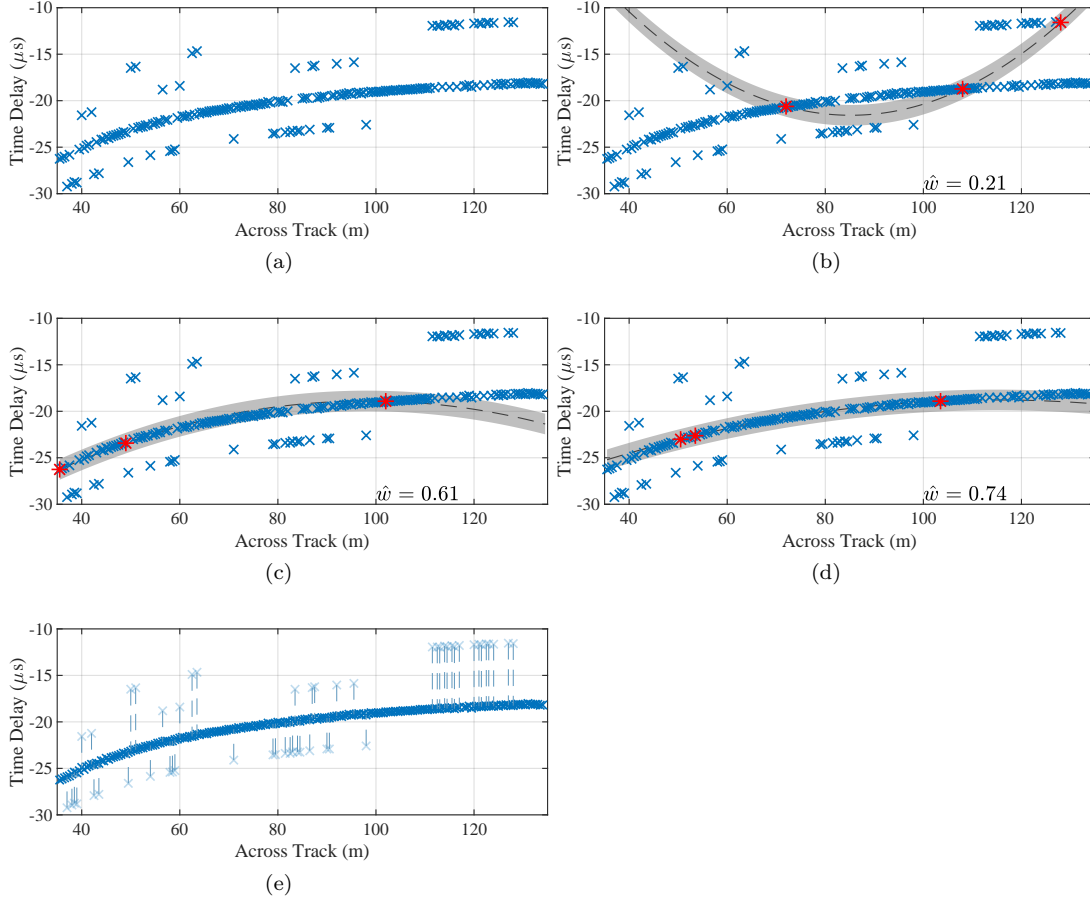
Figure 5.4: Illustration of the 1D RANSAC algorithm using data from MANEX'14. (a) Initial time delays shown by blue crosses. (b) A minimal subset shown by red crosses includes an outlier. The model shown by the black dashed line has few samples within the threshold shown by the grey region. (c) All of a minimal subset are inliers but they define a sub-optimal model. (d) Another all-inlier minimal subset defines the optimal model. (e) Outliers are corrected, shown by blue dashed lines.

is the matrix defining the polynomial model, and

$$\boldsymbol{\tau}_k = \begin{pmatrix} \tau[q_{1,k}] \\ \tau[q_{2,k}] \\ \tau[q_{3,k}] \end{pmatrix} \tag{5.12}$$

is the vector containing the minimal subset of time delay estimate samples, where $q_{1,k}$, $q_{2,k}$ and $q_{3,k}$ are randomly drawn without replacement from $q \in [0, Q-1]$. Having found the coefficients a_k, b_k and c_k, the model time delays at all ranges for trial k can be evaluated by substitution into (5.8), giving the model time delays $\widetilde{\tau}_k(r)$ for all ranges.

The number of samples considered to support the model, or 'inliers', is the total number of

time delay estimates that lie within a predetermined threshold of the model. This number of samples that support the model is given by

$$\eta_k = \sum_{i=0}^{Q-1} \left[|\tau[q] - \widetilde{\tau}_k(r[q])| < \tau_{\mathrm{thresh}} \right] \tag{5.13}$$

where t_{thresh} is the threshold and $[\ldots]$ denotes an Iverson bracket [140]. The value for τ_{thresh} must be chosen such that it is large enough to allow variation of the time delays caused by bathymetry, but small enough for any estimates with phase wrap errors to be rejected. In this work, a value of

$$\tau_{\mathrm{thresh}} = \frac{1}{3f_c} \tag{5.14}$$

has been chosen, which corresponds to one third of a time period for the centre frequency.

For every iteration, if η_k is greater than the previous largest number of inliers $\hat{\eta}$, the best estimate of the inlier fraction and the required number of trials are updated using (5.7) and (5.6) respectively.

An example of a minimal subset of three samples including two inliers and one outlier is shown in Figure 5.4b. The grey band represents the region in which samples are considered to be inliers, i.e. they are within the pre-determined threshold of the model. For this particular minimal subset of 3 data points, the quadratic model has very poor support. In Figure 5.4c an all-inlier minimal subset with poor coverage has been selected. In this case, the model has greater support, but the model selected in Figure 5.4d has even better support and is eventually chosen as the optimal model.

The process is iterated until the adaptively computed number of trials K has been performed, at which point a subset of time delay estimates have been identified as outliers. Figure 5.4e shows the correction of the outliers by adjusting the phase wrap number as follows.

The updated phase wrap number is given by

$$\hat{M}[q] = \left\lfloor f_c \widetilde{\tau}_\kappa(r[q]) + \frac{\alpha[q]}{2\pi} \right\rceil, \tag{5.15}$$

and the resulting refined time delay estimate calculated by

$$\hat{\tau}[q] = \left(-\frac{\alpha[q]}{2\pi} + \hat{M}[q] \right) \frac{1}{f_c} \tag{5.16}$$

is retained if

$$|\hat{\tau}[q] - \widetilde{\tau}_\kappa(r[q])| < \tau_{\mathrm{thresh}} \tag{5.17}$$

and discarded otherwise. In Figure 5.4e, all of the outliers were corrected, with none being discarded.

Algorithm 2 2D RANSAC

// *Setup:*
$k \leftarrow 0$ // *Initialise trial number*
$K \leftarrow \infty$ // *Initialise max. number of trials*
$\hat{\eta} \leftarrow 0$ // *Initialise number of inliers*
// *Iterate:*
while $k < K$ **do**
     // *Draw minimal data subset:*
     $p_{1,k} \sim \{x \in \mathcal{U}(0, P-1)\}$
     $q_{1,k} \sim \{x \in \mathcal{U}(0, Q-1)\}$
     $p_{2,k} \sim \{x \in \mathcal{U}(0, P-1) \,|\, x \notin p_{1,k}\}$
     $q_{2,k} \sim \{x \in \mathcal{U}(0, Q-1) \,|\, x \notin q_{1,k}\}$
     $q_{3,k} \sim \{x \in \mathcal{U}(0, P-1) \,|\, x \notin \{p_{1,k}, p_{2,k}\}\}$
     $q_{3,k} \sim \{x \in \mathcal{U}(0, Q-1) \,|\, x \notin \{q_{1,k}, q_{2,k}\}\}$
     $q_{4,k} \sim \{x \in \mathcal{U}(0, P-1) \,|\, x \notin \{p_{1,k}, p_{2,k}, p_{3,k}\}\}$
     $q_{4,k} \sim \{x \in \mathcal{U}(0, Q-1) \,|\, x \notin \{q_{1,k}, q_{2,k}, q_{3,k}\}\}$
     // *Calculate model coefficients:*
     $\boldsymbol{a}_k \leftarrow \boldsymbol{R}_k^{-1} \boldsymbol{\tau}_k$
     // *Calculate model time delays:*
     $\widetilde{\tau}_k(u, r) = a_k u + b_k u^2 + c_k r + d_k$
     // *Count number of inliers:*
     $\hat{\eta}_k = \sum_{p=0}^{P-1} \sum_{q=0}^{Q-1} \left[|\tau[p,q] - \widetilde{\tau}_k(u[p], r[q])| < \tau_{\text{thresh}} \right]$
     // *Test if model is better than previous best:*
     if $\eta_k > \hat{\eta}$ **then**   // *Update*
         $\hat{\eta} \leftarrow \eta_k$
         $\hat{w} \leftarrow \eta_k / PQ$
         $K \leftarrow \lceil \log_{10}(1 - p_{\text{suc}}) / \log_e(1 - \hat{w}^s) \rceil$
         $\kappa \leftarrow k$ // *Store trial number of best model*
     end if
     $k \leftarrow k + 1$ // *Increment trial number*
end while
// *Re-calculate phase wrap numbers using model:*
$\hat{M}[p,q] = \lfloor f_c \widetilde{\tau}_\kappa(r[p,q]) + \alpha[p,q]/2\pi \rceil$
// *Re-calculate fine time delay estimates:*
$\hat{\tau}[p,q] = \left(-\alpha[p,q]/2\pi + \hat{M}[p,q] \right) / f_c$

5.2.3 Phase wrap error correction using a 2D model

A 2D model can be used to exploit the expected smoothness of time delay estimates in two dimensions (e.g. ping number and range). A 2D sliding rectangular window is used to extract regions of the time delay estimates over which a model is fitted. The choice of model and window size are application dependent but must be chosen such that the windowed time delay estimates can be adequately represented by the chosen model.

The RANSAC algorithm is applied to each 2D window in turn. Outliers are detected by

iteratively fitting a 2D model to a minimal data subset of the windowed time delay estimates, and finding the model with the largest number of inliers. The refined time delay estimates are then calculated using the best model. Duplicate refined time delay estimates can be generated if overlapping 2D windows are used. The mode of any duplicates is taken once refined time delay estimates have been made for all 2D windows. The algorithm for each 2D window is summarised in Algorithm 2.

The RPC micro-navigation algorithm computes time delay estimates at multiple ranges and multiple ping pairs along the vehicle's path. This 2D function can be assumed to be smooth in both dimensions by virtue of the continuous sea-floor in combination with the vehicle's inertia. Consider the fine time delay estimates $\tau[p,q]$, which represent a rectangularly windowed region of time delays indexed by $q \in [0, Q-1]$ and $p \in [0, P-1]$, where Q is the number of range windows and P is the number of pings. Also let $\alpha[p,q]$ represent the measurements of the phase at the peak of the cross-correlation function over the same region.

The RANSAC algorithm randomly selects a minimal subset of time delay estimates to iteratively compute a model. For trial k, a model of the form

$$\widetilde{\tau}_k(r,u) = a_k u + b_k u^2 + c_k r + d_k \tag{5.18}$$

is used, which is linear in the range direction r and quadratic in the along-track direction u. This model has been chosen because the rate of change of time delay in the along-track direction has been observed to be much greater than in the range direction in field data, as can be observed in Figure 5.10a.

For trial $k \in [0, K-1]$, the coefficients a_k b_k, c_k and d_k are computed by

$$\boldsymbol{a}_k = \boldsymbol{R}_k^{-1} \boldsymbol{\tau}_k, \tag{5.19}$$

where

$$\boldsymbol{a}_k = \begin{pmatrix} a_k \\ b_k \\ c_k \\ d_k \end{pmatrix}, \tag{5.20}$$

is the vector containing the model coefficients,

$$\boldsymbol{R}_k = \begin{pmatrix} u[p_{1,k}] & u[p_{1,k}]^2 & r[q_{1,k}] & 1 \\ u[p_{2,k}] & u[p_{2,k}]^2 & r[q_{2,k}] & 1 \\ u[p_{3,k}] & u[p_{3,k}]^2 & r[q_{3,k}] & 1 \\ u[p_{4,k}] & u[p_{4,k}]^2 & r[q_{4,k}] & 1 \end{pmatrix} \tag{5.21}$$

is the matrix defining the model, and

$$
\boldsymbol{\tau}_k =
\begin{pmatrix}
\tau_k[p_{1,k}, q_{1,k}] \\
\tau_k[p_{2,k}, q_{2,k}] \\
\tau_k[p_{3,k}, q_{3,k}] \\
\tau_k[p_{4,k}, q_{4,k}]
\end{pmatrix}
\tag{5.22}
$$

is the vector containing the minimal subset of time delay estimate samples, where $p_{1,k}, ..., p_{4,k}$ and $q_{1,k}, ..., q_{4,k}$ are drawn without replacement from $p \in [0, P-1]$ and $q \in [0, Q-1]$ respectively.

Similarly to the 1D RANSAC algorithm, the model time delays can be evaluated at all ranges by substitution into (5.18), giving the model time delays $\widetilde{\tau}_k(u, r)$. The number of samples that support the model (or inliers) is given by

$$
\hat{\eta}_k = \sum_{p=0}^{P-1} \sum_{q=0}^{Q-1} \left[|\tau[p, q] - \widetilde{\tau}_k(u[p], r[q])| < \tau_{\text{thresh}} \right]
\tag{5.23}
$$

where τ_{thresh} is the threshold and $[\dots]$ denotes an Iverson bracket. If the model has more support than the previous best number of inliers, the number of trials is updated using (5.6), where the new best estimate of the inlier fraction is given by

$$
\hat{w} = \frac{\hat{\eta}}{PQ}.
\tag{5.24}
$$

Once K trials have been completed, a subset of time delay estimates are identified as outliers. The following phase wrap correction can be applied to all time delay estimates, since inliers are unchanged by the correction.

The updated phase wrap number is given by

$$
\hat{M}[p, q] = \left\lfloor f_c \widetilde{\tau}_\kappa[p, q] + \frac{\alpha[p, q]}{2\pi} \right\rceil,
\tag{5.25}
$$

and the resulting refined time delay estimate calculated by

$$
\hat{\tau}[p, q] = \left(-\frac{\alpha[p, q]}{2\pi} + \hat{M}[p, q] \right) \frac{1}{f_c}
\tag{5.26}
$$

is retained if

$$
|\hat{\tau}[p, q] - \widetilde{\tau}(u[p], r[q])| < \tau_{\text{thresh}}
\tag{5.27}
$$

and discarded otherwise. Again, the threshold chosen in this work is given by (5.14).

The algorithm is demonstrated for one particular windowed subset of time delays in Figure 5.5. The initial fine time delay estimates $\tau[p, q]$ are shown in Figure 5.5a, which shows the majority of the time delay estimates vary smoothly in both the ping axis and the across track axis, with some outliers present. Figure 5.5b shows a minimal subset that includes outliers. The grey surfaces represent the upper and lower limits of the region in which the time delay
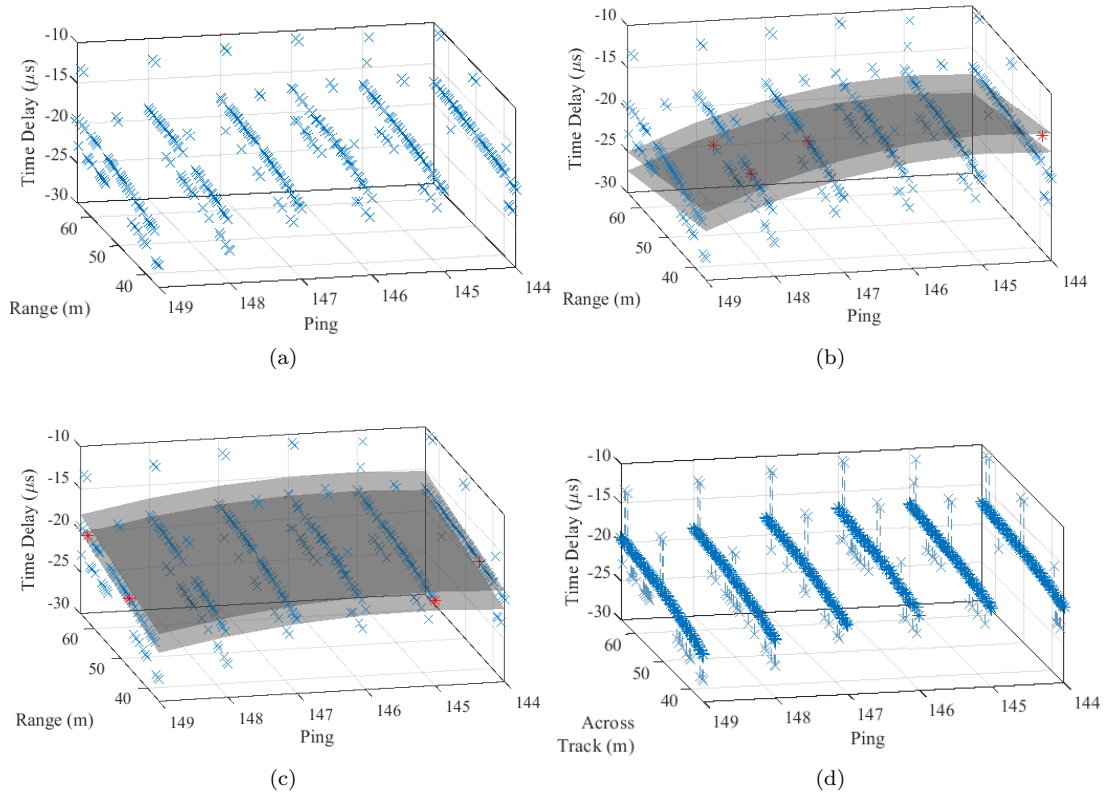
Figure 5.5: Illustration of the 2D RANSAC algorithm using data from MANEX'14. (a) Initial time delay estimates, shown by blue crosses. (b) A minimal subset shown by red crosses includes an outlier, so the model has poor support. The grey surfaces are the upper and lower thresholds. (c) The minimal subset is contains only inliers, and has good support. (d) The blue dashed lines show the outliers being corrected using the optimal model.

estimates are considered inliers. Figure 5.5c shows an iteration where all of the minimal data subset are inliers, which results in a model with the largest support. Once the required number of trials has been performed, the outliers are corrected by adjusting the phase wrap number, the result of which is shown in Figure 5.5d. In this case, no time delay estimates were discarded.

5.3 Experimental method

The 1D and 2D RANSAC methods have been applied to time delay measurements derived from real SAS data collected by the 270-330 kHz SAS of the MUSCLE AUV during the MANEX'14 sea trial. Figure 5.6 shows the location of the trial, which was off the Ligurian coast near the villages of Framura and Bonassola.

Figure 5.6: The MANEX'14 trial was held off the Ligurian coast, close to the villages of Framura and Bonassola. (a) Liguria is in Northern Italy, shown by a black box. (b) A zoomed section, showing the locations of Framura and Bonassola. Map data ©2019 Google.

5.3.1 The MANEX'14 sea trial

The MANEX'14 sea trial was conducted in the coastal waters of Liguria, near the villages of Bonnasola and Framura, using the MUSCLE AUV. The SAS of the MUSCLE AUV has an upper receiver array with 36 elements and a lower receiver array with 12 elements. In single array mode, the PRF is 4 Hz, giving a theoretical maximum range of 187.5 m. In interferometric mode, the PRF is increased to 10 Hz to compensate for the shorter interferometric array. This results in a theoretical maximum range of 75 m. A number of deployments of the MUSCLE AUV were made, both in interferometric mode and single-array mode.

SAS data from the MUSCLE AUV were collected over a frequency range of 270-330 kHz in single array mode. For the example portion of data used in this section, the vehicle was programmed to perform a straight track at a constant altitude of 12 m above the sea-floor. The position of the vehicle over the 600 pings of interest is plotted in Figure 5.7a, and the corresponding depth of the vehicle and sea-floor is shown in Figure 5.7b. The unprocessed SAS echo data collected on a particular track are shown in Figure 5.8a. The inter-ping coherence is shown in Figure 5.8b. The resulting SAS image is shown in Figure 5.8c, which reveals a predominantly sandy, rippled sea-floor, with some rocks and posidonia. It is not possible to generate a bathymetry map using SAS interferometry because the vehicle was running in interferometric mode. However, sidescan interferometry can be used to produce a low-resolution depth map, which is shown in Figure 5.8d. No motion compensation has been applied to the sidescan bathymetry estimates, which explains the spatial differences between Figures 5.8c and 5.8d. A small subset of the echo data, coherence and SAS images have been selected for closer inspection, which are marked by white rectangles in Figure 5.8.
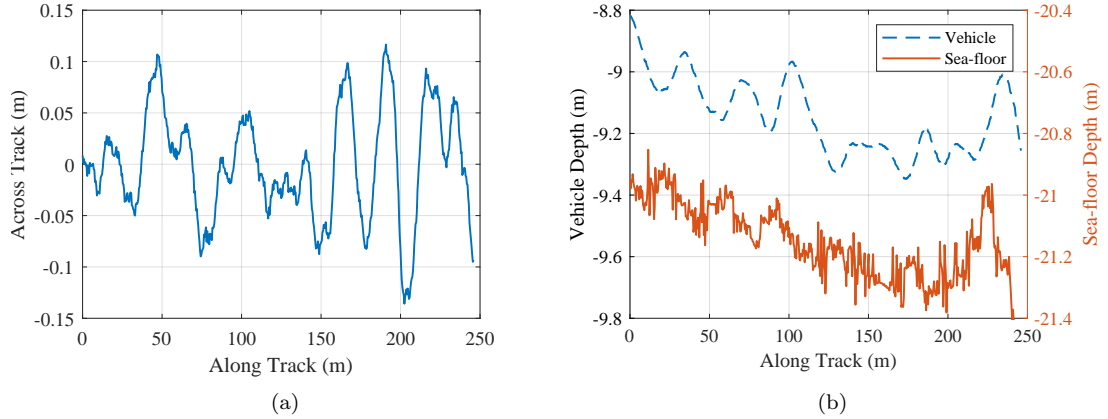
Figure 5.7: Navigation data for a particular survey track. (a) The position of the vehicle over 600 pings. (b) The corresponding depth of the vehicle and the sea-floor below it. Note the vehicle and sea-floor depth axes are offset by 11.6 m.

5.3.2 Emulation of systems with narrow bandwidth

The frequency bandwidth of the data has been windowed to between 60 kHz and 10 kHz using a Tukey window [118] with 10% transition width. This emulates systems with lower fractional bandwidth, demonstrating the effect of reducing the frequency bandwidth of the data. The subsets of the echo data, coherence and SAS image for frequency bandwidths of 10 kHz and 60 kHz are shown in Figure 5.9. A reduction in across-track resolution is evident in Figures 5.9a and 5.9e (10 kHz bandwidth) when compared with Figures 5.9b and 5.9f (60 kHz bandwidth), as expected since the across-track resolution is proportional to the inverse of the bandwidth [33]. The values of the coherence estimates are similar between Figures 5.9c and 5.9d (with mean values of 0.75 and 0.73 for 10 kHz and 60 kHz respectively). The variances of the coherence estimates are 3.5×10^{-3} and 3.8×10^{-3} at 10 kHz and 60 kHz respectively.

5.4 Results

The time delays estimated from the full-bandwidth (60 kHz) data are shown in Figure 5.10a. Subsets of the time delays estimated using the 10 kHz and 60 kHz bandwidth data are shown in Figures 5.11a and 5.11b respectively. Black regions represent samples where no time delay estimate was made due to low coherence magnitude. A coherence threshold of 0.3 is used, which corresponds to a value three standard deviations larger than the expected coherence value for random signals of the same length of the range windows. Randomly distributed phase wrap errors appear to be present, and are much more prevalent in the 10 kHz data (Figures 5.11a) than the 60 kHz data (Figure 5.11b) as expected.

The 1D and 2D RANSAC methods have been applied to the time delays measured using the frequency band-limited data. The branch-cuts method has also been applied over the same window sizes as the 2D RANSAC method for comparison. The resulting refined time delay
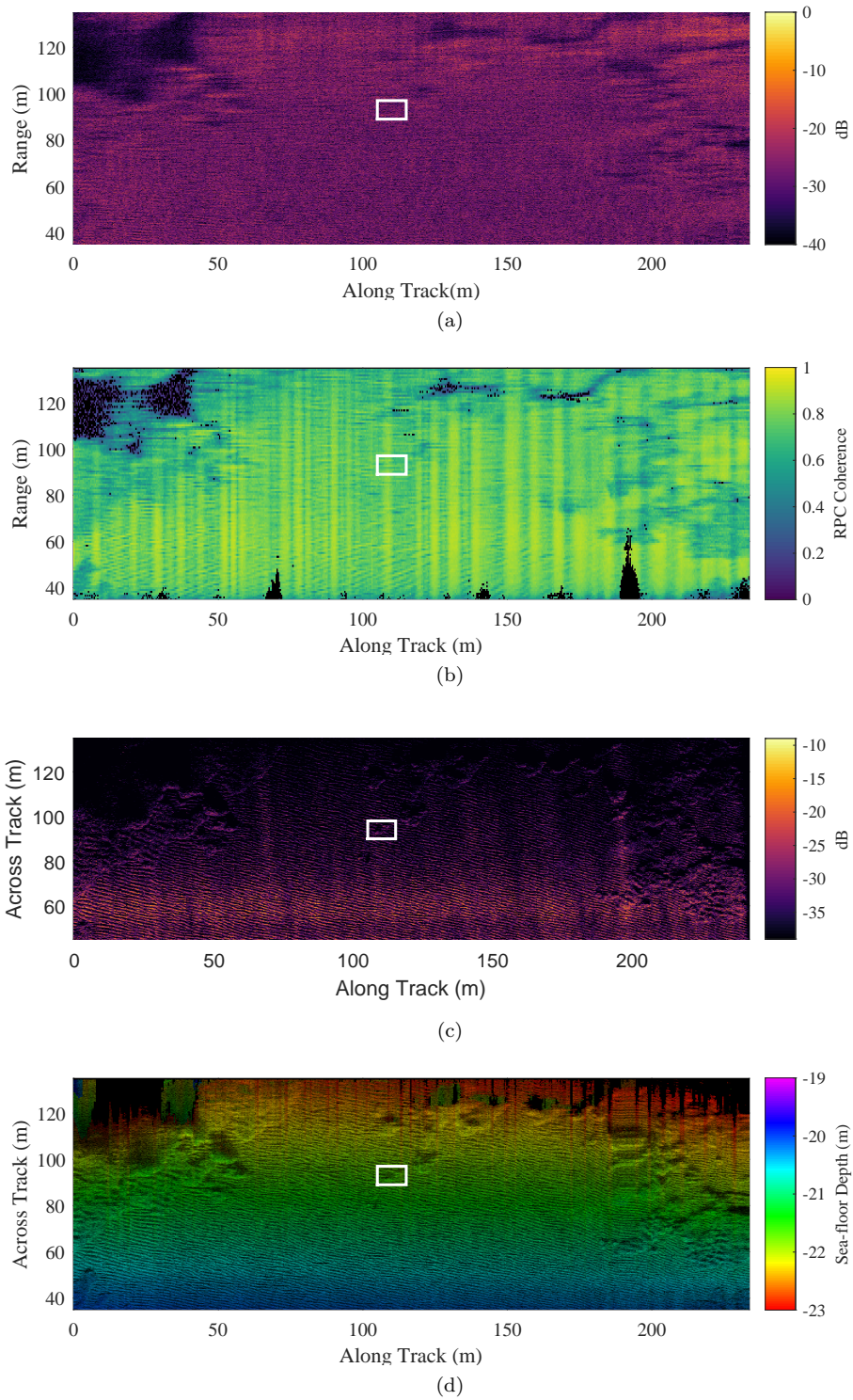
Figure 5.8: (a) Sonar echo data (b) coherence (c) SAS image showing a predominantly rippled, sandy sea-floor (d) Bathymetry generated by sidescan interferometry. A small sub-window has been chosen to show the effect of reducing the frequency bandwidth of the data.

91
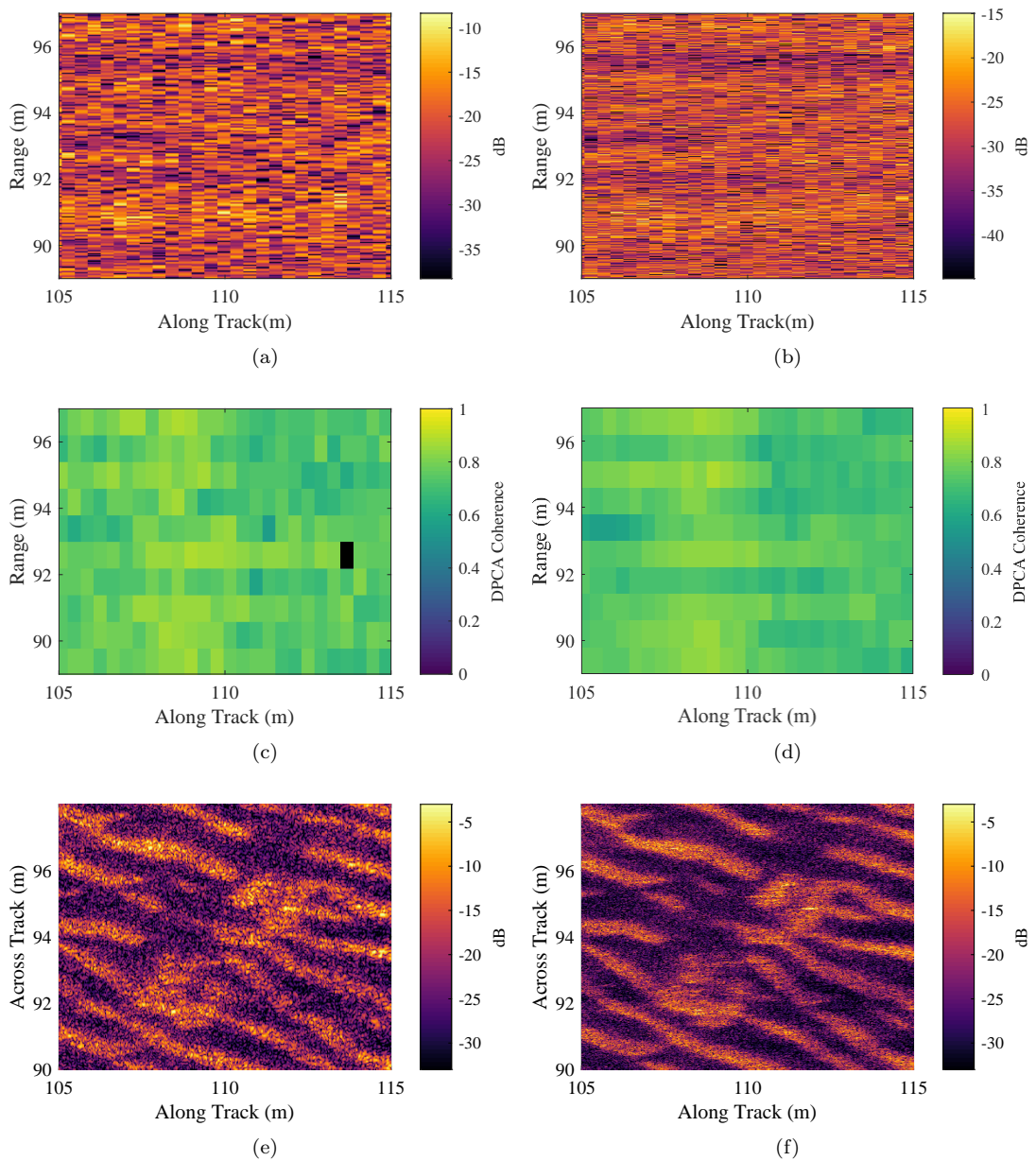
Figure 5.9: Zoom of (a,b) raw SAS data, (c,d) coherence between redundant phase centres, (e,f) SAS images, with bandwidths of (a,c,e) 10 kHz (b,d,f) 60 kHz. A reduction in across-track resolution is visible between the 10 kHz and 60 kHz images in (e) and (f) respectively.
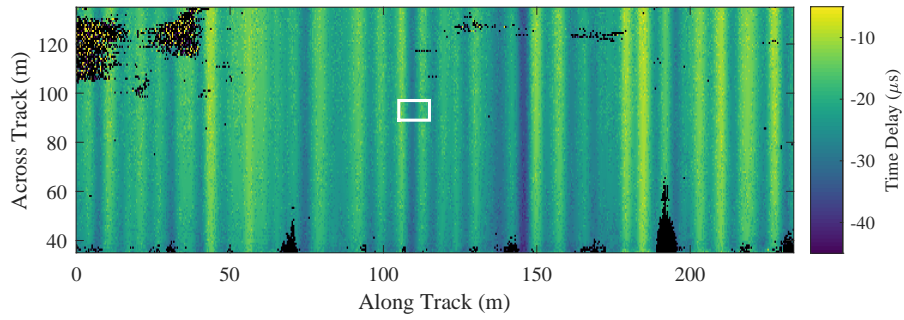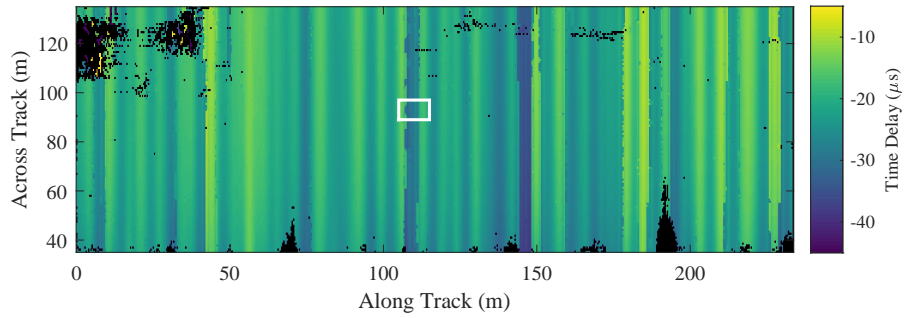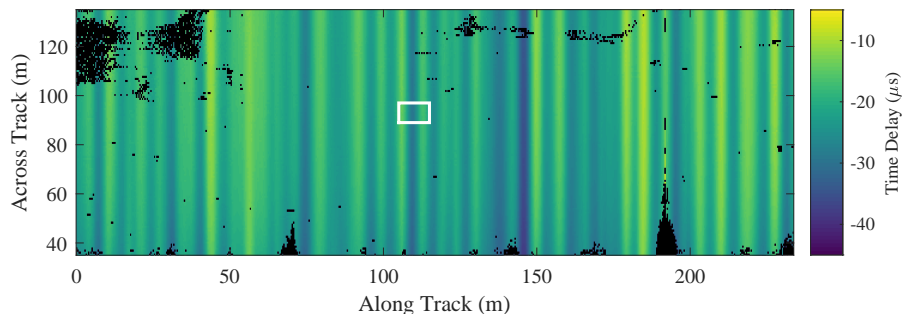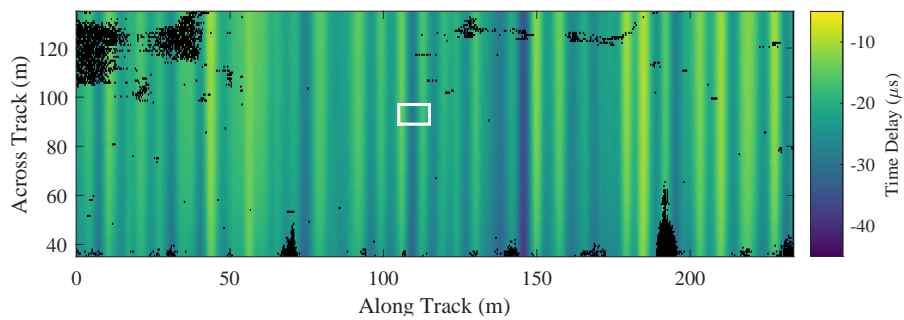
Figure 5.10: (a) Time delays from 60 kHz data (b) Refined time delays using the branch-cuts method (c) Refined time delays using the 1D RANSAC method (d) Refined time delays using the 2D RANSAC method.
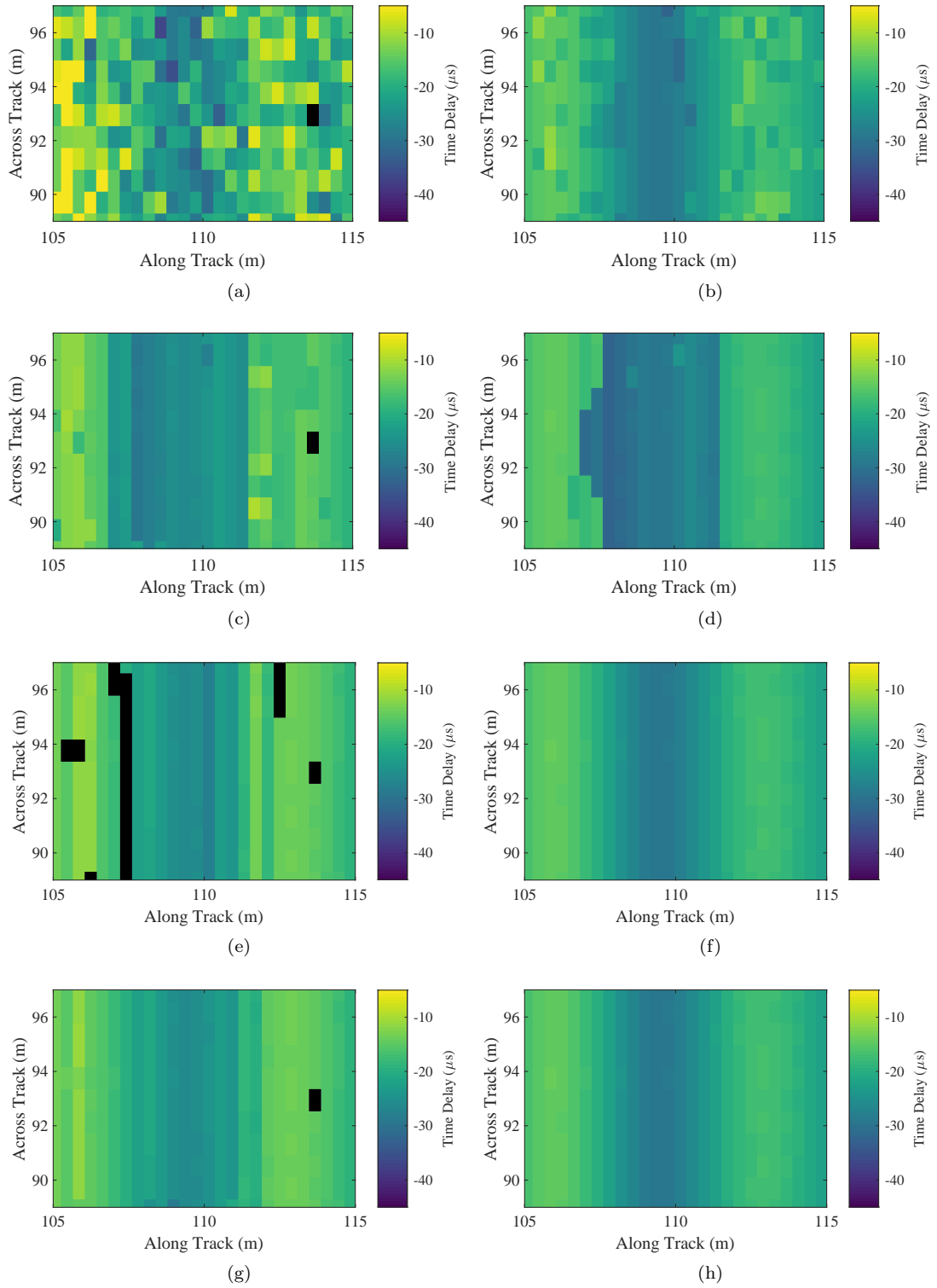
Figure 5.11: Zooms of: (a,b) Unrefined time delays (c,d) Refined time delays using the branch-cuts method (e,f) Refined time delays using the 1D RANSAC method (g,h) Refined time delays using the 2D RANSAC method (a,c,d,g) for 10 kHz bandwidth (b,d,f,h) for 60 kHz bandwidth.
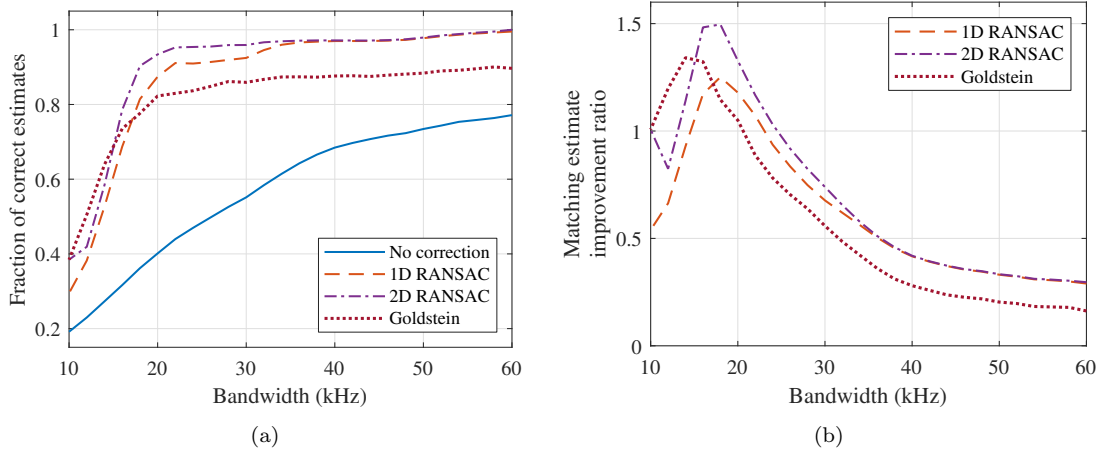
Figure 5.12: (a) Fraction of time delay estimates that match the reference with no correction, after 1D and 2D RANSAC methods, and using the branch-cuts method (b) The matching estimate improvement ratios for each of the methods.

estimates for the 60 kHz data using the 1D and 2D RANSAC methods are shown in Figures 5.10c and 5.10d respectively. The result from the branch-cuts method is shown in Figure 5.10b. Subsets of the refined time delays estimated using the 10 kHz and 60 kHz bandwidth data are shown in Figures 5.11e and 5.11f for the 1D RANSAC method, Figures 5.11g and 5.11h for the 2D RANSAC method, and Figures 5.11c and 5.11d for the branch-cuts method.

At 60 kHz bandwidth, the 1D and 2D RANSAC methods generate extremely similar estimates. However, the branch-cuts method shows discontinuities in the along-track direction (shown in Figure 5.10b), which correspond to regions of large ($> \pi$) phase differences caused by large inter-ping sways. At 10 kHz bandwidth, some time delay estimates refined using the 1D and 2D RANSAC methods have been rejected due to being further than the threshold from the model, which are shown as black regions in Figures 5.11e and 5.11g.

The time delays estimated using the bandwidth-filtered data are denoted by $\hat{\tau}_{b,\mathrm{R1}}[p,q]$, $\hat{\tau}_{b,\mathrm{R2}}[p,q]$ and $\hat{\tau}_{b,\mathrm{GS}}[p,q]$ for the 1D and 2D RANSAC methods and the branch-cuts algorithm respectively, where $b \in \{10, 12, 14, ..., 60\}$ kHz indexes the frequency bandwidths.

The results from the 1D RANSAC, 2D RANSAC and branch-cuts methods at full frequency bandwidth were qualitatively assessed based on the smoothness of the resulting time delay estimates, and the 2D RANSAC method was found to give the best results. The time delay estimates from the 2D RANSAC algorithm, denoted $\hat{\tau}_{B,\mathrm{2D}}[i,j]$, are therefore considered to be the 'gold standard' time delay estimates in the following analysis.

The probability distribution of the error in the coarse time delay estimates (compared to the gold standard time delay estimates) is shown in Figure 5.13. The error distribution at full 60 kHz bandwidth is shown in Figure 5.13a, which is symmetrical and centred on zero error as expected. However, this clearly illustrates the problem that must be solved; the fine time delay estimation procedure described in Section 4.3 gives inaccurate estimates for coarse time delay

Figure 5.13: (a) Probability distribution of error between coarse time delay estimates from 60 kHz bandwidth around the gold standard fine time delay estimates. (b) The probability distribution of the coarse time delay error as a function of bandwidth.

estimates with an error corresponding to more than half a wavelength. Figure 5.13b is the error distribution with varying bandwidth, which shows a broadening of the error distributions with reducing bandwidth. A slight asymmetry is also evident at smaller bandwidths, possibly caused by the assumption of zero relative dilation between signals which may be inaccurate at short range.

Figures 5.14 and 5.15 show how the coarse and fine time delay estimates are distributed around the best-fitting models, for the 1D and 2D methods respectively. The narrow distribution of fine time around the model indicates that the models fit the fine time delay estimates well, only failing to give a good fit for very low bandwidths.

The refined time delay estimates from the 1D and 2D RANSAC methods and the branch-cuts method at each frequency bandwidth are compared with the gold standard time delay estimate. The fraction of time delay estimates that match the gold standard is given by

$$\xi_{b,\mu} = \frac{\sum_{p=0}^{P-1} \sum_{q=0}^{Q-1} \Big[|\hat{\tau}_{b,\mu}[p,q] - \hat{\tau}_{B,\text{2D}}[p,q]| < \tau_{\text{thresh}} \Big]}{PQ} \tag{5.28}$$

where μ denotes the correction method.

The resulting values of $\xi_{b,\mu}$ are plotted in Figure 5.12a. The matching estimate improvement ratios calculated by

$$\zeta_{b,\mu} = \frac{\xi_{b,\mu} - \xi_{b,\text{NC}}}{\xi_{b,\text{NC}}} \tag{5.29}$$

are plotted in Figure 5.12b. This demonstrates that the 1D and 2D RANSAC methods result in what we interpret as improvements of 29-125% and 30-150% respectively compared to 16-134% for the Goldstein branch-cuts method.

The ratio of matching estimates for the unrefined time delay estimates reduces with decreasing bandwidth, because the width of the peak of the correlation function becomes wider with decreasing frequency bandwidth. This broadening of the cross-correlation peak means
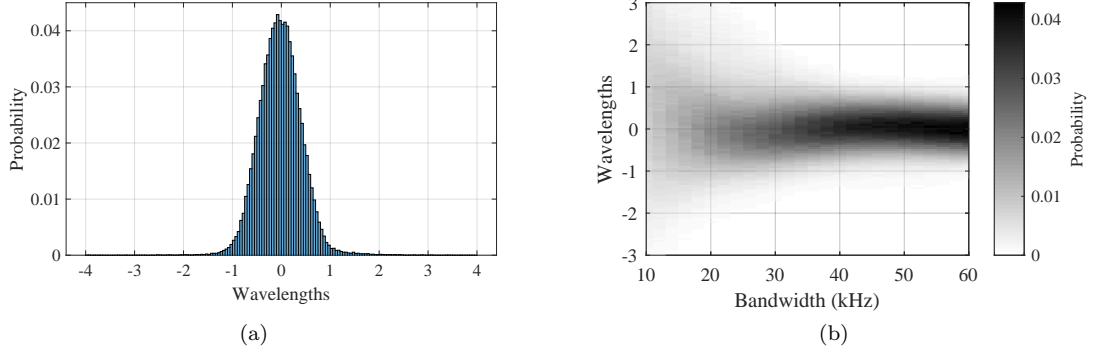
Figure 5.14: (a) Probability distribution of error between the coarse time delay estimates from 60 kHz bandwidth around the 1D model. (b) The probability distribution of the difference between the coarse time delay estimate and the 1D model as a function of bandwidth. (c) Probability distribution of error between the fine time delay estimates from 60 kHz bandwidth around the 1D model. (Note zoomed x axis) (d) The probability distribution of the difference between the fine time delay estimate and the 1D model as a function of bandwidth.

that noise is more likely to cause phase wrap errors. The 1D and 2D RANSAC methods perform at least as well as the branch-cuts method at all frequency bandwidths. The branch-cuts method performs less well than the RANSAC methods at high bandwidths due to its inability to unwrap regions with high phase gradient correctly.

The time taken to perform the methods at each bandwidth is plotted in Figure 5.16. With reducing bandwidth, the time taken for both RANSAC methods increases due to the reducing inlier fraction, which causes the number of RANSAC iterations to increase. However, this is particularly evident for the 2D RANSAC method, because the number of parameters in the model is larger, meaning more trials are required to achieve the same probability of success. The time taken by the branch-cuts method is approximately constant for all frequency bandwidths.

5.5   Summary

Algorithms making use of the RANSAC algorithm with 1D and 2D models have been developed to detect and correct phase wrap errors in time delay estimation applications. Results from field
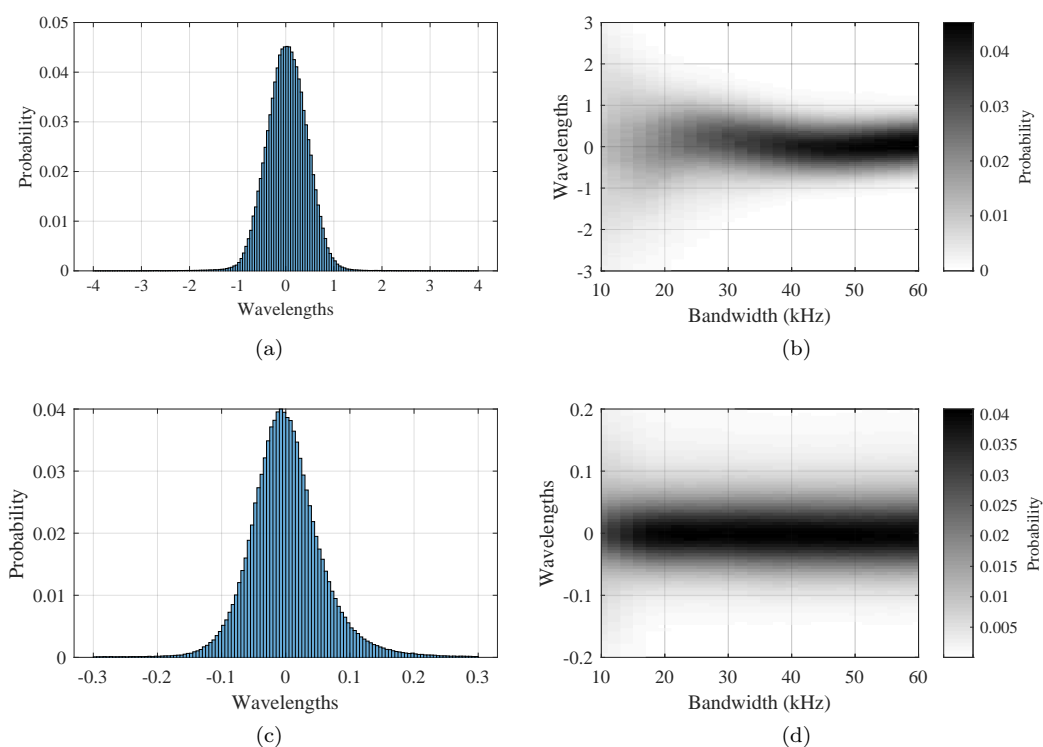
Figure 5.15: (a) Probability distribution of the error between the coarse time delay estimates from 60 kHz bandwidth around the 2D model. (b) The probability distribution of the difference between the coarse time delay estimate and the 2D model as a function of bandwidth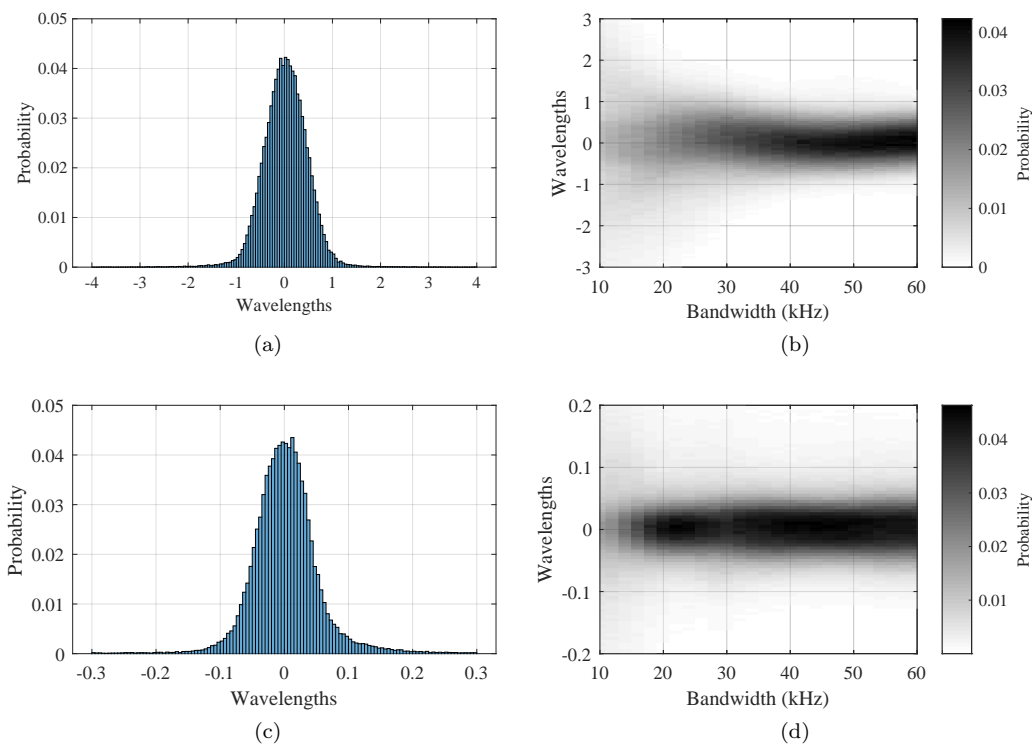. (c) Probability distribution of error between the fine time delay estimates from 60 kHz bandwidth around the 2D model. (Note zoomed x axis) (d) The probability distribution of the difference between the fine time delay estimate and the 2D model as a function of bandwidth.
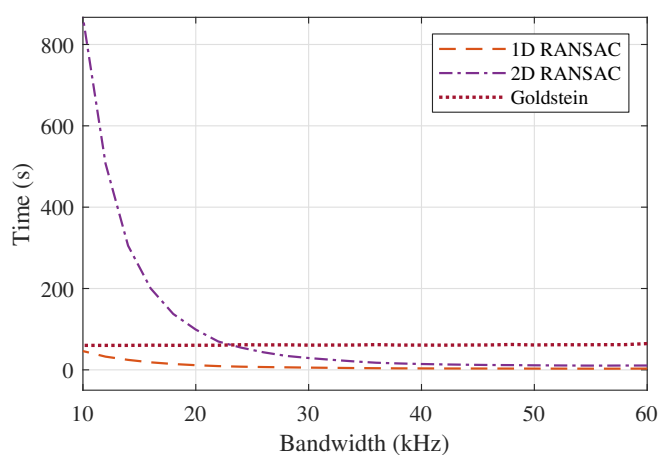
Figure 5.16: Time taken by the 1D RANSAC, 2D RANSAC and Goldstein branch cuts methods.

data collected by the 270-330 kHz SAS of the CMRE MUSCLE AUV show that the 1D and 2D RANSAC methods result in improvements of 29 - 125% and 30 - 150% respectively compared to improvements of 16 - 134% for the Goldstein branch-cuts method. Using a 2D model shows a slight performance benefit, at the expense of greater computational cost than using a 1D model. These model-based approaches to the phase unwrapping problem have been shown to be resilient to regions of high phase gradient, which result in errors for the branch-cuts method.

The 2D RANSAC method is an integral part of the simultaneous navigation and bathymetry estimation algorithm, which requires accurate time delay estimates between redundant signals. The algorithms have been shown to be effective for a large range of bandwidths, which may enable the use of lower cost, low fractional bandwidth systems.

6 Simultaneous estimation of navigation and coarse bathymetry using echo data redundancy

This section describes a new algorithm for simultaneous estimation of high-precision navigation and coarse bathymetry, using the redundant data collected between adjacent pings of an interferometric SAS. Estimating navigation and bathymetry simultaneously in this way has potential to improve the precision of the navigation estimate and allows estimation of the vehicle path in three dimensions. The algorithm utilises measurements of along-track displacement (also referred to as surge) and time delay between multiple pairs of RPC arrays formed between adjacent pings of an interferometric SAS. The algorithm utilises the RANSAC phase wrap error detection and correction method [141] described in Section 5 to improve the accuracy of the time delay measurements. An iterative non-linear minimisation between measured and modelled quantities allows simultaneous estimation of the vehicle position on each ping and the location of a number of control points on the sea-floor. These control point locations represent a coarse bathymetry estimate, onto which SAS images may be focused.

We first revisit the idea of the 'triad of confounding factors' in closer detail in Section 6.1. This exposes some of the limitations of conventional micro-navigation approaches, and motivates the development of the new method. Section 6.2 introduces the multiple redundant array pairs formed between adjacent pings of an interferometric SAS. Measurements made between these multiple redundant array pairs allow formation of sufficient independent equations for joint estimation of the vehicle path and coarse bathymetry. Section 6.3 describes the new algorithm, which consists of a description of the geometrical model (Section 6.3.1) and the iterative non-linear minimisation method (Section 6.3.5).

The algorithm has been applied to field data collected by the 270-330 kHz SAS of the CMRE MUSCLE AUV. Section 6.4 presents navigation and bathymetry estimates made using the raw echo data from each side of the vehicle independently, and simultaneously using both sides. The navigation estimates are compared to the estimates made by the on-board navigation hardware. The method is validated by qualitative assessment of the quality of SAS images focused onto the coarse bathymetry estimate using the navigation estimate. Additionally, the interferograms formed from these images show near-zero phase, suggesting that the coarse bathymetry estimate is consistent with the data. However, there is a lack of ground truth for both navigation and bathymetry which precludes comprehensive algorithm performance analysis. For this reason, a simulation has been performed which mimics the experimental acquisition. The simulated SAS data is generated using a custom MATLAB® implementation of a ray-tracing point scatterer model. Section 6.5 presents the navigation and bathymetry estimates from this simulated data and compares them with ground truth, and the performance of the method is analysed.

6.1 The triad of confounding factors

The concept of the 'triad of confounding factors' is central to the new algorithm. Data-domain micro-navigation algorithms exploit the fact that RPC time delays contain information about
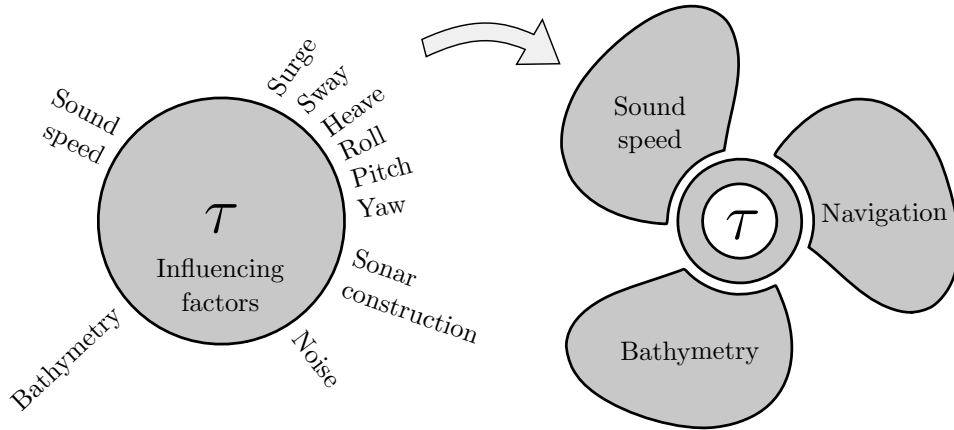
Figure 6.1: The factors that influence time delay measurements τ between redundant signals are: the speed of acoustic propagation, the bathymetry, the motion of the vehicle in the surge, sway, heave, roll, pitch and yaw degrees of freedom, and the geometrical construction of the sonar. Noise causes errors in the time delay estimates. The properties of interest can be grouped into the 'triad of confounding factors', consisting of sound speed, navigation and bathymetry.

the ping-to-ping motion of the sonar, i.e. navigation information. Time delays between the signals received by interferometric arrays contain information about bathymetry; this is the basis of interferometric sidescan and synthetic aperture sonar. Accurate knowledge of the speed of sound is required for accurate through-the-sensor navigation estimation, and speed of sound errors are known to cause bias errors in interferometric bathymetry estimation [16, Ch. 6]. It follows that all time delays, whether measured for the purpose of navigation or bathymetry estimation, are affected by the geometry of the time delay measurement (encompassing navigation and bathymetry) and the speed of sound. This is depicted in Figure 6.1, where τ represents a time delay measurement between redundant signals. The left panel shows the factors that influence such time delay measurements, which are the speed of sound in the medium, the sea-floor bathymetry, and the parameters that define the geometry of the measurement. These parameters encompass the location of the sonar hardware on the vehicle and the motion of the vehicle in all six degrees of freedom. Noise also affects the time delay measurements. The right panel shows the grouping of these factors into the 'triad of confounding factors'; sound speed, bathymetry and navigation.

The triad representation helps to build an intuition that all time delay measurements are affected by, and therefore contain information about, each member of the triad. Given sufficient independent measurements and provided the problem is well-conditioned, it is possible to estimate each member of the triad using the redundant data.

Conventional methods typically assume accurate knowledge of two members of the triad in order to estimate the third. For example, Leier's development [32, Ch. 4.2.6] of Cook's non-linear least squares method [33, Ch. 5.5-5.7] and that used by Sæbø [16, Ch. 5.2.1] use a sequential process of coarse bathymetry estimation followed by fusion with RPC time delay estimates. In these methods, the coarse bathymetry estimate is made using the narrow beam

of the real aperture interferometer in a method termed sidescan bathymetry. The bathymetry estimates are then integrated with slant-plane RPC micro-navigation estimates made using the wider beam of the RPC array, in a non-linear least squares approach.[10] That is, assuming accurate knowledge of bathymetry and sound speed allows estimation of navigation from RPC time delays.

The contrasting approach of Prater [114] makes coarse bathymetry estimates using the small interferometric baseline formed between RPC pairs. The geometry of this interferometric baseline is assumed from the ping-to-ping navigation estimate made by an INS and a constant and known sound speed is assumed. In other words, assuming accurate knowledge of navigation and sound speed allows estimation of bathymetry from RPC time delays.

The simultaneous micro-navigation and bathymetry estimation algorithm introduced in this section represents a step towards joint estimation of all members of the triad. Coarse bathymetry and high-precision navigation parameters are jointly estimated using redundant sonar data under the assumption of a constant and known speed of sound and known sonar geometry. In addition, the vehicle roll, pitch and yaw are assumed to be accurately measured by another sensor such as an INS. The algorithm has similarities to the repeat-pass phase centre double localisation (PCDL) method of Tebaldini [96], adapted for SAS by Kennedy and Marston [80]. The main similarity is the realisation that it is possible to form sufficient independent equations to jointly estimate the vehicle path and the location of a number of control points on the sea-floor, as described in [21]. However, these algorithms are fundamentally different to the new algorithm described here, because:

1. The new algorithm exploits redundancy in the signals received by overlapping portions of the arrays, rather than redundancy in SAS images formed from repeated passes, allowing it to estimate the vehicle position on each ping independently.

2. The new algorithm is easily generalisable, allowing it to be used for navigation along a single path and also for high-precision track registration between repeated passes.

6.2   Use of multiple redundant array pairs

The simultaneous navigation and bathymetry estimation algorithm uses the surge and time delay estimation methods described in Section 4 made between multiple redundant array pairs. Interferometric SAS systems present the opportunity to make more than one measurement of surge and time delay per ping and range window on each side of the vehicle. Fusion of these multiple measurements allows estimation of both the position of the vehicle on each ping and the location of a number of control points on the sea-floor.

Consider a single-sided interferometric SAS with N_a vertically separated receiver arrays performing two pings $p-1$ and p. If the **app!** is less than half of the receiver array length (as is required for algorithms that exploit echo data redundancy), the fore-most phase centres

---

[10]The mismatch between beam widths used for bathymetry and navigation estimation has the potential to introduce navigation errors. A simple solution to this problem would be to use only the overlapping subset of the real aperture interferometer for bathymetry estimation.
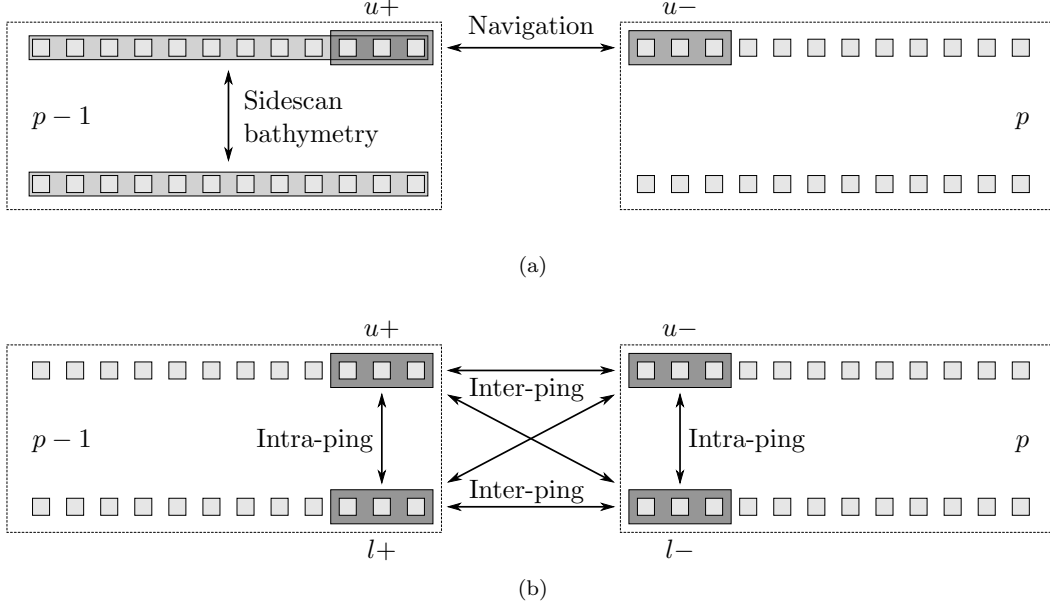
Figure 6.2: Diagrams showing the overlapping phase centre array pairs utilised by (a) the conventional RPC micro-navigation algorithm and (b) the new simultaneous micro-navigation and bathymetry estimation algorithm. Two adjacent pings $p - 1$ and p of a single-sided interferometic SAS with $N_a = 2$ arrays are shown. Arrows indicate the pairs of redundant arrays that are used by each of the micro-navigation algorithms.

of ping $p - 1$ will overlap with the aft-most phase centres of ping p. There are therefore $2N_a$ redundant arrays formed between adjacent pings. The total number of redundant array pairs formed between adjacent pings is

$$P_{\text{total}} = \binom{2N_a}{2} \tag{6.1}$$

where $\binom{\cdot}{\cdot}$ denotes the binomial coefficient. The number of intra-ping pairs is

$$P_{\text{intra-ping}} = 2\binom{N_a}{2} \tag{6.2}$$

and the number of inter-ping pairs is

$$P_{\text{inter-ping}} = P_{\text{total}} - P_{\text{intra-ping}}. \tag{6.3}$$

For a typical InSAS with $N_a = 2$, this results in $P_{\text{total}} = 6$ redundant array pairs between adjacent pings, of which $P_{\text{inter-ping}} = 4$ are between pings and $P_{\text{intra-ping}} = 2$ are within the same ping, as demonstrated in Table 2.

In conventional RPC micro-navigation, sidescan bathymetry estimates are made by measuring time delays between the summed signals from the upper and lower phase centre arrays of the interferometer at multiple temporal windows. This phase centre array pair is labelled 'side-

		Surge				Time delay			
		$p-1$		p		$p-1$		p	
		$u+$	$l+$	$u-$	$l-$	$u+$	$l+$	$u-$	$l-$
$p-1$	$u+$	—	—	✓	✓	—	✓	✓	✓
	$l+$	—	—	✓	✓	—	—	✓	✓
p	$u-$	—	—	—	—	—	—	—	✓
	$l-$	—	—	—	—	—	—	—	—

Table 2: Check-marks indicate the 6 pairs of redundant arrays between adjacent pings $p-1$ and p, between which time delay measurements can be made. Only the inter-ping pairs, denoted by boxed checkmarks, are used for surge estimation.

can bathymetry' in Figure 6.2a. Navigation estimates are made by combining these sidescan bathymetry estimates with time delays measured between pairs of either the upper or lower RPC arrays at each temporal window. For example, the upper RPC array pair is labelled 'navigation'.

In the new simultaneous micro-navigation and bathymetry estimation algorithm each of the six pairs of RPC arrays formed between adjacent pings can be exploited, as shown in Figure 6.2b. These pairs are divided into those within the same ping (intra-ping) and those between adjacent pings (inter-ping). The inter-ping pairs are used for estimation of the along-track displacement between the arrays. Time delays can be measured between all six pairs of RPC arrays at multiple temporal windows. All of these time delay measurements can be used for simultaneous micro-navigation and bathymetry estimation. The new algorithm thus makes more complete use of the redundant data collected by interferometric systems.

6.3 Simultaneous micro-navigation and bathymetry estimation algorithm

The goal of the simultaneous micro-navigation and bathymetry estimation algorithm is to estimate the three dimensional vehicle position at each ping transmission time, while simultaneously estimating the three-dimensional position of multiple control points on the sea-floor. This must be achieved by exploiting measurements made using the redundant data collected between adjacent pings, i.e. along-track displacement (surge) between arrays and time delays between redundant signals at multiple temporal windows.

Therefore, we wish to find the function that outputs navigation and bathymetry estimates given surge and time delay measurements at every temporal window, and given an assumed sound speed and sonar geometry. We denote this unknown function

$$\boldsymbol{\chi} = h(\boldsymbol{\zeta}) \tag{6.4}$$

where $\boldsymbol{\chi}$ denotes the desired navigation and bathymetry estimates and $\boldsymbol{\zeta}$ denotes the measurements of surge and time delay and the corresponding propagation time. However, only the

inverse of this function,

$$\boldsymbol{\zeta} = g(\boldsymbol{\chi}) \tag{6.5}$$

is readily available. The function $g(\boldsymbol{\chi})$ is referred to as the model, which is a non-linear function that outputs surges, time delay and propagation times given navigation, bathymetry, sound speed and sonar geometry.

The simultaneous navigation and bathymetry estimation algorithm operates by inverting the model function. The model is non-linear, so inversion for navigation and bathymetry is performed by minimising the error between measured and modelled surges and time delays over all pings and temporal windows. This is achieved using a weighed Gauss-Newton optimisation scheme.

A schematic description of this non-linear least-squares optimisation method is shown in Figure 6.3. The algorithm begins with initial estimates of navigation and bathymetry in the top left corner, which are used by the models to generate modelled values of surge, time delay and propagation time. Then, the difference between the measured and modelled surges, time delays and propagation times results in the model error. The model is linearised about the most recent estimate of navigation and bathymetry, and a weighted pseudo-inverse is used to calculate the estimation error. The navigation and bathymetry estimate is updated by subtracting the estimation error from the most recent estimate of navigation and bathymetry, and the process is iterated until convergence.

6.3.1 Geometrical models

This section describes the implementation of the models for along-track displacement between phase centre arrays with overlapping elements, and the two-way propagation time from the transmitter to a given location on the sea-floor and back to the receiver. The time delay between redundant signals is modelled by the difference between the relevant propagation times. A constant speed of sound is assumed, from which an assumption of straight acoustic paths follows, however it would be possible to model curved acoustic paths caused by sound speed gradients in the future. A single-sided interferometric SAS is considered here for simplicity, but the method is also applicable to dual-sided systems.

6.3.1.1 Notation

Consider the adjacent pings $p - 1$ and p shown in Figure 6.4, for which redundant signals are received by the fore-most and aft-most elements of both the upper and lower arrays on pings $p - 1$ and p respectively. For brevity of notation, quantities related to receiver arrays are identified by a post-superscript 'u' or 'l' (for upper or lower), and the relevant redundant portion of each array (fore or aft) is identified by '+' or '-'. Quantities related to the transmitter are identified by a post-superscript 'tx', and those related to a control point on the sea-floor are identified by a post-superscript 'b'. As before, the ping index is p, and the temporal window index is q.

The vehicle pose is a function of time t, and the sonar transmits pings at times t_p, where
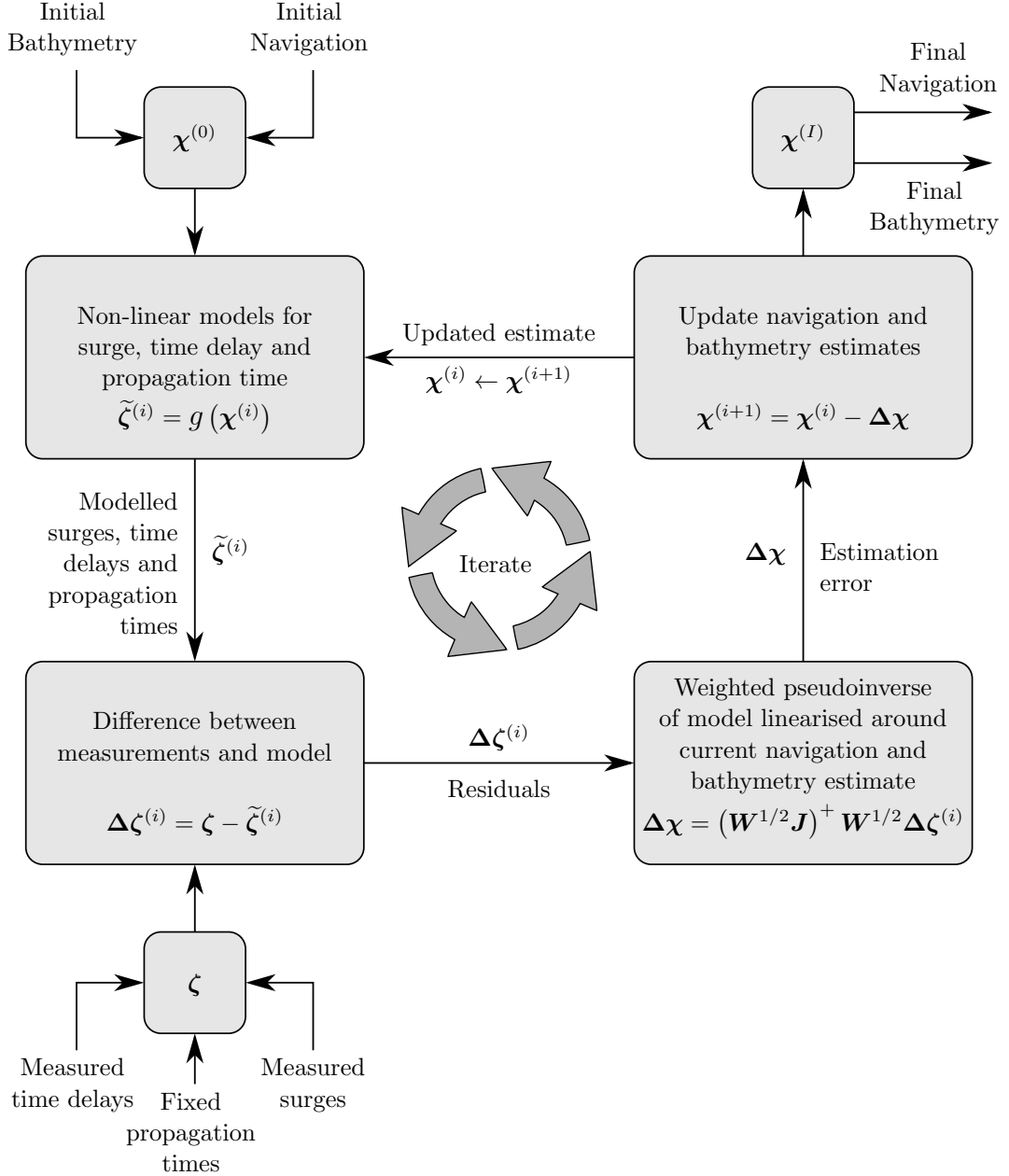
Figure 6.3: An overview of the simultaneous navigation and bathymetry estimation algorithm, which uses the Gauss-Newton algorithm with a weighted pseudo-inverse of a linearised problem on each iteration. Initial estimates of navigation and bathymetry ($\boldsymbol{\chi}^{(0)}$) are used to generate modelled surges, time delays and propagation times ($\widetilde{\boldsymbol{\zeta}}^{(i)}$). The difference between modelled and measured surges, time delays and propagation times gives the vector of residuals $\boldsymbol{\Delta\zeta}^{(i)}$. The residuals are used to find the estimation error by performing a weighted pseudoinverse of the Jacobian ($\boldsymbol{J}$). The navigation and bathymetry estimates are then updated using this estimation error to give $\boldsymbol{\chi}^{(i+1)}$. The process iterates until a termination criterion is met, at which point the final navigation and bathymetry estimates are contained in $\boldsymbol{\chi}^{(I)}$, where I is the total number of iterations.
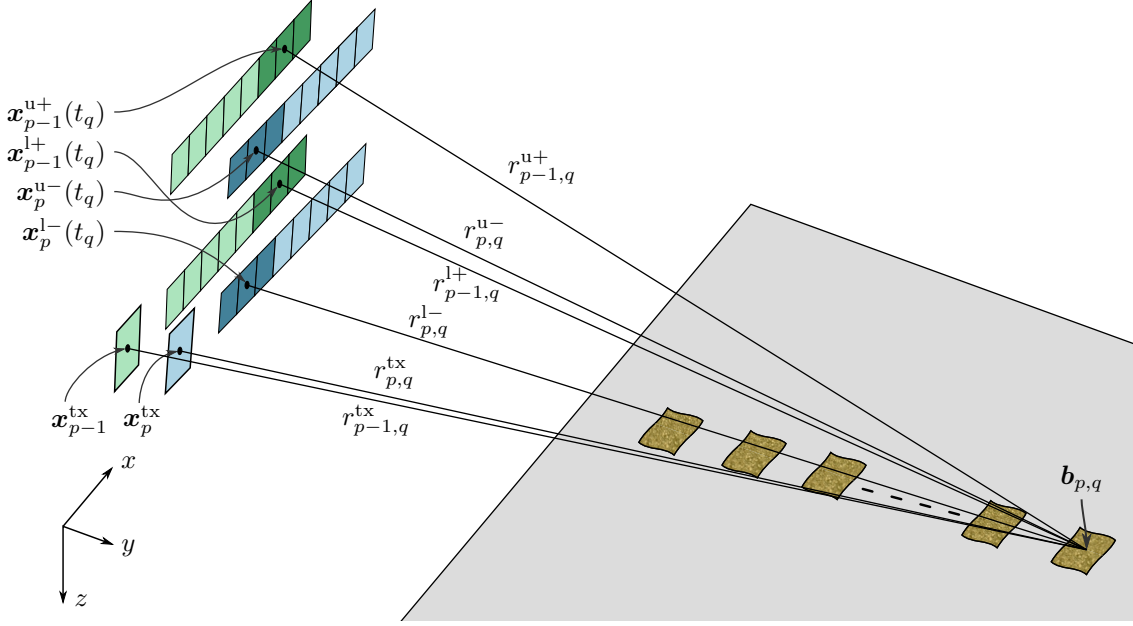
Figure 6.4: The geometry of a single-sided interferometric system for the pair of adjacent pings $p-1$ and p. The transmitter position at the transmission times of pings $p-1$ and p are denoted $\boldsymbol{x}_{p-1}^{\mathrm{tx}}$ and $\boldsymbol{x}_p^{\mathrm{tx}}$ respectively. The position of the centre of the redundant portion of the upper and lower receiver arrays on ping $p-1$ at the time of reception of the middle of the qth range window are denoted $\boldsymbol{x}_{p-1}^{\mathrm{u+}}(t_q)$ and $\boldsymbol{x}_{p-1}^{\mathrm{l+}}(t_q)$ and the position of the centre of the redundant portion of the upper and lower receiver arrays of ping p at the same time are denoted $\boldsymbol{x}_p^{\mathrm{u-}}(t_q)$ and $\boldsymbol{x}_p^{\mathrm{l-}}(t_q)$ respectively. The position of centre of the region of the sea-floor corresponding to the qth range window is denoted $\boldsymbol{b}_{p,q}$. The ranges between the transmitters of pings $p-1$ and p and this sea-floor region are shown, as are the ranges from the sea-floor region to each of the redundant portions of the receiver arrays.

$p \in [0, P-1]$ and P is the total number of pings. The pose of the vehicle consists of its position and orientations $\boldsymbol{X}(t) = [\boldsymbol{x}(t), \boldsymbol{\vartheta}(t)]^{\mathrm{T}}$, where

$$\boldsymbol{x}(t) = \Big(x(t), y(t), z(t)\Big) \quad \text{and} \quad \boldsymbol{\vartheta}(t) = \Big(\theta(t), \phi(t), \psi(t)\Big) \tag{6.6}$$

where θ, ϕ and ψ are the rotations about the vehicle's x, y and z axes respectively, known as roll, pitch and heading. The vehicle pose at ping transmission time t_p is therefore denoted $\boldsymbol{X}(t_p)$, or $\boldsymbol{X}_p$ for brevity. We assume that the vehicle is stationary during the signal transmission.

The vehicle is in constant motion, and therefore has a different pose at the time of reception of each sample of the sonar echo. However we make the assumption that the vehicle is stationary during reception of each range windowed signal, the middle of which is received at a time of τ_q after transmission, where $q \in [0, Q-1]$ and Q is the number of range windows. The pose of the vehicle at the time of reception of the qth range windowed signal is denoted $\boldsymbol{X}(t_p + \tau_q)$, or
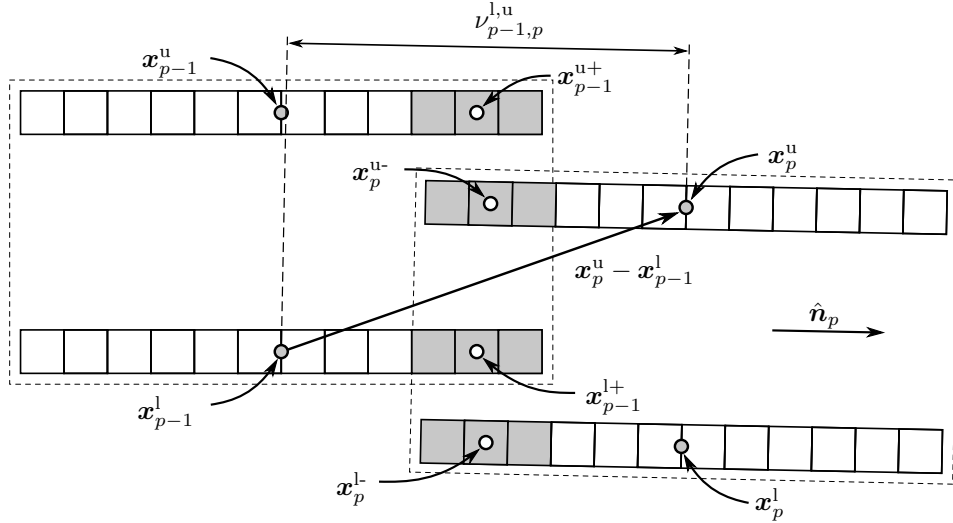
Figure 6.5: Side view of the pair of interferometric phase centre arrays formed between adjacent pings $p - 1$ and p. The modelled surge between the lower RPC array of ping $p - 1$ and the upper RPC array of ping p is shown.

$\boldsymbol{X}_p(\tau_q)$ for brevity. These positions are approximated by linear interpolation,

$$\boldsymbol{X}_p(\tau_q) = \boldsymbol{X}_p + \frac{(\boldsymbol{X}_{p+1} - \boldsymbol{X}_p)\tau_q}{t_{p+1} - t_p},\tag{6.7}$$

where $t_{p+1} - t_p$ is the ping repetition period.

6.3.2   Surge model

Inter-array surge is defined here as the distance between array centres in the direction of the array axis, normally aligned with the vehicle's aft-fore axis. Due to the continuous motion of the platform, this definition is only unambiguous for inter-ping vehicle motions with zero pitch and yaw rates. We therefore assume that the vehicle orientation at the time of transmission of ping p is valid for the duration of the $p - 1$ to p ping pair. Additionally, an assumption of negligible acceleration in the direction of the array axis is made for simplicity, resulting in modelled surge that is independent of the temporal window. This is equivalent to applying the stop-and-hop assumption in the surge direction. This limitation could be addressed in future work, however errors introduced by this assumption are expected to be small, because the high inertia of current SAS-equipped AUVs limits the practical angular and linear accelerations.

Under these assumptions, the modelled surges between the four inter-ping RPC array pairs

formed between pings $p-1$ and p are given by

$$\nu_{p-1,p}^{\text{u,u}} = \hat{\boldsymbol{n}}_p \cdot \left(\boldsymbol{x}_{p-1}^{\text{u}} - \boldsymbol{x}_p^{\text{u}}\right), \tag{6.8}$$

$$\nu_{p-1,p}^{\text{u,l}} = \hat{\boldsymbol{n}}_p \cdot \left(\boldsymbol{x}_{p-1}^{\text{u}} - \boldsymbol{x}_p^{\text{l}}\right), \tag{6.9}$$

$$\nu_{p-1,p}^{\text{l,u}} = \hat{\boldsymbol{n}}_p \cdot \left(\boldsymbol{x}_{p-1}^{\text{l}} - \boldsymbol{x}_p^{\text{u}}\right), \tag{6.10}$$

$$\nu_{p-1,p}^{\text{l,l}} = \hat{\boldsymbol{n}}_p \cdot \left(\boldsymbol{x}_{p-1}^{\text{l}} - \boldsymbol{x}_p^{\text{l}}\right), \tag{6.11}$$

which are the projections of the vectors between the centres of the phase centre arrays in the direction of the array axis at t_p, whose unit vector is given by

$$\hat{\boldsymbol{n}}_p = \boldsymbol{\Psi}_p \boldsymbol{\Phi}_p \begin{pmatrix} 1 \\ 0 \\ 0 \end{pmatrix}. \tag{6.12}$$

where $\boldsymbol{\Psi}_p$ and $\boldsymbol{\Phi}_p$ are the Euler rotation matrices around the yaw and pitch axes respectively. The locations of the centres of the upper and lower phase centre arrays on ping $p-1$ are $\boldsymbol{x}_{p-1}^{\text{u}}$ and $\boldsymbol{x}_{p-1}^{\text{l}}$ respectively, and those on ping p are $\boldsymbol{x}_p^{\text{u}}$ and $\boldsymbol{x}_p^{\text{l}}$.

Figure 6.5 is a side view of the four RPC arrays formed between adjacent pings $p-1$ and p. As an example, the modelled surge between the lower phase centre array of ping $p-1$ (with position $\boldsymbol{x}_{p-1}^{\text{l}}$) and the upper phase centre array of ping p (with position $\boldsymbol{x}_p^{\text{u}}$) is shown.

The positions of the centroids of the phase centre arrays in the world co-ordinate frame are calculated using homogeneous co-ordinates (first proposed by Möbius in 1827 [142]), which allow multiple co-ordinate transforms to be performed as a sequence of matrix multiplications.

The positions of the centres of the phase centre arrays of pings $p-1$ and p in the world co-ordinate frame are given by

$$\boldsymbol{x}_{p-1}^{\text{u}} = \boldsymbol{T}(t_{p-1})\boldsymbol{u}^{\text{u}}, \tag{6.13}$$

$$\boldsymbol{x}_{p-1}^{\text{l}} = \boldsymbol{T}(t_{p-1})\boldsymbol{u}^{\text{l}}, \tag{6.14}$$

$$\boldsymbol{x}_p^{\text{u}} = \boldsymbol{T}(t_p)\boldsymbol{u}^{\text{u}}, \tag{6.15}$$

$$\boldsymbol{x}_p^{\text{l}} = \boldsymbol{T}(t_p)\boldsymbol{u}^{\text{l}}, \tag{6.16}$$

where $\boldsymbol{u}^{\text{u}}$ and $\boldsymbol{u}^{\text{l}}$ are the positions of the centres of the upper and lower phase centre arrays respectively in the vehicle co-ordinate frame. The homogeneous transformation matrix between the vehicle and world co-ordinate frame at t_p is given by

$$\boldsymbol{T}(t_p) = \begin{pmatrix} \boldsymbol{R}(t_p) & \boldsymbol{x}(t_p) \\ 0 \ 0 \ 0 & 1 \end{pmatrix}, \tag{6.17}$$

where

$$\boldsymbol{R}(t_p) = \boldsymbol{\Psi}_p \boldsymbol{\Phi}_p \boldsymbol{\Theta}_p \tag{6.18}$$

is the rotation matrix that defines the vehicle orientation, with components

$$\boldsymbol{\Psi}_p = \begin{pmatrix} \cos(\psi(t_p)) & -\sin(\psi(t_p)) & 0 \\ \sin(\psi(t_p)) & \cos(\psi(t_p)) & 0 \\ 0 & 0 & 1 \end{pmatrix}, \tag{6.19}$$

$$\boldsymbol{\Phi}_p = \begin{pmatrix} \cos(\phi(t_p)) & 0 & \sin(\phi(t_p)) \\ 0 & 1 & 0 \\ -\sin(\phi(t_p)) & 0 & \cos(\phi(t_p)) \end{pmatrix}, \tag{6.20}$$

$$\boldsymbol{\Theta}_p = \begin{pmatrix} 1 & 0 & 0 \\ 0 & \cos(\theta(t_p)) & -\sin(\theta(t_p)) \\ 0 & \sin(\theta(t_p)) & \cos(\theta(t_p)) \end{pmatrix}, \tag{6.21}$$

which perform the rotation around the vehicle's z, y and x axes (heading, pitch and roll) and

$$\boldsymbol{x}(t_p) = \begin{pmatrix} x(t_p) \\ y(t_p) \\ z(t_p) \end{pmatrix} \tag{6.22}$$

performs the translation from the vehicle to the world co-ordinate frame. The positions of the phase centre arrays on ping $p - 1$ can be obtained by substitution of t_{p-1} for t_p in (6.17-6.22).

This simple model generates surge estimates given only the position and orientation of the vehicle on each ping. Minimisation of the least-squares difference between these values and those measured using the redundant data provides the along-track portion of the vehicle path estimate made by the new method.

6.3.3 Propagation time model

The propagation time, also known as the two-way transmission time, is the time taken for the signal to travel from the transmitter, to a point on the sea-floor, and back to the relevant receiver elements. The model for propagation time therefore depends on the relative positions of the transmitter, the redundant portions of the receiver, and control points on the sea-floor.

Transmitter position   The transmitter position on ping p is given by

$$\boldsymbol{x}_p^{\text{tx}} = \boldsymbol{T}(t_p)\boldsymbol{u}^{\text{tx}}, \tag{6.23}$$

where $\boldsymbol{u}^{\text{tx}}$ is the transmitter position in the vehicle co-ordinate frame and the transformation matrix $\boldsymbol{T}(t_p)$ is given by (6.17-6.22), which transforms between the vehicle and world co-ordinate frames.

Redundant receiver positions   The positions of the redundant portions of the receiver arrays are a function of temporal window, due to the continuous motion of the sonar. The

positions of the fore redundant portion of the upper and lower receiver arrays on ping $p-1$ in the world co-ordinate frame are given by

$$x_{p-1,q}^{\text{u+}} = \boldsymbol{T}(t_{p-1} + \tau_q)\boldsymbol{u}^{\text{u+}}, \tag{6.24}$$

$$x_{p-1,q}^{\text{l+}} = \boldsymbol{T}(t_{p-1} + \tau_q)\boldsymbol{u}^{\text{l+}} \tag{6.25}$$

where $\boldsymbol{u}^{\text{u+}}$ and $\boldsymbol{u}^{\text{l+}}$ are the positions of the foremost portions of the upper and lower receiver arrays in the vehicle co-ordinate frame respectively. The position of the aft redundant portion of the upper and lower receiver arrays on ping p in the world co-ordinate frame are given by

$$x_{p,q}^{\text{u-}} = \boldsymbol{T}(t_p + \tau_q)\boldsymbol{u}^{\text{u-}}, \tag{6.26}$$

$$x_{p,q}^{\text{l-}} = \boldsymbol{T}(t_p + \tau_q)\boldsymbol{u}^{\text{l-}}, \tag{6.27}$$

where the transformation matrix $\boldsymbol{T}(t_p + \tau_q)$ is formed in the same manner as (6.17-6.22) but where the pose of the vehicle is interpolated at the time of reception $t_p + \tau_q$ using (6.7).

Control point position The position of each control point is defined in a its own two-dimensional co-ordinate system. This enables each control point to be defined by only two parameters. The origin of each co-ordinate system is given by

$$\boldsymbol{\kappa}_{p,q} = \frac{x_{p-1,q}^{\text{tx}} + x_{p-1,q}^{\text{u+}} + x_{p,q}^{\text{tx}} + x_{p,q}^{\text{u-}}}{4}, \tag{6.28}$$

which is the midpoint of the upper RPC arrays. This co-ordinate frame is defined by the axes a and b, which are normal to the array axis orientation $\hat{\boldsymbol{n}}_p$. A control point corresponding to the qth temporal window of the $p-1$ to p ping pair is defined in this co-ordinate system as

$$\boldsymbol{b}_{p,q}' = \begin{pmatrix} a_{p,q} \\ b_{p,q} \end{pmatrix}, \tag{6.29}$$

which can be transformed into the world co-ordinate frame by

$$\boldsymbol{b}_{p,q} = \boldsymbol{K}(t_p + \tau_q)\boldsymbol{b}_{p,q}', \tag{6.30}$$

where the transformation matrix is given by

$$\boldsymbol{K}(t_p + \tau_q) = \begin{pmatrix} \boldsymbol{\Psi}_p\boldsymbol{\Phi}_p & \boldsymbol{\kappa}_{p,q} \\ 0\ \ 0\ \ 0 & 1 \end{pmatrix}, \tag{6.31}$$

where $\boldsymbol{\Psi}_p$ and $\boldsymbol{\Phi}_p$ are defined in (6.19) and (6.20) respectively.

Two-way propagation time The two-way propagation time is the time taken for a signal to propagate from the transmitter, to a location on the sea-floor, and back to a receiver. There are four redundant arrays formed between adjacent pings of an interferometric SAS, as

described in Section 6.2. The new algorithm exploits two way travel times corresponding to each redundant array and at each temporal window. The two-way propagation time for each redundant array is given by

$$\tau_{p-1,q}^{\mathrm{u}+} = \frac{r_{p-1,q}^{\mathrm{tx}} + r_{p-1,q}^{\mathrm{u}+}}{c}, \tag{6.32}$$

$$\tau_{p-1,q}^{\mathrm{l}+} = \frac{r_{p-1,q}^{\mathrm{tx}} + r_{p-1,q}^{\mathrm{l}+}}{c}, \tag{6.33}$$

$$\tau_{p,q}^{\mathrm{u}-} = \frac{r_{p,q}^{\mathrm{tx}} + r_{p-1,q}^{\mathrm{u}-}}{c}, \tag{6.34}$$

$$\tau_{p,q}^{\mathrm{l}-} = \frac{r_{p,q}^{\mathrm{tx}} + r_{p-1,q}^{\mathrm{l}-}}{c}, \tag{6.35}$$

where c is the speed of sound,

$$r_{p-1,q}^{\mathrm{tx}} = \left\| \boldsymbol{x}_{p-1}^{\mathrm{tx}} - \boldsymbol{b}_{p,q} \right\| \tag{6.36}$$

and

$$r_{p,q}^{\mathrm{tx}} = \left\| \boldsymbol{x}_{p}^{\mathrm{tx}} - \boldsymbol{b}_{p,q} \right\| \tag{6.37}$$

are the ranges from the positions of the transmitters on pings $p-1$ and p respectively to the control point corresponding to the qth temporal window, and

$$r_{p-1,q}^{\mathrm{u}+} = \left\| \boldsymbol{x}_{p-1}^{\mathrm{u}+}(\tau_q) - \boldsymbol{b}_{p,q} \right\|, \tag{6.38}$$

$$r_{p-1,q}^{\mathrm{l}+} = \left\| \boldsymbol{x}_{p-1}^{\mathrm{l}+}(\tau_q) - \boldsymbol{b}_{p,q} \right\|, \tag{6.39}$$

$$r_{p,q}^{\mathrm{u}-} = \left\| \boldsymbol{x}_{p}^{\mathrm{u}\text{-}}(\tau_q) - \boldsymbol{b}_{p,q} \right\|, \tag{6.40}$$

$$r_{p,q}^{\mathrm{l}-} = \left\| \boldsymbol{x}_{p}^{\mathrm{l}\text{-}}(\tau_q) - \boldsymbol{b}_{p,q} \right\| \tag{6.41}$$

are the ranges from the control point to each redundant array. Taking the difference between pairs of these two-way travel times gives the modelled time delays.

6.3.4 Time delay model

Time delays between the signals received by the four redundant arrays formed between adjacent pings can be modelled by taking the difference between pairs of modelled two-way propagation times. There are six possible pairings of these redundant arrays as detailed in Section 6.2, between which time delays can be measured and modelled at each temporal window.

Each pairing consists of a reference redundant array and a comparison redundant array. The modelled time delays with the upper fore redundant array of ping $p-1$ as the reference array are given by

$$\delta\tau_{p-1,p-1,q}^{\mathrm{u}+,\mathrm{l}+} = \tau_{p-1,q}^{\mathrm{l}+} - \tau_{p-1,q}^{\mathrm{u}+}, \tag{6.42}$$

$$\delta\tau_{p-1,p,q}^{\mathrm{u}+,\mathrm{u}-} = \tau_{p,q}^{\mathrm{u}-} - \tau_{p-1,q}^{\mathrm{u}+}, \tag{6.43}$$

$$\delta\tau_{p-1,p,q}^{\mathrm{u}+,\mathrm{l}-} = \tau_{p,q}^{\mathrm{l}-} - \tau_{p-1,q}^{\mathrm{u}+}, \tag{6.44}$$

where the two-way travel times are given by (6.32-6.35). With the lower fore redundant array of ping $p-1$ as the reference array, the modelled time delays are given by

$$\delta\tau_{p-1,p-1,q}^{\mathrm{l+,u+}} = \tau_{p-1,q}^{\mathrm{u+}} - \tau_{p-1,q}^{\mathrm{l+}} \quad \left(= -\delta\tau_{p-1,p-1,q}^{\mathrm{u+,l+}}\right), \tag{6.45}$$

$$\delta\tau_{p-1,p,q}^{\mathrm{l+,u-}} = \tau_{p,q}^{\mathrm{u-}} - \tau_{p-1,q}^{\mathrm{l+}}, \tag{6.46}$$

$$\delta\tau_{p-1,p,q}^{\mathrm{l+,l-}} = \tau_{p,q}^{\mathrm{l-}} - \tau_{p-1,q}^{\mathrm{l+}}, \tag{6.47}$$

where (6.45) is greyed out because it is the negative counterpart of (6.42), and is therefore not independent. Finally, with the upper aft redundant array of ping p as the reference, the modelled time delays are

$$\delta\tau_{p,p-1,q}^{\mathrm{u-,u+}} = \tau_{p-1,q}^{\mathrm{u+}} - \tau_{p,q}^{\mathrm{u-}} \quad \left(= -\delta\tau_{p,p-1,q}^{\mathrm{u+,u-}}\right), \tag{6.48}$$

$$\delta\tau_{p,p-1,q}^{\mathrm{u-,l+}} = \tau_{p-1,q}^{\mathrm{l+}} - \tau_{p,q}^{\mathrm{u-}} \quad \left(= -\delta\tau_{p-1,p,q}^{\mathrm{l+,u-}}\right), \tag{6.49}$$

$$\delta\tau_{p,p,q}^{\mathrm{u-,l-}} = \tau_{p,q}^{\mathrm{l-}} - \tau_{p,q}^{\mathrm{u-}}, \tag{6.50}$$

where (6.48) and (6.49) are greyed out because they are the negative counterparts of (6.43) and (6.46) respectively. Time delays where the lower aft redundant array is the reference are not shown, as they are all negative counterparts of the six independent time delay equations above and hence contain no extra information.

6.3.5   Estimation of navigation and bathymetry

The models for inter-array surge, two-way travel time, and time delay between redundant signals are all non-linear. Consequently, estimation of the vehicle path and the location of the control points can be considered to be a problem of data fitting to a non-linear model. The Gauss-Newton algorithm is an iterative optimisation method which requires computation of first-order derivatives of a residual function. It has been chosen because it is particularly well suited to large, highly sparse problems, and those where computation of second order derivatives is expensive.

The standard least-squares Gauss-Newton algorithm operates by iteratively computing

$$\boldsymbol{\chi}^{(i+1)} = \boldsymbol{\chi}^{(i)} - \boldsymbol{J}^{+}\boldsymbol{\Delta}\boldsymbol{\zeta}^{(i)} \tag{6.51}$$

until a suitable convergence criteria is met, where $\boldsymbol{\chi}$ is the vector of parameters to be estimated,

$$\boldsymbol{\Delta}\boldsymbol{\zeta}^{(i)} = \boldsymbol{\zeta} - \widetilde{\boldsymbol{\zeta}}^{(i)} \tag{6.52}$$

is the vector of residuals between the measurements $\boldsymbol{\zeta}$ and the modelled quantities $\widetilde{\boldsymbol{\zeta}}^{(i)}$, and where $\boldsymbol{J}^{+} = \left(\boldsymbol{J}^{\mathrm{T}}\boldsymbol{J}\right)^{-1}\boldsymbol{J}^{\mathrm{T}}$ is the Moore-Penrose pseudoinverse of the Jacobian with $(\cdot)^{\mathrm{T}}$ denot-

ing the matrix transpose. The elements of the Jacobian indexed by m, n are given by

$$J_{m,n} = \frac{\partial \mathbf{\Delta}\boldsymbol{\zeta}_m^{(i)}}{\partial \boldsymbol{\chi}_n^{(i)}} \tag{6.53}$$

which are the first order derivatives of the residual computed at the current estimate.

In the current application it is desirable to introduce a weighting into the pseudoinverse, such that measurements with higher coherence and hence precision have greater influence. This is achieved by altering (6.51) to the iterative weighted least-squares expression

$$\boldsymbol{\chi}^{(i+1)} = \boldsymbol{\chi}^{(i)} - (\boldsymbol{W}^{1/2}\boldsymbol{J})^+\boldsymbol{W}^{1/2}\mathbf{\Delta}\boldsymbol{\zeta}^{(i)} \tag{6.54}$$

where $\boldsymbol{W}$ is a diagonal matrix of weightings.

Implementation

The implementation of the weighted Gauss-Newton method is now a matter of constructing each of the variables in (6.54), and iterating it until a termination criteria is met. The termination criteria may be a test for convergence, or a maximum number of iterations. The iterative nature of the method is indicated in Figure 6.3. In the following we introduce a tilde $\widetilde{\{\cdot\}}$ in order to denote modelled quantities.

For simplicity we consider the problem of a single-sided interferometer where only the upper-fore and lower-fore redundant arrays of each ping pair are used as references for the time delay measurements. That is, only the time delays defined by (6.42 - 6.47) are utilised. In the current implementation, this results in two separate sets of bathymetry estimates corresponding to the two reference arrays. We therefore introduce a post-superscript to each control point location to identify the reference array. This results in the control point location for the pth ping and the qth temporal window using the upper-fore and lower-fore redundant arrays of each ping pair as reference being denoted $\boldsymbol{b}_{p,q}^{\text{u}+}$ and $\boldsymbol{b}_{p,q}^{\text{l}+}$ respectively.

The vector $\boldsymbol{\chi}$ contains estimates of the vehicle location on each ping, and estimates of the location of the control points that represent the coarse bathymetry estimate. It is formed by

$$\boldsymbol{\chi} = \Big(\boldsymbol{x}_1 \ \boldsymbol{x}_2 \ \cdots \ \boldsymbol{x}_{P-1} \ \vdots \ \boldsymbol{b}_{0,0}^{\text{u}+} \ \boldsymbol{b}_{0,1}^{\text{u}+} \ \cdots \ \boldsymbol{b}_{0,Q-1}^{\text{u}+} \ \vdots \ \cdots \ \vdots \ \boldsymbol{b}_{P-1,0}^{\text{u}+} \ \boldsymbol{b}_{P-1,1}^{\text{u}+} \ \cdots \ \boldsymbol{b}_{P-1,Q-1}^{\text{u}+} \ \vdots$$
$$\boldsymbol{b}_{0,0}^{\text{l}+} \ \boldsymbol{b}_{0,1}^{\text{l}+} \ \cdots \ \boldsymbol{b}_{0,Q-1}^{\text{l}+} \ \vdots \ \cdots \ \vdots \ \boldsymbol{b}_{P-1,0}^{\text{l}+} \ \boldsymbol{b}_{P-1,1}^{\text{l}+} \ \cdots \ \boldsymbol{b}_{P-1,Q-1}^{\text{l}+}\Big)^{\text{T}} \tag{6.55}$$

which is the concatenation of the vehicle location estimates for all but the first ping and the control point location estimates for all pings, reference arrays and temporal windows. The vehicle location on the first ping acts as the position reference, and therefore does not appear in the estimate vector.

The residual vector defined in (6.52) is the difference between the measured and modelled

surges, propagation times and time delays. The vector of modelled quantities is formed by

$$\widetilde{\boldsymbol{\zeta}}^{(i)} = \left(\widetilde{\boldsymbol{\nu}}_0 \ \widetilde{\boldsymbol{\nu}}_1 \ \cdots \ \widetilde{\boldsymbol{\nu}}_{P-1} \ \vdots \ \widetilde{\boldsymbol{\tau}}_0^{\mathrm{u}+} \ \widetilde{\boldsymbol{\tau}}_1^{\mathrm{u}+} \ \cdots \ \widetilde{\boldsymbol{\tau}}_{P-1}^{\mathrm{u}+} \ \vdots \ \widetilde{\boldsymbol{\tau}}_0^{\mathrm{l}+} \ \widetilde{\boldsymbol{\tau}}_1^{\mathrm{l}+} \ \cdots \ \widetilde{\boldsymbol{\tau}}_{P-1}^{\mathrm{l}+} \ \vdots \right.$$
$$\left. \widetilde{\boldsymbol{\delta\tau}}_0^{\mathrm{u}+} \ \widetilde{\boldsymbol{\delta\tau}}_1^{\mathrm{u}+} \ \cdots \ \widetilde{\boldsymbol{\delta\tau}}_{P-1}^{\mathrm{u}+} \ \vdots \ \widetilde{\boldsymbol{\delta\tau}}_0^{\mathrm{l}+} \ \widetilde{\boldsymbol{\delta\tau}}_1^{\mathrm{l}+} \ \cdots \ \widetilde{\boldsymbol{\delta\tau}}_{P-1}^{\mathrm{l}+} \right)^{\mathrm{T}} \tag{6.56}$$

in which

$$\widetilde{\boldsymbol{\nu}}_p = \left(\widetilde{\nu}_{p-1,p}^{\mathrm{u,u}} \ \widetilde{\nu}_{p-1,p}^{\mathrm{u,l}} \ \widetilde{\nu}_{p-1,p}^{\mathrm{l,u}} \ \widetilde{\nu}_{p-1,p}^{\mathrm{l,l}} \right) \tag{6.57}$$

contains the four modelled inter-array surges between each ping pair,

$$\widetilde{\boldsymbol{\tau}}_p^{\mathrm{u}+} = \left(\widetilde{\tau}_{p,0}^{\mathrm{u}+} \ \widetilde{\tau}_{p,1}^{\mathrm{u}+} \ \cdots \ \widetilde{\tau}_{p,Q-1}^{\mathrm{u}+} \right) \tag{6.58}$$

and

$$\widetilde{\boldsymbol{\tau}}_p^{\mathrm{l}+} = \left(\widetilde{\tau}_{p,0}^{\mathrm{l}+} \ \widetilde{\tau}_{p,1}^{\mathrm{l}+} \ \cdots \ \widetilde{\tau}_{p,Q-1}^{\mathrm{l}+} \right) \tag{6.59}$$

contain the modelled times of arrival for each control point of the $p-1$ to p ping pair with the upper-fore and lower-fore redundant arrays as reference respectively, and

$$\widetilde{\boldsymbol{\delta\tau}}_p^{\mathrm{u}+} = \left(\widetilde{\delta\tau}_{p-1,p-1,0}^{\mathrm{u}+,\mathrm{l}+} \ \widetilde{\delta\tau}_{p-1,p,0}^{\mathrm{u}+,\mathrm{u}-} \ \widetilde{\delta\tau}_{p-1,p,0}^{\mathrm{u}+,\mathrm{l}-} \ \vdots \ \widetilde{\delta\tau}_{p-1,p-1,1}^{\mathrm{u}+,\mathrm{l}+} \ \widetilde{\delta\tau}_{p-1,p,1}^{\mathrm{u}+,\mathrm{u}-} \right.$$
$$\left. \widetilde{\delta\tau}_{p-1,p,1}^{\mathrm{u}+,\mathrm{l}-} \ \vdots \ \cdots \ \vdots \ \widetilde{\delta\tau}_{p-1,p-1,Q-1}^{\mathrm{u}+,\mathrm{l}+} \ \widetilde{\delta\tau}_{p-1,p,Q-1}^{\mathrm{u}+,\mathrm{u}-} \ \widetilde{\delta\tau}_{p-1,p,Q-1}^{\mathrm{u}+,\mathrm{l}-} \right) \tag{6.60}$$

and

$$\widetilde{\boldsymbol{\delta\tau}}_p^{\mathrm{u}+} = \left(\widetilde{\delta\tau}_{p-1,p-1,0}^{\mathrm{l}+,\mathrm{u}+} \ \widetilde{\delta\tau}_{p-1,p,0}^{\mathrm{l}+,\mathrm{u}-} \ \widetilde{\delta\tau}_{p-1,p,0}^{\mathrm{l}+,\mathrm{l}-} \ \vdots \ \widetilde{\delta\tau}_{p-1,p-1,1}^{\mathrm{l}+,\mathrm{u}+} \ \widetilde{\delta\tau}_{p-1,p,1}^{\mathrm{l}+,\mathrm{u}-} \right.$$
$$\left. \widetilde{\delta\tau}_{p-1,p,1}^{\mathrm{l}+,\mathrm{l}-} \ \vdots \ \cdots \ \vdots \ \widetilde{\delta\tau}_{p-1,p-1,Q-1}^{\mathrm{l}+,\mathrm{u}+} \ \widetilde{\delta\tau}_{p-1,p,Q-1}^{\mathrm{l}+,\mathrm{u}-} \ \widetilde{\delta\tau}_{p-1,p,Q-1}^{\mathrm{l}+,\mathrm{l}-} \right) \tag{6.61}$$

contain the modelled time delays for each control point of the $p-1$ to p ping pair with the upper-fore and lower-fore redundant arrays as reference respectively. The vector of measured quantities takes the same form as (6.56), where the inter-array surges and time delays are measured using the methods in Section 4 and centre of each temporal window defines the known propagation times corresponding to (6.58 - 6.59).

The diagonal weighting matrix $\boldsymbol{W}$ contains SNR estimates corresponding to each surge measurement, time delay measurement, or propagation time, and takes the form

$$\mathrm{diag}\left\{ \boldsymbol{W} \right\} = \left(\boldsymbol{\Omega}_0 \ \boldsymbol{\Omega}_1 \ \cdots \ \boldsymbol{\Omega}_P \ \vdots \ \infty^{1\times Q} \ \infty^{1\times Q} \ \cdots \ \infty^{1\times Q} \ \vdots \right.$$
$$\left. \infty^{1\times Q} \ \infty^{1\times Q} \ \cdots \ \infty^{1\times Q} \ \vdots \ \boldsymbol{\Upsilon}_0^{\mathrm{u}+} \ \boldsymbol{\Upsilon}_1^{\mathrm{u}+} \ \cdots \ \boldsymbol{\Upsilon}_{P-1}^{\mathrm{u}+} \ \vdots \ \boldsymbol{\Upsilon}_0^{\mathrm{l}+} \ \boldsymbol{\Upsilon}_1^{\mathrm{l}+} \ \cdots \ \boldsymbol{\Upsilon}_{P-1}^{\mathrm{l}+} \right)^{\mathrm{T}} \tag{6.62}$$

where

$$\boldsymbol{\Omega}_p = \left(\bar{\Omega}_{p-1,p}^{\mathrm{u,u}} \ \bar{\Omega}_{p-1,p}^{\mathrm{u,l}} \ \bar{\Omega}_{p-1,p}^{\mathrm{l,u}} \ \bar{\Omega}_{p-1,p}^{\mathrm{l,l}} \right) \tag{6.63}$$

are the SNR estimates corresponding to the inter-array surge estimates, where each element is

115

the mean SNR estimate over all temporal windows. For the upper-fore to upper-aft array pair, this is given by

$$\bar{\Omega}^{u,u}_{p-1,p} = \sum_{0}^{Q-1} \Omega^{u,u}_{p-1,p,q}, \tag{6.64}$$

and the other redundant array pairs take the same form. The $\infty^{1\times Q}$ vectors enforce the given propagation times for each reference array, since these are chosen by the selection of the temporal windows. In practice, infinite weightings cause implementation issues, so a large finite value of e.g. $100\,\text{dB}$ is used instead [1]. The remaining components of $\boldsymbol{W}$ are the SNR estimates corresponding to the time delays measured between redundant signals, with

$$
\boldsymbol{\Upsilon}^{u+}_p = \Big(\Upsilon^{u+,l+}_{p-1,p-1,0} \quad \Upsilon^{u+,u-}_{p-1,p,0} \quad \Upsilon^{u+,l-}_{p-1,p,0} \ \vdots\ \Upsilon^{u+,l+}_{p-1,p-1,1} \quad \Upsilon^{u+,u-}_{p-1,p,1}
$$
$$
\Upsilon^{u+,l-}_{p-1,p,1} \ \vdots\ \cdots\ \vdots\ \Upsilon^{u+,l+}_{p-1,p-1,Q-1} \quad \Upsilon^{u+,u-}_{p-1,p,Q-1} \quad \Upsilon^{u+,l-}_{p-1,p,Q-1} \Big) \tag{6.65}
$$

and

$$
\boldsymbol{\Upsilon}^{l+}_p = \Big(\Upsilon^{l+,u+}_{p-1,p-1,0} \quad \Upsilon^{l+,u-}_{p-1,p,0} \quad \Upsilon^{l+,l-}_{p-1,p,0} \ \vdots\ \Upsilon^{l+,u+}_{p-1,p-1,1} \quad \Upsilon^{l+,u-}_{p-1,p,1}
$$
$$
\Upsilon^{l+,l-}_{p-1,p,1} \ \vdots\ \cdots\ \vdots\ \Upsilon^{l+,u+}_{p-1,p-1,Q-1} \quad \Upsilon^{l+,u-}_{p-1,p,Q-1} \quad \Upsilon^{l+,l-}_{p-1,p,Q-1} \Big) \tag{6.66}
$$

containing the SNR estimates with the upper-fore and lower-fore arrays as reference respectively.

The elements of the Jacobian of the residual function $\boldsymbol{J}$ are each given by (6.53), which can be expanded as

$$\boldsymbol{J}_{m,n} = \frac{\partial \boldsymbol{\Delta\zeta}^{(i)}_m}{\partial \boldsymbol{\chi}^{(i)}_n} \tag{6.67}$$

$$= \frac{\partial \boldsymbol{\zeta}_m}{\partial \boldsymbol{\chi}^{(i)}_n} - \frac{\partial \widetilde{\boldsymbol{\zeta}}^{(i)}_m}{\partial \boldsymbol{\chi}^{(i)}_n} \tag{6.68}$$

$$= -\frac{\partial \widetilde{\boldsymbol{\zeta}}^{(i)}_m}{\partial \boldsymbol{\chi}^{(i)}_n}, \tag{6.69}$$

that is, each element is the negative of the derivative of the model with respect to the relevant parameter (since $\partial \boldsymbol{\zeta}_m / \partial \boldsymbol{\chi}^{(i)}_n = 0$ for all m and n). In this application the Jacobian is highly sparse, and the location of the non-zero elements can be inferred by analysis of the model equations. The values of the non-zero elements can be computed analytically by differentiating (6.8-6.11), (6.32-6.35) and (6.42-6.50). Alternatively, the non-zero elements can be calculated numerically, or by automatic differentiation e.g. [143].

Formation and solution of (6.54) is performed iteratively until a termination criterion is met, as pictured in Figure 6.3. The termination iteration number is denoted I and the resulting estimate vector is therefore denoted $\boldsymbol{\chi}^{(I)}$, from which the vehicle path and the location of the control points are extracted. The control point locations are converted to a coarse bathymetry estimate at the image resolution by linear interpolation. At this point, estimates of the vehicle position on each ping and a coarse estimate of the sea-floor depth at each pixel are available.

116

SAS images from each array can now be focused onto the coarse bathymetry using a time-domain back-projection algorithm. The imaging algorithm should obey the same geometrical models as those used for navigation estimation, which in this case means avoiding the phase centre or stop-and-hop approximations.

The SAS images from the interferometric arrays are well registered when the bathymetry estimates are sufficiently accurate. This allows the bathymetry estimate to be refined using conventional interferometric techniques without requiring prior co-registration.

A note on the optimisation scale It is worthwhile to consider the scale of the optimisation problem, as this is a criteria which helps in the selection of a suitable optimisation strategy when implementing the new method. The number of parameters in the estimate vector is

$$N_{\text{estimates}} = (P - 1) \times (3 + 2QN_{\text{ref}}) \tag{6.70}$$

where N_{ref} is the number of reference arrays (and hence control points per temporal window). For example, a system with usable swath of 125 m with control points every 0.5 m using two arrays as reference makes ≈ 1000 estimates for each ping pair. The number of measurements is given by

$$N_{\text{measurements}} = (P - 1) \times (QN_{\text{ref}} + 3QN_{\text{ref}}), \tag{6.71}$$

which is ≈ 2000 per ping pair for the same system. The size of the Jacobian grows exponentially with the number of ping pairs[11], and a large scale optimisation method that performs sparse matrix algebra is likely to be required in practice. Since the Moore-Penrose pseudoinverse of a sparse matrix is not in general sparse, it is unsuitable for inverting very large Jacobians. However, the expression in (6.54) can be altered to utilise a sparse linear optimisation method instead of the Moore-Penrose pseudoinverse to avoid this implementation problem.

6.4   Results: Experimental data

In this section, experimental results using the simultaneous micro-navigation and bathymetry estimation algorithm are presented. The experimental data was collected by the dual-sided 270-330 kHz InSAS [31] of the MUSCLE AUV during the MANEX 2014 sea trial. The sea-trial was hosted on the Ligurian coast of Northern Italy, near the towns of Framura and Bonassola shown in Figure 5.6.

The upper and lower receiver arrays of the MUSCLE SAS have 36 and 12 elements respectively, spaced 33 mm apart (resulting in total receiver array lengths of 1.2 m and 0.4 m) [54]. In the following we consider only data from the central 12 elements of the upper array that overlap with the lower array, since most interferometric SAS systems have arrays of equal length. The vehicle speed is approximately $1.5 \, \text{m s}^{-1}$ and the PRF is 10 Hz, which corresponds to an advance per ping of 0.15 m. This results in approximately three overlapping phase centres

---

[11]For illustration, with 100 ping pairs the Jacobian in the example would consume ≈ 160 GB stored as a full, double-precision floating point number, compared to ≈ 1.6 GB for 10 ping pairs.
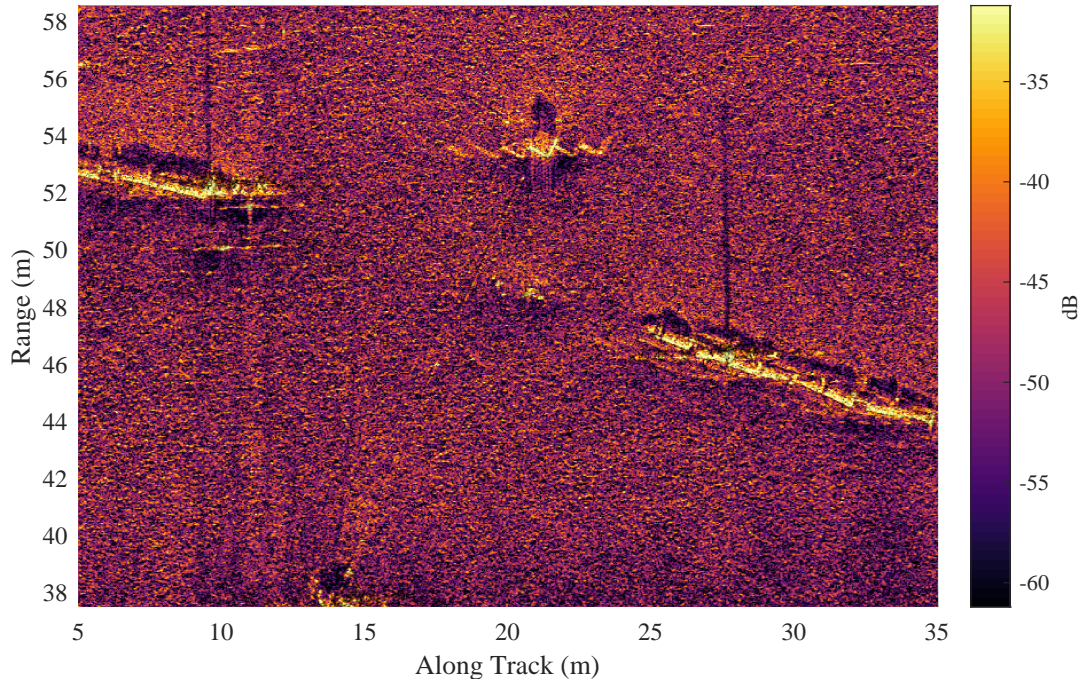
Figure 6.6: A slant-plane SAS image of the scene of interest formed using the navigation estimate from the slant-plane RPC micro-navigation algorithm. Sections of pipe and a concrete block are visible, surrounded by a relatively flat and featureless sea-floor.

between adjacent pings to be used for through-the-sensor navigation estimation. The vehicle navigation hardware comprises an INS, DVL, global positioning system receiver, and a pressure sensor for depth measurement.

The sea-floor in the surveyed area is gently sloping, with a depth of approximately 30 m. The vehicle was programmed to traverse a linear track with targets of opportunity (a pipe and concrete blocks) at approximately 50 m range. Figure 6.6 shows a SAS image of the region of interest formed using the slant-plane RPC micro-navigation algorithm. The image is relatively well focused, but it contains replica targets which are indicative of a quadratic phase error, characteristic of an along-track velocity bias or an error in the assumed speed of sound.

6.4.1 Application of the new method

The simultaneous micro-navigation and bathymetry estimation algorithm has been applied to the 250 pings corresponding to the scene of interest. Three estimates of navigation and bathymetry have been made:

- using through-the-sensor measurements from the port side InSAS only,

- using through-the-sensor measurements from the starboard side InSAS only,

- using through-the-sensor measurements from both InSAS systems simultaneously.

A constant sound speed of $1500\,\mathrm{m\,s^{-1}}$ has been assumed in the method, and the vehicle orientation in roll, pitch and heading is measured by the INS.

Inter-array surge measurements and associated coherences are shown in Figures 6.7 and 6.8 for the port and starboard sides respectively, where each row corresponds to one of the four redundant array pairs formed between adjacent pings. These measurements of inter-array surge do not appear to have a strong range dependence as expected, but do appear to vary around bright targets, particularly for the upper-fore/lower-aft and lower-fore/upper-aft pairings.

Time delay measurements between redundant signals and their corresponding coherences are shown in Figures 6.9 and 6.10 for the port and starboard sides respectively. Consider the time delays on the port side shown in Figure 6.9. The upper row (Figures 6.9a and 6.9b) shows the time delays and coherences between the upper and lower arrays within the first ping of each pair. The middle row (Figures 6.9c and 6.9d) shows the time delays and corresponding coherences between redundant signals from the upper arrays of adjacent pings. The bottom row (Figures 6.9c and 6.9d) shows the time delays and corresponding coherences between the signals received by the upper and lower arrays of adjacent pings. Figure 6.9a shows significant variation in time delay with range and an oscillation in the along-track direction. These variations are predominantly caused by (and therefore contain information about) the depth difference between the sensor and the sea-floor and vehicle roll, respectively, and are conventionally used to estimate bathymetry. Figure 6.9c has little variation with range, and varies slowly in the along-track direction. This along-track variation is predominantly caused by a combination of inter-ping sway and roll. These measurements are the ones conventionally used in slant plane RPC micro-navigation. Figure 6.9e has variations common to the previous two Figures. This is because it includes information about vehicle sway, heave and roll, and sea-floor bathymetry. The coherences shown in Figures 6.9b, 6.9d and 6.9f are sufficiently high to expect high-precision time delay estimates. The corresponding measurements on the starboard side in Figure 6.10 follow a similar pattern.

These measurements are inputs to the simultaneous micro-navigation and bathymetry estimation algorithm, which iteratively minimises the difference between the measurements and the corresponding modelled quantities. For the bilateral case, the weighted sum of the squared residuals for surge, propagation time and time delay as a function of iteration number are shown in Figure 6.11, showing that in this application the algorithm converges in less than 6 iterations.

Figure 6.12a shows the weighted least-squares inter-array surge estimate between all redundant array pairs for each ping pair on both sides of the vehicle. The modelled inter-array surges after 6 iterations are plotted for comparison. The least-squares inter-array surge measurements agree well with each other and the model after 6 iterations. Figure 6.12b shows the surge rate measured by the DVL, which is severely quantised and imprecise (note that the y axis is scaled to 10 times that in Figure 6.12a). The DVL measurements show an offset of approximately $6\,\mathrm{mm}$ per ping compared to the measurements derived from the SAS, which could be caused by a crabbing vehicle motion. However it is not possible to attribute this disparity to either sensor due to the absence of ground-truth.

119

(a) Upper-fore/upper-aft

(b) Upper-fore/upper-aft

(c) Upper-fore/lower-aft

(d) Upper-fore/lower-aft

(e) Lower-fore/upper-aft

(f) Lower-fore/upper-aft

(g) Lower-fore/lower-aft
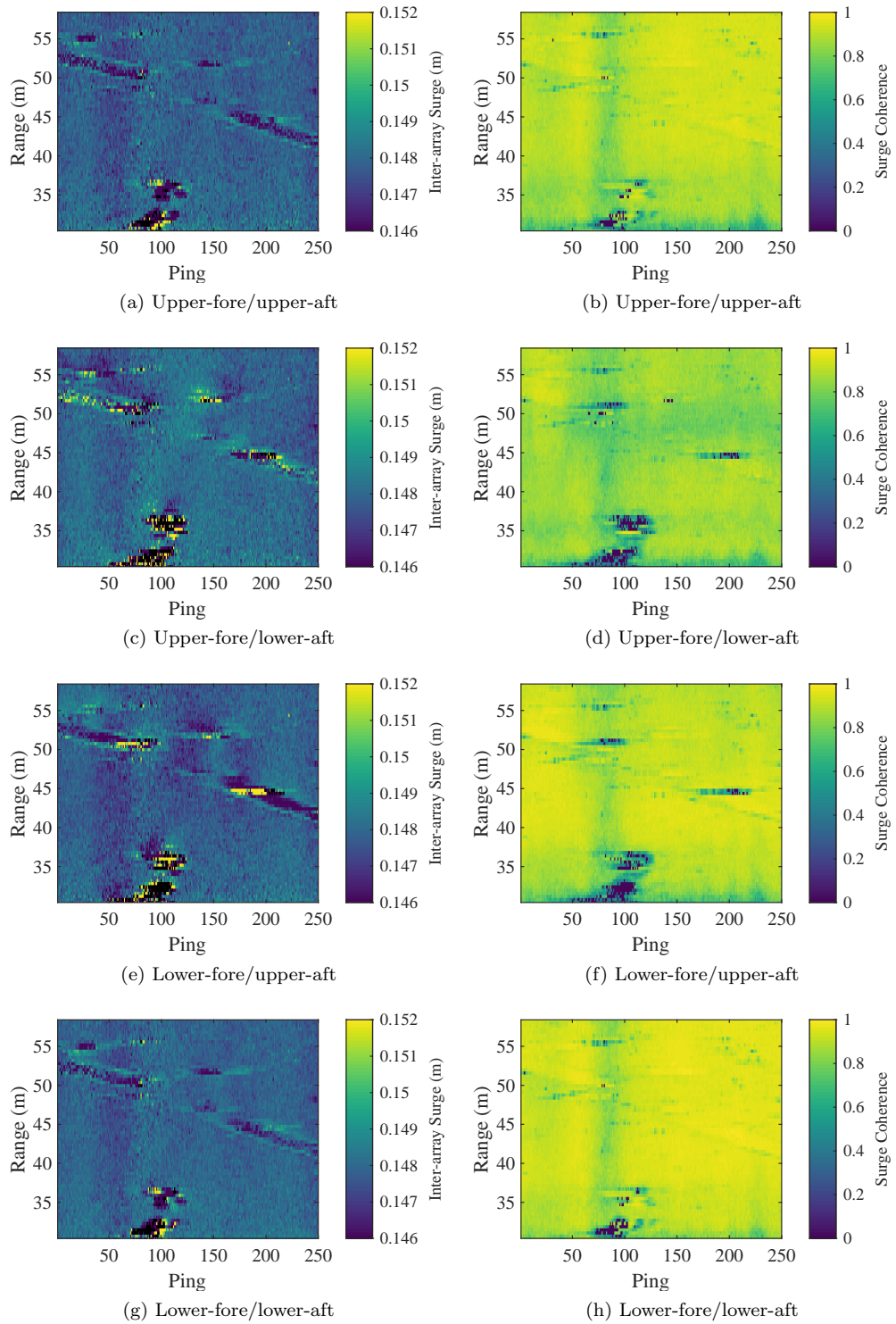
(h) Lower-fore/lower-aft

Figure 6.7: (a,c,e,g) Surge measurements and (b,d,f,h) corresponding coherence estimates between the four pairs of redundant arrays for 250 pings on the port side.
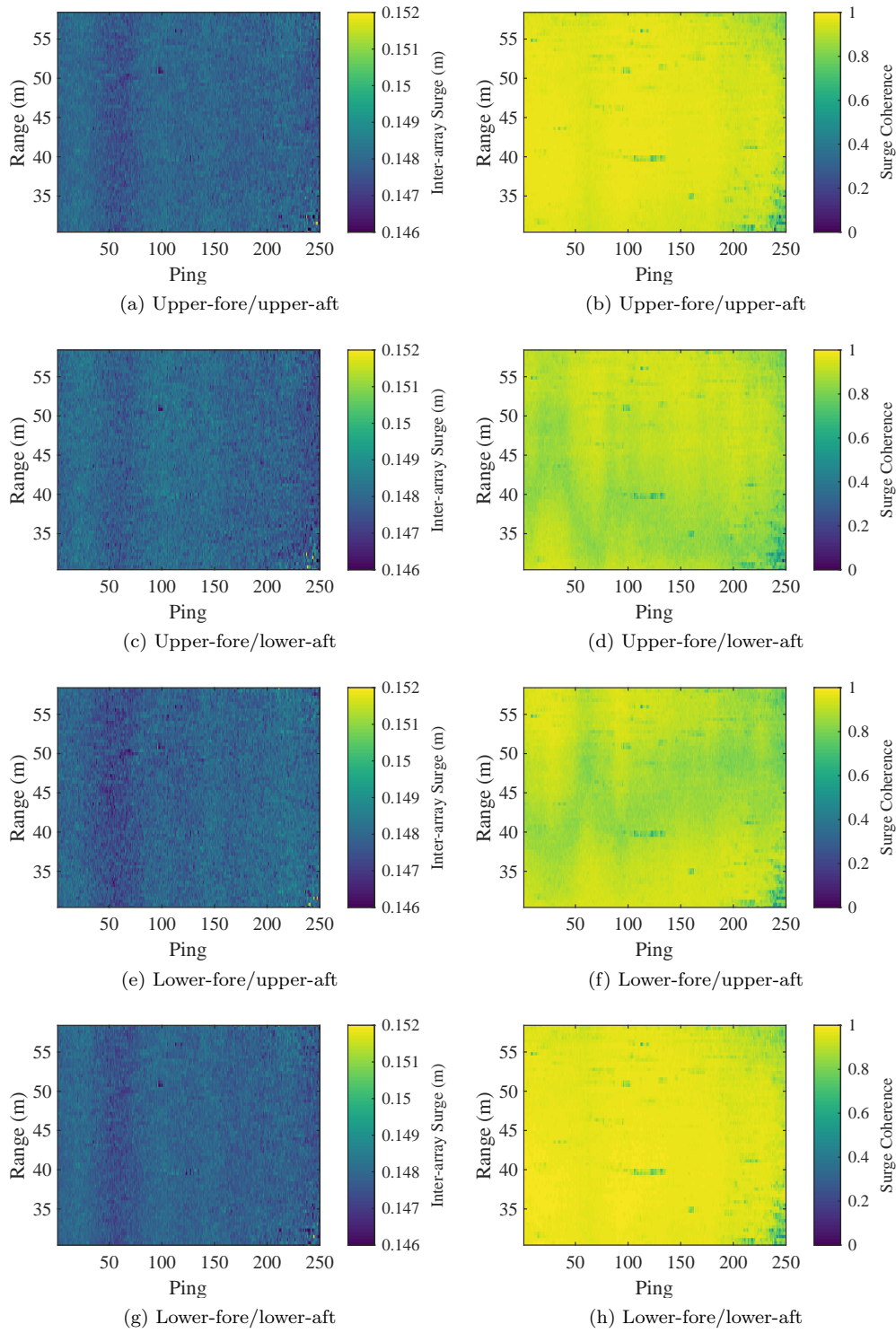
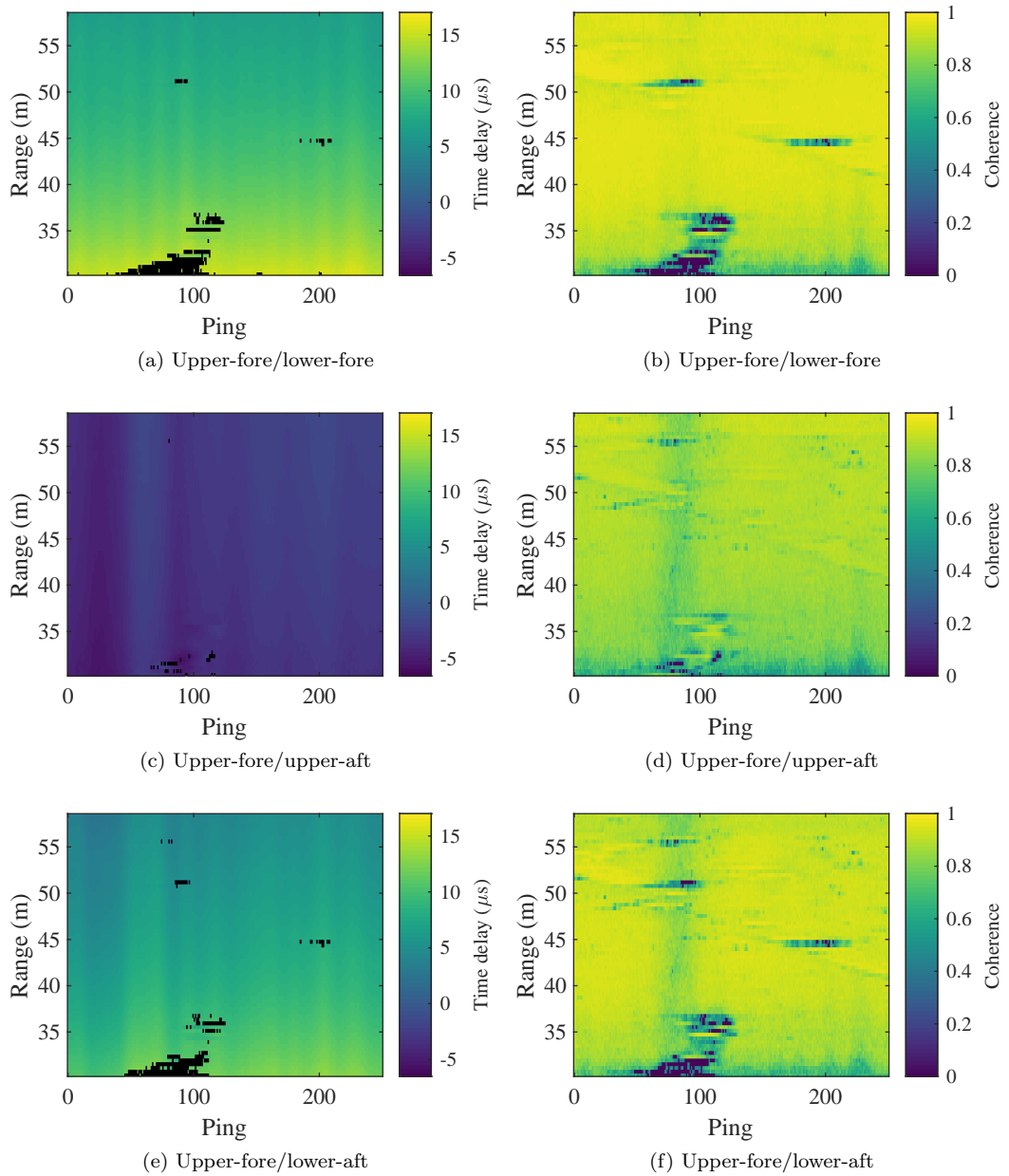(a) Upper-fore/upper-aft

(b) Upper-fore/upper-aft

(c) Upper-fore/lower-aft

(d) Upper-fore/lower-aft

(e) Lower-fore/upper-aft

(f) Lower-fore/upper-aft

(g) Lower-fore/lower-aft

(h) Lower-fore/lower-aft

Figure 6.8: (a,c,e,g) Surge measurements and (b,d,f,h) corresponding coherence estimates between the four pairs of redundant arrays for 250 pings on the starboard side.

Figure 6.9: (a,c,d) Time delays and (b,d,f) corresponding coherences between redundant signals with the upper-fore array of each ping pair as reference, on the port side. The rows correspond to the three possible redundant array pairs; (a,b) upper-fore to lower-fore, (c,d) upper-fore to upper-aft, (e,f) upper-fore to lower-aft.

122

(a) Upper-fore/lower-fore

(b) Upper-fore/lower-fore

(c) Upper-fore/upper-aft

(d) Upper-fore/upper-aft

(e) Upper-fore/lower-aft

(f) Upper-fore/lower-aft
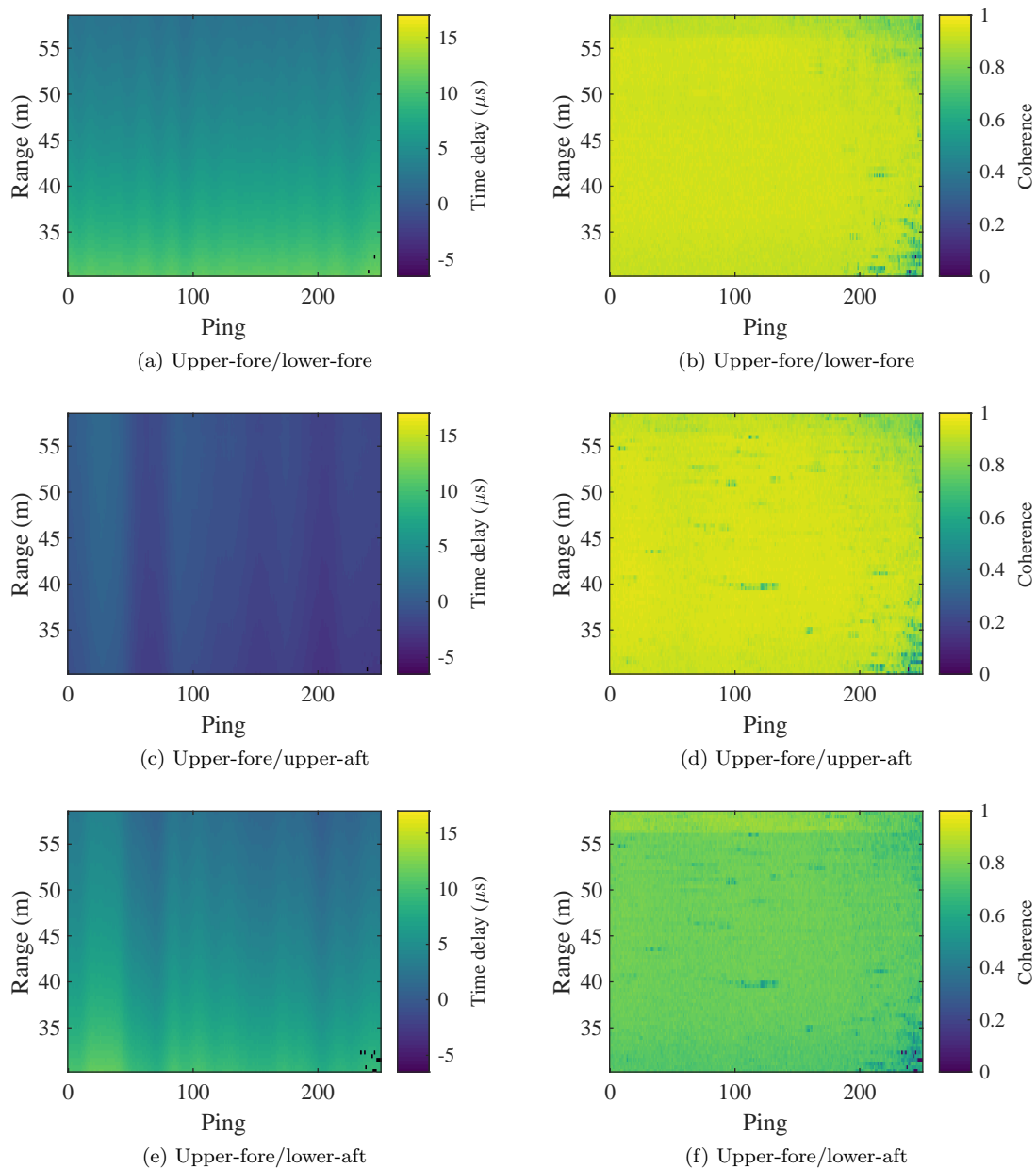
Figure 6.10: (a,c,d) Time delays and (b,d,f) corresponding coherences between redundant signals with the upper-fore array as reference, on the starboard side. The rows correspond to the three possible redundant array pairs; (a,b) upper-fore to lower-fore, (c,d) upper-fore to upper-aft, (e,f) upper-fore to lower-aft.
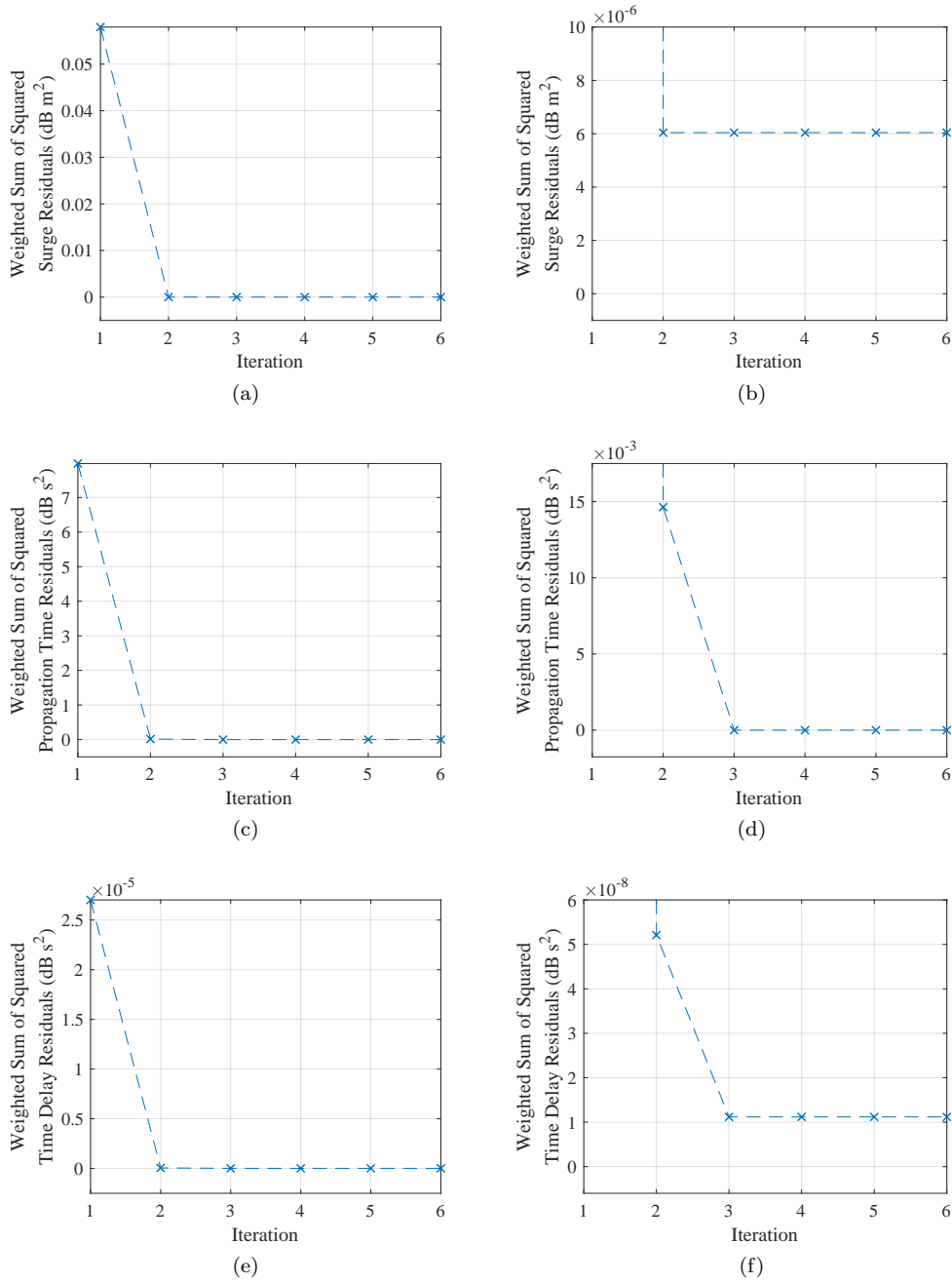
Figure 6.11: The weighted sum of all squared residuals as a function of iteration number for (a,b) inter-array surge, (c,d) propagation delay, and (e,f) time delay, for the bilateral application of the method. The right column has a magnified vertical axis. These plots show that the method converges within 6 iterations in this application.
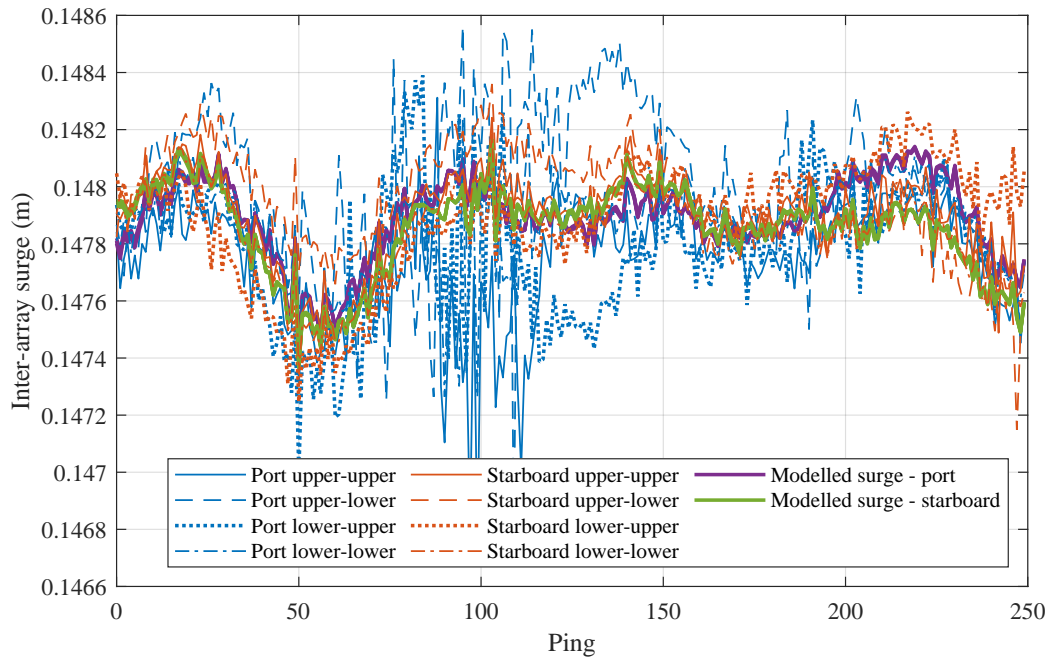
(a)
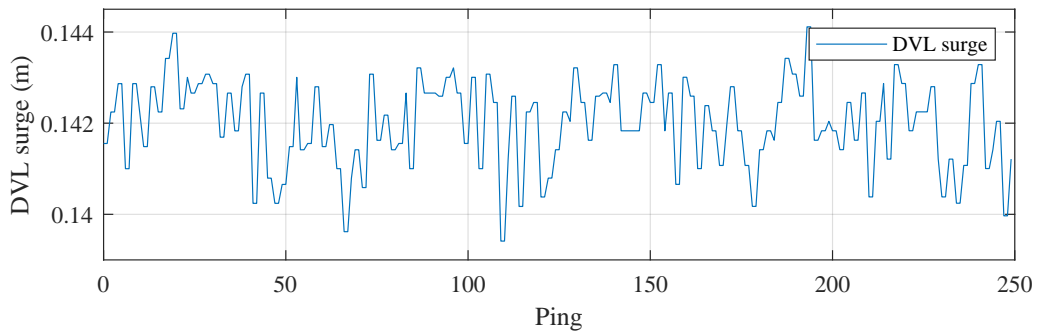
(b)

Figure 6.12: (a) Weighted least-squares inter-array surge measured between all redundant array pairs on both sides of the vehicle. The modelled inter-array surges at convergence is also shown, which agrees well with the measurements. (b) Inter-ping vehicle surge measured by the DVL. There is a constant offset of $\approx 6\,\mathrm{mm}$ per ping between the surge measured using the SAS data and using the DVL.
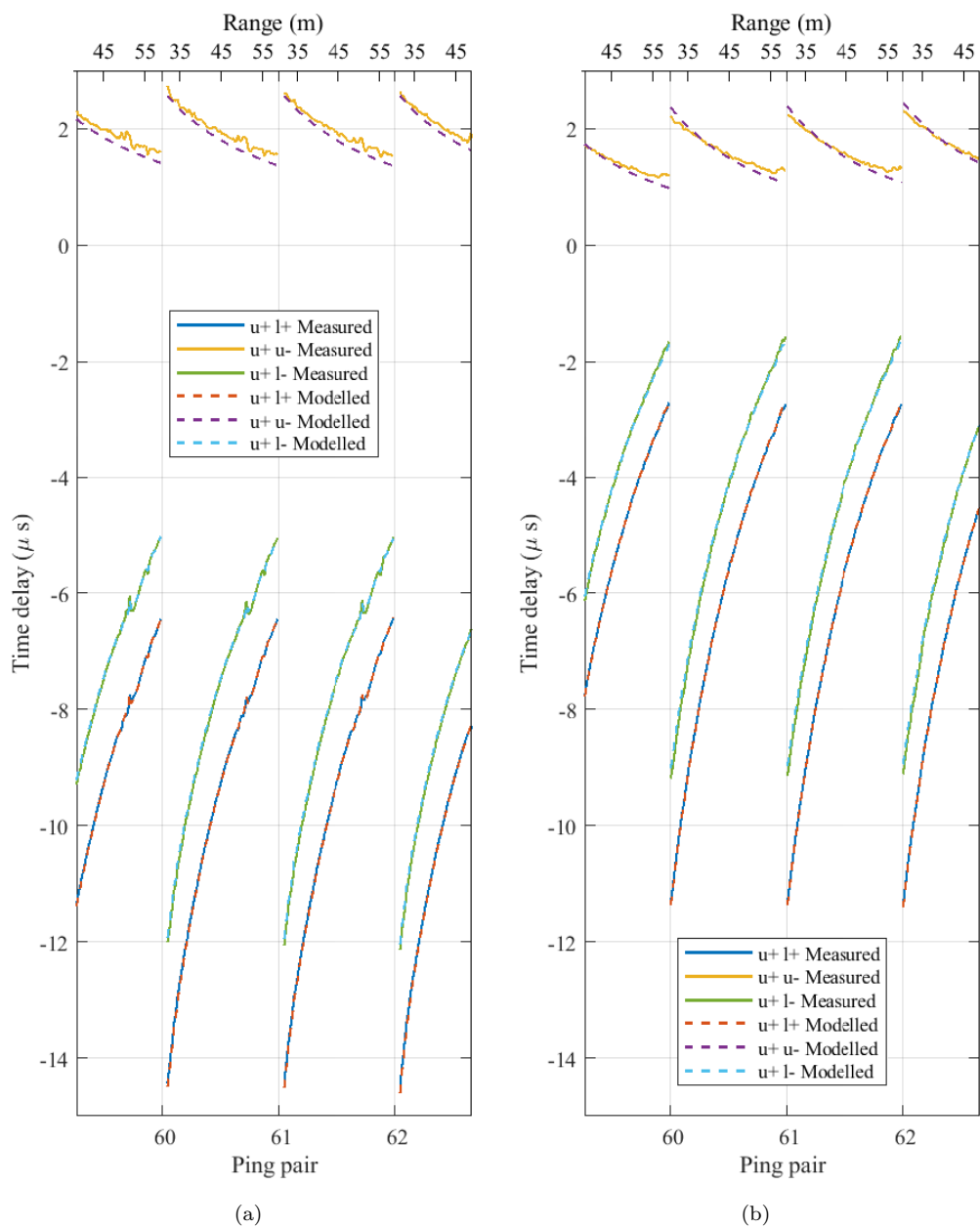
Figure 6.13: Measured time delays between redundant signals for a small subset of pings. The modelled time delays on the final iteration are also shown in dashed lines, which match the measurements very closely. (a) Port side. (b) Starboard side.
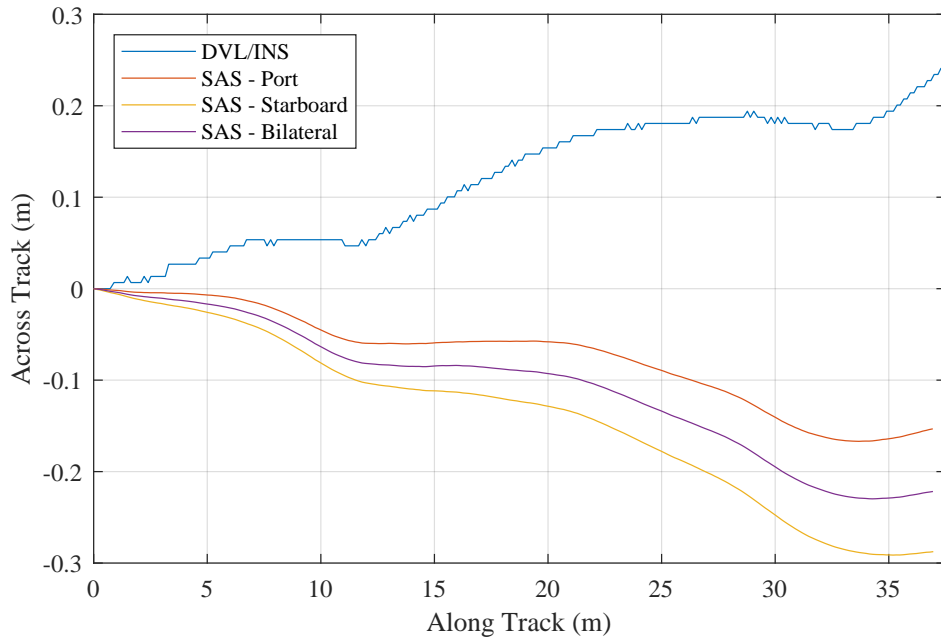
(a)
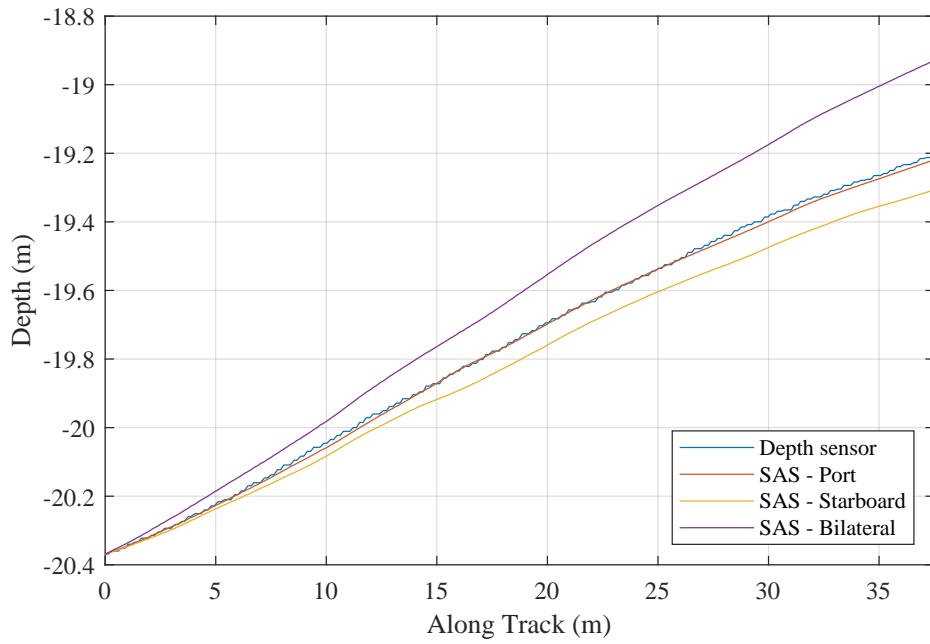
(b)

Figure 6.14: (a) Vehicle track estimated by the vehicle navigation hardware and the new method. (b) Vehicle depth measured by the depth sensor and estimated by the new method.
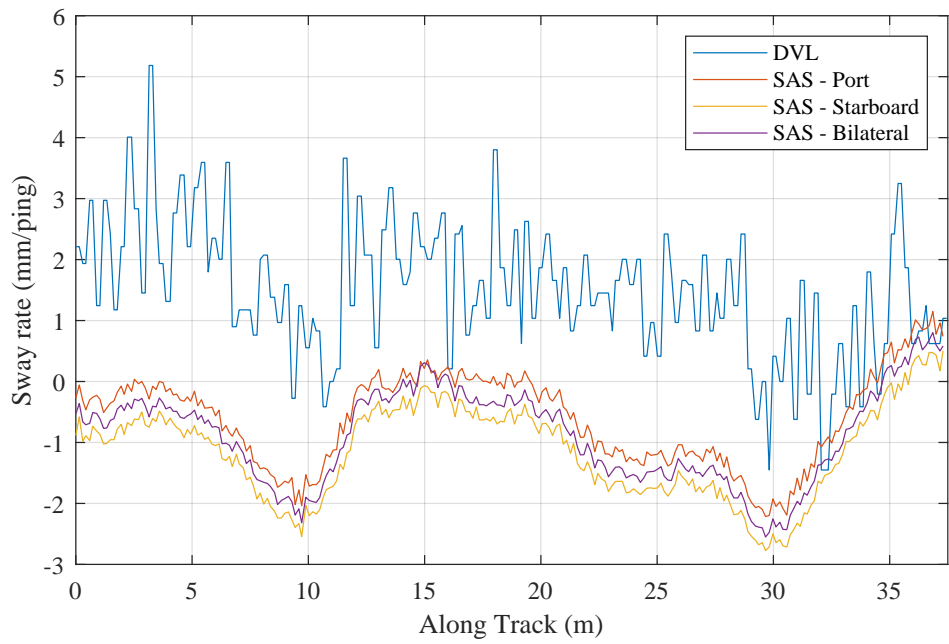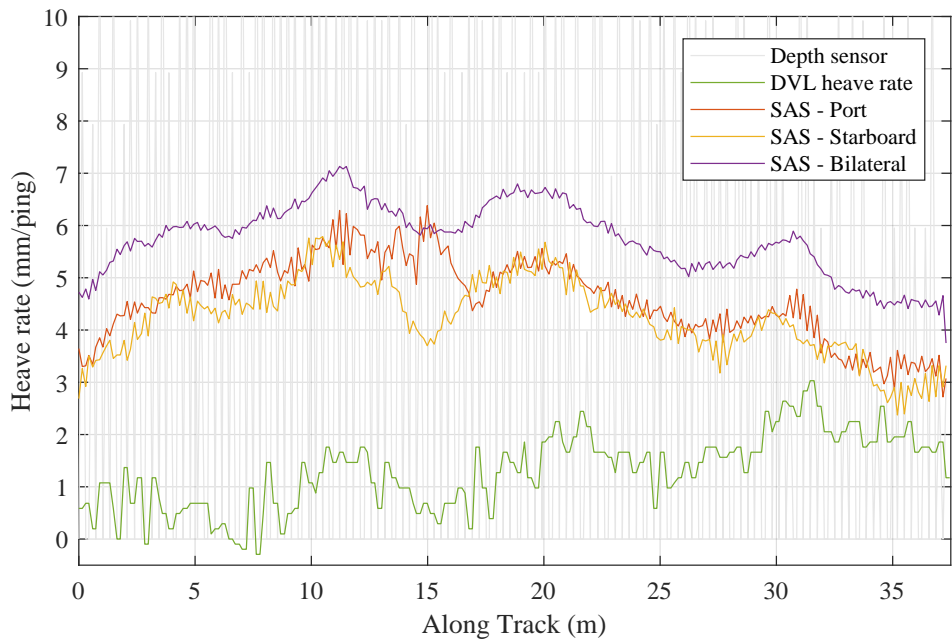
Figure 6.15: (a) The sway rate measured by the DVL and estimated by the new method (b) The vehicle heave rate measured by the depth sensor, the DVL, and estimated by the new method.
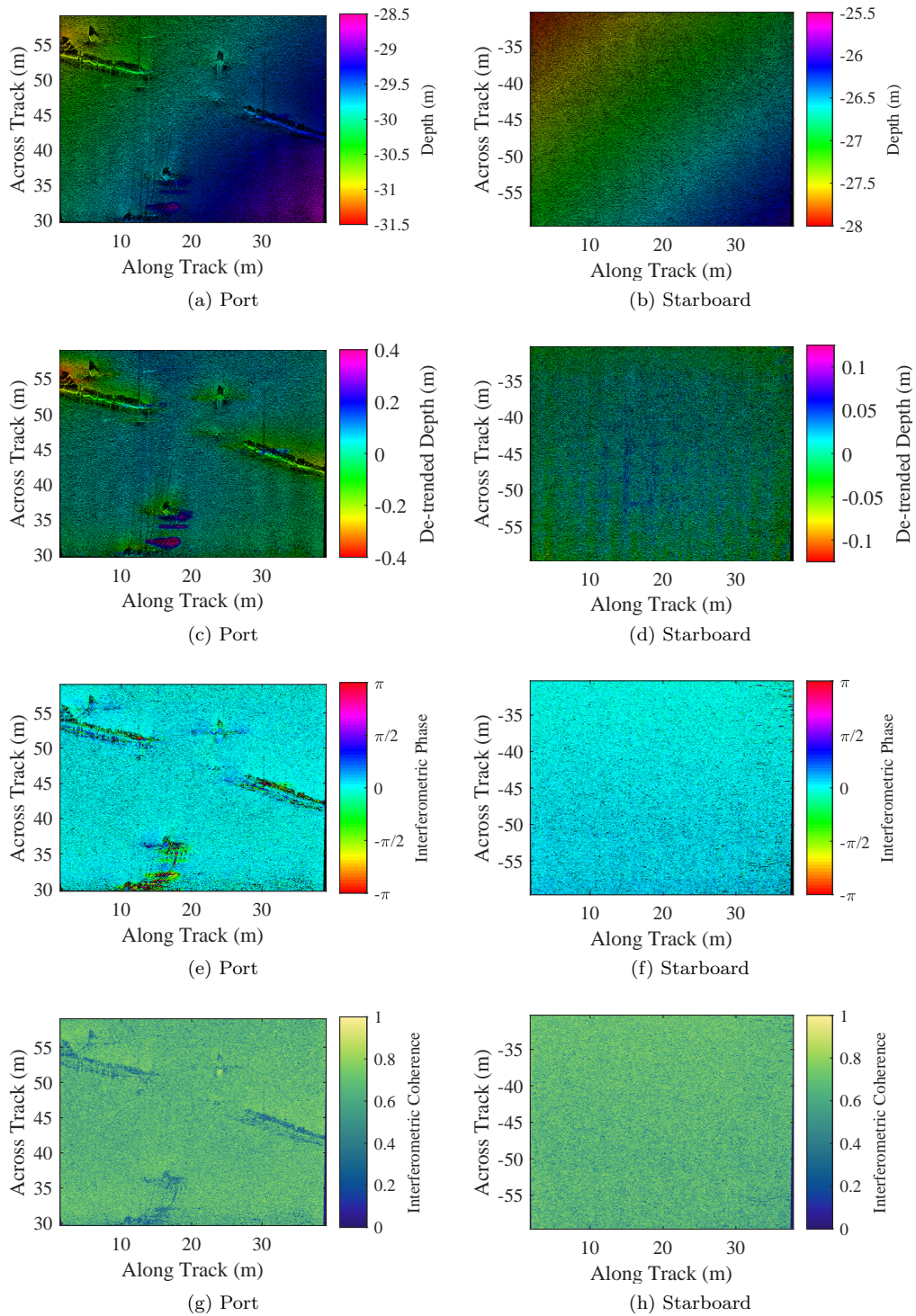
Figure 6.16: (a,b) Fusion of coarse bathymetry estimated by the new method and image intensity. (c,d) Deviation of coarse bathymetry from best-fitting plane. (e,f) Interferometric phase. (g,h) Interferometric coherence.
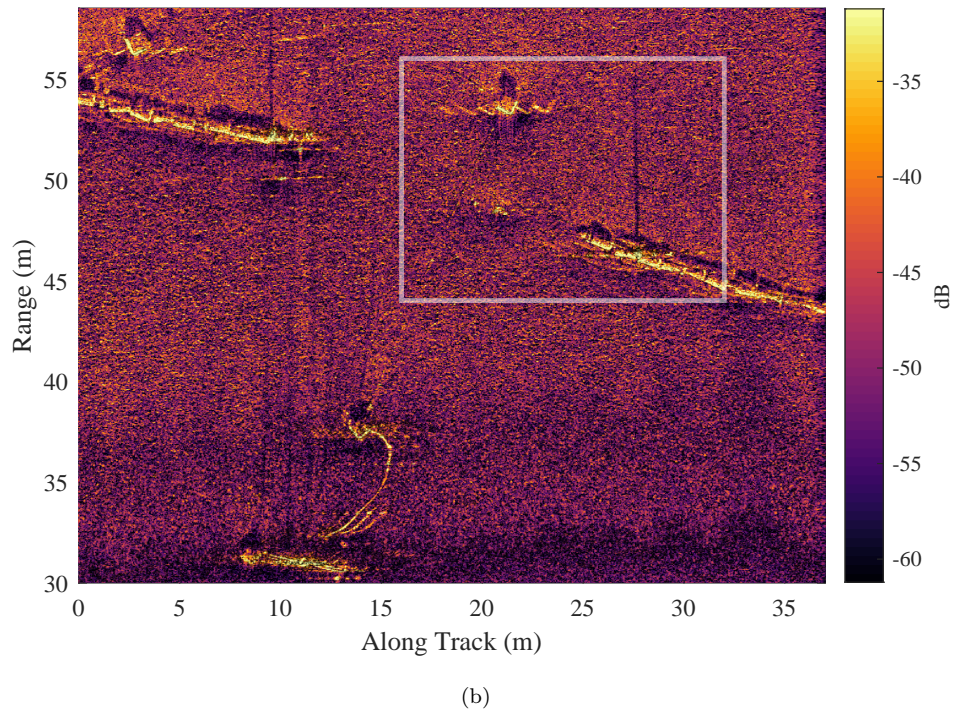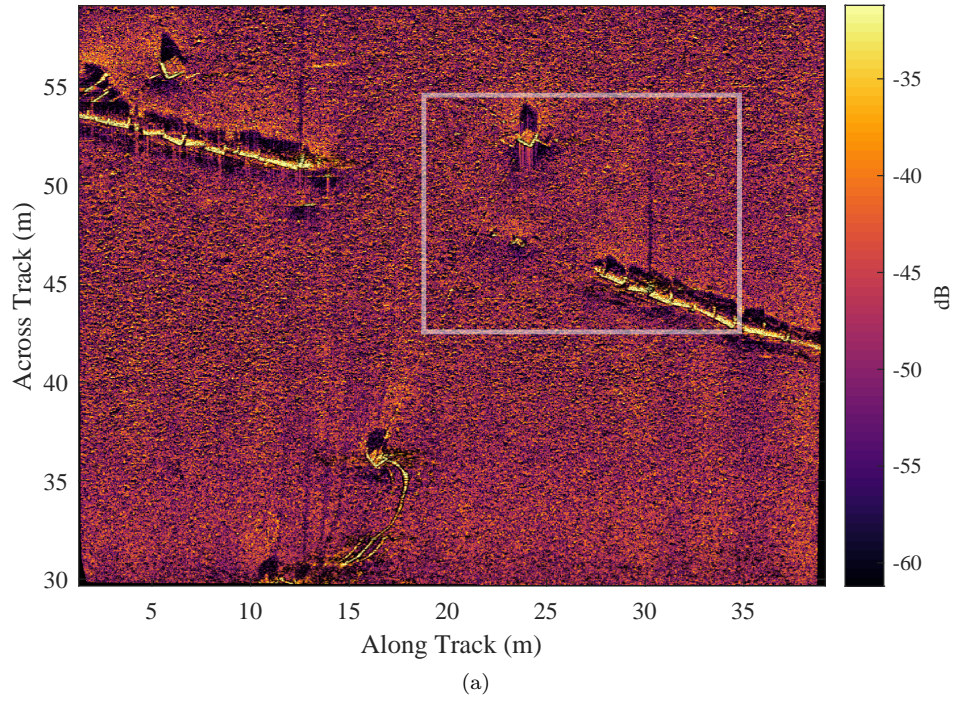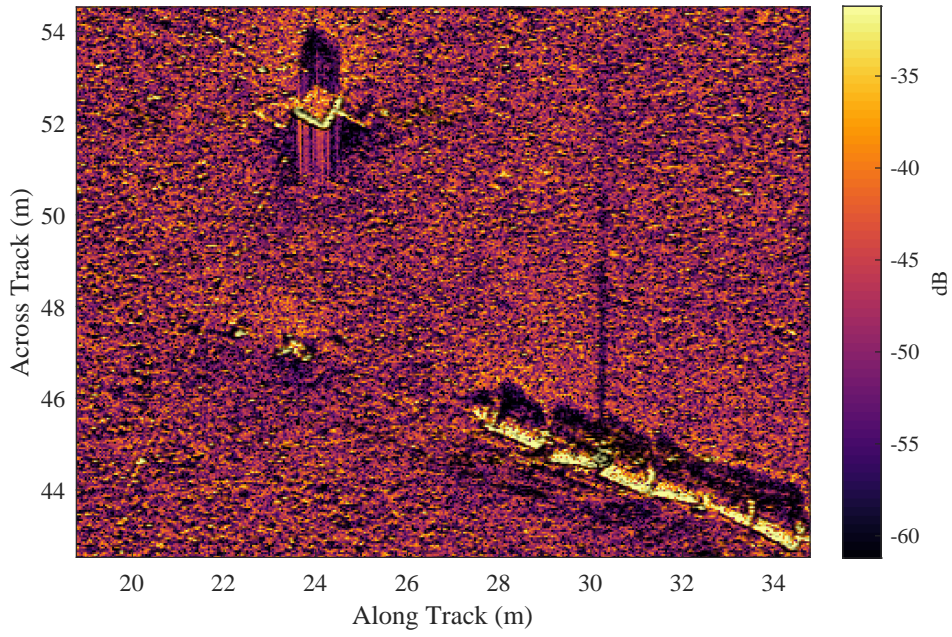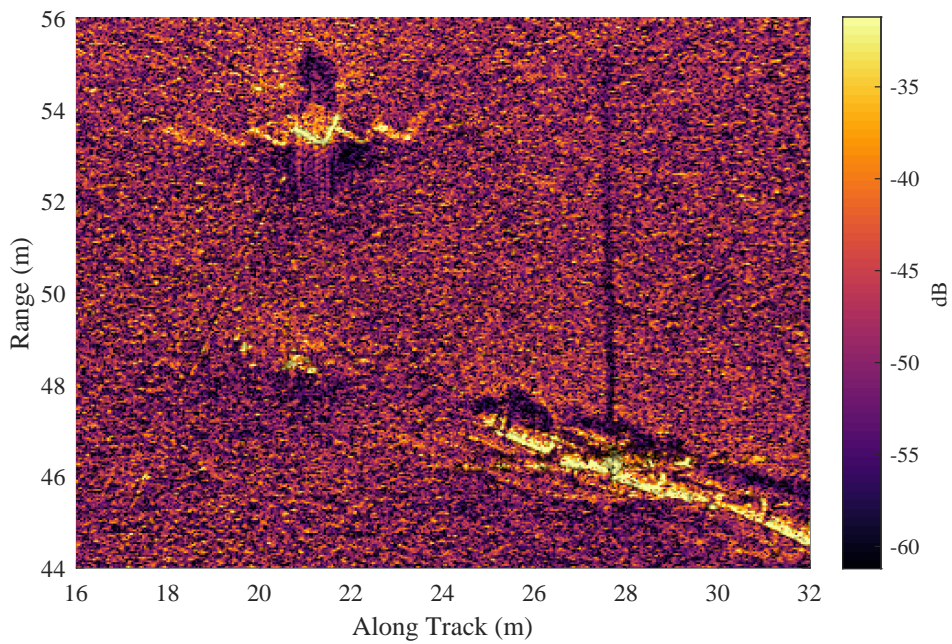
129

Figure 6.17: SAS images from the port side of the vehicle, focused using (a) the navigation and bathymetry estimates from the new method, and (b) the slant-plane RPC micro-navigation algorithm. The boxes indicate sections selected for closer inspection in Figure 6.18.

Figure 6.18: Zooms of SAS images from the port side of the vehicle, focused using (a) the navigation and bathymetry estimates from the new method, and (b) the slant-plane RPC micro-navigation algorithm. While the concrete block and pipe sections are not completely free from replicas in (a), the image contrast and overall quality is considerably improved over (b).
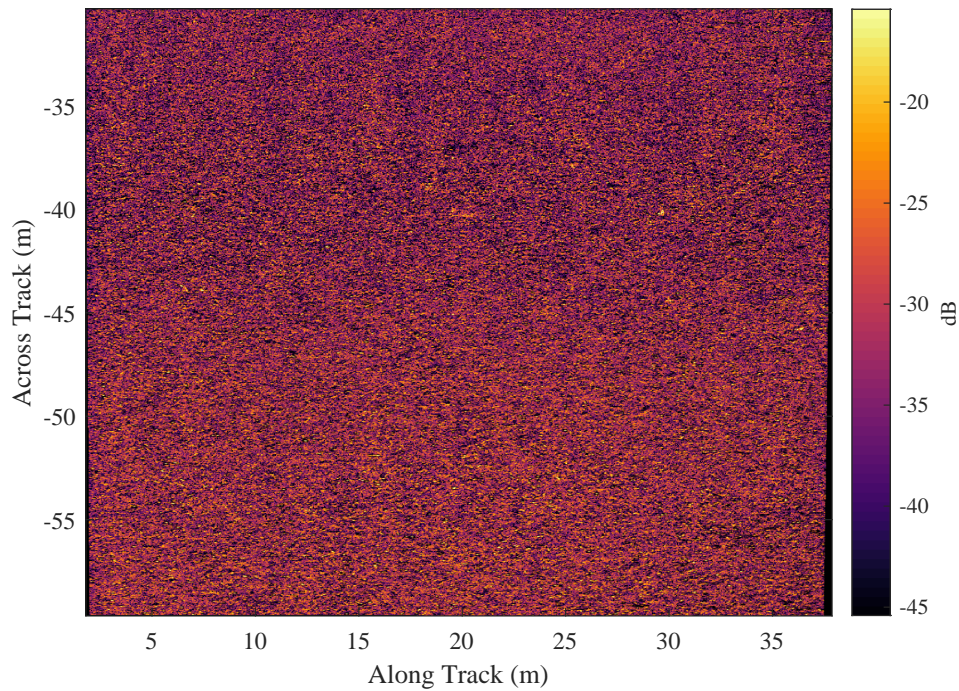
Figure 6.19: SAS image from the starboard side of the vehicle, focused using the navigation and bathymetry estimates from the new method. The scene consists of a flat, sandy sea-floor.

A subset of the time delay measurements from the port and starboard sides are shown in Figure 6.13. The modelled time delays after 6 iterations of the bilateral simultaneous navigation and bathymetry estimation are also plotted, which shows good agreement with the measurements. However, there is some discrepancy between the measurements and model for the time delay between the same arrays of adjacent pings. This suggests that there are relevant parameters which do not appear in the estimate vector, such as array calibration and the speed of sound. Including these parameters in the model could further reduce the residual between the measurements and the modelled quantities.

The resulting navigation estimates are compared in Figure 6.14. Figure 6.14a shows the vehicle path estimates from both the on-board navigation hardware and the new method. Figure 6.15a shows the corresponding across-track motion per ping. All of the navigation estimates exhibit a similar overall shape, although the navigation hardware estimate is severely quantised. The navigation estimates generated from the port and starboard sides independently are not identical, and the navigation estimate estimated using both sides of the vehicle lies between them. The difference appears to be caused by a constant sway rate offset, which could be explained by an array misalignment of as little as 0.1 degrees between the port and starboard arrays.

The vehicle depth estimates made by the pressure sensor and the new method are shown in Figure 6.14b with the corresponding heave per ping shown in 6.15b. The vehicle depth estimated by the pressure sensor is severely quantised, while the estimates made by the new
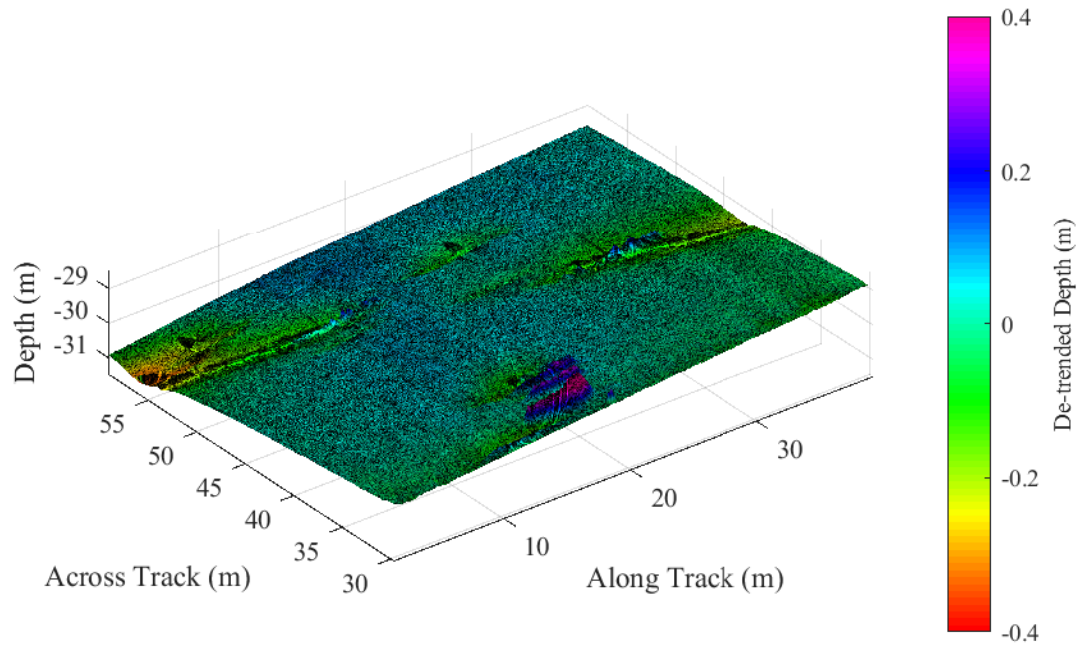
Figure 6.20: The port side coarse bathymetry estimate from the dual-sided navigation and coarse bathymetry estimation algorithm. Colour encodes deviation from the best-fitting plane, and the intensity encodes the SAS image intensity.

method vary smoothly but are not identical. In this case the heave rate estimated by the new method using both sides simultaneously is larger than those estimated using the individual sides independently. This is suggestive of an error in the assumed speed of sound propagation through the medium.

Figure 6.16 shows the bathymetry estimates made by the new method and the resulting interferometric phase and coherence on each side of the vehicle. Figures 6.16a and 6.16b combine information about the scene intensity and the estimated bathymetry. A sloping bathymetry is seen on both sides of the vehicle. This linear trend has been removed from Figures 6.16c and 6.16d, which show bathymetry deviations from the best-fitting plane. Interferograms have been formed between the images from the upper and lower arrays on each side of the vehicle. The interferometric phase shown in Figures 6.16e and 6.16f both show near-zero phase, showing that the bathymetry estimate is consistent with the sonar data and the assumptions of the geometry of the platform. Deviations from near-zero phase are only seen in regions of high complexity. These deviations could be used to refine the coarse bathymetry estimate. In addition, the high interferometric coherence shown in Figures 6.16g and 6.16h suggest that the images are well co-registered.

The SAS images formed using the navigation estimate onto the coarse bathymetry estimate are shown in Figures 6.17a and 6.19 for the port and starboard sides respectively. Figure 6.17

133

shows a comparison between the port side images focused using the new method and the slant plane RPC algorithm, with zoomed sections shown in Figure 6.18. The quality of the image focusing using the new method is very high, which is suggestive of high accuracy navigation and bathymetry estimation. However, replica targets are still faintly visible around bright targets, indicating a quadratic phase error corresponding to along-track velocity error or sound speed error [144]. Inclusion of speed of sound estimation in the method therefore has the potential to improve both the image focus quality and the navigation and bathymetry estimation accuracy.

The image, bathymetry and de-trended bathymetry on the port side are combined in Figure 6.20, where the image intensity encodes the intensity of the SAS image, colour encodes bathymetry deviation from a flat plane and the surface height encodes the bathymetry. This visualisation appears to indicate regions of scour around the proud objects, but the objects themselves do not significantly protrude in the coarse bathymetry estimate. This is expected since the coarse bathymetry estimate is made using relatively large footprints. Higher resolution bathymetry estimation methods such as SAS interferometry are required to improve the resolution of the bathymetry estimate.

The results shown in this section are encouraging, but due to the lack of ground truth it is not possible to assess the accuracy of the navigation and bathymetry estimates. For this reason, synthetic data has been generated which simulates this acquisition, which is discussed in the following section.
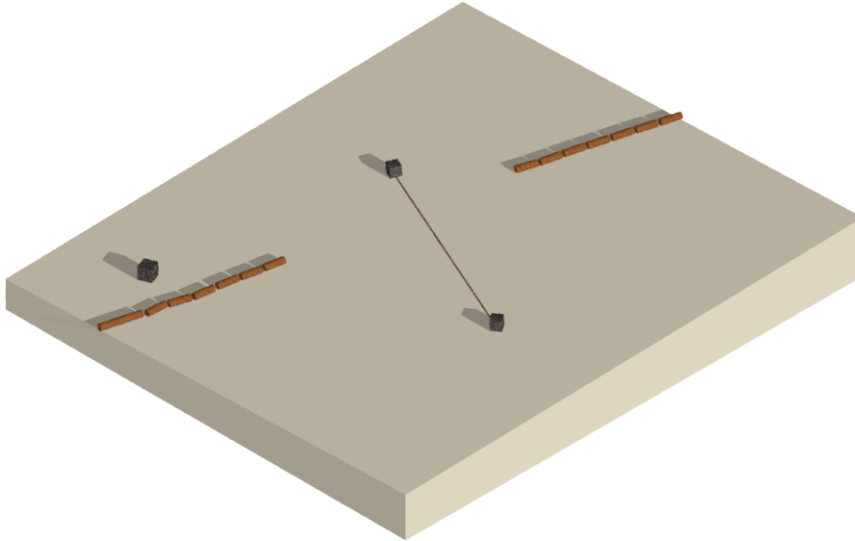
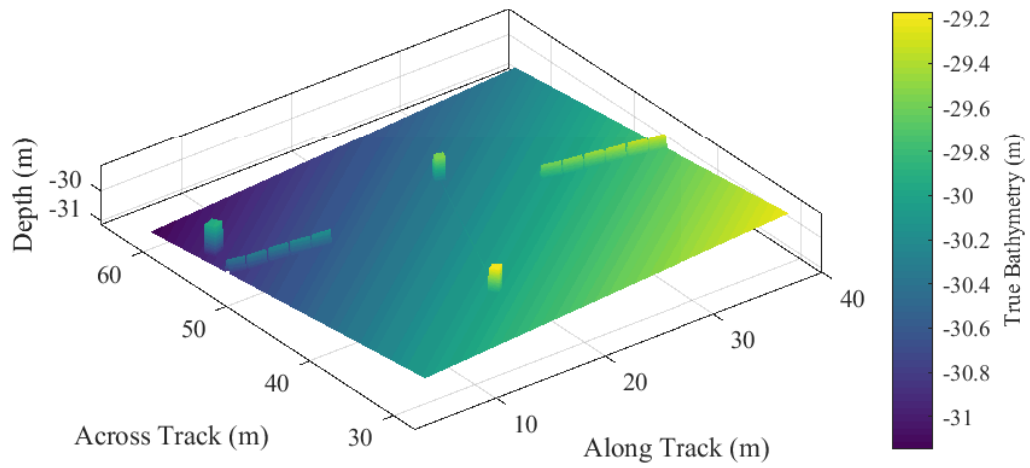Figure 6.21: Simulated scene on the port side.

6.5   Results: Simulated data

The acquisition considered in Section 6.4 has been replicated in simulation in order to validate the algorithm further. The simulated sonar has the same parameters as the 270-330 kHz SAS of the MUSCLE AUV. The receiving arrays consist of 12 elements, with element centres separated by 33 mm. Additive white Gaussian noise has been added to reduce the SNR of the simulated data to a level consistent with the experimental data. The results shown in this section have a SNR of 5.7 dB.

The simulated scene on the port side is shown in Figure 6.21, which consists of a flat, inclined plane, with structures intended to simulate the pipe and concrete blocks seen in Figure 6.17a. A representation of the simulated bathymetry on the port side is shown in Figure 6.22a. The simulated scene on the starboard side consists of a featureless inclined plane. The simulated vehicle path is shown in Figure 6.22b, which is intended to replicate the acquisition of the real data. The vehicle path introduces a total sway of ≈ 0.2 m and total heave of ≈ 1 m over a distance of ≈ 32.5 m.

The scene is represented by ≈ 90 million point scatterers, with an average of 10 scatterers per resolution cell in order to achieve fully developed speckle. Simulated SAS data were generated by a custom ray-tracing simulator implemented in MATLAB. The simulation was performed using the Balena HPC resource at the University of Bath.

Figures 6.23 and 6.24 show the inter-array surge measurements and associated coherence measurements from the simulated data on the port and starboard sides respectively. On the port side, the inter-array surge measurements between adjacent upper arrays and those between adjacent lower arrays (Figures 6.23a and 6.23g respectively) are very similar, and both exhibit minimal variation with range. However, the inter-array surge measured between the upper-

135

(a)
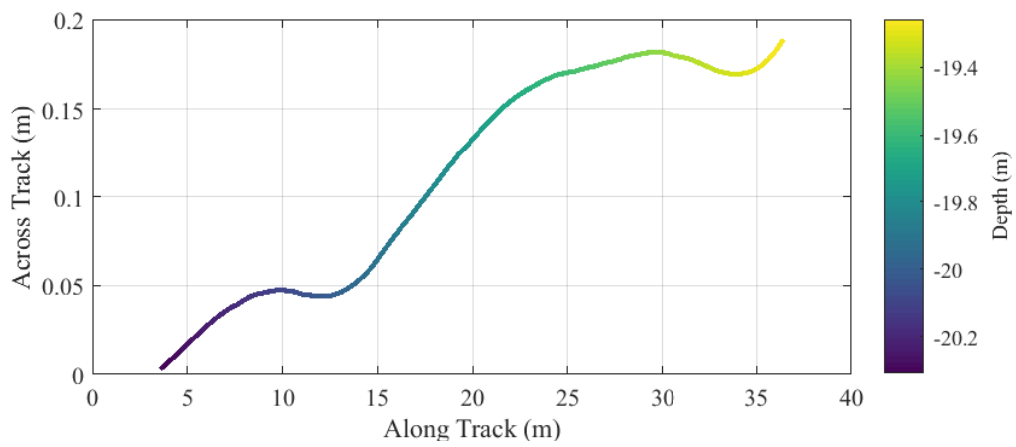
(b)
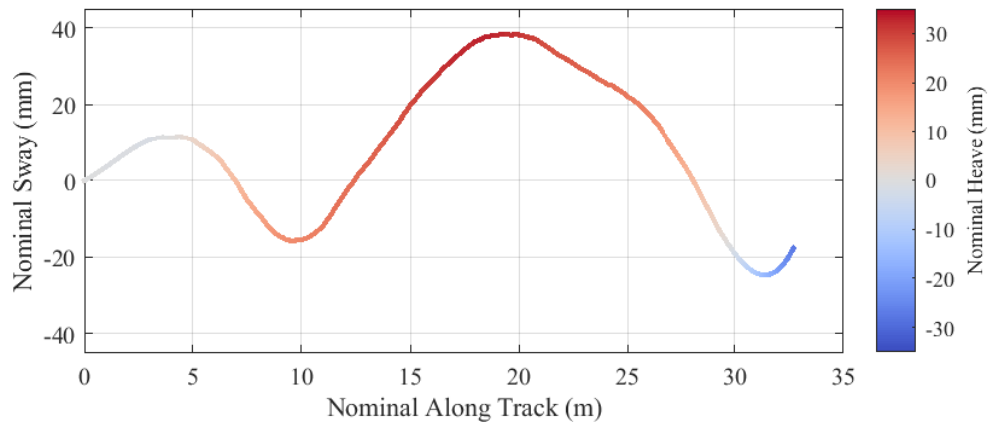
(c)

Figure 6.22: (a) Simulated bathymetry on the port side. (b) Simulated path traversed by the vehicle where the line colour encodes the vehicle depth. (c) Simulated path in a rotated co-ordinate system which improves the alignment between the simulated track and the along-track axis.
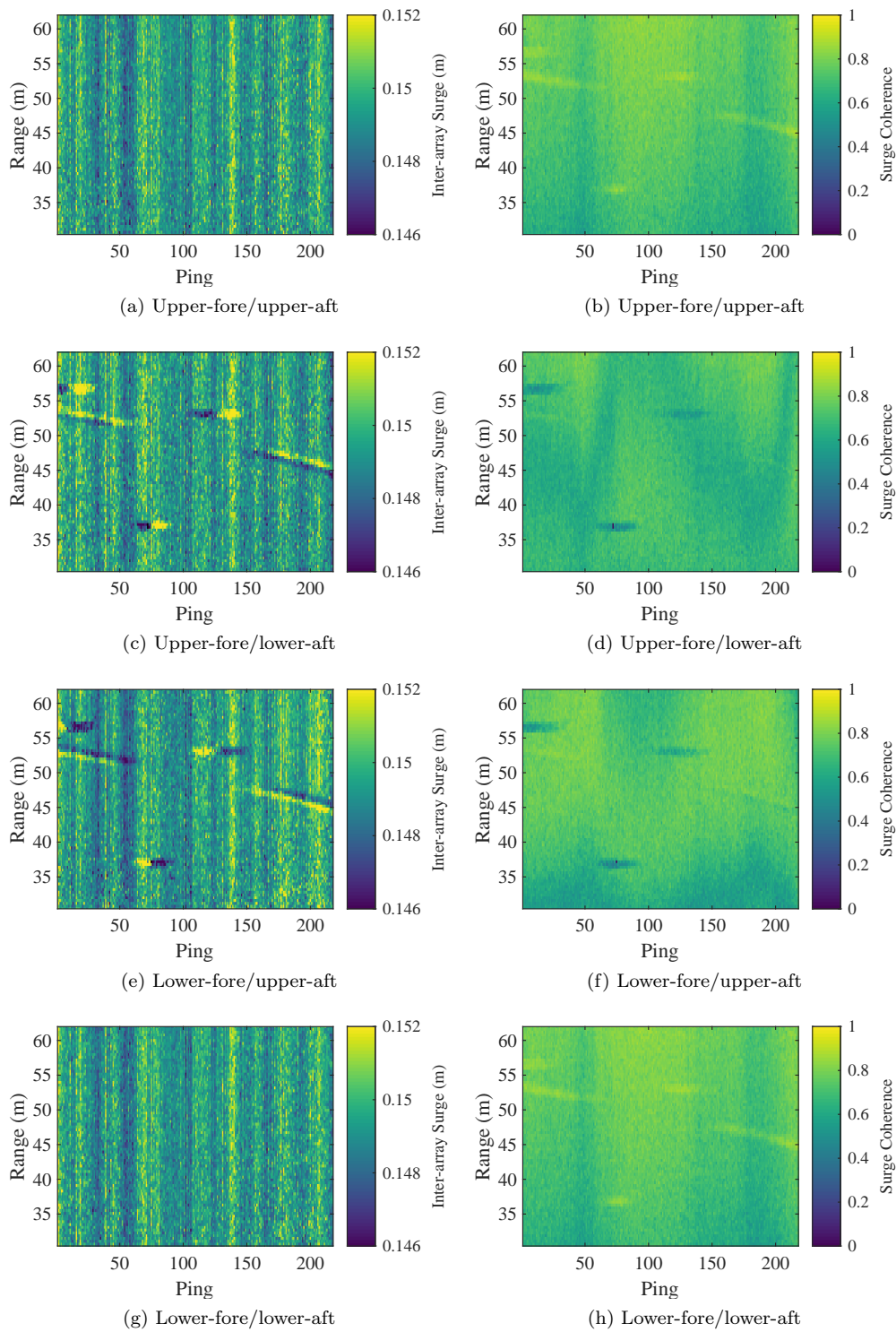
Figure 6.23: (a,c,e,g) Surge measurements and (b,d,f,h) corresponding coherence estimates between the four pairs of redundant arrays for 250 pings.
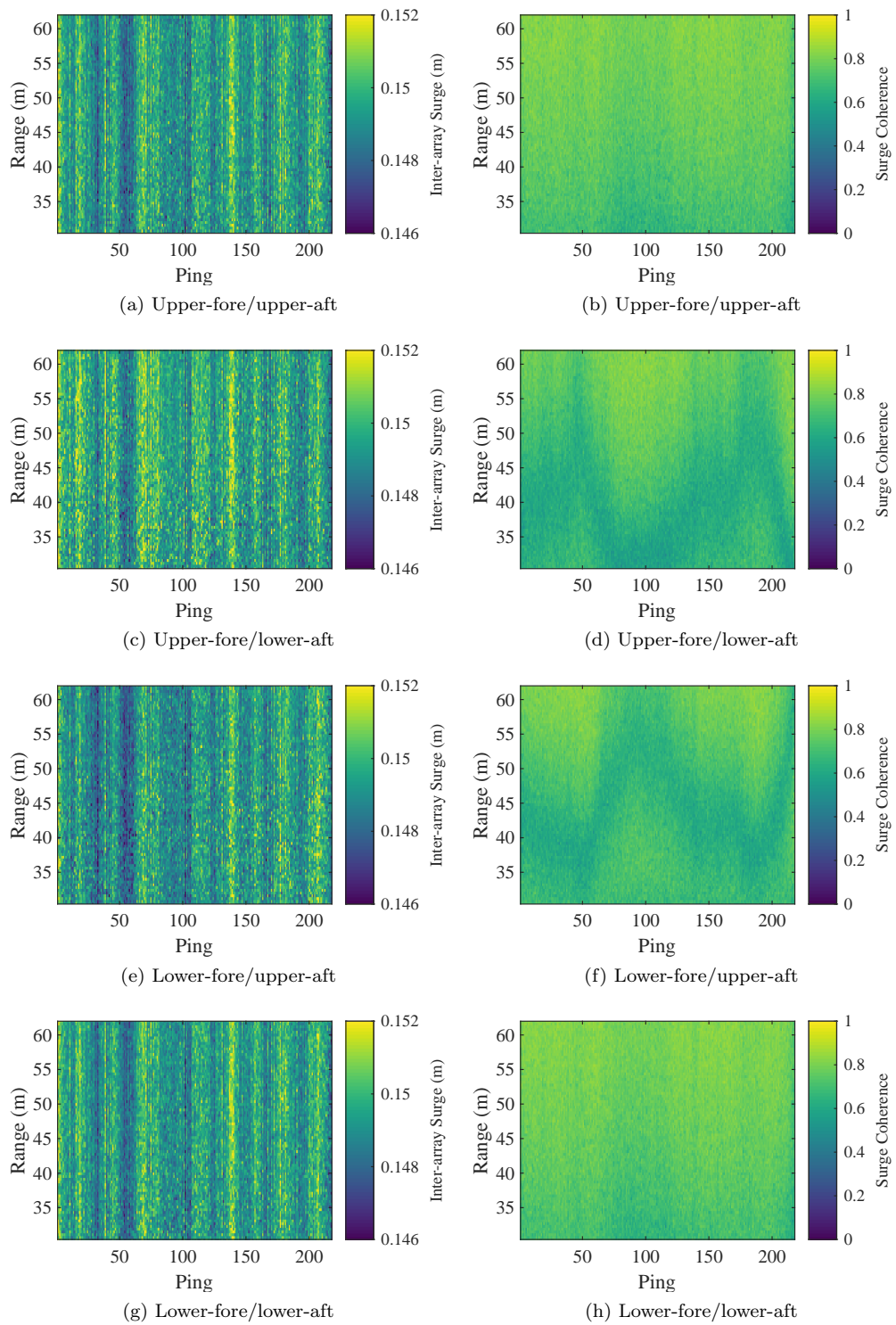
Figure 6.24: (a,c,e,g) Surge measurements and (b,d,f,h) corresponding coherence estimates between the four pairs of redundant arrays for 250 pings.

(a) Upper-fore/lower-fore

(b) Upper-fore/lower-fore

(c) Upper-fore/upper-aft

(d) Upper-fore/upper-aft

(e) Upper-fore/lower-aft

(f) Upper-fore/lower-aft

Figure 6.25: (a,c,d) Time delays and (b,d,f) corresponding coherences between redundant signals with the upper-fore array as reference, on the port side.

(a) Upper-fore/lower-fore

(b) Upper-fore/lower-fore

(c) Upper-fore/upper-aft

(d) Upper-fore/upper-aft

(e) Upper-fore/lower-aft

(f) Upper-fore/lower-aft
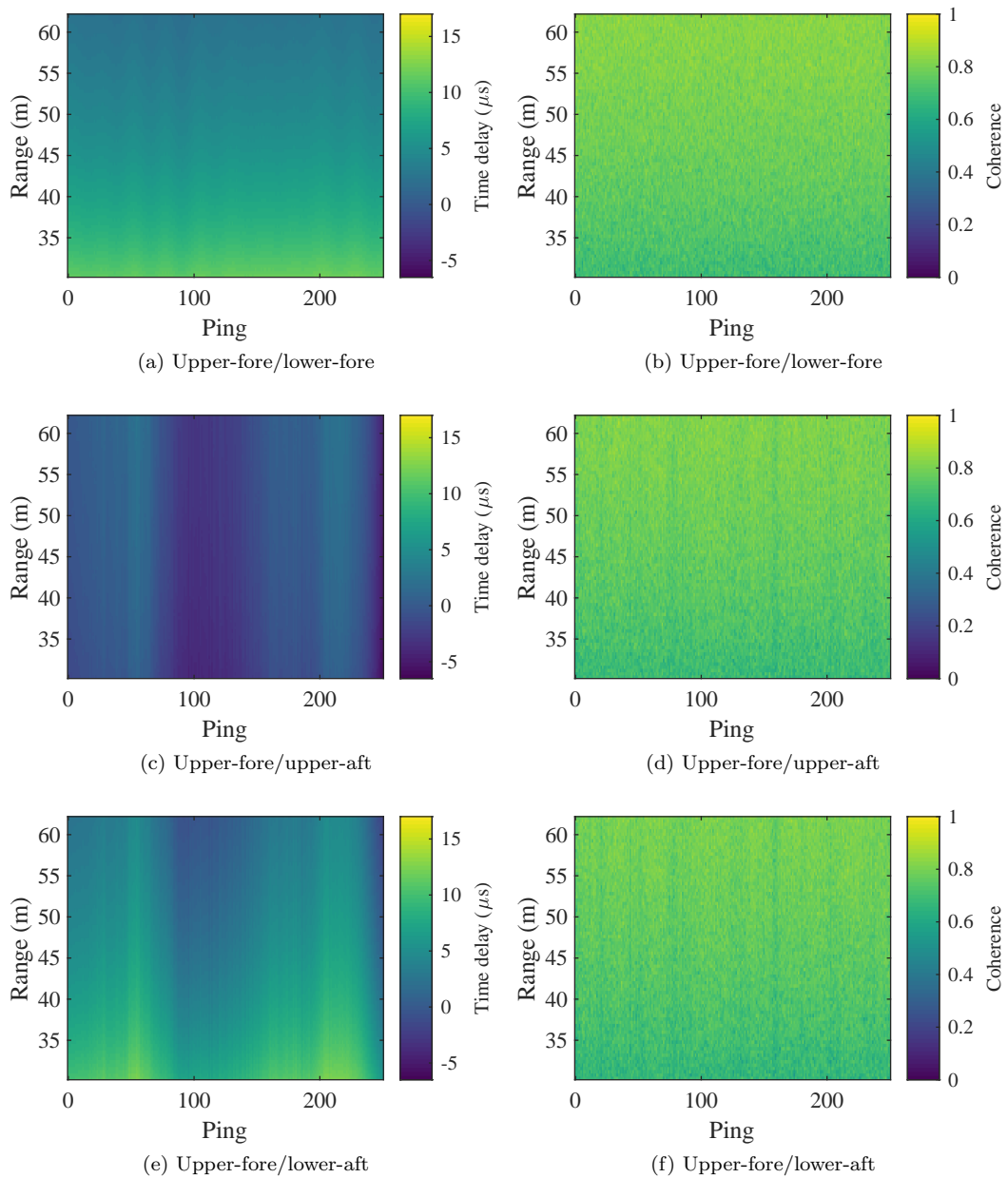
Figure 6.26: (a,c,d) Time delays and (b,d,f) corresponding coherences between redundant signals with the upper-fore array as reference, on the starboard side.
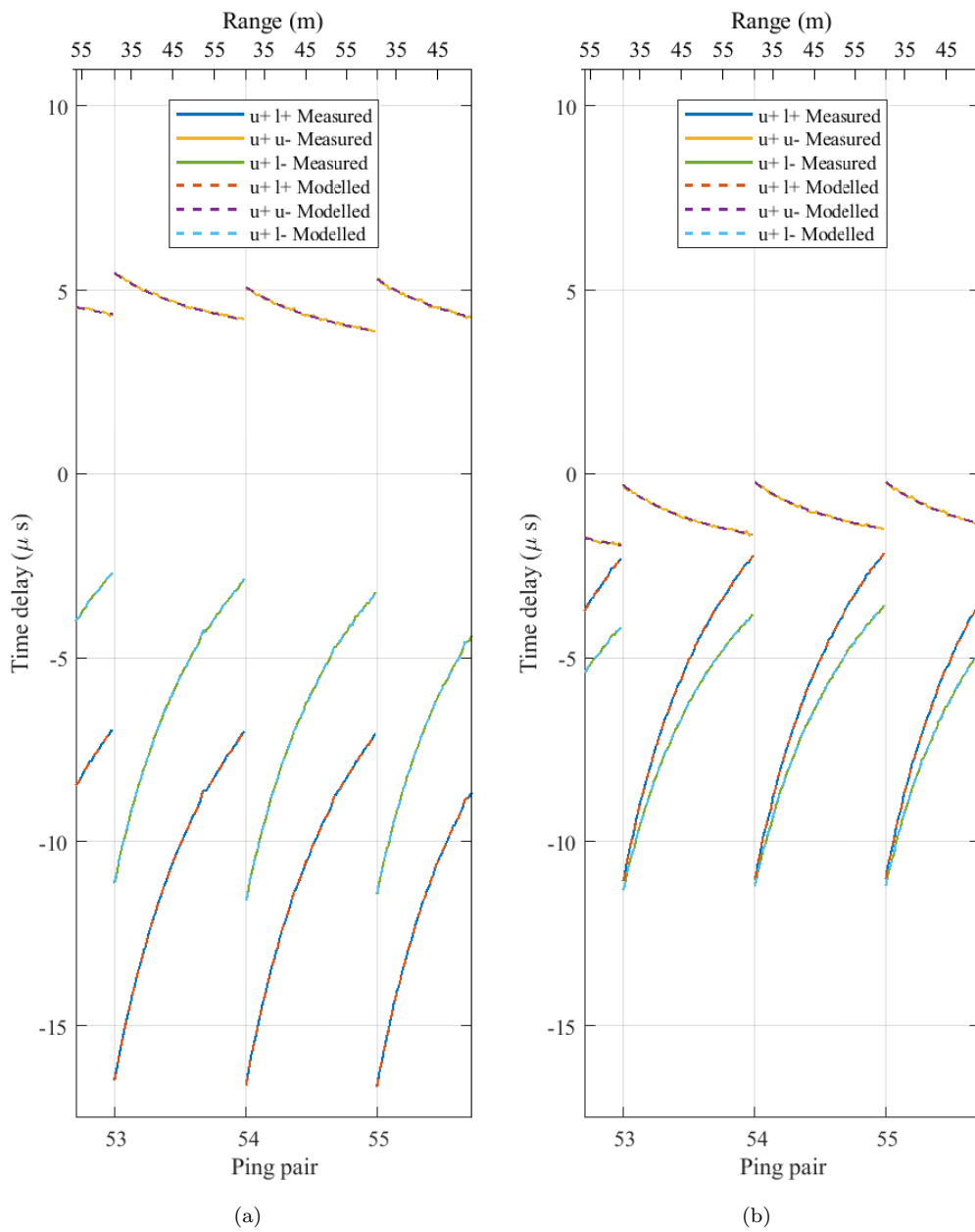
Figure 6.27: Measured time delays between simulated redundant signals for a small subset of pings. The modelled time delays on the final iteration are also shown in dashed lines, which match the measurements very closely. (a) Port side. (b) Starboard side.
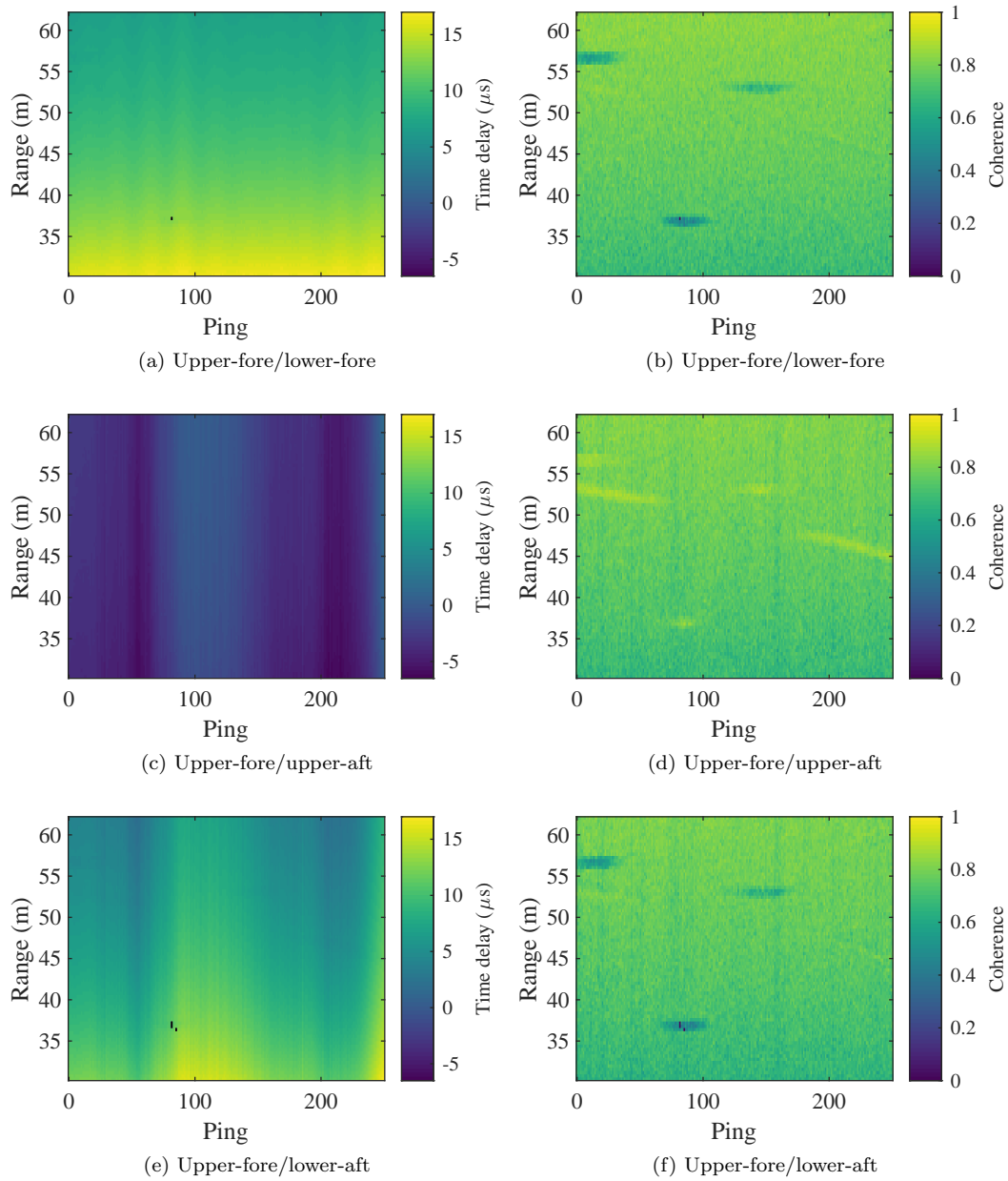
(a) Port   (b) Starboard

(c) Port   (d) Starboard

(e) Port   (f) Starboard

(g) Port   (h) Starboard
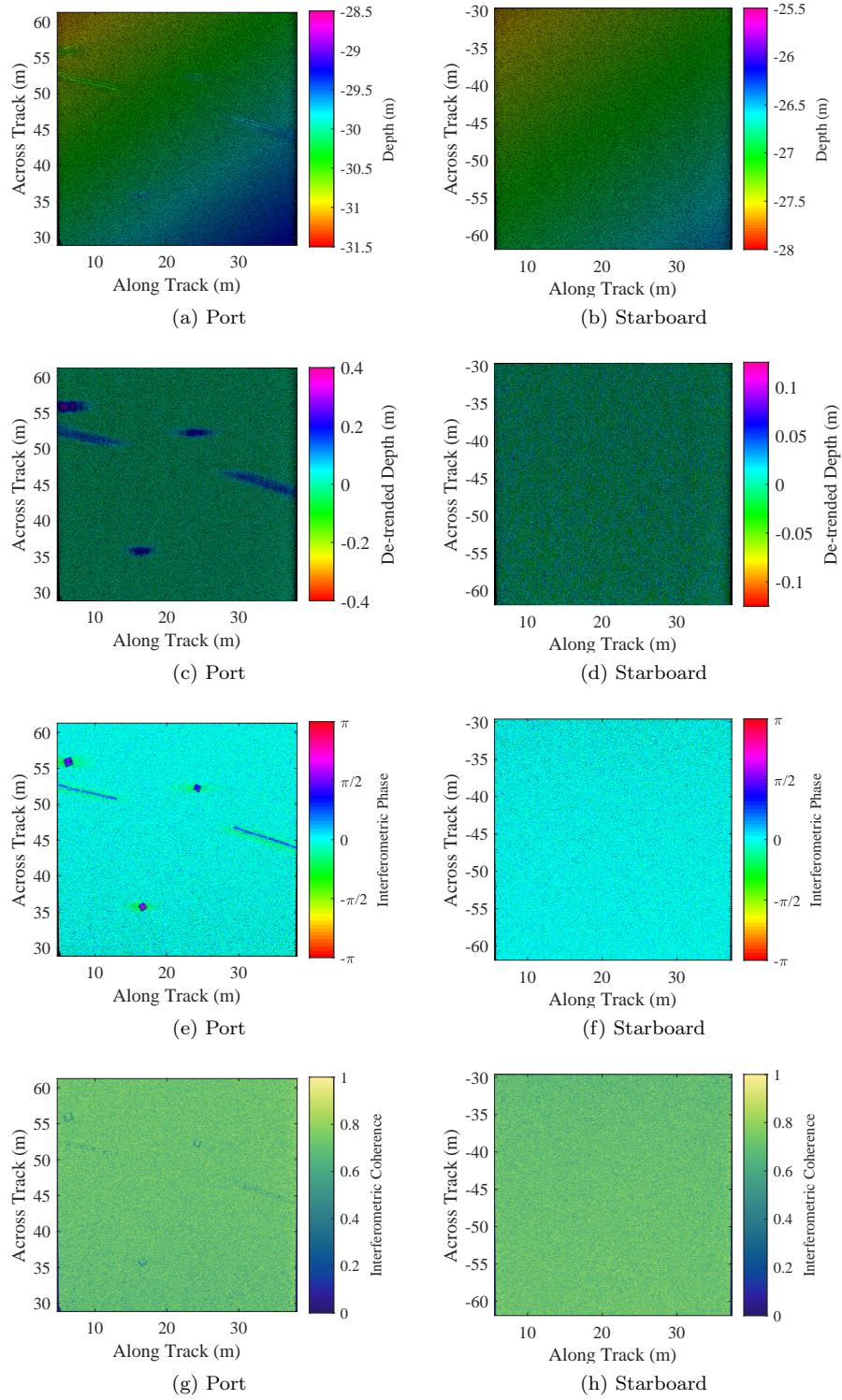
Figure 6.28: (a,b) Coarse bathymetry estimated by the new method. (c,d) Deviation of coarse bathymetry from best-fitting plane. (e,f) Interferometric phase. (g,h) Interferometric coherence.

142
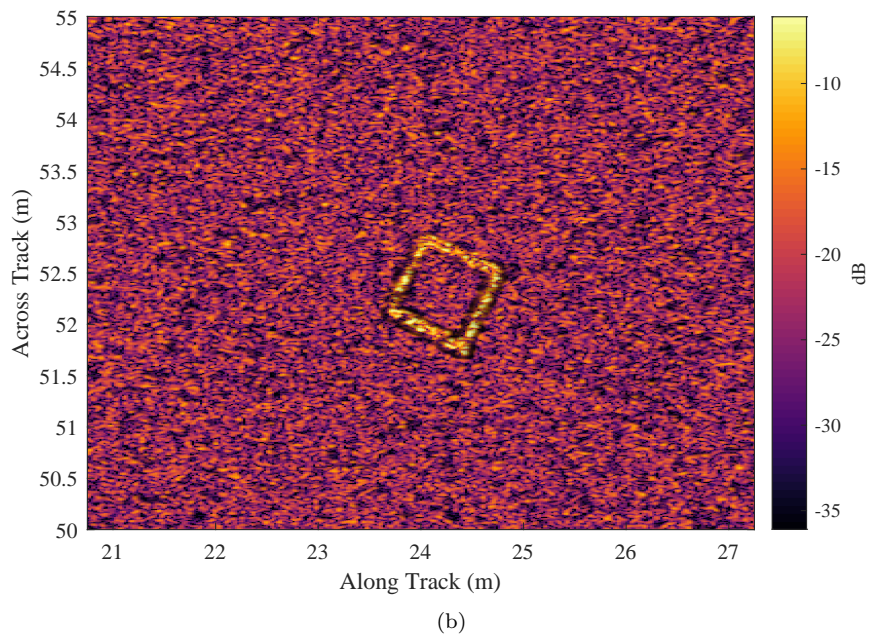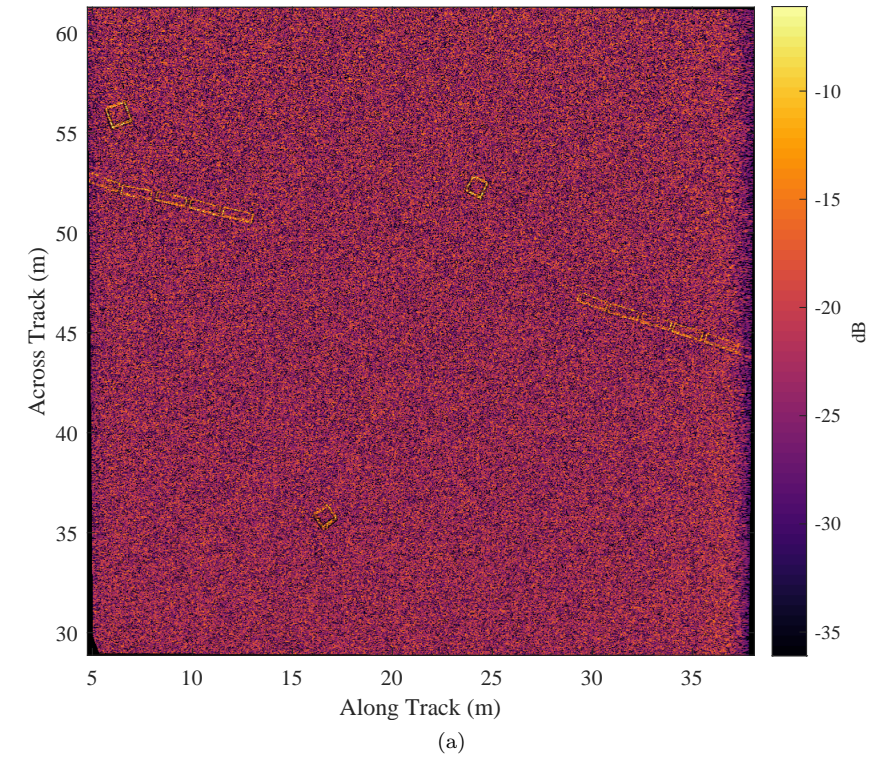
Figure 6.29: (a) SAS images from the port side of the vehicle, focused using the navigation and bathymetry estimates from the new method operating on simulated sonar data. The simulated sections of pipe and concrete blocks are well focused, which can be seen in (b) a zoomed section of the image around one of the simulated concrete blocks. The ray-tracing simulator does not simulate occlusions, which explains the absence of shadows behind proud objects.
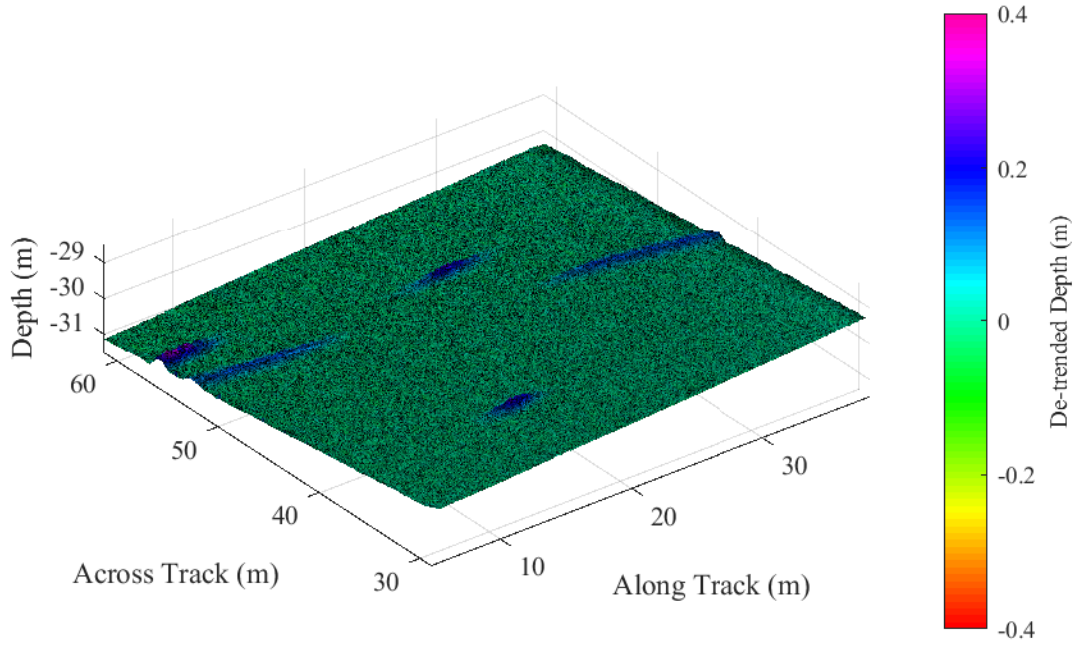
(a)

Figure 6.30: The port side coarse bathymetry estimate from the dual-sided navigation and coarse bathymetry estimation algorithm operating on simulated data. Colour encodes deviation from the best-fitting plane, and the intensity encodes the SAS image intensity.

lower and lower-upper arrays (Figures 6.23c and 6.23e respectively) have some notable features at locations in the image where there are bright targets. The features appear to be angle-dependent modulation of the inter-array surge estimates in the presence of highly reflective targets. This modulation may introduce errors in the vehicle position estimate made by the simultaneous micro-navigation and bathymetry estimation algorithm. Until the cause of these features is known and can be compensated for, care should be taken when using inter-array surge estimates between the upper-lower and lower-upper array pairs for navigation estimation.

Figures 6.25 and 6.26 show the time delays measured between the redundant signals of adjacent pings on the port and starboard sides respectively, with the upper-fore redundant array of each pair as reference. These measurements are very similar to those made using the experimental data, which is expected since the vehicle path and bathymetry are intended to match closely between the experimental data and the simulation.

The simultaneous navigation and bathymetry estimation algorithm has been applied using these inter-array surge and time delay measurements for comparison with the ground truth. The algorithm was seen to converge within 6 iterations, as for the experimental data. In symmetry with Section 6.4, the data from each side has been treated as though it were collected by a single-sided system, and also used simultaneously, resulting in three navigation estimates.

A subset of the time delay measurements are shown in Figure 6.27, which shows measured time delays and the corresponding modelled time delays after the final iteration of the new
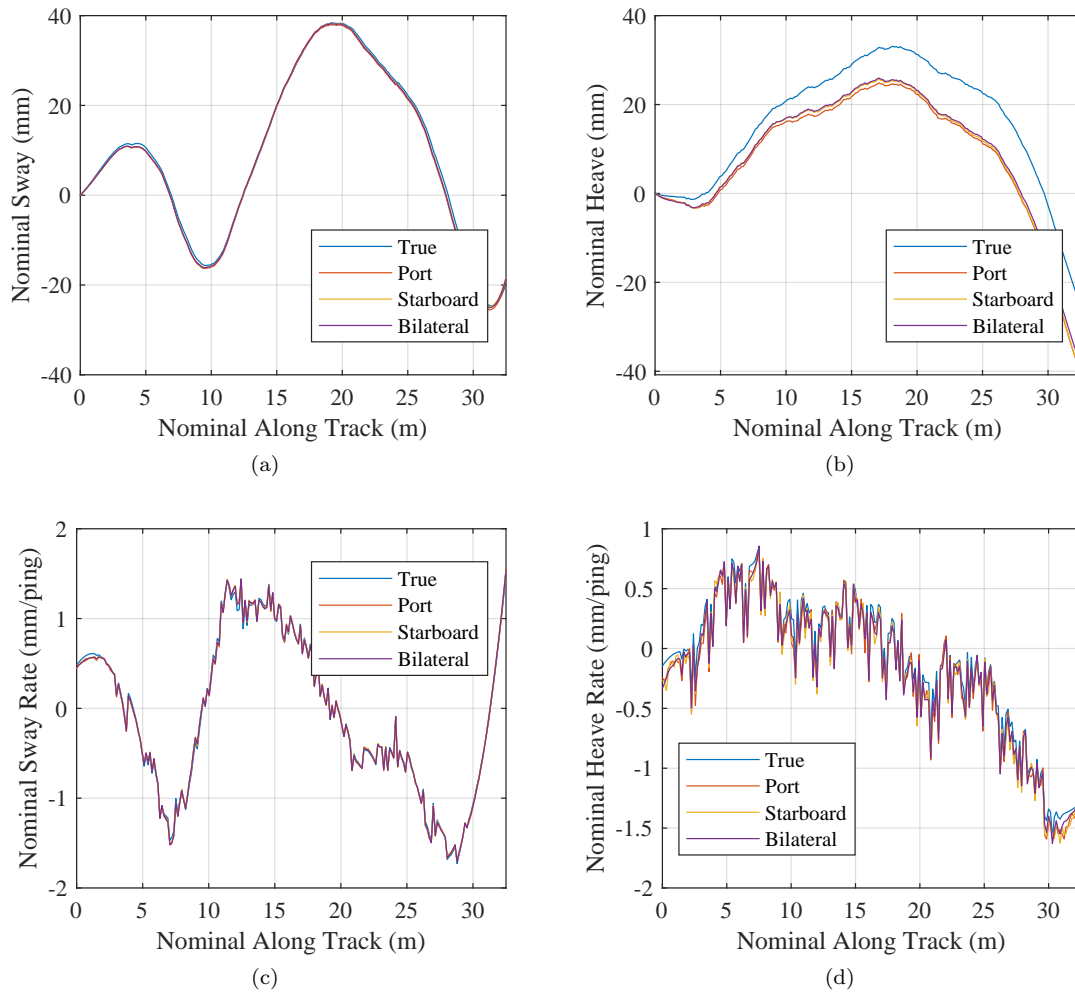
Figure 6.31: (a) Vehicle track: simulated and estimated by the new method. (b) Vehicle depth: simulated and estimated by the new method. (c) Vehicle sway rate: simulated and estimated by the new method (d) Heave rate: simulated and estimated by the new method.

algorithm. The agreement between the measured and modelled time delays is extremely good, which suggests that the resulting navigation and bathymetry estimates are high quality.

Figures 6.28a and 6.28b show the estimated coarse bathymetry using the new method for the port and starboard sides respectively. Figures 6.28c and 6.28d show the same bathymetry estimates after they have been de-trended by removing the best-fitting plane. On the port side, this reveals that the coarse bathymetry estimate is elevated in regions where the simulated pipe sections and cubes were placed in the simulation. Figures 6.28e and 6.28f show the interferometric phase on the port and starboard sides respectively. Regions of near-zero phase are indicative of high-accuracy bathymetry estimates, while deviations from zero suggest bathymetry errors. The interferometric phase may be used to refine the bathymetry estimate. Figures 6.28g and 6.28h show high interferometric coherence on the port and starboard sides

Figure 6.32: Navigation errors in the (a) nominal along-track (b) nominal sway (c) nominal heave directions as a function of ping number. (d) Magnitude of navigation errors as a function of ping number.

respectively, indicating that the images from the upper and lower arrays are well registered.

Figure 6.29a shows the SAS image generated from the simulated port-side data using the navigation and coarse bathymetry estimates made by the new method, with Figure 6.29b showing a zoom around one of the simulated blocks. Since the simulator does not model occlusion, the absence of shadow regions behind proud objects is to be expected. Nevertheless, the quality of the focusing is very high; the edges of the targets are well resolved and no replica targets are present.

Figure 6.30 is a further representation of the coarse bathymetry estimate on the port side. The bathymetry estimate is encoded by the shape of the surface, with the colour representing the bathymetry deviation from the best-fitting plane and the intensity encoding the SAS image intensity.

The navigation estimates are shown in Figure 6.31, with Figure 6.31a showing the estimated path in the along-and across-track directions, Figure 6.31b showing the estimated vehicle depth against along-track position. The per-ping change of across-track position against along-track position is shown in Figure 6.31c. The per-ping change of depth against along-track position is shown in Figure 6.31d. These estimates agree closely with the true navigation values.
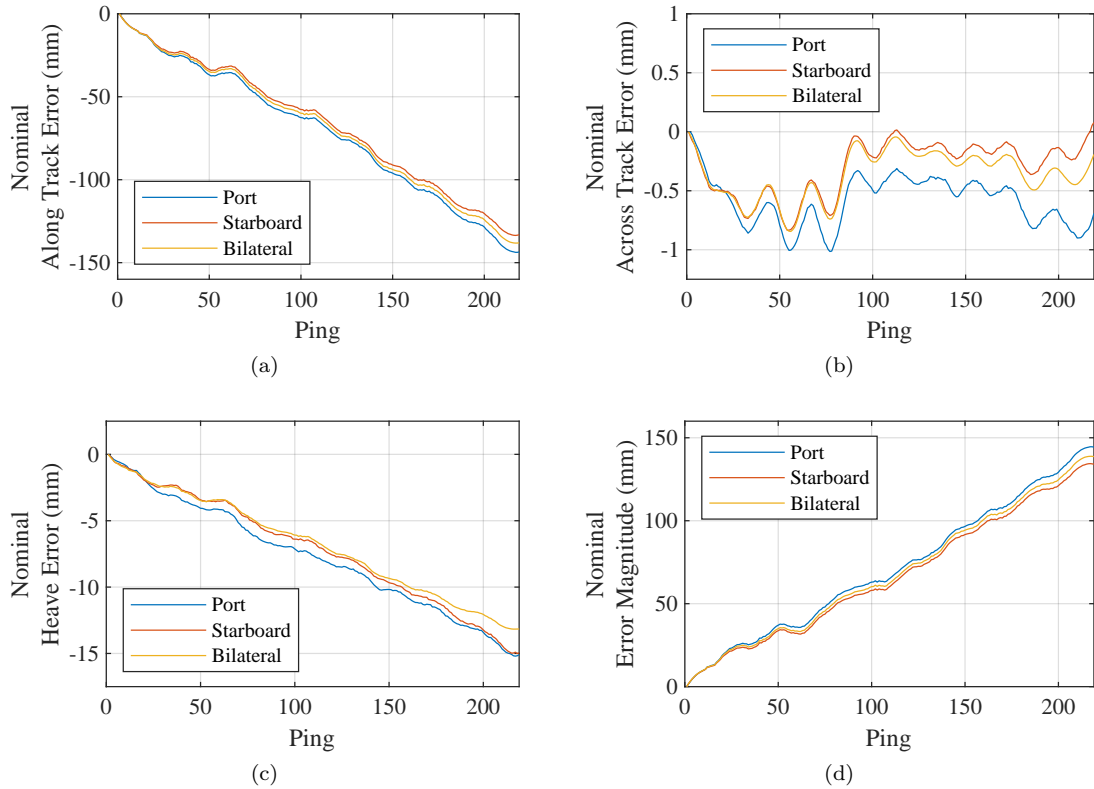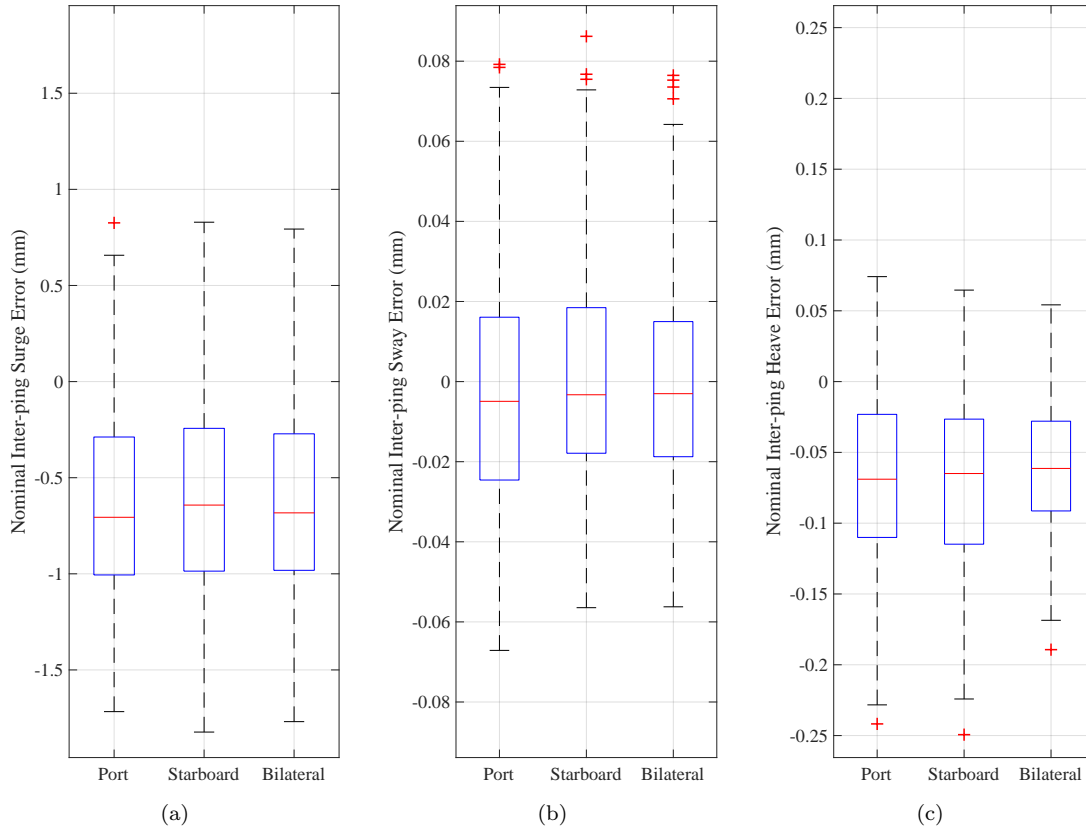
Figure 6.33: Box plots of the inter-ping navigation errors in the (a) nominal along-track (b) nominal sway (c) nominal heave directions as a function of ping number. The median error is shown in red, the 25 percentiles are shown as a blue box, and the remainder of the data spread is represented by the black bars. Red crosses indicate errors which are considered outliers, that is, they are further than 1.5 times the interquartile range away from the 25th or 75th percentile.

Before analysis of the error between the simulated and estimated navigation parameter can be performed, it is necessary to perform a rotation of the co-ordinate system in order to improve the alignment between the simulated track and the nominal along-track axis. This reduces the coupling between the along-track, across-track and vertical directions. The resulting simulated track is shown in Figure 6.22c, which has significantly reduced its nominal sway and heave variation.

The cumulative error in the navigation estimates as a function of ping number is shown in Figure 6.32. Figures 6.32a, 6.32b and 6.32c show the error in the nominal along-track, nominal sway and nominal heave directions respectively. Figure 6.32d shows the total vector magnitude of the error for each ping. This indicates that the along-track error contributes most to the total error magnitude. Errors in the nominal heave and nominal sway directions are approximately one and two orders of magnitude smaller respectively.

The error per ping has also been calculated in each of the nominal along-track, nominal
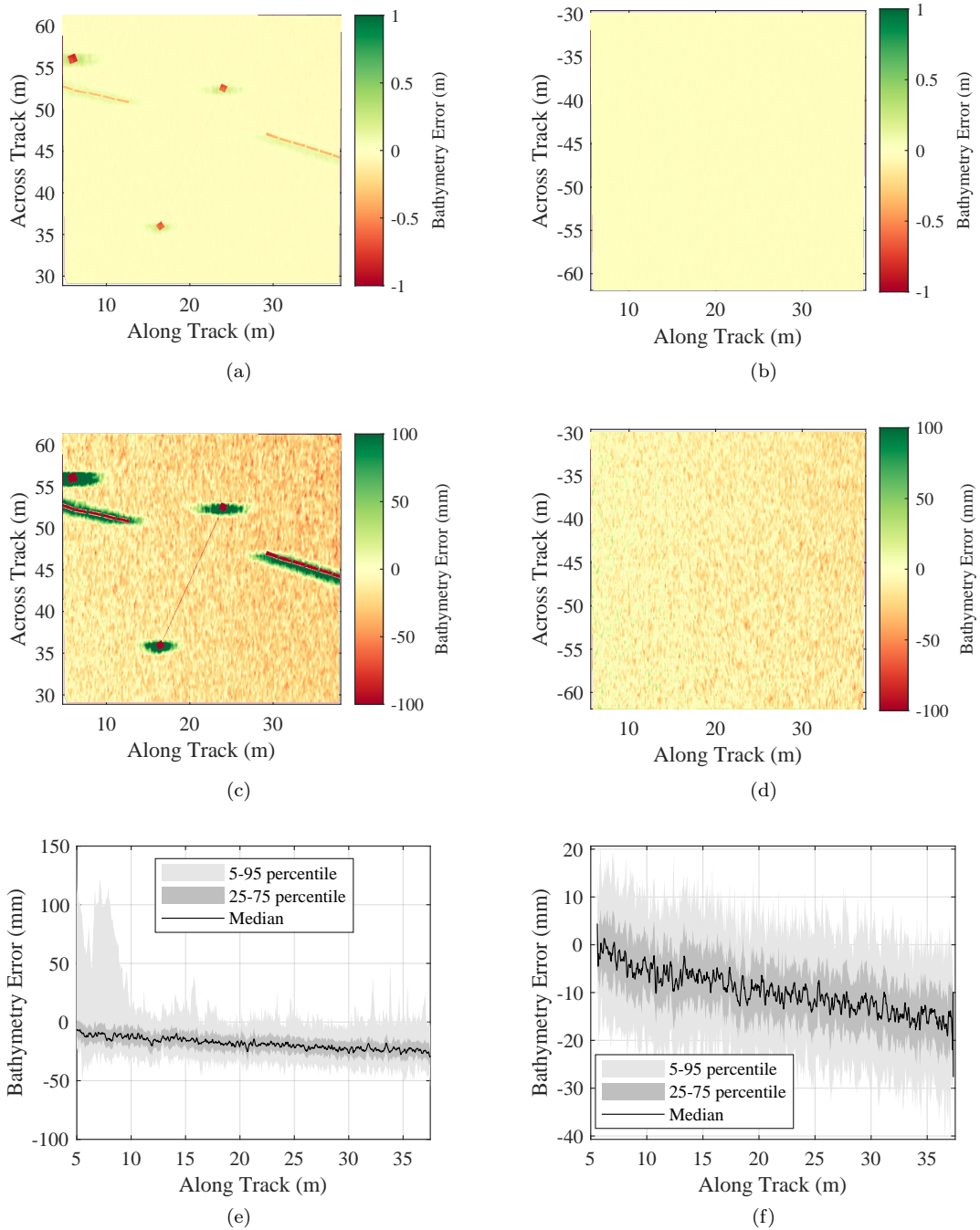
Figure 6.34: Bathymetry errors on the (a,c) port and (b,d) starboard sides using the dual-sided method. The colour axis in the upper Figures is centred on zero, with upper and lower limits chosen to avoid clipping. This shows that the largest bathymetry errors are in regions of high three-dimensional complexity. The lower plots have a smaller colour range, allowing the bathymetry error variability to be visible in regions of low complexity. (e,f) Analysis of the bathymetry error distribution showing the median, 25-75 percentile range and 5-95 percentile range on the port and starboard sides respectively.

sway and nominal heave directions. The distribution of these errors over the simulated track is shown in the box plots in Figure 6.33 for each of the three directions. Figure 6.33a shows that the along-track position estimate appears to have a slight negative bias, and the spread of the surge error does not seem to be significantly affected by using a dual-sided system compared to a single-sided system. The median sway error is very small for both the single- and dual-sided simulations, taking a value of $\approx \lambda_0/1000$, and $\approx 50\%$ of the sway errors are within $\approx \lambda_0/250$. The inter-quartile range of the dual-sided simulation is slightly smaller than the single-sided simulations, suggesting that bilateral processing results in improved precision in the nominal sway direction. In the nominal heave direction, the median error is between -0.06 mm and -0.07 mm per ping, suggesting that the heave estimate is slightly negatively biased. The inter-quartile range of the single-sided heave errors is larger than that using the data from both sides. Again, this suggests that bilateral processing can improve the precision of the heave estimates.

Figure 6.34 presents the error between the estimated bathymetry and the true bathymetry. Figures 6.34a-6.34d show that large bathymetry errors are confined to regions of high complexity, that is, around proud objects. Figures 6.34e and 6.34f show the distribution of the bathymetry error as a function of along-track position on the port and starboard sides respectively. While the large errors on the port side make this challenging to interpret, the starboard side gives some insight into the precision of the coarse bathymetry estimate in benign regions. The median bathymetry error follows a similar trend to the vehicle depth error, while the percentile ranges show that 90% of the bathymetry estimates are within around 15 mm of the median and 50% are within around 5 mm.

The poor spatial resolution of the bathymetry estimates is expected since the length of the redundant portions of the arrays used for estimating navigation and coarse bathymetry is small. However, the spatial resolution of the bathymetry estimates can be improved by SAS interferometry as detailed in Section 2.

6.6   Summary

The novel simultaneous micro-navigation and coarse bathymetry estimation algorithm results in a noticeable improvement in SAS image quality when compared to the conventional SPRPC micro-navigation algorithm on experimental data collected by the MUSCLE AUV. The simulation results demonstrate high ping-to-ping precision in the along-track, sway and heave directions. However, the estimation of both vehicle surge and heave appear to suffer from a slight negative bias, although further simulations with different realisations of the scene are required to confirm this.

Further simulations are recommended for future work which isolate motions in the along-track, across-track and vertical directions. This will allow for improved analysis of the ping-to-ping navigation precision achieved by the new method in the absence of any coupling with motions in other degrees of freedom.

A number of improvements to the simultaneous micro-navigation and coarse bathymetry estimation method are possible and are suggested for future work:

- Integrate the estimation of the local sound speed into the Gauss-Newton optimisation. This has the potential to improve both navigation and coarse bathymetry estimation accuracy, which in turn improves SAS image quality.

- Include estimation of SAS calibration parameters into the method, to estmate, for example, misalignment between the four arrays of a dual-sided InSAS.

- Fuse the navigation estimates made by the SAS with other sensors on the vehicle such as the depth sensor, in order to combat the heave bias.

The new algorithm has been designed to be simple to extend to repeated passes. This will involve including inter-array surge estimates and time delays between redundant signals between pings of repeated passes, which has potential to provide precise, three-dimensional track co-registration with low computational cost. This track registration is a vital step towards improving coherent change detection methods and enabling high precision bathymetry estimation methods using repeat-pass interferometric SAS.

7 Conclusion

The main contribution of this thesis is a new method for simultaneously estimating high-precision vehicle navigation while making a coarse bathymetry estimate using interferometric SAS, described in Chapter 6. The new method has potential to improve the navigation precision of AUVs equipped with interferometric SAS, allowing improved image and bathymetry geo-referencing precision and allowing longer surveys to be performed without surfacing for a radio-navigation fix. This is vital in applications where surfacing is not possible, for example under ice or in covert operations. Also, co-registered SAS images can be formed onto the coarse bathymetry estimate, which allows higher resolution bathymetry estimates to be made by SAS interferometry without requiring an intermediate co-registration step.

The method is built upon the concept we introduced as the 'triad of confounding factors', which states that time delays measured between redundant signals are affected by three factors: the geometry and motion of the sonar, the sea-floor bathymetry, and the speed of sound in the medium. By extension, all time delays measured between redundant signals contain information that can be used to estimate the members of the triad. We frame simultaneous micro-navigation and bathymetry estimation as an optimisation problem, where the objective is to minimise the difference between measured and modelled propagation times, time delays and inter-array surges in a weighted least-squares sense. Framing the algorithm in this way allows it to be easily generalised for various applications and allows the model to be adjusted to the required accuracy. We demonstrate this by applying it to both single- and dual-sided interferometric SAS, using a model that does not employ the phase centre or stop-and-hop approximations. The algorithm has been demonstrated on experimental SAS data collected by the MUSCLE AUV, which resulted in improved SAS image quality when compared to the conventional slant plane RPC micro-navigation algorithm. A preliminary analysis of the method was performed on simulated data in order to allow comparison with ground truth.

Time delay estimates derived from cross-correlation of redundant signals typically exhibit phase wrap errors which reduce their accuracy. These phase wrap errors must be identified and corrected before they can be used in the new micro-navigation and coarse bathymetry estimation algorithm. In Chapter 5, we frame the problem of detection of phase wrap errors as one of robust regression and used the popular RANSAC algorithm to fit a 1D or 2D model to the error-free estimates. Estimates outside a threshold from this model are re-unwrapped around the model. This method is evaluated by comparing its performance to the popular branch-cuts phase unwrapping method at a range of bandwidths, and superior performance is demonstrated.

7.1 Suggestions for future work

We consider the new methods introduced in this thesis to be vital developments in the pursuit of ultra-high precision bathymetry estimation using repeat-pass interferometric SAS. However, there are several areas where further work is required to realise this goal. These areas are categorised into further analysis of the new method, developments to the method, and

generalisation of the method to repeated passes.

7.1.1 Further analysis

In this thesis the method has only been applied to a single realisation of the simulated scene. The resulting navigation estimates appear to exhibit a negative bias in surge and heave. However, further realisations of the scene are required in order to make this conclusion with greater certainty. The simulated acquisition was designed to be representative of a real acquisition, with motions in all degrees of freedom. However, isolating vehicle motions in each degree of freedom is likely to allow simpler analysis.

If the results of this further analysis also suggests that the method makes biased estimates of along-track and vertical inter-ping displacements, the source of the bias should be investigated and if possible removed.

The surge estimates made between the interferometric arrays of adjacent pings, that is the upper-fore/lower-aft and the lower-fore/upper-aft pairs, appear to be affected by highly reflective targets at angles away from broadside. The source of these artefacts must be understood and if possible compensated, before such surge estimates between repeated passes can be exploited effectively.

7.1.2 Algorithm improvements

The current implementation of the model for inter-array surge makes the assumption of zero pitch and heading velocity over the coarse of ping pair, and a weighted sum of surge estimates made at all temporal windows has been shown. However, since the algorithm has been shown to converge in few iterations, this simplification is likely to be unnecessary. Improvements to the model for inter-array surge may reduce the apparent bias in along track position estimates. This is likely a necessary requirement for generalisation of the method to repeated passes, since the assumption of equal pitch and heading of pairs of pings in different passes is unlikely to be valid.

At present, a single time delay estimate is made for each redundant array pair and at each temporal window, at the direction of maximum coherence. However, there is additional information that may be utilised at other beam angles, especially for wide-beam systems. Including this information in the optimisation has potential to improve the precision of through-the-sensor micro-navigation estimation still further.

We currently assume that the positioning of the arrays on the vehicle is known to high accuracy. However, any errors introduced by this assumption are likely to lead to biased navigation estimates. Including estimation of the relative positions of the arrays in the method may result in improved navigation estimation.

Additionally, sound speed is assumed to take a given value, rather than estimating it through-the-sensor. This is conspicuous limitation could be addressed in future. However, implementing this rigorously is a significant challenge; spatially varying sound speeds result in curved ray paths, which are likely to considerably increase the complexity of the models for

propagation time and time delay. Therefore, we suggest that an initial approach could be to estimate a mean sound speed for each individual ping pair.

Of course, the final suggestion for future work is to generalise the method to repeated passes to enable ultra-high precision bathymetry estimation using repeat-pass interferometric SAS. Framing the method as an optimisation problem has the advantage of making this a simple procedure. Each iteration of the micro-navigation and coarse bathymetry estimation method involves solving an over-determined system of equations in a weighted least-squares sense. Generalisation of the method to repeated passes increases the number of these equations and the number of unknowns, but the structure of the method remains unchanged. If the relevant considerations above are addressed, this could result in an enabling algorithm for repeat-pass interferometric SAS for improved ultra-high precision bathymetry estimation.

References

[1] A. J. Hunter, S. Dugelay, and W. L. J. Fox, "Repeat-Pass Synthetic Aperture Sonar Micronavigation Using Redundant Phase Center Arrays," *IEEE Journal of Oceanic Engineering*, vol. 41, no. 4, pp. 820–830, oct 2016. [Online]. Available: http://ieeexplore.ieee.org/document/7451192/

[2] L. J. Cutrona, "Comparison of sonar system performance achievable using syntheticaperture techniques with the performance achievable by more conventional means," *The Journal of the Acoustical Society of America*, vol. 58, no. 2, pp. 336–348, 1975. [Online]. Available: https://asa.scitation.org/doi/10.1121/1.380678

[3] T. G. Fossum, T. O. Sæbø, B. Langli, H. J. Callow, and R. E. Hansen, "HISAS 1030 - High resolution interferometric synthetic aperture sonar," in *Proceedings of the Canadian Hydrographic Conference and National Surveyors Conference*, 2008.

[4] D. Shea, P. Crocker, J. Dillon, and S. Chapman, "AquaPix - A Low-Cost Interferometric Synthetic Aperture Sonar for AUVs : Sea Trials and Results," in *Unmanned untethered submersible technology international symposium*, 2013. [Online]. Available: https://krakenrobotics.com/wp-content/uploads/2019/06/2013-UUST-2013-Paper-AquaPix-A-Low-Cost-InSAS-for-AUVS-Sea-Trials-Results.pdf

[5] J. Dillon, "Real-Time Interferometric SAS Processing with Ultra-Low Power Consumption," in *Proceedings of the MTS/IEEE OCEANS Conference*, Charleston, 2019. [Online]. Available: https://krakenrobotics.com/wp-content/uploads/2019/06/Real-Time-InSAS-Processing-with-Ultra-Low-Power-Consumption.pdf

[6] D. P. Williams, "Fast target detection in synthetic aperture sonar imagery: A new algorithm and large-scale performance analysis," *IEEE Journal of Oceanic Engineering*, vol. 40, no. 1, pp. 71–92, 2015. [Online]. Available: https://ieeexplore.ieee.org/abstract/document/6729126

[7] R. E. Hansen, T. O. Sæbø, O. J. Lorentzen, and S. A. V. Synnes, "Mapping Unexploded Ordnance (UXO) Using Interferometric Synthetic Aperture Sonar," in *Proceedings of the Underwater Acoustics Conference and Exhibition (UACE)*, 2017, pp. 687–694. [Online]. Available: http://www.uaconferences.org/docs/UACE2017{_}Papers/687{_}UACE2017.pdf

[8] Ø. Ødegård, M. Ludvigsen, and P. A. Lagstad, "Using synthetic aperture sonar in marine archaeological surveys - Some first experiences," in *Proceedings of the MTS/IEEE OCEANS Conference*. Bergen: IEEE, 2013. [Online]. Available: https://ieeexplore.ieee.org/document/6608172

[9] Ø. Ødegård, R. E. Hansen, H. Singh, and T. J. Maarleveld, "Archaeological use of Synthetic Aperture Sonar on deepwater wreck sites in Skagerrak," *Journal*

of Archaeological Science, vol. 89, pp. 1–13, 2018. [Online]. Available: https://doi.org/10.1016/j.jas.2017.10.005

[10] T. O. Sæbø, R. E. Hansen, and Ole Jacob Lorentzen, "Using an interferometric synthetic aperture sonar to inspect the Skagerrak World War II chemical munitions dump site," in *Proceedings of the MTS/IEEE OCEANS Conference*. Washington, USA: IEEE, oct 2015, pp. 1–10. [Online]. Available: http://ieeexplore.ieee.org/document/7401927/

[11] R. E. Hansen, T. O. Sæbø, H. J. Callow, and P. E. Hagen, "Interferometric synthetic aperture sonar in pipeline inspection," in *Proceedings of the MTS/IEEE OCEANS Conference*, Sydney, 2010. [Online]. Available: https://ieeexplore.ieee.org/document/5603518

[12] P. K. LeHardy and J. Larsen, "Deepwater synthetic aperture sonar and the search for MH370," in *Proceedings of the MTS/IEEE OCEANS Conference*. Washington, USA: MTS, 2015. [Online]. Available: https://ieeexplore.ieee.org/document/7401838

[13] A. Denny, T. O. Sæbø, R. E. Hansen, and R. B. Pedersen, "The use of synthetic aperture sonar to survey seafloor massive sulfide deposits," *Journal of Ocean Technology*, vol. 10, no. 1, pp. 36–53, 2015. [Online]. Available: https://ffi-publikasjoner.archive.knowledgearc.net/handle/20.500.12242/493

[14] A. E. A. Blomberg, A. Austeng, R. E. Hansen, and R. B. Pedersen, "Alternative SAS processing for gas seep detection," in *Proceedings of the International Conference and Exhibition on Underwater Acoustics*, Rhodes, 2014, pp. 929–936. [Online]. Available: http://www.uaconferences.org/docs/Past{_}Proceedings/UACE2014{_}Proceedings.pdf

[15] D. Shea, D. Dawe, J. Dillon, and S. Chapman, "Real-time SAS processing for high-arctic AUV surveys," in *Proceedings of the IEEE/OES Autonomous Underwater Vehicles (AUV) Conference*. IEEE, 2014. [Online]. Available: https://ieeexplore.ieee.org/document/7054408

[16] T. O. Sæbø, "Seafloor Depth Estimation by means of Interferometric Synthetic Aperture Sonar," PhD Thesis, University of Tromsø, 2010. [Online]. Available: https://munin.uit.no/handle/10037/2793

[17] B. W. Thomas and A. J. Hunter, "An investigation into optimal acquisition geometries for repeat-pass synthetic aperture sonar bathymetric mapping," in *Proceedings of the IOA Acoustic and Environmental Variability, Fluctuations and Coherence Conference*, 2016. [Online]. Available: http://opus.bath.ac.uk/55007/

[18] T. O. Sæbø, R. E. Hansen, and A. Austeng, "Synthetic Aperture Sonar Tomography: A Preliminary Study," in *Proceedings of 10th European Conference on Synthetic Aperture Radar (EUSAR)*, 2014. [Online]. Available: https://ieeexplore.ieee.org/document/6857065

[19] T. M. Marston and J. L. Kennedy, "Volumetric Acoustic Imaging via Circular Multipass Aperture Synthesis," *IEEE Journal of Oceanic Engineering*, vol. 41, no. 4, pp. 852 – 867, 2016. [Online]. Available: https://ieeexplore.ieee.org/document/7416146

[20] V. Wang and M. Hayes, "Synthetic Aperture Sonar Track Registration Using SIFT Image Correspondences," *IEEE Journal of Oceanic Engineering*, vol. 42, no. 4, pp. 901 – 913, 2017. [Online]. Available: https://ieeexplore.ieee.org/document/7812619

[21] B. Thomas, A. J. Hunter, and S. Dugelay, "Repeat-pass micro-navigation and bathymetry estimation using interferometric synthetic aperture sonar," in *IOA Synthetic Aperture Sonar and Synthetic Aperture Radar*, Lerici, Italy, 2018.

[22] T. G-Michael, B. Marchand, J. D. Tucker, T. M. Marston, D. D. Sternlicht, and M. R. Azimi-Sadjadi, "Image-based automated change detection for synthetic aperture sonar by multistage coregistration and canonical correlation analysis," *IEEE Journal of Oceanic Engineering*, vol. 41, no. 3, pp. 592–612, 2016. [Online]. Available: https://ieeexplore.ieee.org/document/7323881

[23] B. Bonnett, "Coherent change detection in repeat-pass synthetic aperture sonar," PhD Thesis, University of Canterbury, 2017. [Online]. Available: https://ir.canterbury.ac.nz/handle/10092/14392

[24] V. Myers, I. Quidu, B. Zerr, T. O. Sabo, and R. E. Hansen, "Synthetic Aperture Sonar Track Registration With Motion Compensation for Coherent Change Detection," *IEEE Journal of Oceanic Engineering*, pp. 1–18, 2019. [Online]. Available: https://ieeexplore.ieee.org/document/8717711

[25] V. Wang and M. Hayes, "Image registration of simulated synthetic aperture sonar images using SIFT," in *International Conference on Image and Vision Computing*, 2014, pp. 31 – 36. [Online]. Available: https://dl.acm.org/doi/10.1145/2683405.2683407

[26] A. J. Hunter, R. V. Vossen, B. A. J. Quesson, and A. I. D. Beckers, "Detection of Underwater UXOs in Mud," TNO, Tech. Rep. April, 2013. [Online]. Available: https://www.serdp-estcp.org/Program-Areas/Munitions-Response/Munitions-Underwater/MR-2200/MR-2200

[27] C. Sanford, A. J. Hunter, and A. Willcox, "Synthetic aperture sonar for a low-cost agile platform: preliminary results," in *Proceedings of the Underwater Acoustics Conference and Exhibition (UACE)*, Hersonissos, Crete, 2019, pp. 703–708. [Online]. Available: http://www.uaconferences.org/docs/2019{_}papers/UACE2019{_}837{_}Sanford.pdf

[28] K. M. Awan, P. A. Shah, K. Iqbal, S. Gillani, W. Ahmad, and Y. Nam, "Underwater Wireless Sensor Networks: A Review of Recent Issues and Challenges," *Wireless Communications and Mobile Computing*, 2019. [Online]. Available: https://www.hindawi.com/journals/wcmc/2019/6470359/

[29] R. E. Kalman, "A new approach to linear filtering and prediction problems," *Journal of Fluids Engineering, Transactions of the ASME*, vol. 82, no. 1, pp. 35–45, 1960. [Online]. Available: http://www.unitedthc.com/DSP/Kalman1960.pdf

[30] D. Billon and F. Fohanno, "Theoretical performance and experimental results for synthetic aperture sonar self-calibration," in *Proceedings of the IEEE/OES OCEANS Conference*. IEEE, 1998, pp. 965–970. [Online]. Available: http://ieeexplore.ieee.org/document/724381/

[31] A. Bellettini and M. Pinto, "Theoretical accuracy of synthetic aperture sonar micronavigation using a displaced phase-center antenna," *IEEE Journal of Oceanic Engineering*, vol. 27, no. 4, pp. 780–789, oct 2002. [Online]. Available: http://ieeexplore.ieee.org/document/1134178/

[32] S. Leier, "Signal Processing Techniques for Seafloor Ground-Range Imaging Using Synthetic Aperture Sonar Systems," PhD Thesis, Technische Universität Darmstadt, 2014. [Online]. Available: http://tuprints.ulb.tu-darmstadt.de/4086/1/Doktorarbeit{_}Leier{_}pub{_}v1.pdf

[33] D. A. Cook, "Synthetic Aperture Sonar Motion Estimation and Compensation," Master's Thesis, Georgia Institute of Technology, 2007. [Online]. Available: https://smartech.gatech.edu/bitstream/handle/1853/14538/cook{_}daniel{_}a{_}200705{_}mast.pdf

[34] J. Dillon, "Aided Inertial Navigation in GPS-denied Environments Using Synthetic Aperture Processing," DRDC, Tech. Rep. DRDC-RDDC-2016-C200, 2016.

[35] J. Groen, H. Schmaljohann, W. Jans, and U. Hölscher-Höbing, "Comparison of fusion approaches for the displaced phase centre antenna method," in *Proceedings of the 2nd International Conference and Exhibition on Underwater Acoustics*, Rhodes, Greece, 2014, pp. 921–928. [Online]. Available: http://www.uaconferences.org/docs/Past{_}Proceedings/UACE2014{_}Proceedings.pdf

[36] R. J. Urick, *Principles of underwater sound*, 2nd ed. McGraw Hill Book Company, New York, 1975.

[37] F. H. Fisher and V. P. Simmons, "Sound absorption in sea water," *The Journal of the Acoustical Society of America*, vol. 62, no. 3, pp. 558–564, sep 1977. [Online]. Available: http://asa.scitation.org/doi/10.1121/1.381574

[38] E. Yeager, F. H. Fisher, J. Miceli, and R. Bressel, "Origin of the low-frequency sound absorption in sea water," *The Journal of the Acoustical Society of America*, vol. 53, no. 6, pp. 1705–1707, 1973. [Online]. Available: https://doi.org/10.1121/1.1913523

[39] M. Schulkin and H. W. Marsh, "Sound Absorption in Sea Water," *The Journal of the Acoustical Society of America*, vol. 34, no. 6, pp. 864–865, jun 1962. [Online]. Available: http://asa.scitation.org/doi/10.1121/1.1918213

[40] M. Eigen and K. Tamm, "Sound absorption in solutions of electrolytes as a consequence of chemical relaxation. 2. Experimental results and relaxation mechanisms for 2-2 electrolytes," *Journal of Electrochemistry*, vol. 66, pp. 107–121, 1962.

[41] A. J. Hunter, "Underwater Acoustic Modelling for Synthetic Aperture Sonar," Ph.D. dissertation, University of Canterbury, Christchurch, New Zealand, 2006. [Online]. Available: http://ir.canterbury.ac.nz/handle/10092/1117

[42] M. P. Hayes and P. T. Gough, "Broad-band Synthetic Aperture Sonar," vol. 17, no. 1, 1992.

[43] P. J. Barclay, "Interferometric Synthetic Aperture Sonar Design and Performance," PhD thesis, University of Canterbury, Christchurch, New Zealand, 2007. [Online]. Available: https://ir.canterbury.ac.nz/handle/10092/1170

[44] E. Kreyszig, *Advanced engineering mathematics*, 10th ed. John Wiley & Sons, 2011.

[45] D. W. Hawkins, "Synthetic Aperture Imaging Algorithms: with application to wide bandwidth sonar," Ph.D. dissertation, University of Canterbury, Christchurch, New Zealand, 1996. [Online]. Available: https://pdfs.semanticscholar.org/6165/08fa3716d8897ab538467635fb75cdfd43b2.pdf

[46] J. W. Goodman, *Fourier Optics*. McGraw Hill Book Company, New York, 1968.

[47] "Edgetech side scan sonar." [Online]. Available: https://www.edgetech.com/product-category/side-scan-sonar/

[48] "Tritech imaging sonars: side scan." [Online]. Available: https://www.tritech.co.uk/product-category/imaging-sonars-towed

[49] "Klein Marine Systems Inc. Side Scan Sonar." [Online]. Available: http://kleinmarinesystems.com/products/side-scan-sonar/

[50] D. W. Hawkins and P. T. Gough, "Temporal doppler effects in SAS," in *Institute of Acoustics - Sonar Signal Processing*, vol. 26, 2004. [Online]. Available: https://pdfs.semanticscholar.org/1287/9516389800649e9c8a553a677ffde5d56c26.pdf

[51] Y. Pailhas, S. Dugelay, and C. Capus, "Impact of temporal Doppler on synthetic aperture sonar imagery," *The Journal of the Acoustical Society of America*, vol. 143, no. 1, pp. 318–329, 2018. [Online]. Available: https://asa.scitation.org/doi/10.1121/1.5021250

[52] U. Herter, B. Bonnett, H. Schmaljohann, and T. Fickenscher, "Impact of temporal doppler on CSAS imagery," in *Proceedings of the Underwater Acoustics Conference and Exhibition (UACE)*, 2019, pp. 163–170. [Online]. Available: http://www.uaconferences.org/docs/2019{_}papers/UACE2019{_}931{_}Herter.pdf

158

[53] H. J. Callow, "Signal Processing for Synthetic Aperture Sonar Image Enhancement," PhD thesis, University of Canterbury, 2003. [Online]. Available: https://pdfs. semanticscholar.org/80c4/8c09f042dd69a352ff0008dabcec6e5491cb.pdf

[54] A. Bellettini and M. A. Pinto, "Design and Experimental Results of a 300-kHz Synthetic Aperture Sonar Optimized for Shallow-Water Operations," *IEEE Journal of Oceanic Engineering*, vol. 34, no. 3, pp. 285–293, 2009. [Online]. Available: https://ieeexplore.ieee.org/document/4674519

[55] J. L. Kennedy, T. M. Marston, K. Lee, J. L. Lopes, and R. Lim, "A rail system for circular synthetic aperture sonar imaging and acoustic target strength measurements: Design/operation/preliminary results," *Review of Scientific Instruments*, vol. 85, no. 1, 2014. [Online]. Available: https://aip.scitation.org/doi/full/10.1063/1.4861353

[56] Y. Pailhas, S. Fioravanti, and S. Dugelay, "The high resolution low frequency synthetic aperture sonar (HR-LFSAS) project," *Proceedings of the Institute of Acoustics*, vol. 40, pp. 66–72, 2018.

[57] Z. Rymansaib, A. J. Hunter, C. Bowen, J. Dillon, and R. Charron, "Preliminary target measurements from a prototype multispectral synthetic aperture sonar," in *Proceedings of the Underwater Acoustics Conference and Exhibition (UACE)*, 2019, pp. 899–904. [Online]. Available: http://www.uaconferences.org/docs/2019{_}papers/UACE2019{_} 945{_}Rymansaib.pdf

[58] M. Jönsson, J. Pihl, and M. Åklint, "Imaging of buried objects by low frequency SAS," in *IEEE OCEANS*, vol. 1, Brest, France, 2005, pp. 669–673. [Online]. Available: https://ieeexplore.ieee.org/document/1511794

[59] Y. Pailhas, Y. Petillot, C. Capus, and R. Hollett, "Study, design and concept of low frequency SAS," *Proceedings of the Institute of Acoustics*, vol. 32, no. 4, pp. 92–97, 2010. [Online]. Available: http://osl.eps.hw.ac.uk/files/uploads/publications/ICSARSAS{_} Pailhas.pdf

[60] D. D. A. Maclean, "Multichannel Detection and Acoustic Color-Based Classification of Underwater UXO in Sonar," Department of Defense Strategic Environmental Research and Development Program (SERDP), Tech. Rep. June, 2015. [Online]. Available: https://apps.dtic.mil/dtic/tr/fulltext/u2/1022213.pdf

[61] J. J. Hall, M. R. Azimi-Sadjadi, S. G. Kargl, Y. Zhao, and K. L. Williams, "Underwater Unexploded Ordnance (UXO) Classification Using a Matched Subspace Classifier With Adaptive Dictionaries," *IEEE Journal of Oceanic Engineering*, vol. 44, no. 3, pp. 739–752, 2018. [Online]. Available: https://ieeexplore.ieee.org/document/8396265

[62] P. E. Hagen and R. E. Hansen, "Area Coverage Rate of Synthetic Aperture Sonars," in *IEEE OCEANS*. Aberdeen: IEEE, 2007, pp. 1–5. [Online]. Available: http://ieeexplore.ieee.org/document/4302382/

[63] M. P. Hayes and P. T. Gough, "Synthetic Aperture Sonar: A Review of Current Status," *IEEE Journal of Oceanic Engineering*, vol. 34, no. 3, pp. 207–224, 2009. [Online]. Available: http://ieeexplore.ieee.org/document/5191242/

[64] D. Johnson and D. Dudgeon, *Array Signal Processing: Concepts and Techniques.* Upper Saddle River, NJ, USA: Prentice-Hall, 1993.

[65] M. Soumekh, *Synthetic Aperture Radar Signal Processing.* New York, NY, USA: Wiley, 1999.

[66] S. A. V. Synnes, A. J. Hunter, R. E. Hansen, T. O. Sabo, H. J. Callow, R. Van Vossen, and A. Austeng, "Wideband Synthetic Aperture Sonar Backprojection with Maximization of Wave Number Domain Support," *IEEE Journal of Oceanic Engineering*, vol. 42, no. 4, pp. 880–891, 2017. [Online]. Available: https://ieeexplore.ieee.org/document/7740850

[67] O. Frey, C. Magnard, M. Rüegg, and E. Meier, "Focusing of airborne synthetic aperture radar data from highly nonlinear flight tracks," *IEEE Transactions on Geoscience and Remote Sensing*, vol. 47, no. 6, pp. 1844–1858, 2009. [Online]. Available: https://ieeexplore.ieee.org/document/4812049

[68] R. Bamler, "A Systematic Comparison Of SAR Focussing Algorithms," in *Proceedings of IEEE International Geoscience and Remote Sensing Symposium*, 1991, pp. 1005–1009. [Online]. Available: https://ieeexplore.ieee.org/document/580289

[69] Richard Bamler, "A Comparison of Range-Doppler and Wavenumber Domain SAR Focusing Algorithms," *IEEE Transactions on Geoscience and Remote Sensing*, vol. 30, no. 4, pp. 706–713, 1992. [Online]. Available: https://ieeexplore.ieee.org/document/158864

[70] R. H. Stolt, "Migration By Fourier Transform," *Geophysics*, vol. 43, no. 1, pp. 23 – 48, 1978.

[71] I. Cumming, F. Wong, and K. Raney, "A SAR processing algorithm with no interpolation," in *International Geoscience and Remote Sensing Symposium (IGARSS)*, vol. 1, 1992, pp. 376–379. [Online]. Available: https://ieeexplore.ieee.org/document/576716

[72] D. W. Hawkins, "An accelerated chirp scaling imaging algorithm for synthetic aperture sonar," in *Proceedings of IEEE International Geoscience and Remote Sensing Symposium*, vol. 1, 1997, pp. 471–473. [Online]. Available: https://ieeexplore.ieee.org/stamp/stamp.jsp?tp={&}arnumber=615918

[73] A. J. Hunter, M. P. Hayes, and P. T. Gough, "A comparison of fast factorised back-projection and wavenumber algorithms," in *Proceedings of the 5th World Congress on Ultrasonics*, 2003, pp. 527–530. [Online]. Available: https://pdfs.semanticscholar.org/bd80/d8febbf66f5dfa0aec9c5321ec5e3250f883.pdf

[74] G. Shippey, "SAS Image Reconstruction using Fast Polar Back Projection : Comparisons with Fast Factored Back Projection and Fourier-Domain," in *Proceedings of the IEEE OCEANS Conference*, Brest, France, 2005, pp. 96–101. [Online]. Available: https://ieeexplore.ieee.org/document/1511691

[75] I. Gerg, "The Advanced Synthetic Aperture Sonar Imaging eNgine (ASASIN), a time-domain backprojection beamformer using graphics processing units," *The Journal of the Acoustical Society of America*, vol. 140, no. 4, pp. 3347–3347, 2016. [Online]. Available: http://asa.scitation.org/doi/10.1121/1.4970697

[76] H. D. Griffiths, "Synthetic Aperture Imaging With Sonar and Radar: A Comparison," in *Proceedings of the 5th World Congress on Ultrasonics*, vol. 53, no. 9, Paris, 2003, pp. 1689–1699. [Online]. Available: http://www.conforg.fr/wcu2003/procs/cd1/articles/000549.pdf

[77] H. D. Griffiths, T. A. Rafik, C. F. N. Cowan, D. K. Anthony, Z. Meng, and H. Shafeeu, "Interferometric synthetic aperture sonar for high-resolution 3-D mapping of the seabed," *IEE Proceedings - Radar, Sonar and Navigation*, vol. 144, no. 2, pp. 96–103, 1997. [Online]. Available: https://ieeexplore.ieee.org/document/591270

[78] L. C. Graham, "Synthetic Interferometer Radar For Topographic Mapping," *Proceedings of the IEEE*, vol. 62, no. 6, pp. 763–768, 1974. [Online]. Available: https://ieeexplore.ieee.org/abstract/document/1451446

[79] T. G. Farr, P. A. Rosen, E. Caro, R. Crippen, R. Duren, S. Hensley, M. Kobrick, M. Paller, E. Rodriguez, L. Roth, D. Seal, S. Shaffer, J. Shimada, J. Umland, M. Werner, M. Oskin, D. Burbank, and D. Alsdorf, "The Shuttle Radar Topography Mission," *Reviews of Geophysics*, vol. 45, no. 2, p. RG2004, may 2007. [Online]. Available: http://doi.wiley.com/10.1029/2005RG000183

[80] J. L. Kennedy, V. Ave, and T. M. Marston, "Multipass and Non-concentric Target Circular Synthetic Aperture Sonar (CSAS): Final Report," Naval Surface Warfare Center Panama City Division, Tech. Rep. January, 2018. [Online]. Available: https://www.serdp-estcp.org/content/download/47862/456074/file/MR-2439FinalReport.pdf

[81] G. C. Carter, C. Knapp, and A. H. Nuttall, "Statistics of the estimate of the magnitute-coherence function," *IEEE Transactions on Audio and Electroacoustics*, vol. 21, no. 4, pp. 388–389, 1973.

[82] R. M. Goldstein, H. A. Zebker, and C. L. Werner, "Satellite radar interferometry: Two-dimensional phase unwrapping," *Radio Science*, vol. 23, no. 4, pp. 713–720, 1988. [Online]. Available: http://doi.wiley.com/10.1029/RS023i004p00713

[83] D. C. Giglia and M. D. Pritt, *Two-Dimensional Phase Unwrapping: Theory, Algorithms, and Software*, 1st ed. Wiley-Interscience, 1998.

[84] H. Yu, Y. Lan, Z. Yuan, J. Xu, and H. Lee, "Phase unwrapping in InSAR : A review," *IEEE Geoscience and Remote Sensing Magazine*, vol. 7, no. 1, pp. 40–58, 2019. [Online]. Available: https://ieeexplore.ieee.org/document/8672140

[85] R. E. Hansen, H. J. Callow, T. O. Sæbø, S. A. V. Synnes, P. E. Hagen, T. G. Fossum, and B. Langli, "Synthetic aperture sonar in challenging environments: Results from the HISAS 1030," in *Proceedings of the 3rd International Conference and Exhibition on Underwater Acoustic Measurements, Technologies and Results*, Nafplion, Greece, 2009, pp. 409–416. [Online]. Available: http://www.uaconferences.org/docs/Past{_} Proceedings/UAM2009{_}Proceedings.pdf

[86] R. E. Hansen, H. J. Callow, T. O. Sæbø, and S. A. V. Synnes, "Challenges in seafloor imaging and mapping with synthetic aperture sonar," *IEEE Transactions on Geoscience and Remote Sensing*, vol. 49, no. 10, pp. 3677–3687, 2011. [Online]. Available: https://ieeexplore.ieee.org/abstract/document/5937049

[87] W. A. Connors, A. J. Hunter, and J. Dillon, "Increasing Navigation Effectiveness in GPS Denied Environments Using Through-The-Sensor SAS Techniques," in *Proceedings of the Institute of Acoustics*, vol. 40, no. 2, 2018, pp. 99–106. [Online]. Available: https://krakenrobotics.com/wp-content/uploads/2019/06/2018-SASSAR{_} coh{_}nav{_}v2-1.pdf

[88] P. Gough and M. Miller, "The SAR map-drift algorithm extended for a multi-hydrophone SAS," in *Proceedings of the MTS/IEEE OCEANS Conference*, 2003, pp. 2427–2432. [Online]. Available: https://ieeexplore.ieee.org/document/1282925

[89] H. Schmaljohann, J. Groen, U. Hölscher-Höbing, and W. Jans, "Dual-sided micronavigation for synthetic aperture sonar," in *Proceedings of the 1st International Conference and Exhibition on Underwater Acoustics*, 2013, pp. 119–126. [Online]. Available: http://www.uaconferences.org/docs/Past{_}Proceedings/UACE2013{_}Proceedings.pdf

[90] B. W. Thomas, A. J. Hunter, and S. Dugelay, "Model-based 3D micro-navigation and bathymetry estimation for interferometric synthetic aperture sonar," in *Proceedings of the Underwater Acoustics Conference and Exhibition (UACE)*, 2019.

[91] S. A. V. Synnes, H. J. Callow, R. E. Hansen, and T. O. Sæbø, "Multipass coherent processing on synthetic aperture sonar data," in *Proceedings of the European Conference on Underwater Acoustics (ECUA)*, Istanbul, 2010. [Online]. Available: https://www.semanticscholar. org/paper/Multipass-coherent-processing-on-synthetic-aperture-Synnes-Callow/ fc5e2de7b083a3e56b587c497c46f1392af56842

[92] A. J. Hunter, W. A. Connors, and S. Dugelay, "An Operational Concept for Correcting Navigation Drift During Sonar Surveys of the Seafloor," *IEEE*

Journal of Oceanic Engineering, pp. 1–14, 2017. [Online]. Available: http://ieeexplore.ieee.org/document/8119508/

[93] J. M. Silkaitis, B. L. Douglas, and H. Lee, "A cascade algorithm for estimating and compensating motion error for synthetic aperture sonar imaging," in *Proceedings of the International Conference on Image Processing, ICIP*, 1994, pp. 905–909. [Online]. Available: https://ieeexplore.ieee.org/document/413443

[94] H. J. Callow, R. E. Hansen, S. A. V. Synnes, and T. O. Sæbø, "Circular synthetic aperure sonar without a beacon," in *Proceedings of the 2nd International Conference and Exhibition on Underwater Acoustic Measurements, Technologies and Results*, 2009. [Online]. Available: https://pdfs.semanticscholar.org/58b2/3cb4716b08d451ce7906c3842d106b633d09.pdf

[95] R. De Paulis, C. Prati, S. Scirpoli, F. Rocca, A. Tesei, P. A. Sletner, S. Biagini, P. Guerrini, F. Gasparoni, C. Carmisciano, and M. Locritani, "SAS multipass interferometry for monitoring seabed deformation using a high-frequency imaging sonar," in *Proceedings of the IEEE OCEANS Conference*. IEEE, 2011, pp. 1–10.

[96] S. Tebaldini, F. Rocca, M. Mariotti D'Alessandro, and L. Ferro-Famil, "Phase calibration of airborne tomographic SAR data via phase center double localization," *IEEE Transactions on Geoscience and Remote Sensing*, vol. 54, no. 3, pp. 1775–1792, 2016. [Online]. Available: https://ieeexplore.ieee.org/document/7308057

[97] P. T. Gough and M. A. Miller, "Displaced ping imaging autofocus for a multi-hydrophone SAS," *IEE Proceedings - Radar, Sonar and Navigation*, vol. 151, no. 3, 2004. [Online]. Available: https://ieeexplore.ieee.org/document/1312059?arnumber=1312059

[98] J. Coote and R. Aldred, "Application of displaced ping imaging autofocus algorithm to SAS trials data," *Proceedings of the Institute of Acoustics*, vol. 63, no. 1, pp. 244–252, 2014.

[99] J. Dillon and V. Myers, "Baseline estimation for repeat-pass interferometric synthetic aperture sonar," in *Proceedings of 10th European Conference on Synthetic Aperture Radar (EUSAR)*, 2014. [Online]. Available: https://ieeexplore.ieee.org/document/6857064

[100] J. Ogilvy, *Theory of Wave Scattering From Random Rough Surfaces*, 1st ed. CRC Press, 1991.

[101] R. S. Raven, "Electronic Stabilization for Displaced Phase Center Systems," U.S. Patent US4 244 036A, 1981.

[102] D. C. Brown, "Modeling and Measurement of Spatial Coherence for Normal Incidence Seafloor Scattering," PhD thesis, The Pennsylvania State University, 2017.

[103] T. O. Sæbø, R. E. Hansen, and A. Hanssen, "Relative height estimation by cross-correlating ground-range synthetic aperture sonar images," *IEEE Journal of Oceanic Engineering*, vol. 32, no. 4, pp. 971–982, 2007. [Online]. Available: https://ieeexplore.ieee.org/document/4445737

[104] S. Chapman and R. Orne, "A Robust Motion Compensation Solution for SAS," in *Proceedings of the 2nd International Conference and Exhibition on Underwater Acoustic Measurements, Technologies and Results*, 2007, p. 299.

[105] W. W. J. Bonifant, "Interferometic synthetic aperture sonar processing," Master's thesis, Georgia Institute of Technology, 1999.

[106] V. Tonard and M. Brussieux, "Towards development of autofocusing schemes for phase compensation of synthetic aperture sonars," in *Proceedings of the MTS/IEEE OCEANS Conference*, 1997, pp. 803–808. [Online]. Available: https://ieeexplore.ieee.org/document/624097

[107] T. O. Sæbø, R. E. Hansen, H. J. Callow, and S. A. V. Synnes, "Coregistration of Synthetic Aperture Sonar Images from Repeated Passes," in *Proceedings of the 4th International Conference and Exhibition on Underwater Acoustic Measurements, Technologies and Results*, 2011. [Online]. Available: http://www.uaconferences.org/docs/Past{_}proceedings/UAM2011{_}Proceedings.pdf

[108] B. Bonnett and M. Hayes, "Data-driven image registration for coherent change detection of synthetic aperture sonar imagery," in *Proceedings of the 29th International Conference on Image and Vision Computing New Zealand - IVCNZ*. New York, New York, USA: ACM Press, 2014, pp. 196–201. [Online]. Available: http://dl.acm.org/citation.cfm?doid=2683405.2683455

[109] R. E. Hansen, T. O. Sæbø, and O. J. Lorentzen, "Challenges in Coregistration of Repeated Passes in Synthetic Aperture Sonar," *Proceedings of the 12th European Conference on Synthetic Aperture Radar (EUSAR)*, pp. 344–349, 2018. [Online]. Available: https://ieeexplore.ieee.org/document/8438022

[110] D. Lowe, "Object recognition from local scale-invariant features," in *Proceedings of the Seventh IEEE International Conference on Computer Vision*. IEEE, 1999, pp. 1150–1157 vol.2. [Online]. Available: http://ieeexplore.ieee.org/document/790410/

[111] H. Bay, T. Tuytelaars, and L. V. Gool, "SURF: Speeded Up Robust Features," in *Computer Vision ECCV*, 2006, pp. 404–417. [Online]. Available: http://link.springer.com/chapter/10.1007/11744023{_}32

[112] T. S. Huang and A. N. Netravali, "Motion and Structure from Feature Correspondences: A Review," *Proceedings of the IEEE*, vol. 82, no. 2, pp. 252–268, 1994. [Online]. Available: https://ieeexplore.ieee.org/document/265351

[113] V. Wang and M. Hayes, "Modelling of feature matching performance on correlated speckle images," in *International Conference on Image and Vision Computing New Zealand (IVCNZ)*. IEEE, 2016. [Online]. Available: http://ieeexplore.ieee.org/document/7804419/

[114] J. L. Prater and T. G-Michael, "Interferometric measurements using redundant phase centers of synthetic aperture sonars," in *Proceedings of the MTS/IEEE OCEANS Conference*. Biloxi: MTS, 2009. [Online]. Available: https://ieeexplore.ieee.org/document/5422295

[115] Q. Ziliang, "Three dimensional SAS motion error estimation employing near-field beamforming," *EUSAR 2018: 12th European Conference on Synthetic Aperture Radar, Proceedings of*, pp. 332–337, 2018. [Online]. Available: https://ieeexplore.ieee.org/document/8438020

[116] I. Gerg, "Moving away from the phase center approximation in micronavigation for synthetic aperture sonar," *The Journal of the Acoustical Society of America*, vol. 140, no. 4, pp. 3348–3348, oct 2016. [Online]. Available: http://asa.scitation.org/doi/10.1121/1.4970698

[117] X. Zhang, X. Chen, and W. Qu, "Influence of the stop-and-hop assumption on synthetic aperture sonar imagery," in *International Conference on Communication Technology Proceedings, ICCT*, 2017, pp. 1601–1607.

[118] F. Harris, "On the use of windows for harmonic analysis with the discrete Fourier transform," *Proceedings of the IEEE*, vol. 66, no. 1, pp. 51–83, 1978. [Online]. Available: http://ieeexplore.ieee.org/document/1455106/

[119] H. A. Zebker and J. Villasenor, "Decorrelation in interferometric radar echoes," *IEEE Transactions on Geoscience and Remote Sensing*, vol. 30, no. 5, pp. 950–959, 1992.

[120] D. C. Brown, A. P. Lyons, and D. A. Cook, "Spatial coherence theory and its application to synthetic aperture systems," *Proceedings of the Institute of Acoustics Conference on Synthetic Aperture Sonar and Synsthetic Aperture Radar*, vol. 36, pp. 104–111, 2014.

[121] F. R. Dickey, "The correlation aircraft navigator, a vertically beamed Doppler radar," in *Proceedings of the National Conference on Aeronautical Electronics*. Institute of Radio Engineers, 1958, pp. 403–468.

[122] ——, "Velocity measuring correlation sonar," *The Journal of the Acoustical Society of America*, vol. 70, no. 3, pp. 914–914, sep 1981. [Online]. Available: http://asa.scitation.org/doi/10.1121/1.386867

[123] P. N. Denbigh, "A Design Study for a Correlation Log to Measure Speed at Sea," *Journal of Navigation*, vol. 35, no. 1, pp. 160–184, 1982. [Online]. Available: https://www.cambridge.org/core/journals/journal-of-navigation/

article/design-study-for-a-correlation-log-to-measure-speed-at-sea/
397A6E99EEACB108B5B876356F5EEE59

[124] V. Dickey, W. Bookheimer, and K. Rhoades, "Implementation and Testing of a Deepwater Correlation Velocity Sonar," in *Proceedings of the Offshore Technology Conference*, apr 1983.

[125] P. Denbigh, "Ship velocity determination by Doppler and correlation techniques," *IEE Proceedings of Communications, Radar and Signal Processing*, vol. 131, no. 3, pp. 315–326, 1984. [Online]. Available: https://ieeexplore.ieee.org/document/4646247

[126] Z. Weiqing, F. Lei, W. Changhong, W. Yuling, and Q. Wei, "Theory and signal processing of acoustic correlation techniques for velocity measurement of vessel," *IEEE Journal of Oceanic Engineering*, vol. 36, no. 2, pp. 338–346, 2011. [Online]. Available: https://ieeexplore.ieee.org/document/5766778

[127] P. Stevens, "Design, calibration and evaluation of a two axis correlation log for use on autonomous underwater vehicle," in *Proceedings of the Symposium on Autonomous Underwater Vehicle Technology*, 1990, pp. 181–185. [Online]. Available: https://ieeexplore.ieee.org/document/110454

[128] G. Campanella and W. Holt, "Correlation-log-based underwater navigation," in *Symposium on Autonomous Underwater Vehicle Technology*. IEEE, 1990, pp. 186–193. [Online]. Available: http://ieeexplore.ieee.org/document/110455/

[129] B. L. Grose, "The application of the correlation sonar to autonomous underwater vehicle navigation," *Proceedings of the Symposium on Autonomous Underwater Vehicle Technology*, pp. 298–303, 1992.

[130] "Tritech AquaTrak CVL." [Online]. Available: https://www.tritech.co.uk/product/aquatrak-cvl

[131] T. E. Blanford, D. C. Brown, and R. Meyer, "Design considerations for a compact correlation velocity log," *The Journal of the Acoustical Society of America*, vol. 143, no. 3, pp. 1762–1762, 2018.

[132] P. Boltryk, M. Hill, A. Keary, B. Phillips, H. Robinson, and P. White, "An ultrasonic transducer array for velocity measurement in underwater vehicles," *Proceedings of Ultrasonics International*, vol. 42, no. 1-9, pp. 473–478, 2004. [Online]. Available: https://www.sciencedirect.com/science/article/pii/S0041624X03002592

[133] J. Groen, "Adaptive motion compensation in sonar array processing," PhD thesis, Technische Universiteit Delft, 2006.

[134] J. W. Oeschger, "Estimating Along-Track Displacement Using Redundant Phase Centers," *Proceedings of the Institute of Acoustics*, vol. 28, pp. 160–167, 2006.

[135] D. C. Brown, I. D. Gerg, and T. E. Blanford, "Interpolation Kernels for Synthetic Aperture Sonar Along-Track Motion Estimation," *IEEE Journal of Oceanic Engineering (Early Access)*, 2019. [Online]. Available: https://ieeexplore.ieee.org/document/8768320/

[136] M. Abramowitz and A. Stegun, *Handbook of Mathematical Functions*, 5th ed. New York, NY, USA: Dover, 1964.

[137] G. Carter, "Time delay estimation for passive sonar signal processing," *IEEE Transactions on Acoustics, Speech, and Signal Processing*, vol. 29, no. 3, pp. 463–470, 1981. [Online]. Available: http://ieeexplore.ieee.org/document/1163560/

[138] A. H. Quazi, "An overview of time delay estimation in active and passive system for target localization," *IEEE Transactions on Acoustics, Speech, and Signal Processing*, vol. 29, no. 3, pp. 527–533, 1981. [Online]. Available: https://ieeexplore.ieee.org/document/1163618

[139] M. A. Fischler and R. C. Bolles, "Random sample consensus: a paradigm for model fitting with applications to image analysis and automated cartography," *Communications of the ACM*, vol. 24, no. 6, pp. 381–395, 1981. [Online]. Available: http://portal.acm.org/citation.cfm?doid=358669.358692

[140] K. Iverson, *A Programming Language.* Wiley, 1962. [Online]. Available: http://www.jsoftware.com/papers/APL.htm

[141] B. Thomas, A. Hunter, and S. Dugelay, "Phase Wrap Error Correction by Random Sample Consensus With Application to Synthetic Aperture Sonar Micronavigation," *IEEE Journal of Oceanic Engineering*, pp. 1–15, 2020. [Online]. Available: https://ieeexplore.ieee.org/document/9001250/

[142] A. F. Möbius, *Der Barycentrische Calcul*, J. Barth, Ed. Franklin Classics Trade Press, 1827.

[143] S. A. Forth, "An efficient overloaded implementation of forward mode automatic differentiation in MATLAB," *ACM Transactions on Mathematical Software*, vol. 32, no. 2, pp. 195–222, 2006. [Online]. Available: http://portal.acm.org/citation.cfm?doid=1141885.1141888

[144] D. A. Cook and D. C. Brown, "Analysis of Phase Error Effects on Stripmap SAS," *IEEE Journal of Oceanic Engineering*, vol. 34, no. 3, pp. 250–261, 2009. [Online]. Available: https://ieeexplore.ieee.org/document/4700812